THE EFFECTS OF MICROSTRUCTURAL INHOMOGENEITY ON DAMAGE ACCUMULATION AND FRACTURE

BY

GENE BURGER

A Thesis

Submitted to the School of Graduate Studies

in Partial Fulfilment of the Requirements

for the Degree

Doctor of Philosophy

McMaster University

 June 1986

ISBN 0-315-33447-9

DAMAGE AND FRACTURE PROCESSES

IN INHOMOGENEOUS SYSTEMS

DOCTOR OF PHILOSOPHY (1986)
(Metallurgy and Materials Science)

McMASTER UNIVERSITY
Hamilton, Ontario

TITLE: The Effects of Microstructural Inhomogeneity on Damage Accumulation and Fracture

AUTHOR: Gene Burger, B.Sc.Eng. (Queen's University)

SUPERVISORS: Dr. J.D. Embury and Dr. D.S. Wilkinson

NUMBER OF PAGES: xxi, 398

ABSTRACT

A theoretical and experimental study has been made which indicates the importance of the spatial distribution of damage and a complete physical description of the operative damage processes in providing a fracture condition.

A continuum damage model is presented which investigates the influence of void coalescence in accelerating damage levels, for a random array of voids growing via a ductile hole growth mechanism. A simple geometric coalescence condition was assumed. The dependence of fracture strain upon initial void volume fraction and stress state history is predicted. This approach is extended in a simulation to predict the void size distribution which develops.

The Dirichlet tessellation was evaluated as a method for characterizing dispersions of points or particles. Point dispersions were generated, ranging from strongly periodic to strongly clustered, and properties of their associated tessellations were evaluated. This suggested parameters which were sensitive indicators of periodicity or clustering in a dispersion. This approach was extended to the characterization of inclusion and particle distributions in steels and several other alloys.

The influence of temperature and stress state on damage and fracture was studied in several continuously-cast HSLA steels. Fracture was controlled by the inclusions, the centre-line transformation products, or the interaction between these two sources of damage. Observations also suggested that the distribution of the banded transformation products could influence damage levels in the ferritic regions.

This study concludes with an investigation of the creep fracture in a Ni-Sn alloy, which contained an inhomogeneous tin distribution. The regions with high tin content accumulated damage rapidly, however, ductility was promoted by the material low in tin which did not cavitate as readily. The influence of stress level on the strain dependence of damage accumulation rate, and the shift to surface crack-controlled fracture was interpreted as an effect of the enhanced relative contribution of grain boundary sliding to total strain at lower stresses.

to Kaye

ACKNOWLEDGEMENTS

The author would like to express his sincere appreciation to his supervisors, Dr.J.D. Embury and Dr. D.S. Wilkinson, for the support and encouragement they have offered during the course of this work.

Helpful discussions with Dr. R. Sowerby and the members of the Mechanical Metallurgy Group are also acknowledged.

The author would like to express his gratitude to Dr. M.F. Ashby (University of Cambridge) for the hospitality and stimulating discussion offered during his visit to the University of Cambridge.

The tensile tests conducted under superimposed pressure were arranged by Dr. O. Richmond and Dr. W.A. Spitzig, for which the author is grateful.

The assistance provided by Mrs. Teresa Castillo in developing metallographic techniques was very much appreciated. In addition, the skill of Tom Bryner in the photographs, Martin Van Oosten in the diagrams and Ed McCaffery with hardware problems are gratefully acknowledged. The quick and accurate typing of Nicole Emslie was instrumental in getting things together on time.

Provision of the Ni-Sn alloy by Falconbridge Nickel Co., and the HSLA steels by the Steel Company of Canada, Ltd., are acknowledged.

Financial support was received from the National Science and Engineering Research Council and through an Ontario Graduate Scholarship during the course of this study.

TABLE OF CONTENT

LIST OF FIGURES

LIST OF TABLES

CHAPTER 1

INTRODUCTION

A variety of fracture modes have been associated with the accumulation of microstructural damage. This damage is usually observed as a distribution of voids or microcracks, whose characteristics are dependent upon temperature, stress state and strain history, and the nature and microstructure of the material. The development of these local fracture processes interrupts continued plastic deformation, and is dependent upon the deformation mechanism(s) operative under the given conditions.

Numerous studies of the influence of (uniaxial) stress and temperature upon the dominant fracture mode have been summarized by Ashby and co-workers (Ashby et. al., 1979; Ghandi and Ashby, 1979) in the form of fracture maps. These maps delineate regions in stress-temperature space where a given mode of fracture is observed. They provide potentially useful guidelines for materials selection and component design, and for the development of new materials.

It has been determined experimentally that the flow stress in metals has only a weak dependence upon the state of hydrostatic stress (Spitzig, 1979; Spitzig and Richmond, 1984). However, when damage is associated with voids and microcracking, there is of necessity a degree of dilatancy involved which corresponds to the average level of damage

which has developed. It is thus expected that the hydrostatic stress state should influence the accumulation of damage. Indeed, it has been observed that the mode of fracture can be altered through the application of hydrostatic pressure during deformation (Bridgman, 1952; Teirlinck, 1983). This has resulted in the development of fracture maps in $\bar{\sigma}$ - P space (Ashby et. al., 1985), where $\bar{\sigma}$ is the effective stress and P the mean stress level.

It has been noted that the occurrence and mode of fracture are also very sensitive to impurity effects and inhomogeneity in microstructure (Ashby et. al., 1979). Heterogeneities in microstructural distribution can result in a marked alteration of the local stress and strain state (Argon, Im and Safoglu, 1975). Thus the local critical conditions and the rate at which damage processes occur may not necessarily be given by the macroscopic conditions. The development of damage and subsequent fracture must be viewed as a spatially heterogeneous process. It is often observed that a degree of void or microcrack coalescence precedes final fracture, due to the formation of a dominant flaw (McClintock, 1968b; Teirlinck, 1983). The critical average damage level resulting in final failure is dependent upon the distribution of damage events throughout the material. This, in turn, is dependent upon the spatial distribution of microstructural components which act as sites for the initiation of damage.

In using current models for damage initiation (Smith, 1966; Goods and Brown, 1979) and growth (McClintock, 1968a; Rice and Tracey, 1969) to predict fracture it is commonly assumed that the distribution

of damage is spatially uniform, i.e., periodic. The use of average microstructural parameters in these models, such as the average inclusion spacing, has contributed to significant discrepancies between predictions of fracture behaviour and experimental observations (Thomason, 1974; McClintock et. al., 1981). In ductile fracture, the more closely-spaced voids may coalesce prior to fracture to produce a larger void. The increase in void size due to coalescence will result in an increase in its rate of growth. Present models of the ductile fracture process do not incorporate the influence of void linkage in enhancing the damage accumulation rate.

A continuum damage model is presented here which illustrates the effects of void coalescence in accelerating damage. An initially random dilute distribution of voids was assumed. As this approach yields only an average damage level, the extension of the method to yield a size distribution of flaws is then treated. The analysis developed here is considered to provide a limit to which a global continuum damage model may realistically describe the level of damage in ductile fracture processes.

However, the effects of non-random microstructural inhomogeneity cannot be incorporated into such models. There is thus a need for techniques to usefully characterize the distribution of microstructural features. These would provide information which could then be used to predict extremes in local damage levels. This approach could provide useful insight into the fracture properties of heterogeneous materials. Practical methods of spatial characterization, however, have not been well developed to date.

We therefore consider an approach to characterizing the distribution of particles in a plane section, though the construction of the Dirichlet tessellation (Wray et. al., 1983). This geometrical construction serves to identify neighbours of a given particle, so that the local surroundings about particles may be quantitatively characterized. These results are then useful in assessing the degree of clustering and anisotropy in a dispersion of, say, inclusions or second-phase precipitates. The parameters used in such a description of microstructural distribution have dimensions of length, or (local) area fraction, and are thus readily incorporated into models of damage accumulation and fracture. In order to evaluate the effectiveness of the tessellation technique, a series of computer-generated point distributions have been analyzed. These exhibit varying degrees of clustering, moving towards a more random dispersion and beyond, approaching a periodic array. This is followed by the analysis of several microstructures which are of practical importance.

A successful damage mechanics approach to predicting fracture should have a physical basis, so that changes in fracture behaviour as conditions of temperature or stress state are varied can be expected. Thus, one must consider the physical mechanisms and processes which contribute to the development of damage, and their relationship with microstructure. For example, damage initiation at a hard particle could be the result of decohesion at the particle/matrix interface, or due to the fracture of the particle. Subsequent growth of the flaw may be through a plastic hole growth process, or via brittle transgranular

cleavage, depending upon the stress state and temperature. It is important to note that these processes operate locally, and in a competitive manner. Thus by changing the conditions under which deformation is occurring, the local conditions can be altered and the dominant fracture process will change. Incorporating models of damage processes with a physical and microstructural basis into a continuum description of flow would provide a more realistic method of predicting damage accumulation and fracture.

The modification of local stresses and strains due to heterogeneity in microstructural distribution can alter the global conditions of stress and strain at which damage initiates, and the subsequent processes which are dominant. As an indication of the local conditions attained and their influence on the character of damage which develops, it would be useful to study the accumulation of damage in inhomogeneous materials under varying conditions of stress, stress state and temperature. The work presented here considers a limited investigation of these effects in continuously-cast hot-rolled HSLA steels for line pipe application. These steels were both microstructurally inhomogeneous and anisotropic in mechanical behaviour.

A series of tensile tests were performed in the rolling, transverse and through-thickness orientations at ambient temperature, to determine the effects of directionality in microstructure on the nature of damage and fracture. Tests were also conducted at -196°C, thereby increasing the flow stress of the ferrite matrix. In addition, the influence of an applied hydrostatic pressure was studied, in an attempt

to estimate critical local stresses involved in the observed damage processes. These results do not represent a complete study, but rather survey a range of damage processes which can operate in a heterogeneous microstructure in a commercial material. Critical conditions are then dependent not only upon the stress level and temperature, but also upon the orientation of the stress axes with respect to the microstructure.

The concepts of damage mechanics have also been applied to high temperature fracture (Kachanov, 1958; Leckie and Hayhurst, 1977). Intergranular failure modes are often observed, associated with voids and/or microcracking which develops on the grain boundaries. Here again a continuum damage approach to failure cannot include the effects of local variations in chemical composition (e.g., impurities and solute levels), grain size, or the distribution of second-phase particles on the cavitation and microcracking processes, as they can operate interactively.

The effect of the distribution of solute on damage accumulation was isolated in an investigation on creep fracture in an alloy of Ni-1 wt % Sn. The distribution of tin in the material followed the segregation pattern developed during solidification. The results were compared with a material of the same nominal composition, which was chill-cast to obtain a more uniform solute distribution (White et. al., 1983). The solute pattern influenced the deformation behaviour and the distribution of damage which developed. By varying the stress level the nature of surface cracking as a competitive source of damage to wedge-cracks and intergranular cavitation was illustrated.

The current study is thus directed towards identifying various forms of damage which accumulate during deformation, and their dependence upon the conditions under which deformation is occurring, on both a local and global scale. The materials studied illustrated effects of heterogeneity upon the nature and distribution of damage which developed, and on the resulting mode of fracture. These results indicate the need for techniques which quantitatively assess the degree of heterogeneity in the initial microstructural distributions. A method employing the Dirichlet tessellation is presented and evaluated as a means of characterizing particle dispersions. The utility of this technique is gained in conjunction with microstructurally-based damage models to provide a description of the spatial distribution of damage which can develop in a given microstructure. The development of a dominant flaw in a region of locally high damage level can then be predicted, enabling the derivation of fracture criteria in heterogeneous microstructures which are based on global, or macroscoppic conditions.

CHAPTER 2

LITERATURE REVIEW

2.1 Introduction

The concept of cumulative material damage which develops during deformation has been addressed on both a phenomenological and a combined mechanistic and microstructural level. Phenomenologically, damage is treated as a variable w, in a continuum sense, and the mechanics of the damage process are developed in the formalism of continuum mechanics. This approach has been applied most commonly in the problem of creep rupture prediction.

The approach taken by materials scientists has been to categorize the various processes which contribute to the development of damage, and then to consider the dominant mechanisms which operate in these processes. Damage initiation criteria and growth rate laws are then developed in a form which can be incorporated into a constitutive law for the deformation process(es) operating.

This chapter first reviews the field of continuum damage mechanics, and is predominantly concerned with creep damage. The success and failure of these methods in life prediction is pointed out.

As the overall level of damage at which fracture occurs can be influenced by the character of the distribution of damage, techniques for quantifying the nature of a distribution of microstructural features

associated with damage or the specific damage features themselves are necessary. Methods of analysis of spatial point distributions applicable to this problem are discussed in the following section.

The damage processes which operate in a given material are dependent upon temperature, stress, and stress state. The processes involved in the major fracture modes observed in the present study under various conditions are reviewed. Thus, a brief survey is presented which discusses the analytical predictions and experimental observations of damage accumulation in ductile, shear, cleavage and high temperature intergranular fracture. Emphasis will be given to the effects of microstructural inhomogeneity on void or microcrack initiation and to the influence of an inhomogeneous distribution of damage on resulting fracture.

The chapter concludes with a review of the influence of microstructure on fracture behaviour in HSLA steels.

2.2 Continuum Damage Mechanics

The development of material damage during deformation, observed as voids, cracks, or substructural arrangements, alters the macroscopic stress-strain or stress-strain rate relationship. This is observed as the tertiary stage in creep deformation, or as the development of serrations in the flow curve at high strains in some aluminum alloys. The continuum damage mechanics approach incorporates the effect of a damage on the $\sigma-\varepsilon$ or $\sigma-\dot{\varepsilon}$ curves through a damage parameter w. This phenomenological approach to the analysis of fracture was initiated by Kachanov

(1958), and subsequently developed by Rabotnov (1969), Hult (1974), and Leckie and co-workers (Leckie and Hayhurst, 1977; Leckie, 1978; Hayhurst, 1983).

The assumption here is that a critical-sized defect in the material is larger than the scale of the inhomogeneity in damage distribution, so that the damage level may be given by a single scalar field parameter w. (For non-proportional loading histories, however, damage may take on directional characteristics. This complication will be discussed later.) This damage parameter is considered to be a state variable, that is, the stress history followed to a given damage level is assumed to have no influence on the damage accumulation rate and resulting failure for the remainder of the deformation path to final fracture. For an unflawed material w takes on a value of 0, and a value of 1 at fracture.

The application of this phenomenological treatment has been largely in the field of creep rupture, although it has been applied to consider the fracture toughness of a damaged material (Janson and Hult, 1977), by analyzing a Dugdale crack model (Dugdale, 1960) modified by damage ahead of the crack. Here, however, we will limit the discussion to developments in the field of creep-damage mechanics.

At elevated temperatures, above 0.3 to 0.5 T_m, where T_m is the melting point of the material, the uniaxial minimum creep strain rates are often described by Norton's law $\frac{\dot{\varepsilon}}{\dot{\varepsilon}_o} = \left(\frac{\sigma}{\sigma_o}\right)^n$, at a given temperature,

where $\dot{\varepsilon}_o$ is the steady-state strain-rate at stress σ_o. The exponent n is material-dependent. (Note that the primary portion of the creep curve has been neglected.)

It is then assumed that the damage accumulation rate $\dot{w}$ depends upon the current stress state and damage level. The form of the damage rate equation usually employed for uniaxial stress at constant temperature is $\frac{\dot{w}}{\dot{w}_o} = \left[\frac{\sigma}{\sigma_o(1 - w)}\right]^m$, where $\dot{w}_o$ is a temperature-dependent rate constant, and m is a material parameter (Leckie and Hayhurst, 1977). The development of damage alters the creep rate, and this relationship is proposed to be (Rabotnov, 1969) $\frac{\dot{\varepsilon}}{\dot{\varepsilon}_o} = \left[\frac{\sigma}{\sigma_o(1 - w)}\right]^n$. This pair of coupled differential equations may be integrated for constant stress between the limits $w = 0$ at $t = 0$ and $w = 1$ at fracture time t_r to give (neglecting primary creep) $t_r = \frac{1}{(m + 1)\dot{w}_o}\left(\frac{\sigma}{\sigma_o}\right)^m$, where $\dot{w}_o = \frac{1}{(m + 1)t_o}$, and t_o is the rupture time at stress σ_o (Leckie and Hayhurst, 1977).

Leckie and Hayhurst (1974) have suggested a testing procedure for determining iso-damage curves in ε-t space, so that points associated with equivalent damage may be located on creep curves for different stress levels. It is assumed that damage is a state variable, and that a single state variable is adequate for defining damage at a point on a creep curve. Thus, a stress change made during a creep test would merely result in relocating on the creep curve for the new stress level

at a position with equivalent damage. The remainder of the creep life would be unaffected by the previous loading history. This is illustrated in Figure 2.1, where the stress level is increased from σ_1 to σ_2 at damage level w_1. By comparing the portion of the creep curve for the remainder of the creep life at stress σ_2 with the complete creep curve at stress σ_2, the position on the curve with equivalent damage level w_1 is obtained. The resulting contours of equivalent damage which can then be developed are illustrated in Figure 2.2 (Leckie and Hayhurst, 1977). These iso-damage plots are useful in predicting creep life under variable (proportional) loading schedules. Note that the primary creep regime, and indeed any transient effects associated with load changes have been ignored in this scheme (Leckie and Ponter, 1974).

Odqvist (1974) has generalized the stress-creep rate relationship for multiaxial stress states. Assuming the influence of damage on the deformation rate to be scalar in nature, the incorporation of the effect of damage into Odqvist's result has been given by Hayhurst (1983) as $\frac{\dot{\varepsilon}_{ij}}{\dot{\varepsilon}_o} = \frac{3}{2}\left(\frac{\sigma_e}{\sigma_o}\right)^{n-1} \frac{1}{(1-w)^n} \frac{S_{ij}}{\sigma_o}$ where σ_e is the effective stress and S_{ij} the components of the deviatoric stress tensor.

The results of Johnson et. al., (1962) on tension-torsion experiments on copper and aluminum alloys indicate that the ratios of the strain rate components remain reasonably constant through steady-state into tertiary creep, giving support to the above relationship.

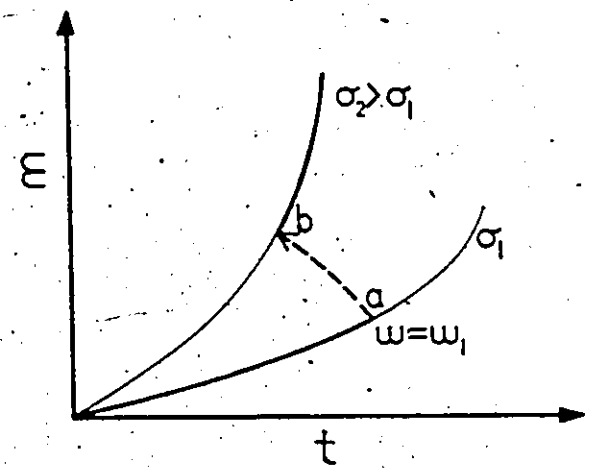

Fig. 2.1: Illustration of testing procedure to determine iso-damage positions on two different creep curves, through a stress change made during the creep test (from Leckie and Hayhurst, 1977).

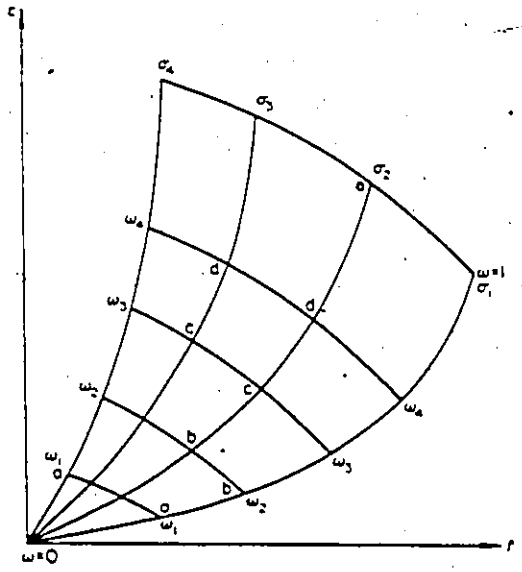

Fig. 2.2: Contours of equivalent damage, developed through stress-change testing procedure (from Leckie and Hayhurst, 1977).

The proposed form for the damage rate law under multiaxial stresses has been given as (Hayhurst, 1983) $\frac{\dot{w}}{\dot{w}_o} = \left[\frac{\Delta(\sigma_{ij}/\sigma_o)}{(1 - w)}\right]^m$, where $\Delta(\sigma_{ij}/\sigma_o)$ is a homogeneous function of the stress state. Experimental observations (Johnson et. al., 1962) indicate that the stress state influences the development of damage, but also show that the influence is material dependent. For copper alloys, the rupture times and thus damage accumulation rates are dependent upon the maximum normal stress σ_1, while in aluminum alloys it is the effective stress σ_e which correlates with rupture behaviour. Thus, in copper alloys $\Delta(\sigma_{ij}/\sigma_o)$ may be taken as σ_1/σ_o and in aluminum alloys as σ_e/σ_o.

The results of uniaxial creep tests are often presented as stress-rupture time curves. Most of the investigations on the effect of multiaxial stress states have not included tertiary strain measurements; only rupture times were recorded. These results are represented in stress space by an isochronous rupture surface, the locus of stress states having identical rupture times (Johnson et. al., 1962). Results indicated that the rupture of copper alloys was controlled by a maximum stress criterion, while in an aluminum alloy the effective stress defined the isochronous surface, as illustrated in Figure 2.3. It should be noted that most materials exhibit behaviour lying between these two extremes (Hayhurst, 1972, 1983; Dyson and McLean, 1977). This led Hayhurst (1972) to propose a general empirical relationship for the

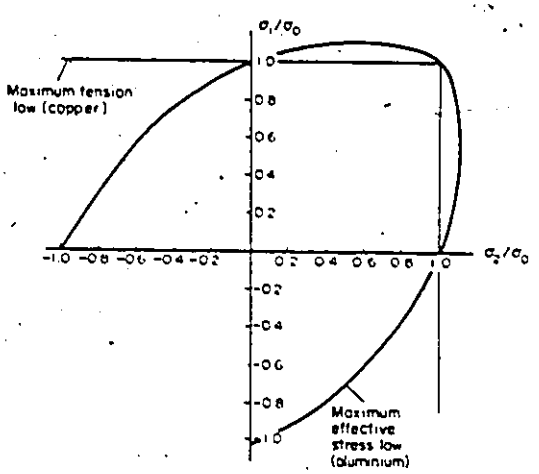

Fig. 2.3: Plane stress isochronous rupture loci for aluminum and copper. The rupture behaviour of aluminum is controlled by the maximum effective stress, while in copper the maximum tensile stress is controlling (from Leckie and Hayhurst, 1977).

insochronous surface in principal stress space as $\Delta\left(\frac{\sigma_{ij}}{\sigma_o}\right) = \alpha \frac{\sigma_1}{\sigma_o} + \beta \frac{\sigma_e}{\sigma_o} + \gamma \frac{J_1}{\sigma_o} = 1$, where J_1 is the first invariant of the stress tensor. Values of α, β and γ are found by conducting uniaxial tension, biaxial, and torsion tests. Hayhurst (1983) has observed that the more important parameters are α and β; usually the dependence upon J_1 is very weak.

The assumption that w is a scalar state variable was verified through experiments which considered both constant and variable load histories. However, the load changes in these earlier studies produced proportional stress states. Creep damage is seen to develop predominantly on grain boundaries normal to the maximum stress (Hull and Rimmer, 1959), even in aluminum alloys (Hayhurst, 1983). Thus the validity of a scalar damage parameter as a fracture predictor is questionable in situations where the direction of maximum principal tensile stress varies (i.e., for non-proportional load changes). Damage may then have vector characteristics.

The results of an investigation on several copper and aluminum alloys under tension-torsion states (Trampczynski et. al., 1981) suggest that failure in aluminum alloys can be adequately predicted by considering damage as a scalar. However, it was observed in copper alloys that the damage level on the most highly damaged plane controls the strain rate behaviour. The development of damage on planes at all orientations must be followed, taking into account the rotation of the

principal stress axes with time. Failure is then predicted to occur on the plane where the fracture criterion is attained first.

While the continuum damage mechanics approach has had a certain degree of success in predicting creep fracture, most notably in copper and aluminum alloys, it has not been successful in dealing with certain commercial high temperature alloys. For example, Dyson and McLean (1983) observed variations in damage level over distances of the order of 200 μm in cast nickel-base superalloys, corresponding to the variation in microstructure with the dendritic solidification pattern. The formalisms of continuum damage mechanics have not been adequately developed to analyze and predict failure in heterogeneous microstructures (Hult, 1979). Results of studies on creep of Nimonic 80A (Hayhurst et. al., 1980; Dyson and McLean, 1977) under non-proportional loading indicated that, in addition to observed directional characteristics of the damage which develops, the damage level was not completely given by a single parameter. A second parameter was required to rationalize their results, which related to the void nucleation rate. This consideration, which is necessary for a more complete understanding of the damage accumulation process in creep fracture, is dependent upon the material microstructure. The physical mechanisms and processes which result in creep damage and their dependence upon microstructure will be discussed in the following sections, leading to a physically-based formulation of damage mechanics.

2.3 The Characterization of Point/Particle Dispersions

The influence of a dispersion of hard particles on the flow stress behaviour of two-phase materials is dependent upon the average volume fraction and size of the second phase particles. The processes involved in fracture, however, are associated with the extreme behaviour of such dispersions, that is, the largest particles, and regions where the local volume fraction is much greater than the average. A large cluster of inclusions, for example, would result in a locally high damage level. This flawed region can markedly deteriorate the fracture properties in high strength steels.

This section reviews several approaches to the characterization of particle distributions in plane sections. For materials with a low average volume fraction of second phase, the dispersion of particles is usually treated as a point distribution defined by the centroids of the particles. Thus, the characterization of spatial point patterns in two dimensions is discussed first. The Dirichlet tessellation has recently been applied to the characterization of dispersions in several materials. This method will be discussed, as it appears to be a useful technique when used in conjunction with modern automatic image analyzers.

2.3.1 Analysis of Point Dispersions

The characterization of a distribution of points is often made by comparison, through a suggested test statistic, with a spatially random dispersion described by a Poisson distribution. This is a spatially

isotropic point distribution, with the probability distribution of n given by

$$P_n = \frac{(\lambda A)^n e^{-\lambda A}}{n!}, \quad n = 0, 1, 2 \ldots$$

where n is the number of points found in a random sample of area A, and λ is the average number of points per unit area (Diggle, 1983). The mean value of n would be λA.

Sparse sampling techniques, in which the point distribution is not mapped but only a portion sampled, consist basically of grid (quadrat) counting or distance methods (Diggle, 1983; Schwartz and Exner, 1983). In using these methods it must be observed that it is not a trivial matter as to whether or not the distribution has been sampled adequately to determine significant deviations from randomness.

Quadrat counts in small sample areas are usually compared with a random distribution through the variance in the point count distribution results. It is suggested (Diggle, 1983) that this provides a sensitive indicator of the deviation from randomness towards aggregation, but it is a relatively weak quantitative indicator of periodicity.

The scale of the pattern of distribution may be indicated by varying the grid size, and observing the change in the variance of point counts (Greig-Smith, 1952; Mead, 1974). Comparison with the results expected for a random dispersion would give a qualitative indication of deviation from randomness, or perhaps a characteristic periodicity in spacing or cluster separation. The quadrat count method can be extended

to further investigate clustering characteristics by varying the aspect ratio of the grid sample area, or to detect anisotropy by varying the orientation of the elongated sample quadrats. However, to obtain results which are sensitive to the specific characteristics of a dispersion, the grid sampling methodology would have to be optimized. To evaluate the properties of a dispersion of particles which control fracture behaviour (e.g., anisotropy, cluster dimensions, cluster spacing) by this approach could thus require a great deal of effort.

Distance methods of analyzing point distributions are often concerned with the distribution of nearest-neighbour or second nearest-neighbour distances from points selected randomly. For a homogeneous planar Poisson point process, the probability distribution functions of nearest-neighbour distance (r_1) and second nearest-neighbour distance (r_2) are, respectively

$$f(r_1) = 2\pi\lambda r_1 \exp(-\pi\lambda r_1^2)$$

and

$$f(r_2) = 2\pi^2\lambda^2 r_2^3 \exp(-\pi\lambda r_2^2)$$

For the nearest-neighbours, the expected mean $E(\bar{r}_1)$ and expected variance $E(s_1^2)$ of r_1 are given by

$$E(\bar{r}_1) = \frac{1}{2\sqrt{\lambda}}$$

and

$$E(s_1^2) = \frac{4 - \pi}{4\pi} \cdot \frac{1}{\lambda}$$ (Schwarz and Exner, 1983)

Schwarz and Exner (1983) used the average and the variance of the nearest-neighbour distance distribution (normalized with respect to the expected values for a random dispersion) together as test statistics to characterize deviation from randomness, and to suggest the nature of the clustering pattern. One should note, however, that Spitzig et. al. (1985) concluded that these parameters are not sensitive to small deviations from a random distribution.

Frequency distributions for the distance from a random position to the nearest point in the dispersion are easily determined. This technique is, in general, not as sensitive a test parameter as point-to-point distances (Diggle, 1983). In attempting to define parameters which are sensitive to non-random characteristics, several more complicated expressions may be defined, which include more than one random variable. As an example, a joint probability distribution function may be derived from two random variables, say d_1 and d_2, where d_1 is the distance from an arbitrarily selected location to the nearest point and d_2 the distance from this point to the nearest other point (Diggle, 1983). This is illustrated in Figure 2.4. Related to this approach several other test statistics are proposed in Diggle (1983), for which the distributions may be evaluated in a random distribution. One important point which should be noted, however, is that these statistical indicators are often not equally sensitive to both deviations towards agglomeration and periodicity.

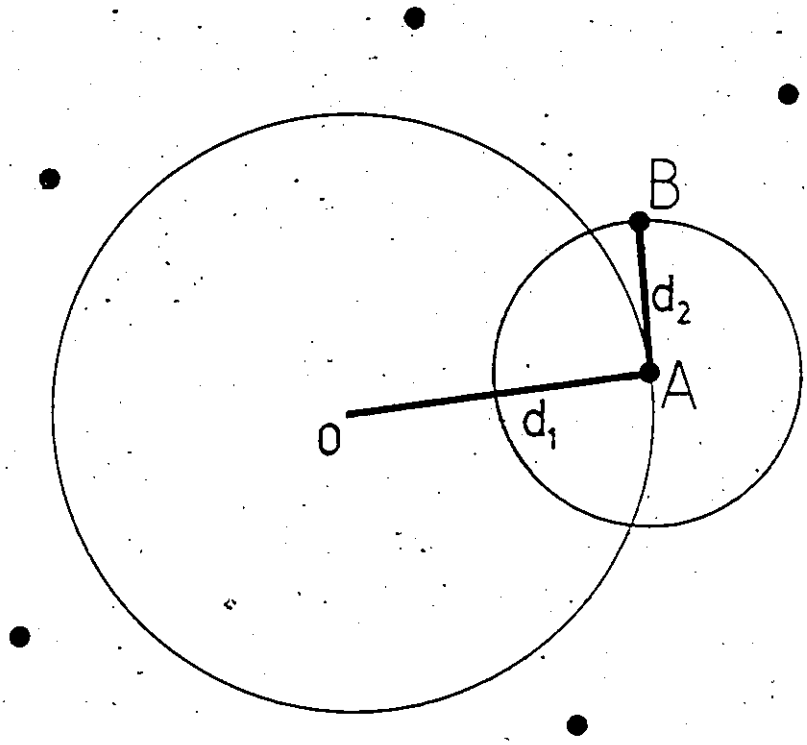

Fig. 2.4: Illustration of the distances d_1 and d_2 used in defining a joint probability distribution function, to characterize a point dispersion. O is a randomly selected location, with point A the nearest point in the dispersion. In turn, point B is the nearest point to point A. Then, d_1 = OA and d_2 = AB.

Schwartz and Exner (1983) proposed a method of analysis which considers a general point dispersion as a distribution of clusters on a random background. They assume that this may be given by the superposition of two independent homogeneous Poisson point processes, one with a high point density and the other with a low density. The point densities of the two distributions were then estimated by fitting the sum of the two different random probability density functions for each of the first and second nearest neighbour distributions to the observed distributions, through their moments. Then, to separate the clustered points from the background they use a critical distance criterion, defined as the separation between two points at which the probability of finding a neighbour is identical for either distribution. Schwartz and Exner give the critical distance for both nearest and second-nearest neighbours, and use these criteria to filter out the points belonging to the background distribution. If the distance from a given point to its nearest or second-nearest neighbour is greater than the associated critical value, the point is an element of the background.

The results showed a qualitative degree of success in separating points in clusters from those considered as the background. Their filtering method however, was more effective when the second-nearest neighbour criterion was used, with a sensitivity which could detect clusters with a point density ten times that of the background.

Another approach to classifying agglomeration makes use of the random theory of clumping (Roach, 1968). If we consider two points as clumped together if their separation is less than r, then in a random

array with N points per unit area, the number of clumps of n per unit area is given approximately by

$$\frac{NP_n}{n} = \frac{NP_1(1 - P_1)^{n-1}}{n}$$

where $P_1 = \exp(-\pi r^2 N)$ is the probability that a random point will have no other point within a distance r. The total number of isolated clumps of all sizes per unit area is then (approximately)

$$C_n = \frac{NP_1 \ell n P_1}{P_1 - 1} = \frac{\pi r^2 N^2}{\exp(\pi r^2 N) - 1}.$$

If one wanted to consider clumps in which all particles were within a distance r of each other, then the range of geometries which allow this must be considered. However, the algebraic difficulties in determining the densities of random clumps of more than three make the problem intractable (Armitage, 1949; Roach, 1968).

Thus, distance methods can be very useful in describing the deviation in the nature of a distribution from randomness. However, the description is necessarily incomplete: spatial anisotropy and the actual size and spacing of clustered regions (i.e., the pattern of clustering) cannot be dealt with. For this a complete mapping of the point distribution is required. Once this data is acquired, a technique utilizing the Dirichlet tessellation can provide additional information on the surroundings of each of the points in the distribution. This method will be discussed next.

2.3.2 The Dirichlet Tessellation

The Dirichlet tessellation is a geometrical construction which is uniquely defined by the positions of a distribution of points. The result is the division of the plane into convex polygonal subregions, each surrounding a single point. If we construct the perpendicular bisectors of the lines joining a particular point to those around it, the polygon, or Dirichlet cell about the given point is defined by the smallest envelope of bisectors. The construction is illustrated in Figure 2.5.

The polygons must therefore be convex and the tessellation is space-filling, in that the vertex of every polygon is the intersection of three perpendicular bisectors constructed between three points. It is useful to note that this vertex is the circumcentre of the triangle formed by these three points. For the perpendicular bisectors associated with three points to constitute a portion of the Dirichlet tessellation, no other point must lie within the circle passing through these three points. This is illustrated in Figure 2.6.

Each Dirichlet cell then encloses a region in which, for any location chosen, the closest point in the distribution is that point about which the cell was constructed. The neighbours of any given point are also uniquely defined by those points which are associated with the construction of the boundaries of the given cell. The cells can thus be used to provide information on the surroundings of each point in the

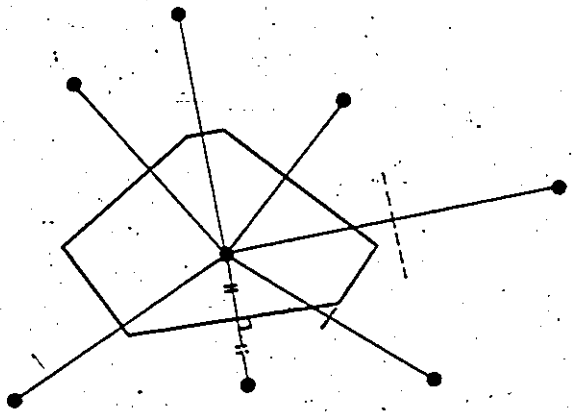

Fig. 2.5: Construction of a Dirichlet cell about a given point, given by the smallest envelope of perpendicular bisectors of the lines joining the given point to all other points in the dispersion.

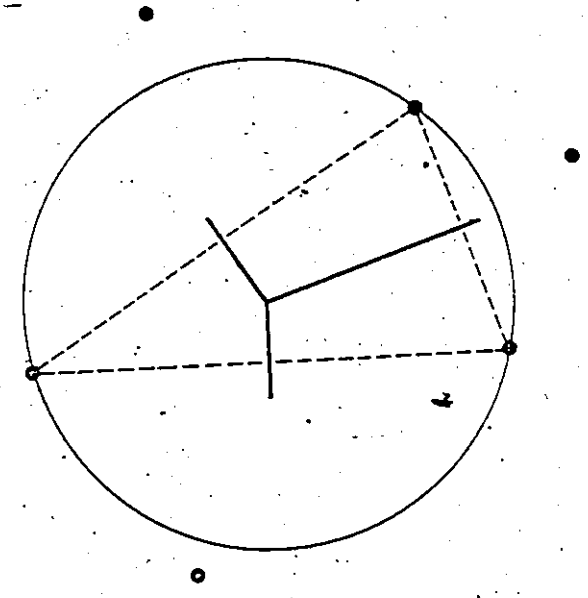

Fig. 2.6: Three perpendicular bisectors of the (dotted) lines joining 3 points in the dispersion intersect at the same location, to give a vertex on the associated cells. Note that no other point in the dispersion may lie within the circle passing through these 3 points.

distribution. Near-neighbour distances, the number of near-neighbours about each point, and the area and shape of the cells can offer an indication of the characteristics of the dispersion.

The basis for assessing a distribution has been the properties of a tessellation about a random point distribution. The expected average number of sides per cell is 6 in this case (Weaire and Rivier, 1984), however, the variance of this frequency distribution is also an important indicator of deviation from randomness (Wray et. al., 1983). Attempts at theoretical derivations of the distribution functions for properties of the tessellation associated with a random array (Meijering, 1953; Miles, 1970, 1972) have not yielded results from which higher moments of the distributions may be evaluated. (Gilbert (1962) however, has calculated the expected second moment for the cell area distribution as $0.28\ \lambda^{-2}$.) Thus, the properties of a random distribution have been estimated from computer-generated pseudo-random distributions. The results of three such investigations on the distribution of the number of sides per cell is given below.

NO. OF POINTS EVALUATED	AVG. NO. OF SIDES/CELL	VARIANCE	REFERENCE
1,377	5.9985	1.7879	Boots (1982)
57,000	5.9967	1.7771	Crain (1978)
2,000,000	5.9997	1.782	Hinde and Miles (1980)

Wray et. al. (1983) have used the tessellation construction to obtain nearest-neighbour and near-neighbour distance distributions, and have shown that these statistics, along with the number of sides per cell and cell areas, all display a degree of sensitivity to the level of aggregation. In this study they examined the distribution of sulphide inclusions in several low carbon steels. In addition, they addressed the problem of spatial anisotropy. Their results suggest that the ratio of the cell intercept lengths along two orthogonal axes, if oriented properly, could serve as an indication of the level of anisotropy or banding in a particle dispersion. In the banding direction, the average cell intercept dimension should be less than in the perpendicular orientation.

Spitzig et. al (1985) have characterized particle dispersions in various microstructures, which included several carbon steels and an aluminum/graphite composite. However, limitations in the use of the random point distribution as a basis for comparison were recognized in this analysis. A finite particle size results in an excluded region which another particle cannot occupy. If we consider a particle dispersion as a distribution of points located at the particle centroids, the requirement of non-overlap of particles can result in a significant deviation from the behaviour of a true random point dispersion. This effect becomes significant at volume fractions of approximately 0.05 and greater (Bansal and Ardell, 1972; Steele, 1976). With this in mind, Spitzig et. al. generated random particle dispersions having particle

size distributions (in the planar section) identical to the microstructures being analyzed, not allowing any overlap. These generated dispersions were compared with the actual distributions with regards to nearest-neighbour spacings and local area fractions (i.e., the fraction of the cell area occupied by a particle). For the carbon steels and the aluminum/graphite composite, no significant differences in the distributions of these parameters were found, indicating randomness in their respective distributions.

To summarize, the Dirichlet tessellation can offer a useful means of characterizing the statistics of a dispersion of points or finite-sized particles in a plane section. Kocks (1966) has discussed its application to work-hardening phenomena. Spitzig (1985) has employed the tessellation procedure to obtain the nearest-neighbour distance distributions for sulphide inclusions in three perpendicular orientations for several hot-rolled C-Mn steels. These results were correlated with the strains to failure in the respective orientations.

The tessellation results, however, can be used to provide more information than just a description of the individual particle surroundings. In high-strength steels the dimensions of the agglomerated regions of inclusions control the fracture properties (Wilson, 1984). The tessellation method could be used to quantitatively evaluate the degree and scale of clustering, to yield parameters which relate more directly to the mechanics of damage accumulation and fracture. This should include, for example, the dimensions of the clustered regions and

the local volume fraction within a cluster, and a measure of the contiguity between particle clusters. This approach to the characterization of particle dispersions is expected to prove useful in relating microstructure to fracture predictions.

2.4 Damage Processes and Mechanisms

In this section we will discuss the mechanisms and processes involved in damage accumulation which operate over different ranges of temperature and stress state. However, only those damage events leading to the development of voids or microcracks will be considered. Instability of plastic deformation, i.e., strain softening, due to geometrical softening (Gil-Sevillano et. al., 1980) or structural softening (Chin et. al., 1964), without the development of dilatant damage, will not be considered.

In viewing the different modes of fracture, it is a useful approach to consider the scale over which the processes involved in damage development occur (McClintock, 1968c). For example, carbide cracking has been associated with cleavage cracks (McMahon and Cohen, 1965), or as the nucleation process of a void which subsequently grows through deformation of a much larger volume of material. The volume of material involved in the growth processes of these two damage features is considerably different. Another situation is the coalescence process involved in the linkage of two voids, which are growing through bulk plastic deformation. This involves a locally perturbed deformation

field between the voids which is considerably different from that of its surroundings, and this material may accumulate damage on a different scale from that observed elsewhere. It is important to note then, that the local microstructure can significantly influence the nature of damage, and can alter conditions so that the competition between continued deformation and the intervention of a local fracture process can change.

2.4.1 Modes of Ductile Fracture

The ductile mode of fracture in metals and alloys is, in general, a process involving the nucleation, growth and coalescence of voids. Regardless of whether the accumulated damage results in deformation instability, the final fracture process is controlled by the nature and the rate at which damage develops. If the deformation field and distribution of damage is relatively homogeneous up to the point of final fracture, the fracture surface is often characterized by a distribution of equiaxed dimples. This mode of ductile fracture is commonly termed the fibrous mode. However, deformation may become localized into a shear band, so that final fracture is controlled by the damage which accumulates in this region of high strain. The high shear strains close to the fracture surface result in dimples which are elongated in the shear direction. This mode of ductile fracture is referred to as the shear mode.

In commercial materials, void initiation has been observed to occur at inclusions or second-phase particles, through particle fracture or decohesion at the particle/matrix interface (Goods and Brown, 1979). An important observation which has been made is that void nucleation is not associated with a unique macroscopic condition of stress and/or strain (Fisher and Gurland, 1981a). The distribution in size, shape and types of particles at which voids initiate results in a continuous process of void nucleation during deformation.

In viewing the void nucleation process, the nature of the dislocation-particle interactions should be considered. For small particles (less than ~ 10 nm, according to Argon, Im and Safoglu (1975)) the stresses around a particle may be relieved at small strains by a plastic relaxation mechanism in which prismatic dislocation loops are generated at the interface (Ashby, 1966). This process cannot occur around larger particles. The validity of continuum models in determining the local stresses and strains about a particle is dependent upon the particle size and the scale over which plastic deformation processes occur. Humphreys and Stewart (1972) have observed that, in adding Zn in solid solution to Cu, the decrease in stacking fault energy results in coarse, planar slip. The high stress concentrations which develop at the interface of a particle intercepting a slip band resulted in a significant decrease in the observed void nucleation strains. Goods and Brown (1979) have estimated that for particles of the order of 1 μ, continuum descriptions provide adequate estimates of the local conditions about a particle for homogeneous deformation.

Lindley et. al. (1970) investigated the cracking of grain boundary cementite films in a low carbon steel. They found an increasing incidence of fracture in carbides which were oriented closer with the tensile axis. Fracture was not located randomly along the carbides, but was observed more frequently towards the centre of the cementite plates. These observations supported a fibre-loading mechanism of particle fracture rather than a dislocation pile-up mechanism, although it was concluded that both mechanisms were necessary to explain the cracking behaviour. These results indicated that cavity nucleation is not determined by the applied stress, but by the local deformation conditions. One should note that a fibre-loading mechanism essentially gives a strain criterion for nucleation.

Gurland (1972) determined the effect of stress state on particle fracture in a spheroidized carbon tool steel. He observed that, in tension, compression or torsion particle cracking occurred preferentially on planes perpendicular to the direction of maximum principal strain. The larger more irregular-shaped particles fractured at lower strains. Gurland concluded that fracture criteria for particles based on fibre-loading or dislocation pile-up models could not explain the observed preferential cracking of the largest particles. However, he did not consider the sensitivity of the particle fracture strength to particle size. In investigations of void development in a Ni maraging steel, Cox and Low (1974) and Argon and Im (1975) determined that void nucleation occurred through the fracture of cuboidal titanium carbonitrides, and that the larger particles fractured at lower strains. This

was interpreted as a statistical effect of size on the fracture strength of the particles.

Fisher and Gurland (1981a) studied void nucleation in spheroidized carbon steels. Irregular-shaped cementite particles often fractured, but the majority of voids were observed to nucleate through partial decohesion at the particle interface at the poles along the tensile axis. Larger particles nucleated voids at lower strains, as observed by Palmer and Smith (1968). In addition, it was observed that the distribution of carbides influenced nucleation behaviour, as initiation through interfacial decohesion was frequently observed when two particles were closely spaced along the tensile axis. This result suggested that nucleation was controlled by the local stress at the particle/matrix interface.

A critical interfacial stress criterion for void nucleation has been proposed by Argon, Im, and Safoglu (1975). Obtaining bounds defined by an elastic-plastic non-hardening and linear elastic solutions, they estimated that the maximum interfacial stress at the particle in pure shear deformation is approximately equal to the matrix flow stress in tension. Thus the interfacial stress σ_{loc} was given by $\sigma_{loc} = Y(\bar{\varepsilon}^P) + \sigma_m$, where $Y(\bar{\varepsilon}^P)$ is the flow stress in tension, and σ_m is the mean stress component. In addition, a model was presented in which the secondary plastic relaxation zone about a particle was represented by a cylinder of matrix material which was punched out. Their approximate analysis gave the stress at the particle/matrix interface as

$$\sigma_{loc} = k_o \left[\left(\frac{\gamma}{\gamma_o}\right)^n + \sqrt{3} \left(\frac{\sqrt{6}\ (1+n)}{nm} \frac{\gamma}{\gamma_o}\right)^{\frac{n}{1+n}} \right]$$

where k_o is the yield stress in shear of the polycrystal, γ and γ_o are the current and yield shear strain respectively, n is the strain-hardening exponent, and m is the Taylor factor (~ 3.1). Note that this treatment does not predict a particle size dependence. An approximate solution was also given to the interfacial stresses which arise when particles are sufficiently close that their secondary plastic zones interact. This enhances the stress at the particle interface to a level given by

$$\sigma_{loc} = k_o \left[\left(\frac{\gamma}{\gamma_o}\right)^n + \sqrt{3} \left(\frac{\sqrt{3}\left(\frac{\gamma}{\gamma_o}\right)}{\left(\frac{\lambda}{\rho}\right)}\right)^n + \frac{\sqrt{6}}{m} \left(\frac{\lambda}{\rho}\right) \right]$$

where $\frac{\gamma}{\rho}$ is the ratio of interparticle spacing to particle radius.

Argon and Im (1975) used the above results in an investigation of void nucleation in a spheroidized steel, a Cu-Cr alloy, and a maraging steel. The local variations in $\frac{\gamma}{\rho}$ were measured, and it was concluded that particles did interact. In the steel, where the volume fraction of carbides was ~ 12%, interaction was predicted to occur almost at the onset of yielding. The experimentally determined value for the carbide/ferrite interface strength was corrected for proximity effects, to obtain a value of 1670 MPa. The results of Argon and Im suggested that the criterion for matrix-particle separation is a critical interfacial stress criterion, and that the effects of particle clustering to enhance the stresses at the interface can be significant.

Brown and Stobbs (Brown and Stobbs, 1976; Goods and Brown, 1979) have presented a model for the stress at the particle interface which does give a particle size dependence. It is based upon a combined continuum and micromechanical approach. Brown and Stobbs consider local relaxation about the particle to occur through secondary slip. This results in local work-hardening about the particle, so that continued relaxation requires higher stresses. The relationship between the local flow stress σ_l and the local dislocation density ρ_l is given by $\sigma_l = \alpha\mu b (\rho_l)^{\frac{1}{2}}$, where μ is the matrix shear modulus, b the Burger's vector, and $\alpha = 1/7$. However, the plastic constraint the particle offers results in a higher local stress σ_{loc} at the interface than the local flow stress. Brown and Stobbs obtain a continuum plasticity solution, which gives $\sigma_{loc} = 4.2\ \sigma_l$. The have also calculated the dislocation density around a particle of radius r as $\rho_l = 1.7\ \frac{\varepsilon_p}{rb}$, where ε_p is the symmetrical macroscopic shear. Thus, they find

$$\sigma_{loc} = 5.4\ \alpha\mu\ \left(\frac{\varepsilon_p b}{r}\right)^{\frac{1}{2}}.$$

The total stress at the matrix/particle interface must include the macroscopic flow stress and any imposed hydrostatic stress. Goods and Brown (1979) have given the dependence of the flow stress upon strain and particle size and volume fraction, however, they note that the local stress is usually more significant than the flow stress in acting to open up the interface. The local stress is proportional to $r^{-\frac{1}{2}}$, and if void nucleation is controlled by the interface stress this

analysis suggests that nucleation occurs first at smaller particles. This is contrary to the observations of Fisher and Gurland (1981a) and Teirlinck (1983) in spheroidized steels.

Thomson and Hancock (1984a) studied void nucleation in Swedish iron, containing a 1% volume fraction of iron oxide particles. They concluded that the nucleation behaviour did not correlate with applied stress, strain or particle size, but was rather a statistical event. The distribution of particles was uniform so that clustering effects could not explain these results. It is thus important to recognize that the interfacial strength may vary considerably between particles, possibly due to impurity effects (Hippsley and Druce, 1983).

Various continuum plasticity solutions have been given to describe void growth, which include the influence of the stress state upon the growth rate. It should be noted, however, that the results obtained do not consider the influence of the particle at which the void nucleates. The effect of a hard particle on the local deformation could be significant in altering the initial void growth rate.

McClintock (1968a) considered the growth of long cylindrical isolated voids having an elliptical cross-section. He obtained a solution for the void growth rate in a strain-hardening material as an extrapolation between the limiting cases of a perfectly plastic and a viscous material. Assuming periodic void spacing, and that fracture occurred when the void size was equal to the void spacing, McClintock integrated the growth equations to give an approximate expression for the strain to fracture as

$$\varepsilon_f = \frac{(1 - n) \ln F}{\sinh\left[\frac{\sqrt{3}}{2}(1 - n)\frac{\sigma_1 + \sigma_2}{\bar{\sigma}}\right]}$$

Here n is the strain-hardening exponent, and σ_1 and σ_2 are the transverse stress components normal to the long axis of the void. F is a relative hole growth factor at fracture, defined by $F = (d/l)/(d_o/l_o)$, where d_o and l_o are the initial hole diameter and spacing respectively, and d and l their values at fracture. Note that this result assumed a constant stress ratio. Also, as the growth rate of an isolated void was used, effects of interaction between voids on the growth rate have been neglected.

Rice and Tracey (1969) have analyzed the initial growth of an isolated spherical void in an infinite matrix. The solution for the non-hardening case in axisymmetric deformation has been modified by LeRoy et. al. (1981) to include the effect of the change in void shape as it grows. This was accomplished through an amplification factor $\gamma_a = 1 + \frac{r_2}{r_1}$, where r_1 and r_2 are the semi-axes of the ellipsoidal void parallel and transverse to the applied tensile axis. The γ_a term essentially gives the stress amplification around the periphery of the void. The void growth rate equations thus obtained are

$$\dot{r}_1 = r_1 \left[\gamma_a + D\right] \dot{\varepsilon}^{\infty}$$

$$\dot{r}_2 = r_2 \left[-\gamma_a + D\right] \dot{\varepsilon}^{\infty}$$

where $\dot{\varepsilon}^{\infty}$ is the tensile strain rate at infinity, and D is a factor giving the volume change of the void. For a non-hardening material $D = 0.56 \sinh (\frac{3}{2} \frac{\sigma_m}{\bar{\sigma}})$.

Tracey (1971) presented an analysis which considered infinitely long cylindrical voids, as McClintock did. However, the cylinder of material containing the void had a finite diameter. Thus, by setting this diameter equal to the hole spacing, an estimate of the effects of interaction between adjacent holes on the transverse growth could be made. Tracey obtained upper and lower bounds to the hole growth rate in terms of the hardening exponent and the stress triaxiality. His results show that an increase in the strain-hardening exponent can produce a significant reduction in the initial growth rate, and that at large strains the growth rate accelerates due to interaction between voids. The reduction in growth rate with increased strain hardening was large at high levels of stress triaxiality, but was much less significant at low levels.

Thus, void growth models predict a marked influence of hydrostatic tension on the growth rate. In addition, the results of Tracey (1971) (see also Needleman, 1972) show the influence of void interaction in accelerating void growth rates. The application of this result to void growth in a region of locally high damage however, would be suspect, as the increase in local dilation rate would have to be accomodated by the surrounding material.

LeRoy et. al. (1981) and Teirlinck (1983) were quite successful in their predictions of the rate of damage accumulation in spheroidized steels, employing the Rice-Tracey growth equations. However, several investigations have produced more direct measurements of void growth which can be compared with predictions. Beremin (1981) concluded, from axisymmetric notched-bar tests in a medium-strength C-Mn steel, that void growth rates were given approximately by the Rice-Tracey equations. These voids initiated at MnS inclusions. However, in a mild steel (Beremin, 1982) growth rates were underestimated. Application of McClintock's results to experimental observations of void growth in a 4340 and a maraging steel (Cox and Low, 1974), and to void growth about graphite filaments in copper (Perra and Finnie, 1977) yielded an underestimate of the actual growth rates. Barnby et. al. (1984) studied void growth over a wide range of stress triaxiality in a C-Mn structural steel. With $\sigma_m / \bar{\sigma}$ less than about 1.2, they found void growth predicted by the Rice-Tracey equations to slightly underestimate the observations, however, for larger stress triaxialities the predicted void growth overestimated observations. This latter result would be predicted from Tracey's (1971) analysis of the influence of work hardening.

The application of plastic hole-growth theories to the prediction of ductile fracture has been reviewed by Thomason (1974). In this approach, voids are assumed to have a spacing equal to the average inclusion or particle spacing, and fracture is assumed to occur when the voids have grown to a dimension equal to their spacing. A nucleation strain must also be assumed. Figure 2.7, from Thomason (1974), compares

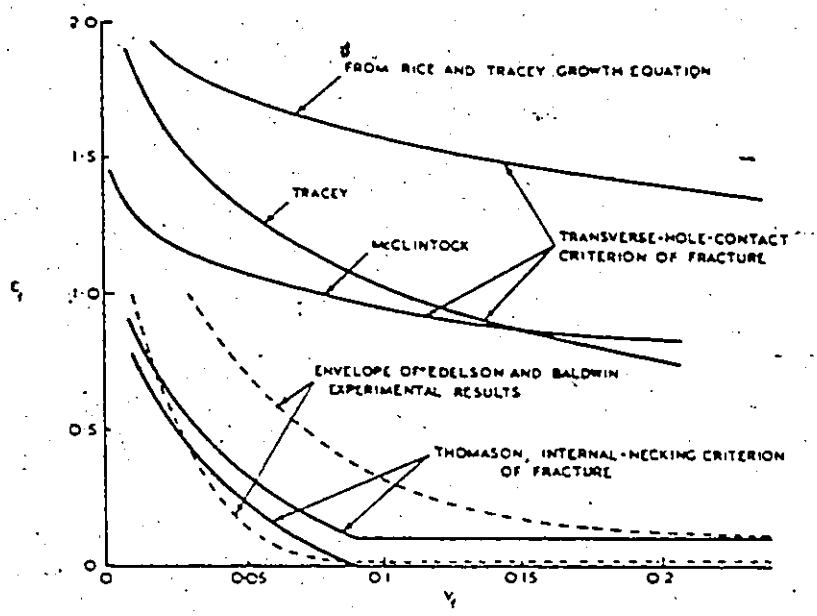

Fig. 2.7: Comparison between predicted ductile fracture strains, through several hole-growth models and Thomason's model, and the experimental results of Edelson and Baldwin (1962) (from Thomason, 1974). ε_f is the fracture strain obtained in a uniaxial tension test, and v_f the volume fraction of holes or particles.

the fracture strains predicted by these hole-growth analyses with the results of Edelson and Baldwin (1962).

Thomason suggests that the discrepancy between predictions and experiment arises because coalescence should be viewed as an unstable process. Thus, he has presented a hole-growth model of ductile fracture (Thomason, 1968), developed for a rigid-perfectly plastic solid deforming in plane strain containing a periodic array of square prismatic cavities. The influence of stress triaxiality on the rate of void growth, however, was neglected. Because of the plastic constraint on the ligament of material between two adjacent voids, the tensile yield stress of the material in this region is higher than in the surroundings. It is energetically more favourable for the material to deform homogeneously. However, as the holes elongate in the tensile direction, this constraint decreases, until a point is reached at which the external work done in the deformation of the ligaments between voids becomes less than the work done in deforming the entire volume of material. This work criterion defines the onset of unstable internal necking of the matrix material between voids. As deformation is then confined to the material along a sheet of voids, the contribution of internal necking to overall strain is assumed negligible, and the fracture strain is given by the internal-necking criterion. An inverse square root dependence of the fracture strain upon initial void volume is predicted. Figure 2.7 also presents the predictions of Thomason's model, which compare favourably with the experimental results. Thomason (1985a,b) has extended the calculation of the constraint factor to

obtain an upper bound for the plastic limit-load for internal necking in the three-dimensional case. He includes the effects of the mean stress on void growth, so that the influence of both stress state and volume fraction upon the fracture condition can be predicted. Results suggested that the influence of the mean stress on ductile fracture is primarily in promoting the plastic limit-load failure of the inter-void matrix (i.e., linkage), rather than in promoting dilational growth of the voids.

Melander (1980a) has proposed a fracture criterion, in which the strain localization leading to final fracture is allowable when the macroscopic work done per unit effective strain no longer continues to increase with effective macroscopic strain. The energy to deform a unit volume of material is $dW = \bar{\sigma} \cdot d\bar{E} - P \cdot dE_{nn}$, where $\bar{\sigma}$ and $\bar{E}$ are the equivalent macroscopic stress and strain, P is the macroscopic hydrostatic pressure, and E_{nn} the macroscopic dilation. The instability criterion is thus given by

$$\frac{d^2W}{d\bar{E}^2} = \frac{d\bar{\sigma}}{d\bar{E}} - \frac{dP}{d\bar{E}} \cdot \frac{dE_{nn}}{d\bar{E}} - P \cdot \frac{d^2E_{nn}}{d\bar{E}^2} = 0$$

The first term on the right-hand side of this equation is the macroscopic work-hardening rate, which is determined by the work-hardening rate of the matrix material and the softening effect due to void growth. Melander obtained an approximate dependence of $\bar{\sigma}$ upon f_v (the void volume fraction), using Gurson's (1977) results. He uses an experimentally-determined void growth expression (Melander, 1980b) obtained for

the growth of voids at oxide particles in copper, and employs the Bridgman correction (Bridgman, 1952) for the stress state in the neck of a tensile sample, so that he can solve the instability criterion for the strain at instability. Melander's predictions of failure agreed satisfactorily with the fracture strains obtained for copper with two different strain-hardening characteristics.

Melander's instability criterion differs from Thomason's in that it does not consider the influence of void size, shape or spacing. In this respect, Melander and Stahlberg (1980) have employed the ductile fracture theory of Thomason (1968) to predict the effect of void size, shape and distribution. A distribution of voids with two different void sizes was predicted to have a higher ductility than a uniform size distribution with the same initial void volume fraction. In addition, a void distribution with two alternating void spacings was predicted to have a higher ductility than a periodic distribution. The influence of a non-periodic spatial distribution of damage was also studied by Melander (1979), in a computer simulation of ductile fracture in a random distribution of voids. A random two-dimensional array of voids was generated, and the material subjected to plane strain tension. Several fracture paths were chosen, for which the fracture strain was calculated using Thomason's upper bound solution for internal necking between voids. The path giving the smallest fracture strain was thus the predicted fracture strain of the material. An important result from this simulation was that the fracture strain in a material with a random array of voids was substantially larger than one with a regular array.

It should be noted here that the models proposed by Thomason and Melander have not considered the effects of continued void nucleation. The effect of a region with a high local level of damage, leading to the development and growth of a crack-like flaw cannot be predicted, so that the applicability of their results to real materials should be considered carefully.

The ductile fracture model of Thomason (1968) considers a specific instability, associated with internal necking of the ligaments between voids. However, McClintock (1968b) has presented an approximate analysis of the termination of ductile fracture by localized shear. This instability is given by a change in deformation pattern from a homogeneous mode to that localized in a shear band between voids. This is illustrated in Figure 2.8, where the damage is associated with a periodic array of ellipsoidal holes. The first condition which must be satisfied for the shift in deformation mode is that the loads for the shear and homogeneous modes become equal. McClintock considers a plane 45° to the tensile axis, and through an upper bound technique obtains the localization condition as

$$\frac{\sqrt{3}}{2} > \left[1 - \frac{\pi ab}{l_a l_b}\sqrt{2/(1+\frac{a^2}{b^2})}\right] \Big/ \left[1 - \frac{4}{3}\pi \frac{a}{l_a}(\frac{b}{l_b})^2\right]$$

Note that this condition is independent of the strain-hardening rate, once the critical hole configuration has been reached.

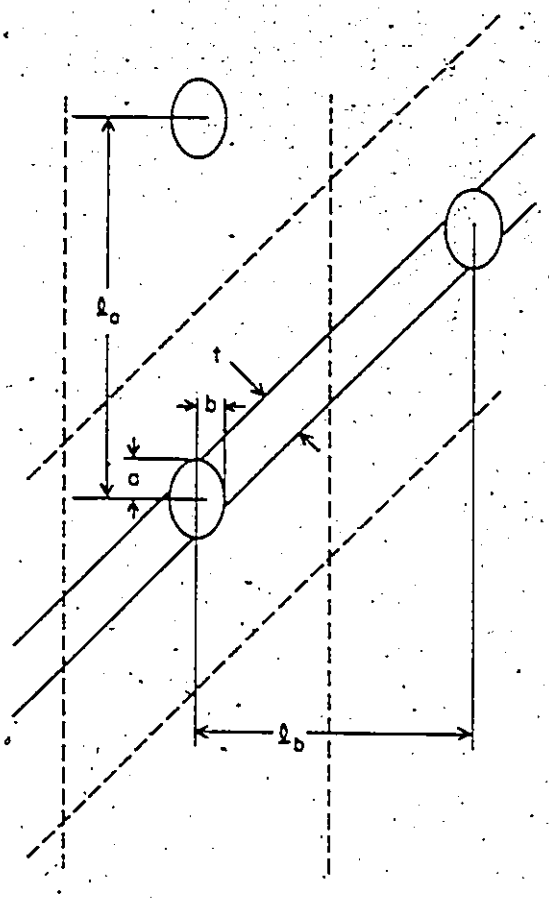

Fig. 2.8: Shear band which joins periodically-spaced ellipsoidal holes with semi-axes a, b and c, in elements having dimensions l_a, l_b and l_c. The c-direction is out of the page (from McClintock, 1968b).

The difficulty in forming a shear band in this manner arises from the increase in flow stress required in going from uniaxial stress to plane strain, as McClintock points out. Thus, a second condition for localization was considered, in which the shear instability can occur when the maximum load has been attained. The deformation mode assumed that the shear band was thin enough relative to the void dimensions that the void would be sheared without producing any other deformation. Then, an upper bound estimate of the localization condition was obtained as follows. In shearing, the increase in the area A_h of a hole in the shear plane is given by the shear displacement u times the hole dimension 2c, normal to the plane of Figure 2.8. Thus $dA_h = 2c \cdot du$. We may assume b = c. The shear displacement is related to the shear strain $d\gamma$ in the band of thickness t, and thus to the equivalent strain $d\bar{\varepsilon}$ by $du = t \cdot d\gamma$, with $d\gamma = \sqrt{3}\, d\bar{\varepsilon}$. McClintock gives an approximate expression for A_h. Then the net area of an element surrounding a given void, A_n, is the total area A_g minus the hole area A_h intercepted by the shear plane. Thus

$$A_n = \sqrt{2}\, l_b l_c - \pi bc \sqrt{2/\left(\frac{a^2}{b^2} + 1\right)}$$

At localization the load decreases. This condition occurs when the loss in load due to the decrease in net section is greater than the increase in load due to strain hardening. Thus, the localization condition is $dP = \tau\, dA_n + A_n d\tau < 0$. With $\frac{d\tau}{\tau} = \frac{d\bar{\sigma}}{\bar{\sigma}}$, this gives the localization criterion as

$$\frac{1}{\bar{\sigma}} \frac{d\bar{\sigma}}{d\bar{\varepsilon}} < \sqrt{6}\ ct/l_b l_c$$

If we take $t = \sqrt{a^2 + b^2}$, then one obtains

$$\frac{1}{\bar{\sigma}} \frac{d\bar{\sigma}}{d\bar{\varepsilon}} < \sqrt{6}\ c\sqrt{a^2 + b^2}/l_b l_c$$

Dodd and Atkins (1983) have shown that data on shear strain flow instabilities can be explained by an isothermal geometric softening effect due to voids, as McClintock proposed. Previous attempts to predict localization strains by thermoplastic theory, involving quasi-adiabatic thermal softening along shear bands, considerably over-estimated experimental results.

The shear mode of ductile fracture in thin sheets of mild steel in both spheroidized and pearlitic conditions has been studied by French and Weinrich (1979a,b). The presence of elongated MnS inclusions oriented along the tensile axis resulted in the development of elongated voids prior to necking. Upon necking, shear bands developed which crossed at the centre of the specimen. In the spheroidized material, very little damage was observed about the carbides prior to the development of the shear bands, but once formed, the voids associated with the carbides developed only within the shear band. In the pearlitic steel there was some damage associated with the pearlite prior to the initiation of the shear band, however, subsequent damage development was confined to the shear band. The enhanced damage rate in the pearlitic

microstructure resulted in a lower fracture strain than in the spheroidized material. The crack which developed at the centre of the specimen was initiated through the coalescence of two large closely-spaced inclusion-related voids. These results illustrate an important aspect of fracture in commercial materials. Damage may accumulate on several different scales, related to large inclusions or smaller carbides, and the conditions under which damage associated with different microstructural components develops can be markedly different. However, in considering the conditions which control final fracture, contributions from all sources of damage should be taken account of.

McClintock et. al. (1966) have developed expressions for the growth rates of voids in shear bands. French and Weinrich (1979a) have applied these results to predict the fracture strains in shear in a spheroidized steel. The model over-estimated experimental observations. However, the average inclusion size and spacing was used in this calculation. French and Weinrich have suggested that early coalescence of voids associated with the more closely-spaced carbides and/or inclusions could lead to general coalescence at lower strains than expected for a periodic array of voids. Thus, it appears that the effects of the distribution of damage may be significant in controlling final fracture.

A continuum approach to the coalescence process has been presented by Rudnicki and Rice (1975). Rather than treating the mechanism by which voids interact as they grow, they proposed that ductility is limited by a change from a homogeneous to a localized deformation mode, resulting in a shear band. This was analyzed as a bifurcation from the

homogeneous mode, and was dependent upon the material constitutive equations. These constitutive equations can include the effects of yield vertices due to anisotropy, non-normality of plastic flow, and the influence of plastic dilation due to void growth (Gurson, 1977). Rice (1976) has noted that, using reasonable average void volume fractions, predicted bifurcation strains are much higher than measured fracture strains. This suggests that in non-uniform void distributions failure may initiate at an earlier stage, in a region of locally high porosity. Yamamoto (1978) considered these as unbounded planar bands of high porosity, and obtained realistic strains at which localization can occur. Ohno and Hutchinson (1984) have considered a finite disc-shaped region with a locally high damage level in axisymmetric deformation, and noted a strong influence of the hydrostatic stress state on the initiation of localization.

The continuum bifurcation analyses require kinematic compatibility as a condition for localization. Thus, the component of the velocity field normal to the boundary of a shear band must be continuous across the boundary. This is satisfied when the boundaries are non-deforming surfaces such that the normal strain increments at the boundary are zero, which occurs for states of incremental plane strain. Thus, bifurcation analyses predict that localization is promoted in plane strain, and inhibited in axisymmetric straining.

Clausing (1970) tested plane strain and axisymmetric tensile specimens of mild and structural steels, and noted that the strain to failure in plane strain conditions was less than that obtained in the axisymmetric strain state. This difference increased with the yield

strength of the material. However, Clausing's results are complicated by an increased stress triaxiality in the plane strain tests. MacKenzie et. al. (1977) and Hancock and Brown (1983) have conducted experiments on axisymmetric notched and plane strain specimens of high-strength structural steels, to examine the influence of stress state on ductile fracture initiation. They concluded that the strain to initiate failure was independent of the strain state, but correlated with the state of stress. The initiation of failure was defined by a small sudden load drop prior to final failure. Hancock and MacKenzie (1976) determined that this was associated with the coalescence of two large inclusion-related voids.

The coalescence step was then independent of the strain state because the region of material separating two large voids is relatively independent of the macroscopic strain state. Tvergaard (1982) has concluded this result from numerical studies. The effect of the stress state is given by its influence upon void growth rates to attain a localization condition between voids. Thus, experimental evidence suggests that failure in these commercial materials initiates in regions of high local porosity, contained by surrounding material with a lower average level of damage. The degree of inclusion clustering could then considerably alter the conditions at which the coalescence step occurs in high strength materials. These regions of high local porosity have been modelled by Thomson and Hancock (1985) as porous patches contained in a less porous matrix. The local hardening rate, a function of porosity and stress triaxiality, was calculated for a region having an initial

porosity ten times the average (observed in the steels mentioned previously). Negative values were attained at the observed fracture strains, indicating the significance of these regions in promoting fracture.

The coalescence of the large voids was observed to occur through strain localization in a narrow region separating the voids, a mode which interrupted linkage through a more homogeneous deformation mode. The coalescence of voids via localized shear has been observed in several other investigations (Bluhm and Morrissey, 1966; Cox and Low, 1974; Beremin, 1981), where the void spacing-to-size ratio at coalescence was as high as 5 to 10. The linkage step was observed to be associated with the development of damage on a smaller scale, at carbides. Enhanced levels of damage about carbides were observed in the strain fields (Thomson and Hancock, 1984b) about the large inclusion-related voids, especially in the sheared zone involved in coalescence. The development of voids about carbides was also observed to contribute to the hole growth mechanism of the larger voids. The applicability of continuum hole growth models to the situation where void growth involves a damage mechanism is not likely to yield realistic predictions.

Thomson and Hancock (1984a) suggest that the enhanced damage in the ligament separating two large voids promotes the onset of coalescence through localization of flow. Hancock and Brown (1983) have thus suggested that the continuum bifurcation approach to localization may apply over the scale of the ligament separating two inclusions, where the local damage is associated with carbides. Tvergaard (1982) has

analyzed the localization of flow which develops in the material between two large voids. The matrix was plastically dilatant, associated with damage initiated at small particles, for which a void nucleation scheme was introduced. Tvergaard introduced both of these effects into the constitutive equation, and predicted that flow localizations could occur between large voids when the matrix continues to accumulate damage.

The importance of void nucleation at small carbides in the coalescence of large inclusion-related voids, and subsequent fracture behaviour has been suggested by Cox and Low (1974), and demonstrated by Hippsley and Druce (1983). Cox and Low observed that the coalescence of large voids in a 4340 steel was promoted through the development of damage at the larger carbides. They suggested that this could explain the lower toughness of the material relative to a maraging steel, and that if the carbide size were refined, void nucleation at carbides could be delayed to produce an improvement in toughness. Hippsley and Druce studied the influence of ageing on the ductile fracture properties of a low-alloy steel. The ageing treatment did not significantly alter the flow stress or the carbide distribution, however, segregation of phosphorus to the carbide/matrix interface was detected. This resulted in an increase in the level of damage initiated at the carbides, due to a decrease in the carbide/matrix interfacial energy and/or strength. The process of coalescence between the large inclusion-related voids was affected, with the result that measured J_{1c} toughness and reduction in area were significantly reduced. The 17% decrease in reduction in area

suggests that the damage associated with carbides can influence the onset of coalescence between large voids.

To summarize this review of ductile fracture modes, we note that the influence of the distribution of microstructure on void nucleation has been demonstrated theoretically and experimentally, especially in materials with second phase volume fractions of 10% and greater. Interactions between closely-spaced voids can promote enhanced growth and coalescence, and deviations from average damage accumulation rates on a local scale have been observed to influence overall fracture behaviour, especially in high-strength materials. The influence of inclusion content and distribution can thus be significant in controlling fracture in these materials. However, the development of damage should be considered on several scales, associated with different components of the microstructure. The influence of the relative contributions made by the different sources of damage can be expressed in both the bulk behaviour, such as in the reduction in area, or on a more local level, as given by the toughness of the material.

2.4.2 Transgranular Cleavage Fracture

In ferritic steels and other b.c.c. metals such as tungsten and molybdenum, a transition to a brittle cleavage mode is observed as temperatures decrease. This occurs by transgranular cleavage along crystallographic planes: in ferrite these are {100} planes.

Low (1954), in a comparison of cleavage fracture in tension with yield stress in compression in a mild steel at -196°C, showed that the fracture stress was always equal to or greater than the uniaxial yield stress. Thus, plastic flow is necessary in the cleavage process and yielding, whether by slip or by twinning, is involved in the nucleation of cleavage fracture. These results suggest that cleavage fracture is mechanism controlled. Accordingly, Zener (1948) and Stroh (1954) developed a model in which the stress levels at the end of a dislocation pile-up resulted in cleavage initiation. The crack nucleus resulted from dislocations being squeezed together. This condition also satisfied the energy balance for subsequent propagation, providing the surface energy remained constant. Smith and Barnby (1976) corrected Stroh's result to include the effect of local shear stresses in propagating the crack, however, the prediction that cleavage was nucleation controlled was still maintained.

Stroh's analysis predicted a fracture stress with a $d^{-\frac{1}{2}}$ dependence, where d is the grain size, assuming the slip band extended across the entire grain. Knott (1966) however, showed that the cleavage fracture in mild steel was governed by a critical tensile stress criterion. This result could not be predicted by Stroh's model. Since tensile stress controls the propagation of a crack nucleus, Knott's findings imply that cleavage fracture in mild steel is propagation controlled. If the Zener-Stroh mechanism does result in crack nucleation, that cleavage fracture is propagation controlled suggests a brittle second phase providing a region with low surface energy, with subsequent arrest of the crack nucleus at the phase boundary.

Cottrell (1958) proposed another dislocation mechanism for cleavage crack nucleation in b.c.c. metals, in which two dislocations moving on intersecting {101} planes interact to form a dislocation whose Burger's vector is normal to the cleavage plane. This occurs with a reduction in total dislocation energy, favouring crack nucleation. Cleavage fracture through this mechanism is then propagation controlled, with the cleavage fracture stress σ_f given by

$$\sigma_f > \frac{2\mu\gamma}{k_y^s} d^{-\frac{1}{2}}$$

Where μ is the shear modulus, γ the surface energy, and k_y^s the Hall-Petch yielding constant. This model thus predicts a tensile-stress controlled cleavage fracture and includes the effects of grain size and yielding parameters. However, the influence of microstructural variables other than the grain size cannot be predicted.

McMahon and Cohen (1965) performed tensile tests on mild steels with identical yield and flow properties, but different carbide size distributions. Coarse carbide particles promoted cleavage fracture, while a fine carbide distribution resulted in ductile behaviour. Grain boundary carbides were observed to crack during plastic deformation, and careful and continued metallographic sectioning indicated that microcracks in the ferrite were usually related to carbide cracking. However, cleavage cracks were also associated with the intersection of deformation twins (see also Knott and Cottrell, 1963; Oates, 1969). The cementite thus provides a region with an effectively low surface energy in which the crack may nucleate.

Argon and Im (1975) have estimated that the local tensile stress required to fracture cementite particles in a ferrite matrix is approximately 1500 MPa, well below the theoretical strength. At this stress, the Griffith crack size in a carbide particle is estimated (Hahn, 1984) to be about 0.7 μ, which suggests that carbide fracture does not result from defects, but from other local stress raisers, such as a dislocation pile-up. Smith (1966) has proposed a model in which a dislocation pile-up against a carbide results in particle fracture. The microcrack formed subsequently propagates as a Griffith defect with both the applied stress and the pile-up contributing to the crack driving force. The change in energy with crack length was examined as the crack propagated from the carbide into the surrounding ferrite. The result is thus a propagation-controlled criterion, giving the cleavage fracture stress σ_f by

$$\frac{C_o}{d}\sigma_f^2 + \tau_e^2\left[1 + \frac{4}{\pi}\left(\frac{C_o}{d}\right)^{\frac{1}{2}}\frac{\tau_i}{\tau_e}\right]^2 > \frac{4 E \gamma_p}{\pi(1-\nu^2)d}$$

where C_o is the thickness of the grain boundary carbide, E the Young's modulus, ν Poission's ratio, and γ_p the effective surface energy of ferrite. The effective shear stress is τ_e and the lattice friction stress τ_i. This result demonstrates the influence of carbide thickness. Although the model proposed by Smith considers particle cracking due to a dislocation pile-up, experimental observations (Lindley et. al., 1970) have shown that elongated carbides may also crack through a fibre-loading mechanism.

Note that if the effective shear stress is replaced with the Hall-Petch relationship $\tau_e = k_y^s d^{-\frac{1}{2}}$, Smith's result predicts that the only microstructural parameter affecting the fracture stress is the carbide thickness. Curry and Knott (1978) have noted that the contribution of the pile-up term to crack propagation is usually negligible, so that the ferrite grain size dependence is maintained. The critical event is still, however, the Griffith propagation of a crack nucleated in the carbide into the surrounding ferrite. For spheroidal carbides σ_f is given by

$$\sigma_f = \left(\frac{\pi E \gamma_p}{2 C_o} \right)^{\frac{1}{2}}$$

where C_o is the carbide diameter.

Curry and Knott (1978) have shown a general relationship between ferrite grain size and the coarsest observed carbide thickness in normalized and annealed mild steels. They proposed that the ferrite grain size dependence of the fracture stress is coincidental, and the dependence is more correctly assigned to the thickness of the coarsest carbides. The dependence of σ_f upon $d^{-\frac{1}{2}}$ was shown to be non-linear, however, in substituting the dependence of C_o upon d a much better correlation between fracture stress and grain size resulted. Comparable results for spheroidal carbides were obtained by taking C_o as the 95th percentile of the carbide size distribution. Agreement with experimental results for both spherical and plate-like grain boundary carbides was obtained with an assumed value of 14 Jm^{-2} for γ_p. The elastic work

of fracture, however, is estimated at only 2 Jm^{-2}. Knott (1977) has suggested that this discrepancy arises because the full atomistic fracture criterion at the crack tip should be viewed as a critical displacement, requiring the creation and limited movement of dislocations near the crack tip. This additional work done would raise the effective surface energy to approximately the observed value.

The assumption that the critical cleavage event in cleavage fracture is the propagation of a carbide microcrack into the ferrite matrix should be questioned, in light of experimental observations. McMahon and Cohen (1965) and Groom and Knott (1975) have reported grain-sized microcracks which have arrested at the grain boundary. Once arrested, these cracks are observed to blunt due to plastic flow at the crack tip (Hahn, 1984). McMahon and Cohen observed that if a microcrack across a ferrite grain arrested it would not repropagate even under an increased load. Thus it is not the propagation of ferrite grain-size microcracks which controls cleavage fracture in mild steels. Observations of microcrack arrest have led Hahn (1984) to view the Griffith energy term γ as an arrest toughness parameter, associated with a microcrack crossing a boundary, whether it be carbide-ferrite or ferrite-ferrite.

The origin of brittleness in crystals has been viewed as the result of a competition between bond rupture and dislocation processes which blunt the crack tip. The dislocations may be generated at the crack tip (Rice and Thomson, 1974) or may already exist (Ashby and Embury, 1985). Brittle behaviour arises when bonds rupture before dislocations can be emitted from the crack tip, or the crack tip moves

faster than the existing dislocations can, so that they cannot contribute to crack tip plasticity. For a stationary crack, the results of Rice and Thomson suggest that iron is brittle only at temperatures close to 0°K. However for a rapidly advancing crack, the time available for dislocations to contribute to crack tip blunting is much less (Hahn, 1984; Jokl et. al., 1980). Thus, the fracture of a brittle carbide presents the adjacent ferrite with a rapidly advancing crack. This crack can penetrate the ferrite because the toughness of the carbide-ferrite boundary is at a brittle level at this crack velocity. However, if the crack velocity and nature of the grain boundary is such that the Griffith condition is not satisfied, the crack will arrest and blunt at the grain boundary. The stationary crack will then not reinitiate propagation.

It should be noted that variations in boundary toughness values occur. These are determined in part by the relative orientation between a crack in a carbide and the cleavage plane in the adjacent ferrite, or by the orientation between two grains. Thus, an influence of local texture or grain size in controlling the local critical fracture stress may be expected, through the influence on grain boundary toughness or the size of the crack in the ferrite grain (Cheng et. al., 1982).

In addition to the role of carbides in cleavage fracture, McRobie and Knott (1985) (see also Knott, 1984) have identified inclusions as active cleavage initiation sites. These consisted of silicates and oxides in as-deposited C-Mn weld metal. The microstructure consisted of

ferrite nucleated on the prior austenite grain boundaries, which surrounded acicular ferrite. Fracture surface observations indicated that critical microcrack nuclei formed at the non-metallic inclusions in the grain boundary ferrite, even though the thickest carbides were found in between the acicular grains. Observations also showed that the cleavage cracks propagated preferentially through the coarse grain boundary ferrite.

Cleavage fracture also occurs in pearlitic, bainitic, and martensitic steels. Microcracks in the pearlite nucleate in individual carbide lamellae in linear arrays, and then join by the failure of the intervening ferrite to form pearlite colony - and prior austenite grain-size cracks (Hahn, 1984). It is not clear, however, whether the critical dimension of the microcrack which determines the fracture stress σ_f (in the framework of a boundary arrest toughness) is the colony or austenite grain diameter, or the lamella thickness (Hahn, 1984; see also Lewandowski and Thompson, 1985). Lewandowski and Thompson concluded that σ_f is controlled by the lamella thickness, while Hahn reports investigations where the prior austenite grain size is controlling.

In bainitic and martensitic microstructures, cleavage appears to be controlled by the packet size, where the packet boundaries defined the facets observed on the fracture surface (Brozzo et. al., 1977; Kolilainen, 1980a,b; Kotilainen et. al., 1982). The different crystallographic planes on which cleavage can occur result in only low angle deviations necessary for a crack to cross from one lath to another (Curry, 1980a). However, the misorientation across packet boundaries is

much larger, with a greater associated boundary toughness. It should be noted that although particle-sized microcracks have been observed in bainitic structures, none were evident in the work of Kotilainen (1980b). Kotilainen did, however, associate packet-sized cracks with the carbides on packet boundaries.

Figure 2.9, from Hahn (1984), summarizes brittle fracture stress-particle size relations for a variety of microstructures. The particle size, given by d or C_o, is the size of the controlling microstructural element. The value of K_{1a}^B is the associated boundary toughness, so that fracture is controlled by this property and the size of the microstructural feature involved.

The results of Ritchie, Knott and Rice (1973) indicated that the cleavage toughness in a mild steel increased with temperature. This was interpreted as the result of the temperature dependence of the yield stress. Ritchie et. al. postulated that a steel's cleavage stress had to be exceeded over a microstructurally-determined distance ahead of the crack tip for fracture to occur. An increase in temperature results in a decrease in yield stress, so that an increase in the applied stress intensity factor is required to achieve the critical combination of stress and distance ahead of the crack tip. Assuming a characteristic distance of two grain diameters, the temperature dependence of the fracture toughness in a given steel was accurately predicted.

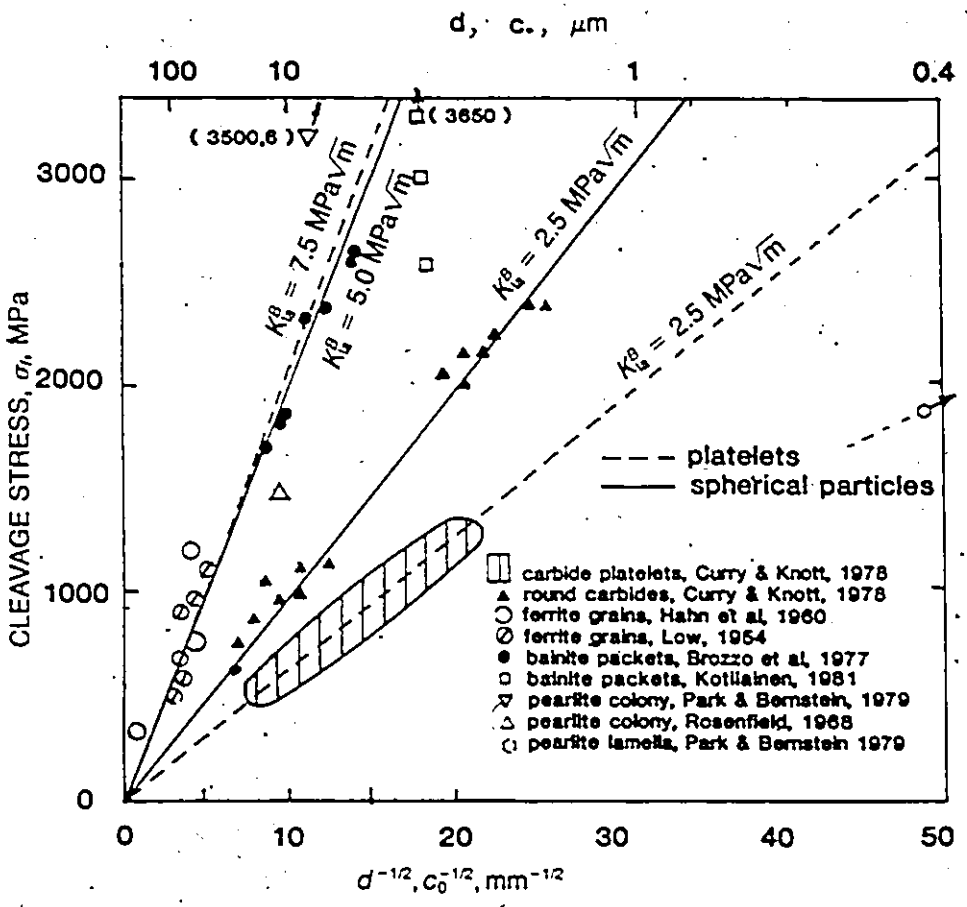

Fig. 2.9: Experimental measurements of brittle fracture stress vs. particle dimension for different microstructures, indicating the characteristic values of K_{Ia}^B (from Hahn, 1984).

However, Curry and Knott (1976) determined the grain size dependence of the characteristic distance in a mild steel, and found it to be independent of grain size. This led Curry and Knott to interpret the characteristic distance as a measure of the volume of material which must be sampled to ensure the presence of a cracked carbide of dimension greater than the critical size, which can result in fracture, i.e., an "eligible" particle. As there is a distribution of carbide sizes within a microstructure, there will be spatially distributed variations in the local fracture stress. At a sharp crack, the stress gradients are significant with respect to microstructural dimensions, and a statistical effect in sampling an eligible particle becomes important. Thus, the size of the stressed volume will influence the measured value of fracture stress. In a bainitic steel Kotilainen (1980b) has noted an an increase in measured fracture stress for tensile vs. charpy v-notch vs. K_{IC} specimens (in order of ascending measured fracture stress), due to the decrease in volume of stressed material sampled.

Curry and Knott (1979) (see also Curry, 1980b; Wallin et. al, 1984) have proposed a statistically-based analysis of carbide-nucleated cleavage fracture in quenched and tempered steels with spheroidized microstructures. Their analysis recognizes contributions from all the eligible particles in the plane of the crack, and involves three statistical quantities: (i) $P(f,r_i)$, the probability a particle of radius r_i

will be cracked and be subjected to a sufficiently high stress to initiate fracture, (ii) $P(r_i)$, the probability a particle has a radius r_i, and (iii) Θ, the probability a particle is "eligible". They give $P(f,r_i)$ by

$$P(f,r_i) = \Theta s X_i^2 n_a P(r_i)$$

where X_i is the distance from the crack tip for which the fracture condition is satisfied for r_i-particles, n_a is the total number of particles per unit area and s is a factor of order unity describing the shape of the stressed region. The critical fracture condition is defined by summing $P(f,r_i)$ over all carbide radii and setting this sum equal to unity, i.e., one carbide particle must be subjected to its critical stress for fracture to occur. Thus $\sum_1^n P(f,r_i) = 1$ defines the condition for crack extension.

Results of this analysis indicated that the ~ 5% of the particle size distribution with the largest radii are the most probable source of fracture in the crack tip region. An arbitrary constant had to be chosen related to the value of Θ, however, a single value allowed correlation between tests at different temperatures with different microstructures, and in different steels, thus giving support to the statistical nature of cleavage fracture. It should be noted that, in this model, it is assumed that the carbide particle distribution is homogeneous over the scale of the sampling volume. If large scale inhomogeneity is present in the material, then particle sampling becomes spatially dependent in a more complicated way.

An important sampling effect has been noted by Knott (1984) in coarse two-phase ferrite-martensite microstructures. If the size of the regions of constituent phases was small, the scatter in measured toughness values was small. However, as the dimensions of microstructural components increased, the scatter increased to ± 18%. This effect was related to the propagation of a critical crack in the ferrite, and its association with the stressed region ahead of a notch. With an increase in the coarseness of the microstructure, the probability of sampling a region of ferrite decreases.

Thus, it is seen that statistical effects in cleavage fracture are related, along with other chemical and microstructural factors, to the distribution of "eligible" particles and phases. If the distribution of microstructural components becomes very non-uniform over a scale greater than the volume of material which is critically-stressed, it can be expected that a degree of scatter in measured mechanical properties will result. The prediction of this scatter requires detailed information on the nature of the microstructural distribution.

2.4.3 High Temperature Intergranular Fracture

At elevated temperatures (~ 0.5 T_m, where T_m is the melting point), the damage leading to failure in many metals and alloys under practical service conditions accumulates predominantly along grain boundaries. Failure is the result of the nucleation, growth, and coalescence of grain boundary voids to produce a dominant flaw in the material. Voids are observed at grain boundary triple points (wedge

cracks) and along the grain boundaries (r-voids), usually on those oriented normal to the tensile axis.

It was initially proposed that cavity nucleation occurred through the condensation of vacancies on grain boundaries which experience a normal tensile stress. However, Balluffi and Siegle (1955) have shown that the excess vacancy concentration required to nucleate cavities in this manner is considerably greater than that which normally occurs in metals under creep conditions. Intrater and Machlin (1959) demonstrated in copper bicrystals that the grain boundary void density was proportional to the amount of sliding, independent of temperature and stress. This result does not support a vacancy condensation mechanism. Voids were often associated with the intersection of a slip band with the grain boundary, however, the observed void spacing was less than the slip band spacing. The nucleation mechanism proposed involved jogs in the grain boundary, due to either slip bands or sub-grain boundaries, which open up under the local stresses generated during grain boundary sliding.

Argon (1983) has noted that this mechanism requires that the boundary does not migrate under the local stresses, to remove the jog. This may occur in more pure materials, where solute effects and second-phase particles do not inhibit grain boundary migration. Chen and Machlin (1958) observed decreased cavitation and enhanced creep ductility in copper under these conditions. Indeed, Mullendore and Grant (1965) have shown experimentally that grain boundary sliding along boundaries containing hard particles is necessary in producing grain

boundary cavitation. Hard second-phase particles have been observed to provide potent nucleation sites. Dyson et. al. (1976) noted this in Nimonic 80A, where the intersection of slip bands with grain boundary particles resulted in cavity nucleation. Thus, void nucleation is considered to occur in many materials through decohesion at the matrix/particle interface. The high local stresses required at the interface result from either the interaction of a slip band with the particle or the inhibition of grain boundary sliding at the particle.

Argon et. al (1980, 1981) have analyzed the stress concentrations that can arise at a non-deformable particle on a sliding grain boundary. Their analysis includes both diffusion and power-law creep in the matrix as mechanisms through which local stresses may be relaxed. The results indicated that the transient stresses which develop at the particle interface are higher than those at the triple points. A stress concentration of up to 20 was predicted under typical conditions at the particle interface, while at the triple point it was no greater than two. The stress which develops at the interface was considered sufficient to result in cavity nucleation (Argon et. al, 1980). It should be noted, however, that the stress at the triple point was influenced by the inhibition of sliding at the particles. These transient stresses were predicted to exist over a period of a few minutes, so that the incubation times for cavity nucleation observed experimentally (Argon et. al., 1980) could be explained.

The two mechanisms proposed for cavity nucleation at a hard particle, interface decohesion and vacancy condensation, both essentially predict a threshold stress for nucleation. Argon et. al. (1980) have concluded that the stress required for nucleation via vacancy condensation is quite close to that for decohesion. Thus the experimental determination of whether the nucleation process is controlled by athermal or thermal considerations is expected to be difficult. In addition, critical nuclei in metals are the order of 2 nm (Argon, 1983), below the resolution of SEM and TEM techniques, so that considerable growth has occurred before voids can be observed. At present the mechanisms involved in cavity nucleation are not amenable to experimental determination. However, it appears that nucleation does require the local conditions which exist around hard particles.

If cavity nucleation required grain boundary sliding, we would expect cavitation to occur most frequently on grain boundaries which slide the most, i.e., on those oriented at 45° to the tensile axis. Optical microscopy however, shows a majority of cavities on boundaries oriented normal to the maximum tensile stress axis (Hull and Rimmer, 1959). This result is likely due to the variation in void growth rate with boundary orientation relative to the tensile axis, and the level of resolution of the observations. Johannesson and Tholen (1969), using electron microscopy techniques, saw in copper that cavities less than 3 μ were randomly distributed along grain boundaries, but larger cavities were on boundaries approximately normal to the tensile axis. Taplin (1969) saw in alpha-brass, that for small grain sizes a maximum

in cavitation occurred on boundaries 45° to the tensile axis, and that this angle moved towards 90° with increasing grain size. The importance of grain boundary sliding as a deformation mechanism in small-grained metals could account for a significant growth component in these observations.

Experiments have shown that cavities initiate early in the primary creep stage (Boettner and Robertson, 1961; Ratcliffe and Greenwood, 1965), and continue to nucleate throughout creep. Dyson (1983) (see also Argon, 1983) has concluded from experimental observations in several Nimonic and Cr-Mo alloys, as well as in α-iron, that in any engineering alloys void nucleation occurs over a large portion of the creep life, although in some cases a saturation point is attained. Dyson has suggested that the cavity number density is dependent only upon the strain, independent of the applied stress. (Ratcliffe and Greenwood (1965), however, have reported an influence of superimposed pressure in inhibiting observed cavity nucleation in magnesium). It should be noted that the cavity density measurements reported include a growth component, due to the resolution involved in the microscopy. Thus quantitative comparisons are questionable, however, the qualitative conclusion that cavity nucleation occurs continuously appears reasonable.

Both diffusion and power-law creep have been proposed as mechanisms involved in cavity growth. Hull and Rimmer (1959) showed in copper that only tensile stresses resulted in void growth, and that superposition of a hydrostatic pressure upon an applied tensile stress eliminated cavity growth (see also Needham and Greenwood, 1975). This result could be explained in terms of a vacancy condensation mechanism.

The models which have been developed to predict void growth rates have considered three controlling mechanisms: (i) grain boundary diffusion, (ii) surface diffusion along the cavity surface, and (iii) power-law creep in the surrounding matrix. These are illustrated in Figure 2.10. In Figures 2.10a and b, note that the arrows indicating the diffusion flux refer to the material. The vacancy flux is in the opposite direction.

We will present here only the predictions given by the analyses of void growth rates, under the controlling mechanisms given above. They have been fully developed in the review of Cocks and Ashby (1982a) and summarized in Svensson and Dunlop (1981), to which further reference can be made.

At creep temperatures, vacancy diffusion in the lattice is usually orders of magnitude slower than along the grain boundary, so that the flux of lattice vacancies is usually neglected in diffusional void growth models. In void growth controlled by the diffusion of vacancies along the grain boundary, the driving force for vacancy transport to the cavity/grain boundary junction is the gradient in local traction across the boundary established during creep. Solutions to diffusion equation which give the cavity growth rate assume that the grain boundary acts as a perfect vacancy source and sink (Herring, 1950) and that at the void/boundary junction the normal stress across the boundary is completely relaxed to the sintering stress level. In addition, to obtain an analytic solution a periodic void spacing is assumed, and the voids are considered to all nucleate at the same time. Thus,

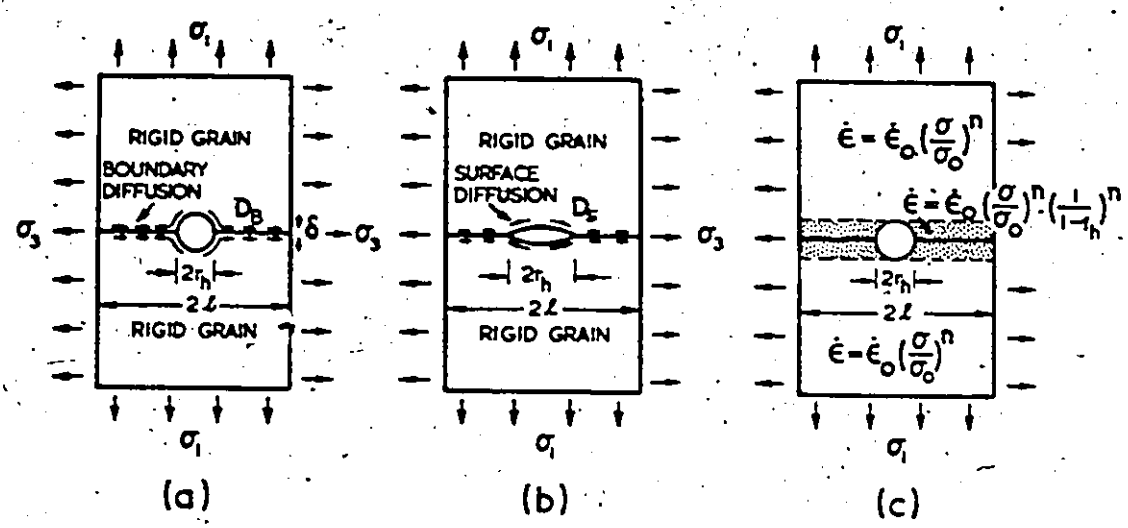

Fig. 2.10: Controlling mechanisms in void growth: (a) grain boundary diffusion control, (b) surface diffusion control, and (c) power-law creep control. Note that in (a) and (b), the flux directions refer to the material (from Cocks and Ashby, 1982a).

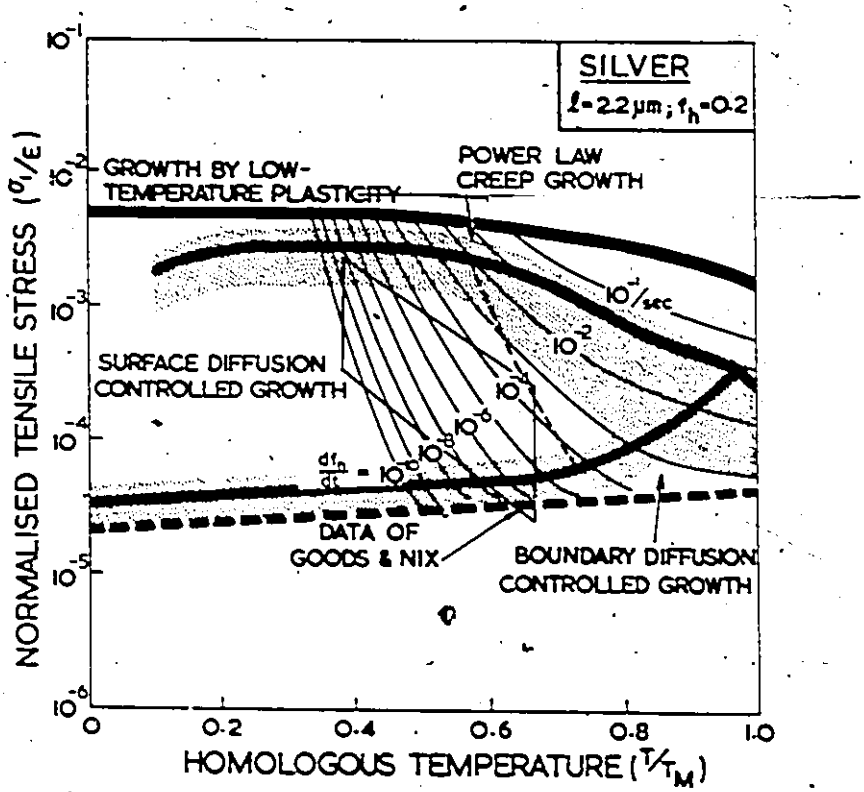

Fig. 2.11: Void growth map for silver, for an area fraction cavitated of 0.2 and a void spacing of 4.4 μ (from Cocks and Ashby, 1982a).

the analysis needs only to consider the growth of a single void. Fracture is then assumed to occur when the cavity size-to-spacing ratio attains a critical value, i.e., a critical area fraction cavitated defines the onset of the final, rapid fracture process.

The results obtained for grain boundary diffusion control predict that cavity growth rates have a linear stress dependence. Assuming cavities are present at the onset of creep, the creep rupture time varies inversely with stress, and the activation energy corresponds to that of grain boundary diffusion.

In grain boundary diffusion controlled growth, it is assumed that transport of material along the surface of the cavity is rapid enough that the chemical potential gradient is negligibly small. If surface diffusion rates are not rapid enough to redistribute material along the cavity surface however, the curvature of the surface will vary. The cavity will evolve with time into a crack-like defect. Cane and Greenwood (1975) have observed this change in cavity shape with growth in α-iron. Chuang and Rice (1973) introduced a model to account for the effect of surface diffusion in producing a non-equilibrium void shape. In the extreme case where surface diffusion is much slower than grain boundary diffusion the rupture time is predicted to vary with stress as σ^{-3}, with the activation energy associated with creep fracture given by that for surface diffusion.

Subsequent analyses (Goods and Nix, 1978a; Chuang et. al., 1979; Wilkinson and Vitek, 1982) of surface diffusion controlled growth in the crack-like mode have given two limiting forms for the void growth rate,

dependent upon the cavity spacing c, the stress σ, and the ratio $\Delta = \frac{D_s \delta_s}{D_b \delta_b}$. Here D_s and D_b are the surface and boundary diffusion coefficients, respectively, and δ_s and δ_b are the width of the vacancy diffusion paths along the void surface and boundary, respectively. When the product $c\sigma\Delta$ is high, cavity growth rates are proportional to $\sigma^{3/2}$, while at the opposite extreme a σ^3 dependence is predicted.

Chuang et. al. (1979) give values for D_s and D_b for a number of metals which suggests that $\Delta > 1$ in most cases. Thus, quasi-equilibrium (i.e., grain boundary diffusion control) or mixed-mode growth is predicted to occur most frequently. However, the numerical studies of Pharr and Nix (1979) have shown that if Δ is close to unity, a transition from equilibrium to crack-like cavity growth can occur, and a unique stress dependence for the cavity growth rate would not be realized. This effect could complicate the analysis of experimental results.

The analysis of void growth through power-law creep of the surrounding matrix has been given by Edward and Ashby (1979), to obtain an upper bound solution for the growth rate. Cocks and Ashby (1982b) have extended the analysis to the multiaxial stress case, and found that void growth was enhanced by a hydrostatic tension (-p) through a factor $\beta = \sinh\left[-2\left(\frac{n - 0.5}{n + 0.5}\right)\frac{p}{\sigma}\right]$, where n is the creep stress exponent. Predicted failure times were enhanced by a factor of $\frac{1}{\beta}$. The dependence of cavity growth rate upon $\frac{p}{\sigma}$ is thus predicted to be quite strong, how-

ever, in this analysis cavities were assumed to remain equiaxed. This would be expected to hold only for high $\frac{p}{\sigma}$ ratios, unless surface diffusion were very rapid.

In treating grain boundary cavity growth by power-law creep, it is assumed that the deformation behaviour near the grain boundary is the same as that within the grain, and indeed that of the material on a macroscopic level. Etch-pit observations in aluminum have indicated a much smaller subgrain size near the grain boundary (Grant and Chaudhuri, 1965), which suggests that this assumption may not be valid.

Edward and Ashby (1979) obtained a lower bound for the time to fracture through void growth by power-law creep. The resulting values obtained for a Monkman-Grant constant $C_{MG} = \dot{\varepsilon}_{ss} t_f$ (where $\dot{\varepsilon}_{ss}$ is the steady-state creep rate and t_f the fracture time), however, were much higher than those observed in practice. They then proposed that both grain boundary diffusion and power-law creep may operate simultaneously to give an enhanced void growth rate. In this model, the diffusion field about a cavity did not extend to the midpoint of the ligament separating neighbouring cavities. The strain resulting from the diffusive plating of material from the void along the grain boundary was accommodated through creep in the surrounding material. Edward and Ashby were able to derive explicit equations for the time and strain to fracture for this coupled growth mechanism, and using observed values for cavity spacings were able to obtain values for C_{MG} which were close

to those observed experimentally. The coupling of grain boundary diffusion and power-law creep has been analyzed again by Cocks and Ashby (1982b) to obtain a better bound on the rate of hole growth, which compares well with the finite element calculations of Needleman and Rice (1980). They find that simply adding the separate contributions of diffusion and power-law creep to obtain a cavity growth rate underestimates the coupled growth rate by no worse than a factor of two.

Cocks and Ashby (1982a) have treated the case of void growth by coupled surface diffusion and power-law creep, and present a simplified analysis of coupled surface and boundary diffusion control. They conclude that the cavity growth rates for these coupled processes are also well approximated by adding the separate contributions from the two mechanisms involved. The results they have obtained may be presented as void growth maps in $\frac{\sigma}{E} - \frac{T}{T_m}$ space, where E is the Young's modulus, and $\frac{T}{T_m}$ the homologous temperature. These maps indicate regions (for a given void spacing and area fraction cavitated) where individual mechanisms dominate the void growth rate and where coupling between mechanisms is significant. A void growth map for silver is presented in Figure 2.11, for a void spacing of 4.4 μ and area fraction cavitated 0.2. The utility of these maps is in the predictions they make regarding variations in cavity growth kinetics as conditions of stress, temperature, and damage level change.

The experimental identification of the controlling void growth mechanism, through the stress and temperature dependence of cavity growth or rupture time, is often complicated by the continuous nucleation of cavities during creep (Goods, and Nieh, 1983). Cane and Greenwood (1975) recognized this, and in an investigation of cavity growth in α-iron at 700°C they recorded the maximum observed cavity size as a measure of the size of voids which nucleated very early in the creep life. The growth rate of these cavities was proportional to σ^3, and the rupture time t_f varied with σ^{-3}. Their results suggested a surface diffusion controlled mechanism.

To remove the effects of continuous nucleation, a number of investigations have studied materials which have been implanted with a well-defined distribution of voids along the grain boundaries prior to creep deformation. In these materials the cavity spacing prior to creep corresponded with the dimple spacing on the fracture surface, so that fracture occurred through the growth of only those voids which were present before creep testing. Cavity growth kinetics were thus isolated, and obtained directly from the measured cavity sizes.

Mancuso and Li (1979) measured the cavity growth rate in nickel containing pre-existing CH_4 bubbles, and obtained a σ^3 dependence. Stanzl et. al. (1983) studied cavity growth in copper with implanted water vapour bubbles at 500°C, under tension and torsion. Times to fracture correlated with the maximum principal stress, indicating a third power dependence. These results suggest that void growth was surface diffusion controlled.

Goods and Nix (1978a,b) have implanted water vapour bubbles along grain boundaries in silver, with a diameter of 1 μ and spacing of 10 μ. They conducted tests over a range of stress and temperature to obtain both the stress dependence and the activation energy associated with rupture time. The creep life varied with $\sigma^{-3.7}$, and the activation energy was 85.5 kJ/mole. The stress exponent is close to that for surface diffusion control, however, the activation energy is somewhat low for surface diffusion in silver (Cocks and Ashby, 1982a). The presence of water vapour within the voids could have influenced surface diffusion rates, as Goods and Nix point out. Similarly, Nieh and Nix (1980) investigated creep fracture in OFHC copper implanted with grain boundary water vapour bubbles. The rupture time was found to vary as σ^{-3}, and the temperature dependence for fracture was characterized by an activation energy of 92 kJ/mole. The surface diffusion activation energy for copper reported in Butrymowicz et. al. (1977) is 86 kJ/mole, so that the results support a surface diffusion controlled mechanism.

Hanna and Greenwood (1982) also investigated creep fracture in tough pitch copper implanted with water vapour bubbles, but at low stress levels (4 to 8 MPa). The stress dependence of both the time to failure and the rate of void growth (through density measurements) were measured. At low stresses it was shown that the fractional volume increase due to cavity growth was equal to the measured creep strain, supporting a rigid grain model with the strain due only to the diffusive plating of material on the grain boundaries. The void growth rate exhibited a linear stress dependence, however, the failure time showed a

stress dependence of $\sigma^{-2.4}$, with an activation energy of 104 kJ/mole. The void growth measurements and activation energy support a grain boundary diffusion controlled mechanism, but the stress dependence of the failure time did not agree with predictions based on this mechanism.

Nieh and Nix (1979) showed that, in the investigation of Goods and Nix (1978a,b) creep deformation could not account for cavity growth. By strengthening silver with a fine dispersion of MgO particles they decreased the steady-state creep rate in the material by an order of magnitude. A similar distribution of grain boundary water vapour bubbles was introduced into this material, with the result that the rupture time was identical to that of the pure silver. Thus, cavity growth was a process which occurred independently from creep deformation in this material. It is important to note that the Monkman-Grant relationship did not describe cavity growth. The stress and temperature dependence of the rupture time strongly suggest that a diffusional process controlled the kinetics of fracture. The frequent observation of Monkman-Grant behaviour has been interpreted by Goods and Nieh (1983) as an expression of the influence of deformation on cavity nucleation, and that it is cavity nucleation which controls the creep life of many materials.

It is often observed that not all of the grain facets in a material become cavitated. The local dilation associated with void growth must then be accommodated by the surrounding undamaged material, so that cavity growth may be constrained by the rate at which the material deforms macroscopically. This concept was first introduced by Dyson

(1976). In maintaining compatibility between grains, load must be transferred from the cavitated boundaries to the uncavitated surroundings. The rate at which cavity growth can continue under these conditions depends on the actual tractions maintained on the cavitating boundary by the creeping surroundings.

Cocks and Ashby (1982a) have examined several cases where void growth and grain deformation can occur by diffusion or power-law creep mechanisms. Equations were obtained for damage growth rates on the cavitated boundaries for a given ratio of grain size to spacing between cavitated facets. The extent of the damaged region considered was one grain facet in this analysis.

The constrained-growth situation which has been treated most often is that in which void growth occurs through grain boundary diffusion control, while the surrounding matrix deforms by power-law creep. Rice (1981) has analyzed this problem in an approximate manner, for an isolated cavitated grain facet (see Anderson and Rice (1985) for the 3-dimensional case). The time t_f was calculated for the complete separation of a grain boundary facet of extent d for a given initial cavity radius a and cavity spacing b, to obtain

$$t_f = \frac{4h(\Psi)}{3\alpha} \left(\frac{b}{d}\right) \left[1 - \left(\frac{a}{b}\right)^3\right] \left(\frac{1}{\dot{\epsilon}_e}\right)$$

where $h(\Psi)$ is a constant given by the cavity/boundary dihedral angle, $\dot{\epsilon}_e$ is the equivalent strain rate of the distant strain field, and α is a numerical constant (for a power-law creep exponent of 5, $\alpha = 0.9$). Note

that this result gives a Monkman-Grant relationship, which is independent of the grain boundary diffusion coefficient. Dyson (1979) and Raj and Ghosh (1981) have shown that, for cases where an inhomogeneous distribution of damage was observed, as in the study of Pavinich and Raj (1977), a contrained growth model could explain the fracture behaviour. It is interesting that Pavinich and Raj noted a rapid increase in creep rate towards failure when cracks the size of a grain facet became observable. This supports the assumption in constrained growth models that failure is imminent when an isolated facet becomes fully cavitated.

It should be noted that the results from experiments on bubble-implanted materials are not complicated by the effects of constraint. (Note that the arguments of Anderson and Rice (1985) do not apply to these materials, as all the grain boundary facets are cavitated.) Grain boundaries in these materials were all uniformly cavitated, so that the void growth rates were not controlled by the overall deformation, as Nieh and Nix (1979) concluded.

The influence of both continuous nucleation on isolated grain boundaries and subsequent constrained growth on fracture has been treated by Argon (1982) and Riedel (1985). They have demonstrated that a Monkman-Grant relationship can be predicted with reasonable values, assuming a nucleation rate proportional to strain rate, and independent of stress. Riedel has compared predictions with the creep rupture behaviour of several Cr-Mo and stainless steels, and found reasonable agreement.

Another scale of inhomogeneity in cavity distribution has recently been addressed by Wilkinson (1986), in which the effects of a non-periodic void spacing on a grain boundary is analyzed. If voids are not periodically distributed on a grain boundary, coalescence will occur prior to the fracture of the facet, so that the average void spacing will increase. Diffusional void growth models predict a sensitivity to the void spacing, with the result that if void growth is controlled by grain boundary diffusion, the growth rate will decrease with coalescence. Wilkinson has treated an initially random distribution of voids, assuming the average growth rate for each void in the distribution. He obtains expressions for the influence of coalescence on the average growth rate, for coupled growth mechanisms involving either surface or grain boundary diffusion, and power-law creep. Power-law creep becomes the dominant mechanism involved in coalescence at high void area fractions, due to the increase in stress with depleted cross-section. This has been verified in silver by Goods and Nix (1978b). The results for void growth initially controlled by surface diffusion do not predict a significant effect of coalescence on time to failure.

However, for void growth initially controlled by grain boundary diffusion, growth rates are drastically reduced with increasing void area fraction, due to coalescence effects. Failure times are much longer than that predicted from a periodic void spacing, with final failure occurring through power-law creep controlled void growth. The predicted time to failure varies with σ^{-m}, where $m = (n + 2)/3$, and n is the creep stress exponent. The activation energy associated with

rupture behaviour is given by $Q_r = Q_c/3 + 2Q_b/3$, with Q_c the activation energy for power-law creep, and Q_b the activation energy for boundary diffusion. Wilkinson has obtained good agreement between the predictions of this model and the experimental results of Goods and Nix (1978a) and Hanna and Greenwood (1982).

To summarize, there have been several important advances over the past ten years in the prediction of creep life. Although the actual mechanisms involved in cavity nucleation are not resolved, the importance of the continuous nucleation of cavities during creep in controlling fracture, and the relationship of nucleation to local deformation processes have been recognized. The mechanisms involved in cavity growth are well understood, and have been identified in some materials. However, it has become apparent that the spatial distribution of cavities can influence cavity growth rates and the subsequent failure condition. The scale over which the inhomogeneity in distribution can affect damage accumulation rates may be over a distance of many grain sizes, or on a single grain facet.

2.5 HSLA Steels: Processing-Microstructure-Fracture Property Relations

High strength low alloy (HSLA) steels were developed to satisfy a need for steels with increased yield strength, improved low temperature toughness, and better weldability. These properties have been achieved by lowering the carbon level and strengthening through a refined ferrite grain size, controlled precipitation and substructural development. In

addition, improvements in casting practice and tundish technology to minimize reoxidation and entrap oxide inclusions (Ushijama et. al., 1984), and the use of sulphide shape-controlling additions (Wilson and McLean, 1980; McLean and Kay, 1977) have markedly reduced the effects of inclusions on the fracture behaviour of HSLA steels.

Today, HSLA steels have diversified from what were initially carbon-manganese steels micro-alloyed with columbium, vanadium or titanium into acicular ferrite or low carbon bainitic steels, quenched and tempered steels, cold rolled and annealed steels, dual phase steels, and the higher carbon more pearlitic steels. These have been reviewed recently by Pickering (1984). We will be concerned here mainly with the ferrite-pearlite class of steels, which however, are often observed to contain other transformation products.

A reduction in ferrite grain size results in both an increase in yield strength and a decrease in the impact transition temperature ITT (Gladman et. al., 1977). This was initially accomplished by increasing the manganese content, which depresses the Ar_3 temperature and results in a higher ferrite nucleation rate. However the decrease in ferrite grain size was limited by the transformation to bainite or martensite. Further reductions in grain size were accomplished through reductions in the austenite grain size, via an intimate sequence of controlled rolling and precipitation. The influence of the thermo-mechanical route taken in the controlled rolling process on microstructure has been reviewed by Tanaka (1981). He discusses controlled rolling as a three-stage process, with: (i) deformation in the austenite recrystallization region,

(ii) deformation above the Ar_3 temperature, in a region where the austenite does not recrystallize, and (iii) deformation in the two phase austenite-ferrite region. This is illustrated in Figure 2.12. Deformation in the recrystallization region produces a smaller uniform austenite grain size, with nitrides of titanium and aluminum or columbium carbo-nitrides inhibiting grain growth. Columbium effectively retards austenite recrystallization in deformation at lower temperatures, so that elongated grains with well-developed deformation bands are produced. Austenite grain boundaries and the deformation bands are potent ferrite nucleation sites, and this arrangement of grain shape and deformation banding leads to the impingement of growing ferrite grains. A fine grain size results.

Further increases in yield strength have been obtained through precipitation-hardening and the development of dislocation substructure by deformation in the austenite-ferrite region and through controlled cooling rates. Although columbium carbo-nitrides do offer a degree of precipitation strengthening, its solubility product at transformation temperatures is low. Vanadium carbide has a higher solubility in austenite, and the precipitation of these particles at the austenite/ferrite boundary contributes more effectively to an increase in yield strengh. The effectiveness of a micro-alloying addition in increasing the yield strength is dependent upon the rate of cooling, the transformation temperature and the deviation of the steel composition from stoichoimetric composition with respect to the carbide or nitride considered (Gladman

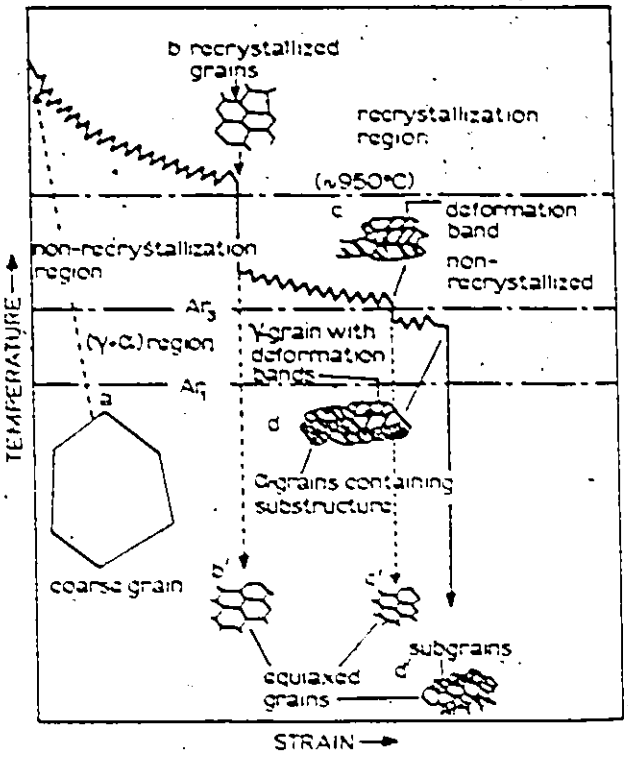

Fig. 2.12: Schematic illustration of the three stages in the controlled-rolling process, and change in microstructure due to deformation at each stage (from Tanaka, 1981).

et. al., 1977). The increase in yield strength gained through precipitation-hardening, however, is accompanied by an increase in ITT. Similarly, deformation in the austenite-ferrite region produces a dislocation substructure which increases the yield strength, along with the ITT. The deterioration in impact properties is influenced by precipitation, which pins the dislocations. In acicular ferrite, where the increase in dislocation density is an increase in the mobile dislocation density, the low temperature toughness and ductility are enhanced (Pickering, 1977; Boyd, 1979).

Inhomogeneity in austenite grain size results in variations in the local transformation characteristics, so that a large austenite grain size yields a large ferrite grain size, or possibility transformation to bainite (Tanaka, 1981). A deterioration in low temperature properties follows the development of these microstructural features. Tanaka et. al. (1982) point out that insufficient deformation in the recrystallization regime may not produce a uniform austenite grain size. In the non-recrystallization domain, inadequate reduction can result in variations in austenite grain shape and deformation substructure, which will also lead to variations in ferrite grain size. In addition, extensive hold times between rolling passes at lower temperatures can result in partial austenite recrystallization, to produce a non-uniform ferrite grain size. Pickering (1984) has noted that, if alloying additions are far removed from the stoichiometric composition, large precipitates of TiN up to 0.5 μ in size may result, which can serve as ferrite nucleation sites. This can also lead to an inhomogeneous ferrite grain size.

Although finish rolling temperatures in the austenite-ferrite region increase the yield strength, an inhomogeneous, anisotropic microstructure is produced. This often leads to a more pronounced non-uniform ferrite grain size distribution, with regions of large ferrite grains elongated in the rolling direction (Cheng et. al., 1982). It has been shown that the effective ferrite grain size which determines low temperature fracture behaviour is given by the grain intercept length measured in the direction of fracture propagation (Gladman et. al., 1977). Anisotropy in fracture properties may thus be expected in products rolled in the two-phase region. This was shown in the work of Cheng et. al., where the through-thickness properties were inferior to those in the rolling direction. Also influencing their results, however, was the preferred ferrite orientation with {001} planes parallel to the rolling plane. The development of this texture through low temperature finish rolling has been noted in other work, e.g., Speich and Dabkowski (1977). Their results indicated a strong (001) texture present at the plate centre-line, however, at the plate surface no preferred orientation was detected.

Manganese segregation during solidification leads to pearlite banding along the rolling plane, and this is accentuated by low finish rolling temperatures. Transformation temperatures are influenced by deformation and the cooling rate, which in turn influence the volume fraction and morphology of the pearlite (Embury et. al., 1977). As the amount and nature of the pearlite influences low temperature toughness (Pickering, 1978; Hahn, 1984), both the amount of deformation at low

temperatures and cooling rates involved in the rolling schedule affect the impact transition temperature, through their influence on the transformation products. Embury and Cooper (1975) (see also Embury et. al., 1977) have noted that the development of grain boundary carbides is also related to the thermo-mechanical history.

Thus, in attempting to predict the ductile-brittle transition in controlled-rolled HSLA steels, one must consider the presence of several microstructural constituents. Dependent upon the ferrite grain size or the volume fraction of a given component, different features may control fracture. Local fracture parameters such as the critical cleavage stress cannot be related to a unique feature of the microstructure, such as the ferrite grain size. In addition, gradients in the microstructure are often seen in moving from the plate surface to the centre, the result of segregation and differences in cooling rates (Embury et. al., 1977). Thus, average microstructural parameters may not correlate with the critical local parameters relating to fracture. The spatial distribution of microstructural features, and spatial correlation between different components are then necessary to the prediction of fracture behaviour. The relationship of microstructure with fracture properties is further complicated by the influence of dislocation substructure. Kotilainen (1980b) has determined that, in bainitic structures, the cleavage fracture strength was dependent upon the dislocation density. A unique relation between bainite packet size and cleavage fracture was not observed. The combined effect of deformation in the austenite-ferrite region and precipitation in influencing the low temperature

properties of ferrite is also expected to be complicated (Boyd, 1979), and at present is not fully appreciated.

The competition between the local fracture processes associated with various microstructural components in controlling fracture is sensitive to the scale and distribution of features. As the microstructure varies through and along the plate, the overall control of fracture behaviour at a given stress and temperature will be dependent upon the volume of material under the test conditions, relative to the scale and nature of the microstructural distribution. A range of possible mechanisms compete among each other, or may interact, to control fracture.

In the transition range between brittle and ductile failure, splitting or delamination is often observed along planes parallel to the rolling plane. This problem is most evident in products which have been rolled in the two-phase region. It results in a sloping transition interval on the impact energy absorption curve, with the upper shelf energy promoted to higher temperatures (Evensen, et. al., 1979). Various mechanisms have been proposed which may contribute to this phenomenon (Bramfitt and Marder, 1979) which include the influence of

(i) grain boundary carbides,

(ii) a duplex elongated ferrite grain size,

(iii) pearlite banding,

(iv) segregation to ferrite or prior austenite grain boundaries,

(v) elongated non-metallic inclusions, or planar clusters of inclusions,

(vi) the development of a (100) texture in the rolling plane,

(vii) the influence of residual stresses which arise through deformation and transformations.

Although results indicate that the above features may contribute to splitting or delamination, the phenomenon has been observed in the absence of many of them. Thus, it appears that splitting or delamination can occur through different mechanisms (Bramfitt and Marder, 1979).

An important source of weakness in delamination has been identified as the ferrite grain boundaries which contain a distribution of carbides (Hero et. al., 1975; Evensen et. al., 1979), along which splitting was observed to propagate. Evensen et. al. concluded that delamination could occur through a ductile process, in which void nucleation at the grain boundary carbides provided the critical event in the onset of delamination. Their results indicated that this process was controlled by a critical shear stress criterion. However, the influence of non-metallic inclusions was also noted in another material, so that in a given steel we may expect the possibility of several mechanisms contributing to the delamination process. The criterion for delamination will not be unique then. Baldi and Buzzichelli (1978) have concluded that a critical tensile stress criterion described delamination behaviour in several acicular and polygonal-acicular steels.

In ductile fracture processes, voids are observed to nucleate at non-metallic inclusions, and at or in the non-ferritic transformation

products (Embury et. al., 1977). However, the coalescence of voids is frequently observed to occur by localized shear, terminating continued void growth. A high dislocation density in the ferrite matrix, due to the low transformation and finish rolling temperatures, results in a low rate of work hardening relative to the flow stress. This promotes localized shear in the ligament separating voids. Thus, although the size of the process zone ahead of a crack tip is in many cases determined largely by the sulphide spacing (Evensen et. al., 1979), it is the work-hardening capacity and distribution of non-ferritic phases which controls the local strain to failure in void coalescence. The influence of pearlite in decreasing the strain rate sensitivity was indicated by Spitzig (1983b), an effect which would also promote localized flow. Evensen et. al. (1979) suggest that, although COD values can be increased through desulphurization and sulphide shape control, the ability of the matrix to work harden will impose a limit to the toughness that can be attained in HSLA steels.

The volume fraction and size of inclusions can significantly alter the ductility and toughness of HSLA steels (Baker and Charles, 1971). However, the distribution and shape of inclusions have marked effects on through-thickness ductility and lamellar tearing in welding, and can reduce the upper shelf impact energy (Pickering, 1978). At the lower finish rolling temperatures used, manganese sulphides become more plastic than the matrix, so that the final rolling stages produce stringered sulphides (Pickering, 1979). Clusters of alumina inclusions, the result of nozzle blockage deposits or agglomeration in the molten

steel, become oriented into planar arrays during rolling. These clusters of alumina inclusions and elongated sulphides, oriented in the rolling plane and in the rolling direction , result in poor through-thickness and transverse properties. Spitzig (1983a) has concluded that, in banded C-Mn steels, the presence of banded pearlite does not significantly influence the ductility and impact shelf energy. Thus he has shown that it is the sulphide orientation which controls the anisotropy in behaviour. In addition, Wilson (1984) has noted that the through-thickness ductility and impact shelf energy in several HSLA steels were dependent upon the size of the inclusion clusters. Therefore, the influence of inclusions on fracture behaviour is expressed both in the anisotropy and level of clustering of the distribution.

Sulphides are often present in HSLA steels in considerably higher levels than are other inclusions, so that these inclusions dominate the mechanical properties. Manganese sulphide is the most predominant form. The morphology (classed as type I, II or III) and the plasticity of manganese sulphides are dependent upon the level of deoxidation of the melt (Pickering, 1979). However, as the ability of the inclusion to deform within the matrix is dependent upon both the deformation characteristics of the inclusion material and the initial geometry of the inclusion, it is not clear which type of manganese sulphide has a greater deformability relative to the steel. Pickering (1979) suggests that the type II manganese sulphides, formed at intermediate levels of deoxidation, give rise to the arrays of coplanar ribbons of inclusions during low temperature rolling.

It is important to note that the sulphides precipitate out during solidification, so that they cannot be removed by stirring methods and improvements in tundish design, as many oxides can (Ushijima et. al., 1984). In particular, the more injurious type II manganese sulphides precipitate interdendritically during later stages of solidification. Thus, to prevent the development of long thin sulphides additions are made in the ladle which globularize and/or decrease the deformability of the sulphides (McLean and Kay, 1977; Pickering, 1979; Wilson and McLean, 1980; Wilson, 1984). The additions made to control the shape of sulphides include zirconium, titanium, rare earths such as cerium and lanthanum, and calcium. Calcium also globularizes aluminum oxides, due to the formation of a more plastic calcium aluminate in the melt. Control over inclusion shape can increase the transverse impact energy and through-thickness ductility to levels almost equivalent to that in the longitudinal direction.

There are problems associated with the use of the above-mentioned sulphide shape modifiers. For example, titanium and zirconium have high affinities for nitrogen, and must be added in relatively large quantities in steels which owe their strength to vanadium nitride precipitation. However if the addition levels are too high, carbo-sulphides can form, which result in cracking problems during primary rolling. Rare earths are very expensive, and have a high affinity for oxygen. Thus, steels should be deoxidized before rare-earth additions are made (McLean and Kay, 1977). The effectiveness of cerium has been erratic (Pickering, 1978).

Calcium is becoming a commonly employed sulphide modifier, in addition to the benefits gained as a deoxidant. There are difficulties in introducing calcium into liquid steel, due to its low solubility, a vapour pressure greater than one atmosphere at 1600°C, and because many calcium alloys are light and quickly float to the top of the ladle (Pickering, 1979). However, the use barium additions which decrease the activity of calcium in the melt, and the development of ladle injection techniques blowing calcium carbide powders in an argon carrier gas have resulted in acceptable efficiency levels (Wilson, 1984).

Manganese sulphide can dissolve calcium to a level of ~ 13%, which leads to an equiaxed inclusion which resists plastic deformation. Often the sulphur is associated with the highly stable CaS, which is very resistant to deformation (Pickering, 1979). Depending upon the level of calcium which has been introduced into the melt, the (Mn,Ca)S may frequently be associated with calcium aluminate inclusions. This is observed as a peripheral rim about the calcium aluminate, which gives support to the sulphide and thus reduces its ability to deform. The various forms of calcium aluminate/(Mn,Ca)S duplex inclusions which can develop, dependent upon the effectiveness of the calcium treatment, have been presented by Wilson (1984). Wilson also notes that, in addition to its effectiveness as a shape-controller, the use of calcium can also result in a cleaner steel. Sulphides containing calcium begin to precipitate out at higher temperatures. Thus, they are not trapped in the interdendritic regions in the late stages of solidification, and can rise and float out of the melt.

A serious problem in continuously-cast HSLA steels which results in microstructural inhomogeneity arises due to centre-line segregation. This leads to unacceptable levels of impurities, alloying additions and inclusions along the centre of the final product (Ushijima et. al., 1984). Thus, the transformation products and inclusion content along the centre-line can be very different from the rest of the material. Indeed, the microstructure both in and away from the centre region may not be optimal for a given rolling schedule due to the segregation pattern. Lowering the superheat can reduce centre-line segregation, however, this can result in nozzle clogging and poor steel cleanliness. The use of electro-magnetic stirring in and below the mold leads to lower levels of segregation, but does not completely eliminate it. The nature of the solidification path in continuously-cast HSLA steels thus can result in the development and distribution of microstructural components which does not optimize the properties with respect to that which could be obtained in a steel with a more uniform composition.

CHAPTER 3

A CONTINUUM DAMAGE MODEL OF DUCTILE FRACTURE

3.1 Introduction

As discussed in the literature review, the classical continuum approach to damage mechanics uses the concept of the net section stress to provide a description of the accumulation of material damage. An increase in the level of damage increases the net section stress, thus accelerating the damage rate. The empiricism of this approach, however, makes it difficult to predict or separate the effects of continued damage nucleation and coalescence in promoting enhanced rates of damage accumulation.

In the ductile fracture mode, fracture predictions based on continuum analyses of void growth require that the intervoid spacing be known. This is usually taken as a fraction of the average void or inclusion spacing in a material. This is equivalent to assuming a periodic distribution of second phase particles or voids, which is rarely observed in real materials. In a distribution of voids which is non-periodic, coalescence of voids in a clustered region to produce a large flaw will occur at strains lower than that required for coalescence in a regular array of voids.

The influence of continuous void nucleation on accelerated damage accumulation in ductile fracture has been studied by Teirlinck (1983). To complement this work an analysis is presented here of the effect of void coalescence on the damage process. A probabilistic model is developed which predicts the global damage level, given by the average void area fraction in a plane normal to the tensile axis. This is based upon a simple geometrical criterion for coalescence, assuming a dilute random distribution of voids.

Following this, an approach to the simulation of the development of a distribution of void sizes due to coalescence is presented.

3.2 Development of the Model

Let us consider the case of simple uniaxial tension (plus an additional hydrostatic component, if present), where all of the voids have nucleated at a strain ε_{nuc}. The resulting voids are assumed to be axisymmetric ellipsoids, with semi-axis along the tensile direction given by r_1 and semi-axis normal to the tensile direction given by r_2. The primary result of the model is a prediction of a global, or average damage parameter, taken as the area fraction of voids in a random plane section normal to the tensile axis.

The basic assumption in the model presented here is that the criterion for void linkage is purely geometrical, and is determined by the proximity of voids in a plane normal to the tensile axis. The separation which defines the coalescence condition is assumed to be dependent upon the void dimensions. If two voids cannot be sectioned by the

same plane, the possibility of coalescence is discounted. Figure 3.1 illustrates the situation where two voids satisfy this condition. The amount by which voids must overlap the section plane in order for coalescence to be allowed is assumed to be δr_1, where δ is an adjustable parameter.

The continuum models of void growth (e.g., Rice and Tracey, 1969) predict that the extension rate $\dot{r}_1/r_1$ of voids along the tensile direction should be greater than the macroscopic strain rate $\dot{\epsilon}$, for low work-hardening rates. This results in an increase in the void number density in a plane normal to the tensile axis with continued straining, a feature which is crucial in the present model. The continuous addition of voids to the section plane (or rather, holes, due to the intersection of the plane with the void) due to growth results in an increased probability of void coalescence.

With this in mind, the model is developed by first considering a (random) plane normal to the tensile axis. Although the voids are ellipsoidal so that the cross-section varies with distance from the centroid, their intersection with the plane is approximated by a circle of radius r_2. Circular discs (corresponding to the intersection of the plane with the void) are added sequentially to the plane, and the increase in the probability P that an additional disc will interact with others already in the plane is calculated. The interaction zone around a disc corresponds to a circular region lying in the section plane about a void, the size of which is dependent upon the void dimensions. Thus we are considering an overlap problem in a plane, where the features are

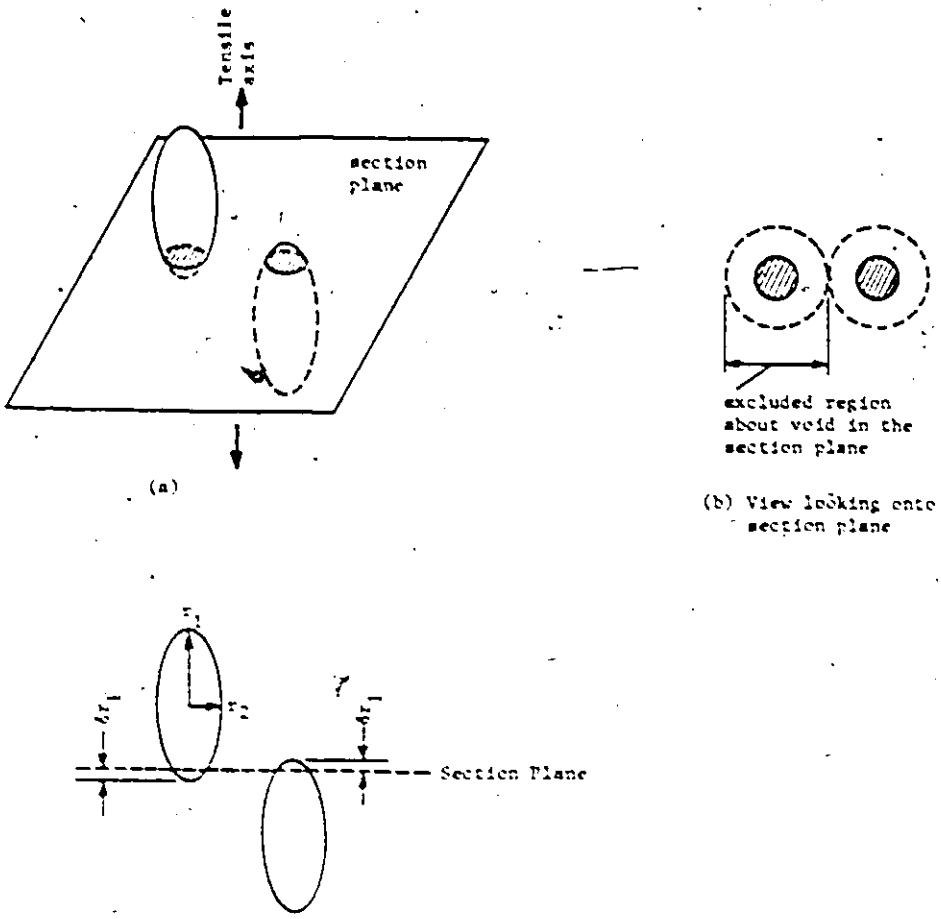

Fig. 3.1: Illustration of the condition in which two voids are sectioned by a plane normal to the tensile axis. The regions in the plane intersecting the voids are given by the shaded circles. The coalescence condition is defined in (b).

an excluded region about the voids, given by the dotted circles in Figure 3.1b. As the spatial distribution of voids is assumed to be random, the calculation of the coalescence probability P can be based upon the area fraction of excluded regions in the section plane.

Two simple criteria for coalescence will be discussed here. We first consider a criterion where the void separation in the section plane resulting in coalescence is dependent linearly upon the dimension r_2 of the voids, and secondly, the case of a linear dependence upon r_1. These conditions for coalescence relate to the removal of plastic constraint in the region between two closely-spaced voids. A slip line field can then be drawn between the two voids, allowing the internal necking associated with the linkage step (Brown and Embury, 1973).

(i) Critical Separation Linearly Dependent Upon r_2

Here we assume the excluded region about a void is given in the section plane by a circle of radius αr_2. To avoid overlap with any excluded regions and resulting void coalescence, the centre of an added void must not lie within a circle of area $\pi(2\alpha r_2)^2$ centered about each of the other voids in the section plane. The coalescence condition is met as shown in Figure 3.2. Thus, the addition of each void to the section plane results in a decrease in area of $\pi(2\alpha r_2)^2$ in which the centre of another void may lie without coalescing with others.

To account for the increase in void fraction due to the coalescence process, we replace an added void which coalesces with a void of radius $S r_2$ in the section plane. Thus, with P the probability that a

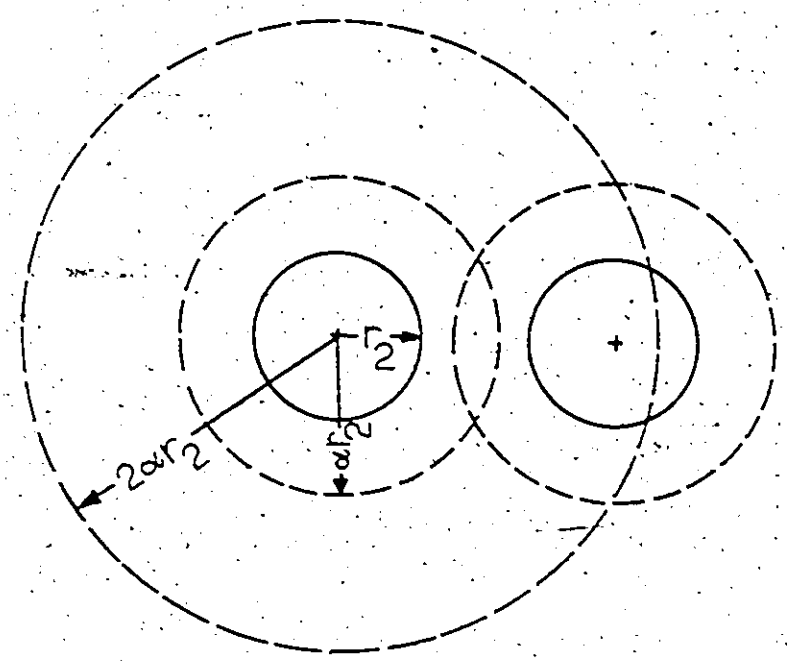

Fig. 3.2: View onto the section plane, illustrating the coalescence condition using the r_2 criterion. Two voids, given by the circles of radius r_2 in the section plane, have a centre-to-centre spacing less than $2\alpha r_2$.

void added to the section plane will coalesce with voids already existing in the plane, and N_A the areal void number density in the plane, we add dN_A voids (or rather, discs) to the plane, of radius r_2. This results in an increase in P given by

$$\begin{aligned} dP &= \pi(2\alpha r_2)^2 dN_A + P\pi[(\alpha\beta + \alpha)r_2]^2 dN_A - P\pi(2\alpha r_2)^2 dN_A \\ &= \pi\alpha^2 r_2^2[4 + (\beta + 3)(\beta - 1)P]dN_A \end{aligned} \tag{3.1}$$

The factor $(\alpha\beta + \alpha)$ in the second term results from a consideration of the interaction between voids of radius βr_2 and r_2, illustrated in Figure 3.3. In solving for P we perform the integration between $N_A = 0$ and $N_A = N_A$ (noting that, as N_A approaches zero P also approaches zero). One then obtains

$$P = \frac{4}{(\beta + 3)(\beta - 1)}\left[\exp\left(\pi\alpha^2 (\beta + 3)(\beta - 1)r_2^2 N_A\right) - 1\right] \tag{3.2}$$

Note that, for small N_A, $P = \pi (2\alpha r_2)^2 N_A$, the result expected for the dilute void case.

In view of the dilute void approximation, two factors have not been included in equation 3.1. The first is that no voids of radius βr_2 have been added to the plane, only those with radius r_2. Note that the addition of voids of radius βr_2 in the second term is due to the coalescence upon addition of dN_A voids of radius r_2, and not due to the addition of larger voids. At higher damage levels, we thus underestimate P. The other factor, which contributes to an overestimate of P is illustrated in Figure 3.4. Here the two voids are separated sufficiently

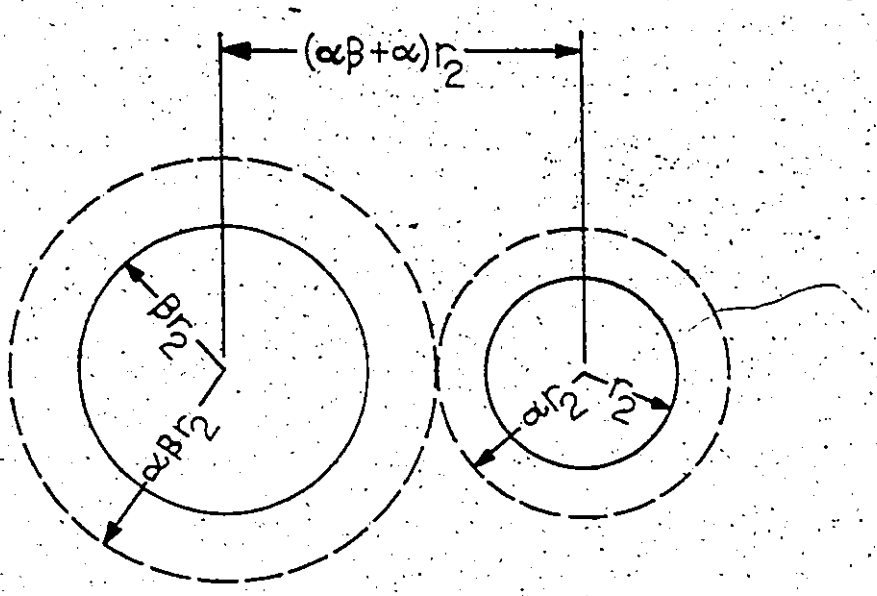

Fig. 3.3: View onto the section plane, in which the coalescence condition (r_2 criterion) between voids of lateral dimension r_2 and βr_2 is defined.

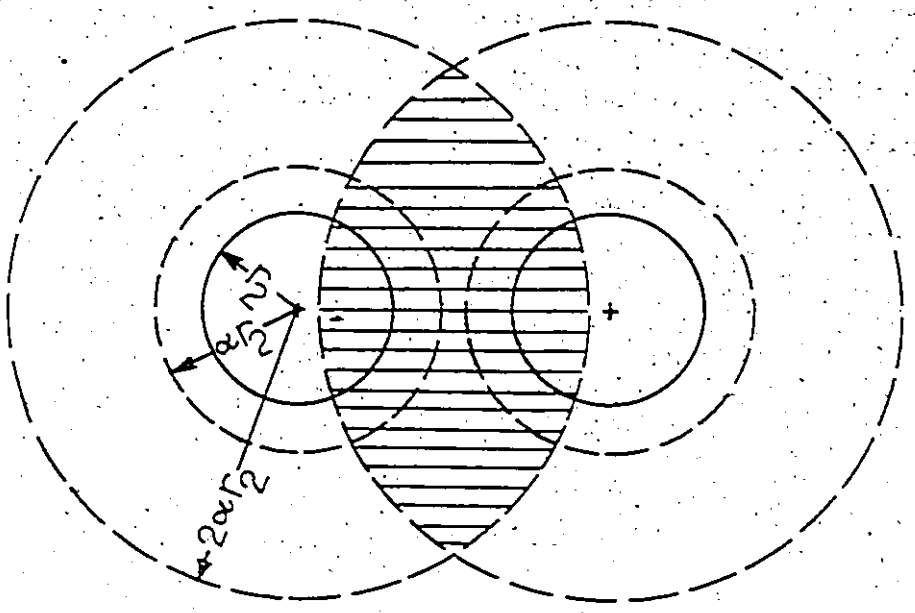

Fig. 3.4: View onto the section plane, illustrating overlap of the excluded regions about two isolated voids, shown as the shaded region. This effect leads to an overestimate of the coalescence probability.

so that they will not coalesce, however, the excluded regions of radius $2\alpha r_2$ about each of the voids overlap in the shaded portion indicated. At higher void densities in the section plane, this effect becomes non-negligible, so that we have overestimated the actual total excluded area.

Since the addition of voids to the section plane results from the growth of voids in the tensile direction into the plane, the centre of the added void which coalesces may lie within 0 to $2\alpha r_2$ from the centre of a void already sectioned by the plane. Thus the value of β would be expected to have a distribution of values. This effect, however, is taken care of in the following calculation of f_A, the area fraction of voids in the section plane.

With the addition of dN_A voids (of radius r_2) per unit area to the section plane, the increase in void area fraction is given by

$$\begin{aligned} df_A &= [\pi r_2^2 dN_A + P\pi(\beta r_2)^2 dN_A - P\pi r_2^2 dN_A] \cdot (1 - f_A) \\ &= \pi r_2^2[1 + (\beta^2 - 1)P] dN_A \cdot (1 - f_A) \end{aligned} \tag{3.3}$$

The $(1 - f_A)$ term accounts for the existing void cross-sections in the plane occluding others which grow into the plane. Substitution of equation 3.2 into 3.3 and integrating between $N_A = 0$ and $N_A = N_A$ gives

$$f_A = 1 - \exp\left[-\left(C_1\pi r_2^2 N_A + C_2\left[\exp(C_3\pi r_2^2 N_A) - 1\right]\right)\right] \tag{3.4}$$

where

$$C_1 = 1 - \frac{4(\beta + 1)}{(\beta + 3)}$$

$$C_2 = \frac{4(\beta + 1)}{\alpha^2(\beta + 3)^2(\beta - 1)}$$

$$C_3 = \alpha^2(\beta + 3)(\beta - 1)$$

Note that for small N_A we obtain $f_A = \pi r_2^2 N_A$, as expected.

To relate the areal void number density in the section plane N_A to the number density of voids per unit volume N_V, we use $N_A = 2r_1 N_V$, a standard expression for a random void distribution. However, consideration of the overlap distance (see Figure 3.1(c)) δr_1, which a void must cross over the section plane so that it be included in the coalescence process gives the eligible areal density of voids in the plane as

$$N_A = 2(1 - \delta)r_1 N_V \tag{3.5}$$

If all of the voids present initiated at the same strain with no further nucleation, N_V would decrease with continued coalescence in the development of a real void size distribution. However, because we treat coalescence by replacing a void of radius r_2 in the plane with one of radius βr_2, we take N_V as constant throughout the strain history.

If the volume fraction of voids at the nucleation condition is f_V, then $f_V = \frac{4}{3}\pi r_{01} r_{02}^2 N_V$, where r_{01} and r_{02} are the dimensions of a void at nucleation (all assumed identical). Then

$$\pi r_2^2 N_A = \frac{3}{2} f_V (1 - \delta) \frac{r_2^2 r_1}{r_{02}^2 r_{01}} \tag{3.6}$$

Substitution of equation 3.6 into 3.5 gives

$$f_A = 1 - \exp\left[-\left(K_1 f_V \frac{r_2^2 r_1}{r_{02}^2 r_{01}} + K_2 \left[\exp.\left(K_3 f_V \frac{r_2^2 r_1}{r_{02}^2 r_{01}} \right) - 1 \right] \right) \right] \tag{3.7}$$

where

$$K_1 = \frac{3}{2}(1 - \delta)\left[1 - \frac{4(\beta + 1)}{(\beta + 3)} \right]$$

$$K_2 = \frac{4(\beta + 1)}{\alpha^2 (\beta + 3)^2 (\beta - 1)}$$

$$K_3 = \frac{3}{2}(1 - \delta)\, \alpha^2\, (\beta + 3)(\beta - 1)$$

Note here that r_1 and r_2 are the current semi-major and minor axes of a void which has grown in isolation to the current strain ε. In introducing a void growth law into equation 3.7 we will assume that growth is unperturbed by the presence of surrounding voids which are not within the critical coalescence spacing. We will thus use solutions for the growth of isolated voids in an infinite medium. However, once the coalescence conditional is attained, the linkage process is assumed to occur with negligible additional strain. We will employ here the results of Rice and Tracey (1969), as modified by LeRoy et. al. (1981) for a non-hardening material. Their analysis gives the following growth

equations for an axisymmetric ellipsoidal void in the case of uniaxial tension with an additional mean stress σ_m:

$$\begin{aligned} \dot{r}_1 &= r_1[\gamma_a \dot{\varepsilon} + D\dot{\varepsilon}] \\ \dot{r}_2 &= r_2[-\tfrac{1}{2}\gamma_a \dot{\varepsilon} + D\dot{\varepsilon}] \end{aligned} \tag{3.8}$$

where $\gamma_a = \left(1 + \frac{r_2}{r_1}\right)$ and $D = 0.56 \sinh\left(\frac{3\sigma_m}{2\bar{\sigma}}\right)$

and $\bar{\sigma}$ is the effective stress.

Equations 3.8 lead to the result

$$\frac{dr_1}{r_1} + 2\frac{dr_2}{r_2} = d(\ln r_2^2 r_1) = 3D d\varepsilon$$

Integration of this result from the nucleation strain ε_{nuc} to the current strain ε gives

$$\frac{r_2^2 r_1}{r_{02}^2 r_{01}} = \exp\left(3 \int_{\varepsilon_{nuc}}^{\varepsilon} D d\varepsilon\right) \tag{3.9}$$

Substitution of equation 3.9 into 3.7 finally yields

$$f_A = 1 - \exp\left[- \left(K_1 f_V \exp\left(3 \int_{\varepsilon_{nuc}}^{\varepsilon} D d\varepsilon\right) + K_2 \left(\exp\left[K_3 f_V \exp\left(3 \int_{\varepsilon_{nuc}}^{\varepsilon} D d\varepsilon\right)\right] - 1\right)\right)\right] \tag{3.10}$$

In uniaxial tension, if no neck develops in the sample, $\sigma_m = \frac{1}{3}\bar{\sigma}$, so that $\exp\left(3\int_{\varepsilon_{nuc}}^{\varepsilon} D d\varepsilon\right) = \exp\left[0.875\ (\varepsilon - \varepsilon_{nuc})\right]$. Beyond the point at which necking initiates, we will use Bridgman's (1952) solution for the state of stress in the neck of an axisymmetric tensile sample to evaluate D. The result gives

$$\frac{3}{2}\left(\frac{\sigma_m}{\bar{\sigma}}\right) = \tfrac{1}{2}\left[1 + 3\ln\left(1 + \frac{a}{2R}\right)\right] \qquad (3.11)$$

where a is the radius of the minimum cross-section of the sample, and R is the radius of the neck profile. Bridgman also noted that the development of the neck is described adequately by the empirical relationship

$$\frac{a}{R} = k(\varepsilon - \varepsilon_{neck}) \qquad (3.12)$$

where ε_{neck} is the strain at which the neck initiates, and k is an experimentally determined constant for a given material. Thus, if the void nucleation strain is less than that at which the neck initiates, use of equations 3.11 and 3.12 give

$$\int_{\varepsilon_{nuc}}^{\varepsilon} D d\varepsilon = \int_{\varepsilon_{nuc}}^{\varepsilon_{neck}} D d\varepsilon + \int_{\varepsilon_{neck}}^{\varepsilon} D d\varepsilon$$

$$= 0.2918\ (\varepsilon_{neck} - \varepsilon_{nuc}) + \frac{0.3693}{k}\left[\xi^{5/2} - 1\right] + \frac{0.6793}{k}\left[\xi^{-1/2} - 1\right] \qquad (3.13)$$

where $\xi = 1 + \frac{1}{2}k\,(\varepsilon - \varepsilon_{neck})$

This result allows the evaluation of f_A in equation 3.10.

In selecting a value for β, one should note that the value of this parameter is dependent upon the value of α chosen. Two reasonable lower and upper bounds for β are suggested as follows. A lower bound is obtained by equating the area of the void (in the section plane) which has coalesced with that of the shaded region shown in Figure 3.5. This would give $\beta = (4\alpha/\pi)^{\frac{1}{2}}$. An upper bound is obtained by equating the void separation with the dimension of the coalesced void, which results in $\beta = \alpha$.

(ii) Critical Separation Linearly Dependent Upon r_1

In this section we will develop an expression for f_A as in the previous section, where here a void added to the section plane coalesces if its centre lies within a distance $2\gamma r_1$ from the centre of a void already sectioned by the plane. However, the procedure of replacing a void which coalesces by one with the same dimension in the tensile direction would not provide an increase in the excluded area in the section plane. If we consider Figure 3.1c, we see that the semi-axis of a void formed through coalescence may range from a minimum of r_1 to a maximum of $2r_1(1 - \delta)$. We will not replace a void which coalesces with one having a larger dimension in the tensile direction, but rather, the

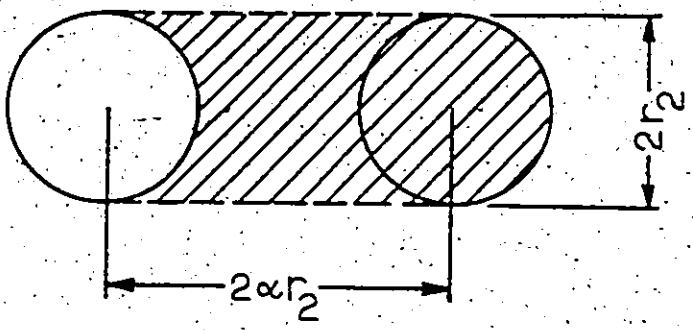

Fig. 3.5: View onto the section plane. The lateral (r_2) dimension of the coalesced void, in the section plane, is given by a circle with area equal to the shaded region. This gives the lower bound $\beta = (4\alpha/\pi)^2$.

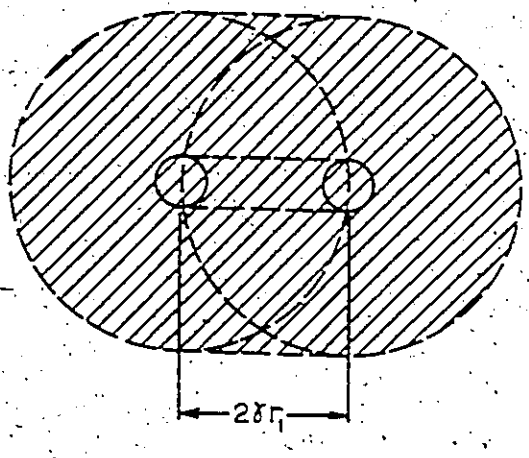

Fig. 3.6: View onto the section plane. The shaded region defines the excluded region about an added void which has coalesced, employing the r_1 criterion.

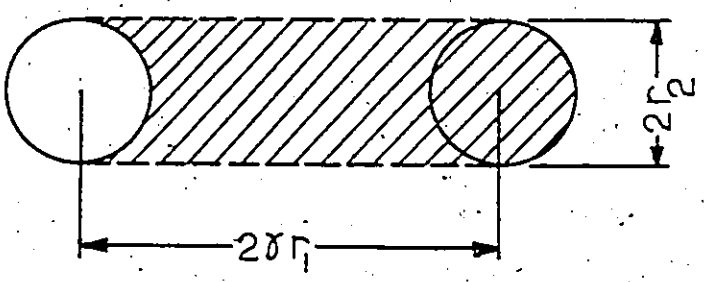

Fig. 3.7: View onto the section plane. The shaded region defines the area in the section plane occupied by the coalesced void, employing the r_1 criterion, to give a lower bound $\beta = \frac{4\gamma}{\pi}\frac{r_1}{r_2}$.

increase in size of the excluded region will be interpreted as the result of an increase in the periphery of the coalesced void. If we consider Figure 3.6, a view onto the section plane, coalescence produces a void which is elongated in the plane. We take the excluded region of the coalesced void to be the entire shaded region in Figure 3.6. This gives the ratio of the excluded region about a void which has coalesced to that which is isolated as $\beta' = 1 + \frac{2}{\pi}$.

Then the addition of dN_A voids per unit area to the section plane would result in an increase in P given by

$$\begin{aligned} dP &= \pi(2\gamma r_1)^2 dN_A + P \cdot \beta' \pi(2\gamma r_1)^2 dN_A - P\pi(2\gamma r_1)^2 dN_A \\ &= 4\pi\gamma^2 r_1^2 [1 + P(\beta' - 1)] dN_A \end{aligned} \tag{3.14}$$

Integration between $N_A = 0$ and $N_A = N_A$ gives the following expression for P:

$$P = \frac{1}{(\beta' - 1)} \left[\exp\left(4\pi\gamma^2 (\beta' - 1) r_1^2 N_A\right) - 1 \right] \tag{3.15}$$

The increase in area fraction of voids due to the addition of dN_A voids is then

$$\begin{aligned} df_A &= [\pi r_2^2 dN_A + P\beta\pi r_2^2 dN_A - P\pi r_2^2 dN_A](1 - f_A) \\ &= \pi r_2^2 [1 + (\beta - 1)P] dN_A \cdot (1 - f_A) \end{aligned} \tag{3.16}$$

We then substitute equations 3.6 and 3.15 into 3.16 and integrate between $N_A = 0$ to $N_A = N_A$, to obtain

$$f_A = 1 - \exp\left[-\left(G_1 f_V \frac{r_2^2 r_1}{r_{02}^2 r_{01}} + G_2 \left(\frac{r_2}{r_1}\right)^2 \left[\exp\left(G_3 f_V \frac{r_1^3}{r_{02}^2 r_{01}} \right) - 1 \right] \right) \right] \quad (3.17)$$

where

$$G_1 = \frac{3}{2}(1 - \delta)\left[1 - \frac{(\beta - 1)}{(\beta' - 1)} \right]$$

$$G_2 = \frac{(\beta - 1)}{4\gamma^2 (\beta' - 1)^2}$$

$$G_3 = 6\gamma^2 (\beta' - 1)(1 - \delta)$$

To obtain reasonable lower and upper limits on β, we consider Figure 3.7, and, as in the previous section, obtain a lower estimate of β (using the shaded area of the coalesced void in the section plane) as $\frac{4\gamma}{\pi} \frac{r_1}{r_2}$. An upper estimate of β, obtained by equating the void separation $2\gamma r_1$ to the diameter of the coalesced void in the section plane, gives $\beta = \left(\gamma \frac{r_1}{r_2}\right)^2$.

The void growth equations (3.8) used here cannot be integrated in a coupled manner to give explicit expressions for $\frac{r_2}{r_1}$ and $\frac{r_1^3}{r_{02}^2 r_{01}}$ as they can (equation 3.9) for the term $\frac{r_2^2 r_1}{r_{02}^2 r_{01}}$. This is because the first two expressions above are dependent upon the shape of the void, while the latter is simply the ratio of the current volume of an isolated void to its volume at nucleation. Equations 3.8 give $\frac{dV}{d\varepsilon} = 3DV$ where V is the volume of a void, so that the rate of change of volume of a void is dependent only upon its current volume V and the parameter D, and not

upon its shape. The terms $\frac{r_2}{r_1}$ and $\frac{r_1^3}{r_{02}^2 r_{01}}$ must be evaluated by integrating equations 3.8a and b simultaneously, in order to evaluate f_A.

In uniaxial tension, the ratio $\frac{r_1}{r_2}$ can become considerably greater than unity. The ratio $\frac{r_1^3}{r_{02}^2 r_{01}}$ in equation 3.17 appears in the argument of an exponential function, so that the increase in damage level predicted through the r_1 criterion for coalescence is expected to be steeper than that predicted using the r_2 criterion.

3.3 Results and Discussion of Model Predictions

The result in equation 3.10, based on the r_2 criterion, may be used to predict the influence of initial volume fraction of voids on the fracture strain, for low fractions. If the fracture strain ε_f occurs at a critical void area fraction, say f_A^c, then equation 3.10 may be rearranged, assuming arguments of the exponentials to be small, to give

$$\frac{f_A^c}{(K_1 + K_2 K_3) f_V} = \frac{K}{f_V} = \exp\left(3 \int_{\varepsilon_{nuc}}^{\varepsilon_f} D d\varepsilon\right)$$

or

$$\ln \frac{K}{f_V} = 3 \int_{\varepsilon_{nuc}}^{\varepsilon_f} D d\varepsilon \qquad (3.18)$$

If the sample does not neck, the right hand side of equation 3.18 equals $0.875\ (\varepsilon_f - \varepsilon_{nuc})$, so that

$$\varepsilon_f = \varepsilon_{nuc} + \ell n \left(\frac{K}{f_V}\right)^{1.14} \qquad (3.19)$$

The dependence of fracture strain upon volume fraction predicted by equation 3.19 is stronger than that predicted by Brown and Embury (1973) (see also Brown, 1976) based on a simple critical void size-to-average spacing, or by Thomason (1968), which is given by the plastic limit-load of the ligament between two voids in a periodic array. Both of these analyses predict the fracture strain to vary with $\ell n \left(\frac{1}{f_V}\right)^{\frac{1}{2}}$. Experimental observations indicate a much stronger influence of volume fraction upon strain to failure than this (Edelson and Baldwin, 1962), so that the influence of clustering and resulting coalescence may be important in determining the fracture condition.

It is an interesting prediction of equation 3.18 that, although the fracture strain is reduced with an increase in hydrostatic tension, the dependence of ε_f upon f_V becomes weaker as σ_m increases. However, one should view these predictions as a conservative estimate. The approximation of the exponential terms in equation 3.10 by the first two terms in the series expansion may not always be adequate. If this is so then the fracture strain will be more sensitive to f_V than indicated by equation 3.19.

Using ductile hole growth equations developed for long cylindrical voids with elliptical cross-section, McClintock (1968b) has given the expression for the fracture strain (assuming a nucleation strain of zero) as

$$\varepsilon_f = \frac{(1 - n) \ln \left(\frac{1}{f_V}\right)^{1/3}}{\sinh \left[(1 - n) \cdot \frac{\sqrt{3}}{2} \frac{(\sigma_a + \sigma_b)}{\bar{\sigma}} \right]}$$

where n is the strain-hardening exponent, $\bar{\sigma}$ the effective stress, and σ_a and σ_b are the stress components transverse to the axis of the cylindrical voids. This result assumes a constant stress ratio $\frac{\sigma_a + \sigma_b}{\bar{\sigma}}$ throughout the strain path, and a periodic void distribution.

We may evaluate the influence of volume fraction on fracture strain in an initially random distribution of voids using the above expression for ε_f, along with an extension of the approach suggested by McClintock (1968b). To accomplish this, the fracture condition must first be defined. Thus it is assumed that fracture will occur when, in a volume δV initially containing a critical minimum number N_c of voids, these voids have grown to a size where they come into contact, producing a critical-sized flaw. δV is equivalent to a critical flaw size. The volume δV contains an average of N voids initially, where N must be greater than or equal to one. The probability P that a given volume δV contains fewer than N_c voids can be obtained approximately by summing terms in the Poisson distribution with a mean value of N. Thus

$$P = 1 - \sum_{r=N_c}^{\infty} \left(\frac{e^{-N_N} r}{r!}\right)$$

If the total volume of the sample is V, then the number of volume elements in the sample is $\frac{V}{\delta V}$. The probability P* that all of these elements have less than N_c voids initially is then

$$P^* = \left(1 - \sum_{r=N_c}^{\infty} \frac{e^{-N_N r}}{r!}\right)^{\frac{V}{\delta V}}$$

For large $\frac{V}{\delta V}$ and reasonable values of $\frac{N_c}{N}$ the above expression may be approximated by

$$P^* = 1 - \frac{V}{\delta V} \sum_{r=N_c}^{\infty} \left(\frac{e^{-N_N r}}{r!}\right)$$

If the critical flaw defined by δV and N_c is independent of volume fraction, we may express the dependence of ε_f upon f_V as a ratio between the fracture strains associated with two different initial volume fractions. Absolute values for fracture strains, however, are not obtained, as we are only giving a ratio of the probabilities that a volume δV contains at least N_c voids, in two distributions of different average volume fractions. The average number of voids in δV with an average volume fraction f_{V_1}, is assumed to be given by $N_1 = \frac{f_{V_1}}{v}$, and with average volume fraction f_{V_2}, $N_2 = \frac{f_{V_2}}{v}$. The initial voids in both distributions are all assumed to have volume v.

Thus, in the distribution with volume fraction f_{V_1}, the probability that at least one element δV will have at least N_c voids is

$$1 - P_1^* = \frac{V}{\delta V} \sum_{r=N_c}^{\infty} \frac{e^{-\left(\frac{f_{V_1}}{v}\right)} \left(\frac{f_{V_1}}{v}\right)^r}{r!}$$

and with volume fraction f_{V_2} it is

$$1 - P_2^* = \frac{V}{\delta V} \sum_{r=N_c}^{\infty} \frac{e^{-\left(\frac{f_{V_2}}{v}\right)} \left(\frac{f_{V_2}}{v}\right)^r}{r!}$$

The ratio of the fracture strains $\varepsilon_f^{(1)}$ and $\varepsilon_f^{(2)}$ in the two materials having volume fractions f_{V_1} and f_{V_2}, respectively is then

$$\frac{\varepsilon_f^{(2)}}{\varepsilon_f^{(1)}} = \frac{(1 - P_2^*) \cdot \ln \left(\frac{1}{f_{V_2}}\right)^{1/3}}{(1 - P_1^*) \cdot \ln \left(\frac{1}{f_{V_1}}\right)^{1/3}}$$

$$= \frac{\left[\sum_{r=N_c}^{\infty} \frac{e^{-\left(\frac{f_{V_2}}{v}\right)} \left(\frac{f_{V_2}}{v}\right)^r}{r!}\right] \cdot \ln f_{V_2}}{\left[\sum_{r=N_c}^{\infty} \frac{e^{-\left(\frac{f_{V_1}}{v}\right)} \left(\frac{f_{V_1}}{v}\right)^r}{r!}\right] \cdot \ln f_{V_1}}$$

It should be emphasized here that we have assumed the same fracture condition in the two materials, independent of volume fraction, and the same sample volume in both cases.

If N is small and N_c/N relatively large, we may approximate each of the series in the above expression by its first term, to obtain

$$\frac{\varepsilon_f^{(2)}}{\varepsilon_f^{(1)}} = K^{(f_{V_2} - f_{V_1})} \left(\frac{f_{V_2}}{f_{V1}}\right)^{N_c} \frac{\ell n f_{V_2}}{\ell n f_{V_1}},$$

where $K = \varepsilon^{-\frac{1}{v}}$. Note that in considering the hole growth to coalescence, we have assumed the distribution of the N_c (or greater) voids in the volume δV to be periodic.

With the above assumption of a critical flaw giving the fracture criterion, a strong dependence of fracture strain upon volume fraction is predicted in a random distribution of voids. The predictions of the two models presented here, in view of experimental observations, indicate the effects of clustering and early void coalescence may be important in determining the damage condition at which fracture occurs.

In the remainder of this section we will present and discuss the effects which the parameters in the coalescence model have on the acceleration of damage accumulation towards fracture. The value of δ was set equal to zero, so that two voids need only lie in the same section plane at their ends to be allowed to coalesce, if they are within the critical separation.

As this study is intended to focus on the effects of coalescence in accelerating damage, it is convenient to choose a nucleation strain of zero in all cases. The results obtained using the r_2 criterion were determined using the upper limit for β, i.e., $\beta = \alpha$. In light of our choice for β' in the approach employing the r_1 criterion, we will use the lower limit for β in these calculations, i.e. $\beta = \frac{4\gamma}{\pi}\frac{r_1}{r_2}$ in the r_1 criterion. An additional parameter investigated here which was not previously mentioned was the aspect ratio of the voids at nucleation, where they were assumed to be axisymmetric ellipsoids with an aspect ratio $\phi = \frac{r_{01}}{r_{02}}$.

We will first present results employing the r_2 criterion for coalescence. As the development of the model assumed a dilute distribution of voids, we limit the plotted results to a maximum area fraction of 0.10, above which the rate of increase of f_A is very rapid.

Figure 3.8 gives the void area fraction vs. true strain, with $f_V = 0.002$ and $\alpha = \beta = 2$. Two situations are presented here, which illustrate the effect of the stress state which develops in the neck of a tensile sample. The radial stresses promote a rapid increase in the rate of coalescence due to the effect on the growth of voids normal to the tensile axis. As f_A (equation 3.7) is dependent upon r_2^2 in the argument of exponential terms, this sensitivity of damage rate to hydrostatic tension is expected. The stress history in the centre of the neck was calculated using data from Teirlinck (1983) for the development of necking in a spheroidized steel, which gave $k = 0.865$ and

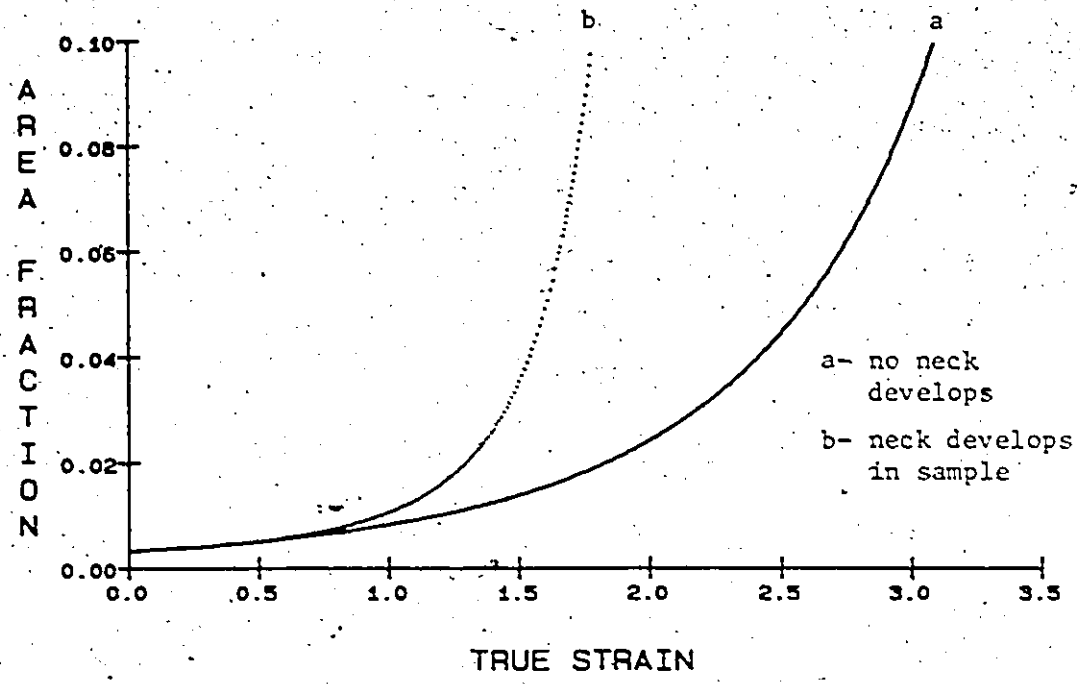

Fig. 3.8: Void area fraction vs. strain, employing the r_2 criterion. The influence of the stress state developed in the neck of a tensile sample (1045 C-steel) is illustrated. (f_v = 0.002, $\alpha = \beta = 2$)

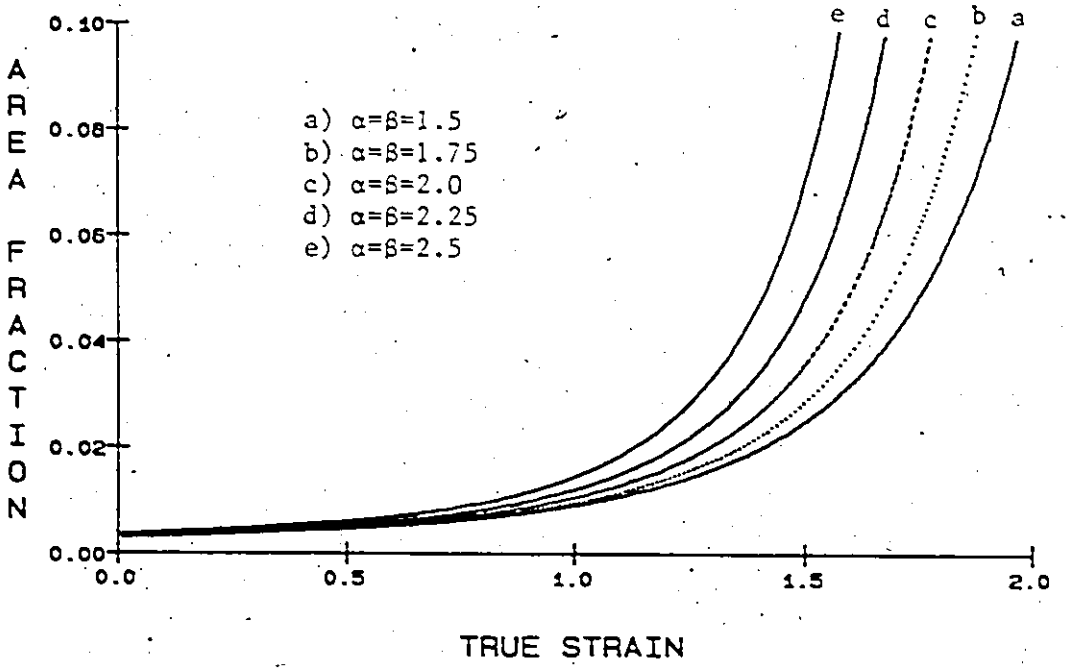

Fig. 3.9: Void area fraction vs. strain, employing the r_2 criterion. The sensitivity of damage accumulation rate to the coalescence condition is illustrated. (f_v = 0.002)

$\varepsilon_{neck} = 0.416$. Because of its importance in the development of damage, this stress history is included in all subsequent damage calculations presented here. It is important to point out here that we assume that the stress state near the centre of the neck is reasonably constant over a volume of material large enough so that the fracture criterion will be given by a critical damage level in this region. No size effect can be included in the present damage model.

Figure 3.9 illustrates the influence of the critical void separation for coalescence, with $f_V = 0.002$. The range of values for α chosen (with $\alpha = \beta$) cover a range of spacings between the void surfaces from 0.5 to 1.5 times the diameter of the void transverse to the tensile axis.

We note that a more pronounced neck develops at the higher strains attained with a low α value, which further promotes coalescence. Thus, it appears that over a reasonable range of α values the onset of rapid damage accumulation is quite sensitive to the coalescence spacing.

Figure 3.10 shows the effect of the initial void volume fraction, considering a range of f_V over an order of magnitude from 0.001 to 0.010, with $\alpha = \beta = 2$. The initial rate of damage accumulation is seen to increase with initial void fraction. However, again considering the hydrostatic tension in the neck at the higher strains attained with lower volume fractions, these results suggest a very strong influence of initial volume fraction on the coalescence process.

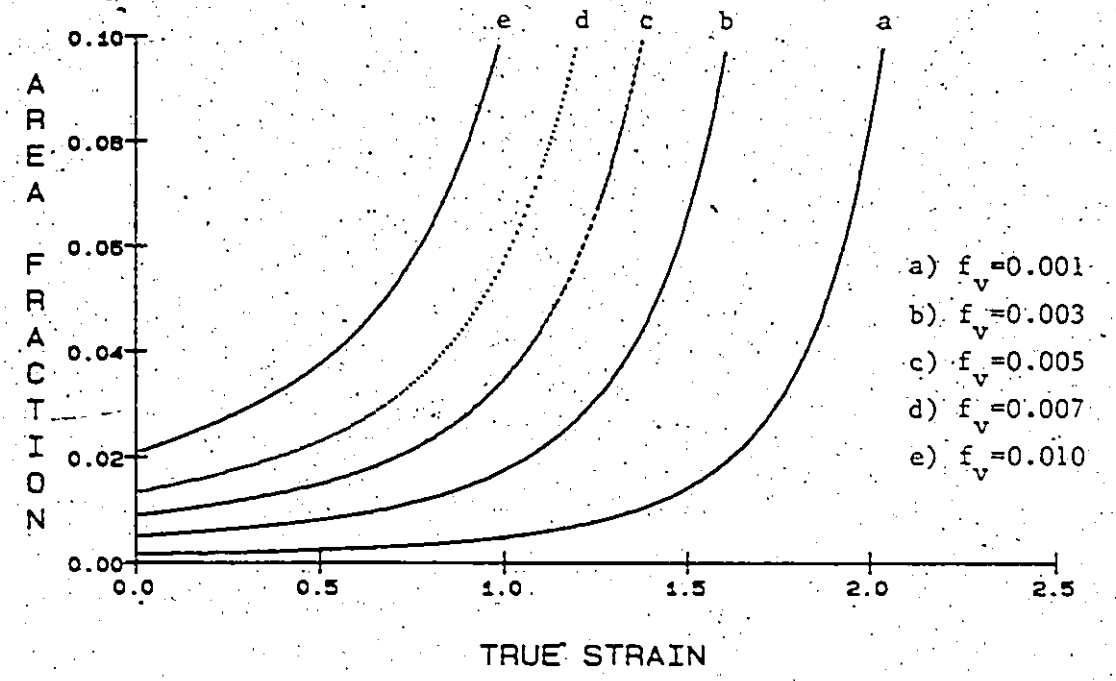

Fig. 3.10: Void area fraction vs. strain, employing the r_2 criterion. The influence of initial void fraction on subsequent damage accumulation is illustrated. ($\alpha = \beta = 2$)

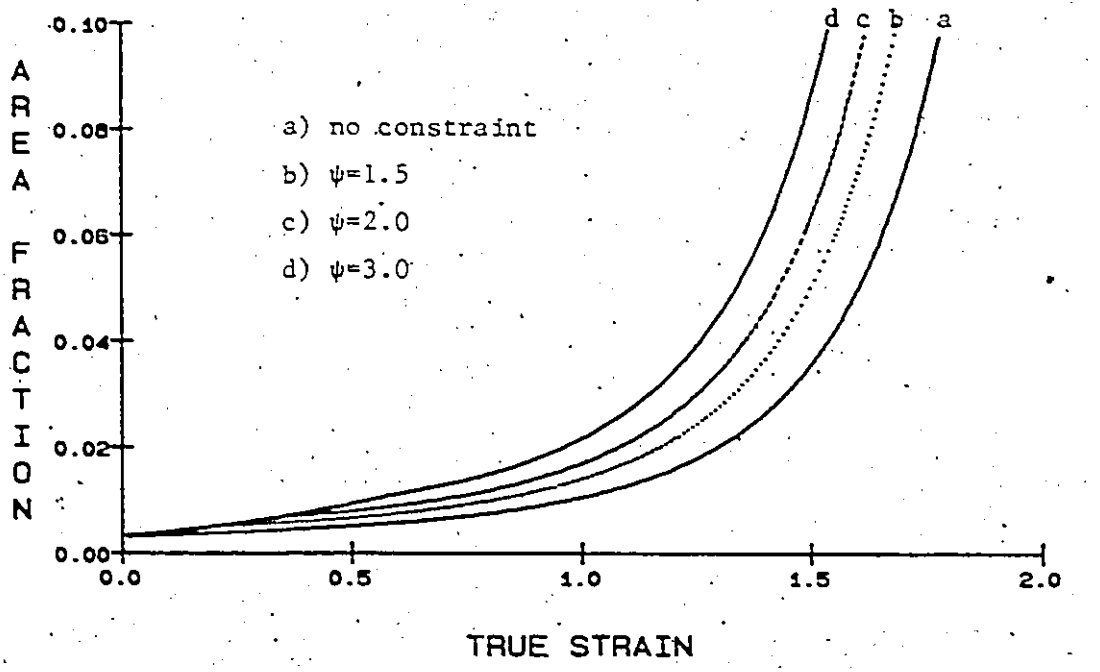

Fig. 3.11: Void area fraction vs. strain, employing the r_2 criterion. The influence of constraint to void contraction is illustrated. ψ is defined in the text. ($f_v = 0.002$, $\alpha = \beta = 2$)

As discussed previously, the initial void shape does not influence the rate of coalescence predicted using the r_2 criterion, a consequence of the low work-hardening rate assumed in the void growth equations. Thus all calculations presented for the r_2 criterion have used $\phi = 1$.

If voids nucleate around second phase particles which do not subsequently deform, the presence of hard particles within the voids could significantly influence void growth at low strains (Brown, 1976). The void growth equations used predict that an initially sperical void will contract in the direction transverse to the tensile axis in simple uniaxial tension. Dilation occurs only under the influence of the neck which develops. Any constraint which a particle offers to void contraction in the early stages of growth will subsequently alter the growth rate, due to the influence on void shape. Figure 3.11 illustrates the influence which various degrees of constraint to void contraction have on subsequent damage accumulation. Here we have, for simplicity, assumed that the constraint a hard particle offers to lateral void contraction (and thus the stresses at the particle/void contact) does not influence the elongation rate of the void along the tensile axis. Voids were not allowed to contract until they attained a certain aspect ratio $\Psi = \frac{r_1}{r_2}$. At this point, the influence of a spherical particle on the contraction of an elongated void was assumed to become negligible. The removal of constraint was affected in order to account for lateral contraction away from the particle/void surface contact. Although the influence of a hard particle in constraining void contraction must

continuously decrease as the void elongates, the results of Figure 3.11 are taken as a useful prediction. The effect of a finite interfacial strength between a particle and the matrix of the order of the flow stress, however, is expected to result in a much greater effect on the initial void growth rate and thus on the strain at which coalescence begins to contribute dominantly to the accumulation of damage.

Note that the restriction to void contraction altered the void growth law, so that equation 3.10 could not be used directly in the damage calculation. Thus, in Figures 3.11 and 3.13 the void growth was followed explicitly in the damage calculation.

The pioneering work of Bridgman (1952) in studying the influence of a superimposed pressure on failure has been extended is many subsequent investigations (see Teirlinck, 1983). Figure 3.12 predicts the influence which imposed pressures of up to 1100 MPa have on the coalescence process. The flow stress and necking behaviour used in the calculation were that of the spheroidized 1045 steel quoted previously, with $f_v = 0.002$ and $\alpha = \beta = 2$. The initial void contraction at high imposed pressures results in an initially decreasing damage level, and the retardation of rapid coalescence to very high strains. Here, the influence of a non-deformable particle in constraining void contraction can be marked, as illustrated in Figure 3.13. We have again assumed complete decoherence at the matrix/particle interface, and a value of $\Psi = 2$ to obtain these plots. The release of particle constraint to contraction is indicated by the sudden change in slope of the curves. The particle effect in a real material may not be as strong as that indicated here, however, even the presence of a deformable incompressible material in a void, such as a sulphide in a steel matrix, would maintain a level of damage which would not decrease.

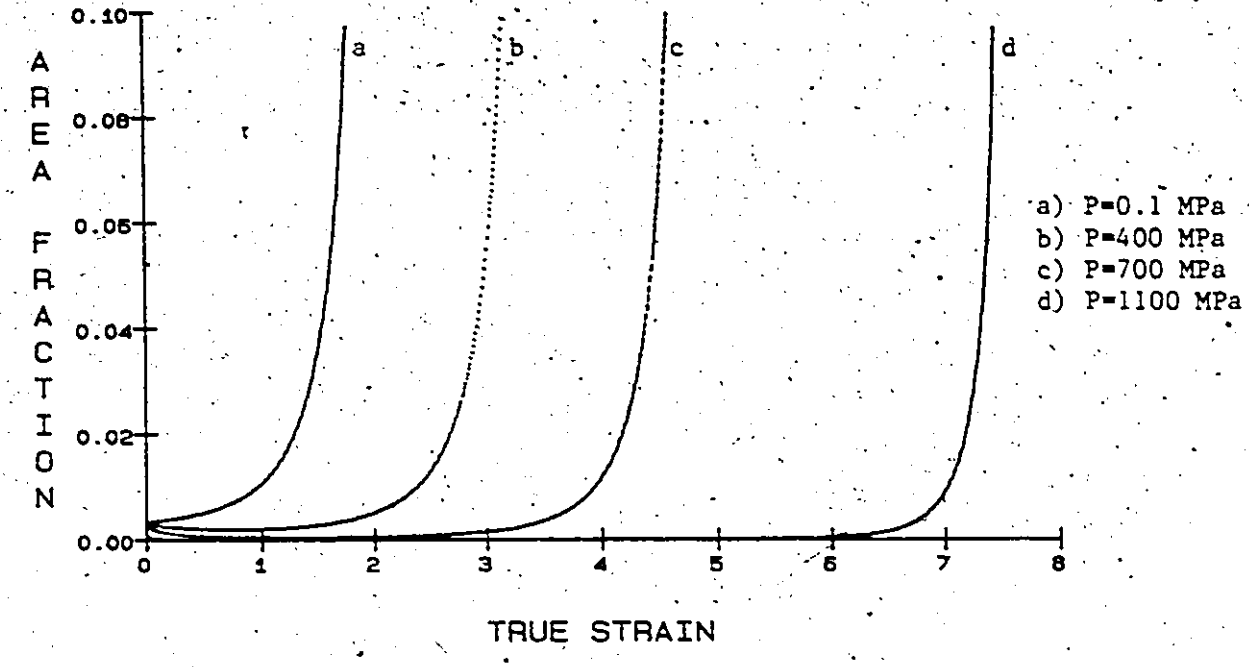

Fig. 3.12: Void area fraction vs. strain, employing the r_2 criterion. The influence of an imposed pressure P in retarding void growth and coalescence is illustrated. ($f_v = 0.002$, $\alpha = \beta = 2$)

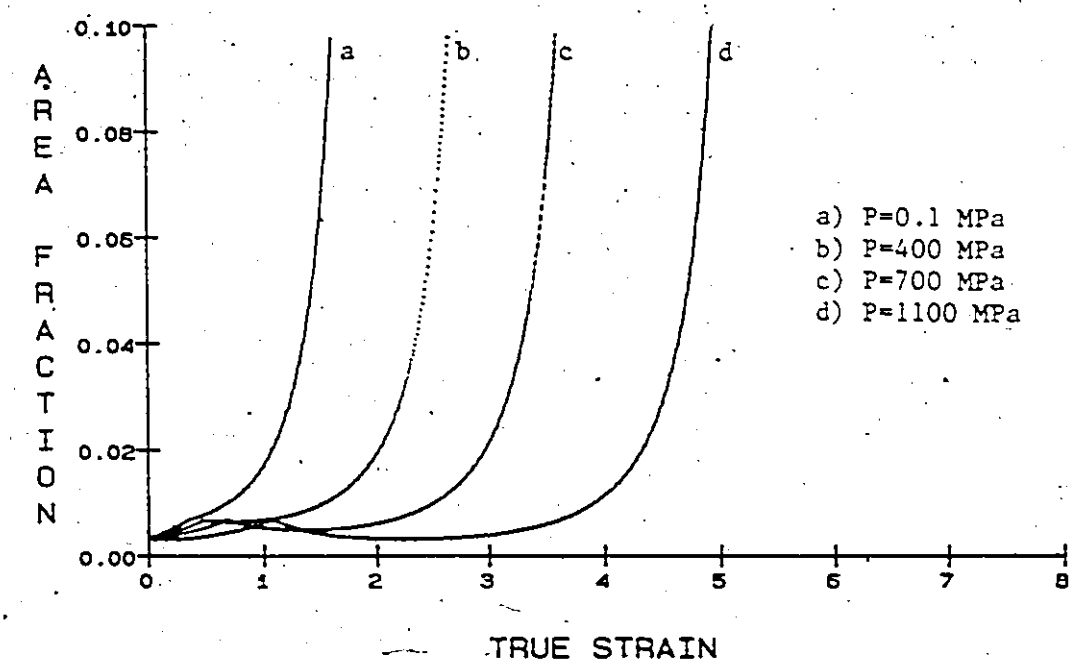

Fig. 3.13: Void area fraction vs. strain, employing the r_2 criterion. The combined influence of imposed pressure and constraint to void contraction (for $\phi = 2$) on damage accumulation is illustrated. ($f_v = 0.002$, $\alpha = \beta = 2$)

We consider next the influence which the parameters involved in the use of the r_1 criterion have on damage prediction.

In Figure 3.14, the sensitivity of the damage accumulation rate to the value of γ is illustrated, for an initial void volume fraction of 0.002. In choosing any value of γ less than unity (with initially spherical voids) there is a strain interval over which the only voids which coalesce with those already present in the chosen section plane are those which grow into other voids in a direction along the tensile axis. However, at higher strains where void aspect ratios may be of the order of 5 to 10, or greater, values of γ less than one are reasonable. As expected, these damage curves in general rise more steeply than those predicted using the r_2 criterion.

Figure 3.15 indicates the influence of initial volume fraction on the damage rates which develop, with $\gamma = 0.3$. In comparison with the results of Figure 3.10, it is seen that the initial rate of damage accumulation at low strains and the strain at which the damage level begins to rise rapidly is not as sensitive to initial volume fraction when the r_1 criterion for coalescence is employed. This statement should consider the actual values of α, β and γ chosen, but as a general result for reasonable values of these parameters the conclusion holds.

The void-shape dependent terms $\frac{r_2}{r_1}$ and $\frac{r_1^3}{r_{02}^2 r_{01}}$ in equation 3.17 result in the dependence of the damage rate on initial void aspect ratio, as illustrated in Figure 3.16. As expected, higher initial aspect ratios promote the onset of rapid damage accumulation. Thus, in

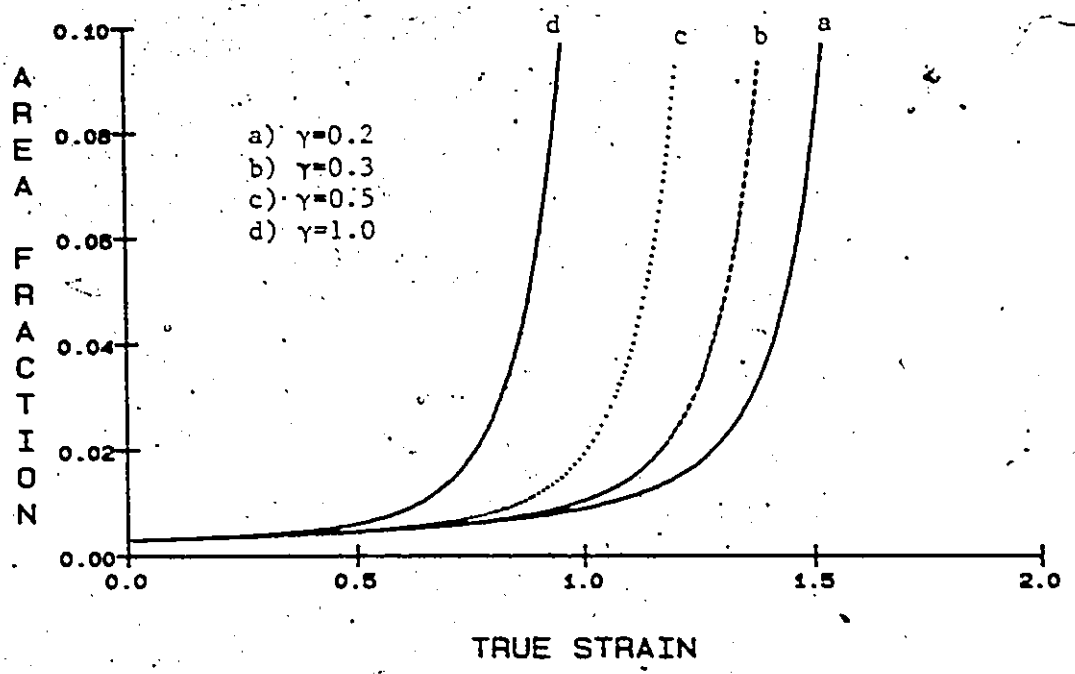

Fig. 3.14: Void area fraction vs. strain, employing the r_1 criterion. The sensitivity of damage accumulation rate to the coalescence condition is illustrated. (f_v = 0.002, ϕ = 1.0)

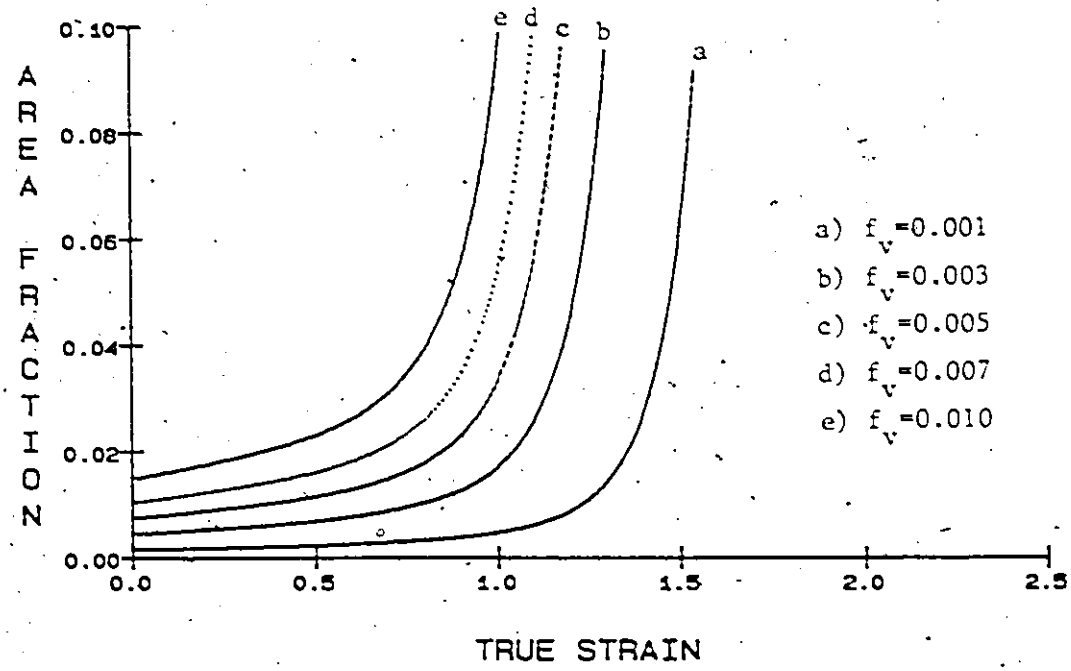

Fig. 3.15: Void area fraction vs. strain, employing the r_1 criterion. The influence of initial void fraction on subsequent damage accumulation is illustrated. (γ = 0.3, ϕ = 1.0)

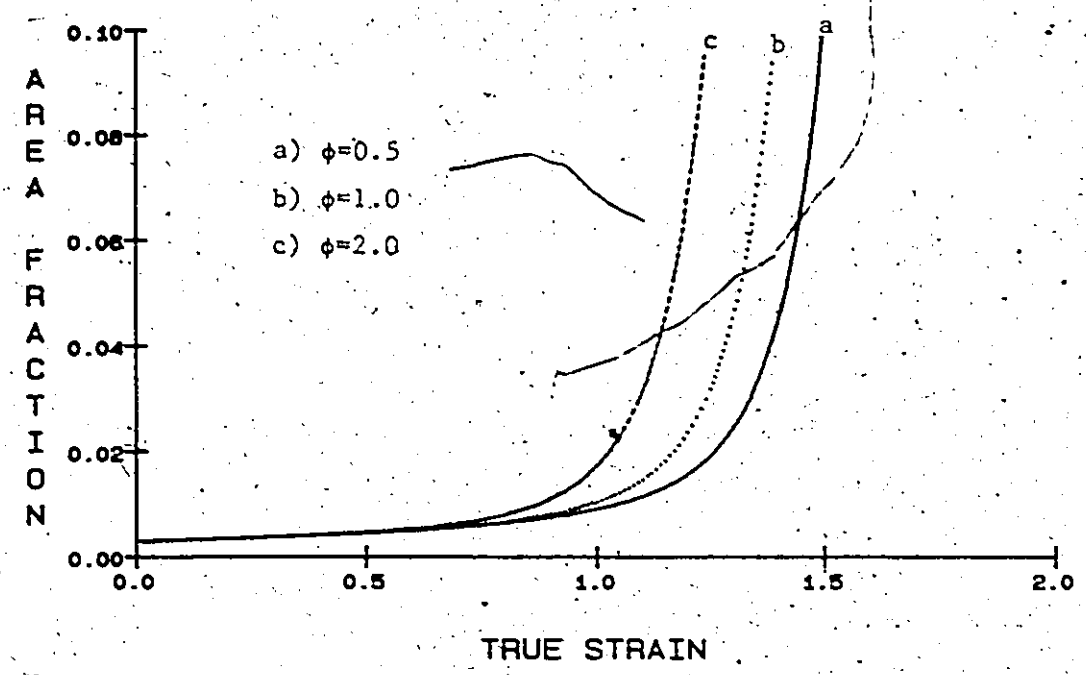

Fig. 3.16: Void area fraction vs. strain, employing the r_1 criterion. The influence of initial void aspect ratio ϕ on subsequent damage accumulation is illustrated. (f_v = 0.002, γ = 0.3)

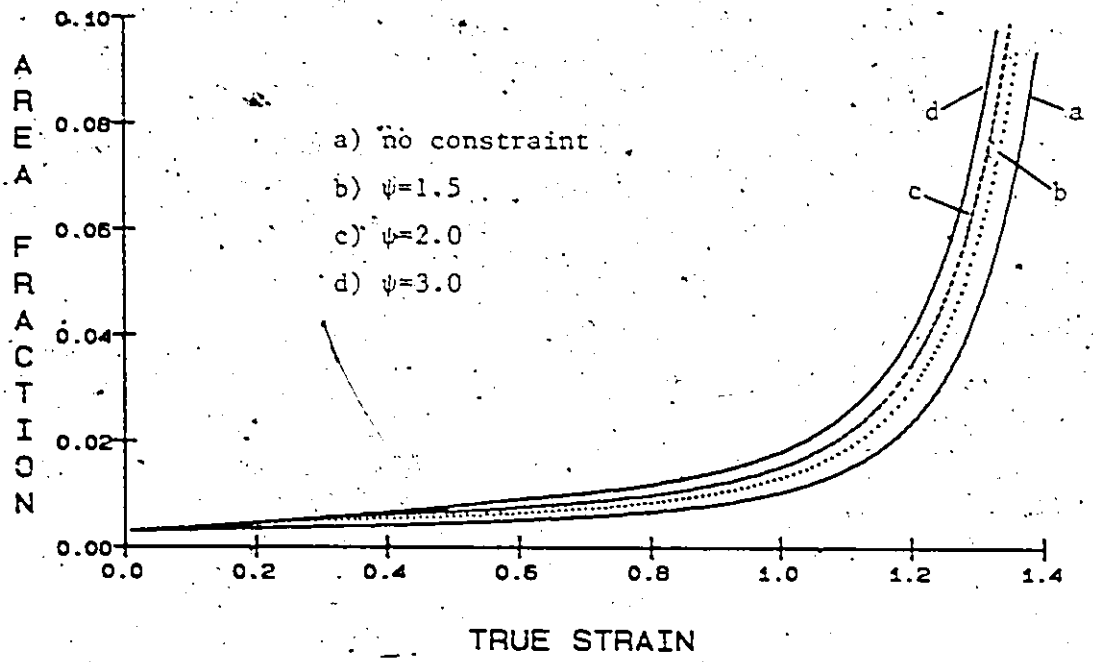

Fig. 3.17: Void area fraction vs. strain, employing the r_1 criterion. The influence of constraint to void contraction is illustrated. (f_v = 0.002, γ = 0.3)

a material with a distribution of elongated voids or inclusions, an anisotropy in fracture behaviour would be predicted, the fracture strain being a maximum when the tensile axis is oriented normal to the elongated voids. In real materials with a distribution of elongated inclusions, however the fracture strain is usually a minimum in the orientation normal to that of the elongated inclusions. This is because of the scale of the inclusions relative to microstructural features, so that the assumption of continuum void growth is replaced with crack-like flaw growth with a fracture process zone ahead of the flaw.

The effect of any particle constraint to lateral void contraction is not predicted, through the r_1 criterion, to significantly influence the onset of rapid damage accumulation. This is seen in Figure 3.17. As the constraint the particle offers does not markedly alter the void growth rate along the tensile axis, only a slight increase in elongation rate and coalescence rate results. However, the constraint a hard particle offers to void contraction in tests performed under an imposed hydrostatic pressure can significantly affect the onset of rapid damage accumulation, as seen by comparing Figures 3.18 and 3.19.

The foregoing results have served to illustrate the sensitivity of the component of damage accumulation due to void coalescence, with respect to the geometrical condition giving the coalescence criterion, the initial void volume fraction at the nucleation strain, and factors which affect the void growth rate. However, the procedure of removing a void which has coalesced, and replacing it with another larger void is

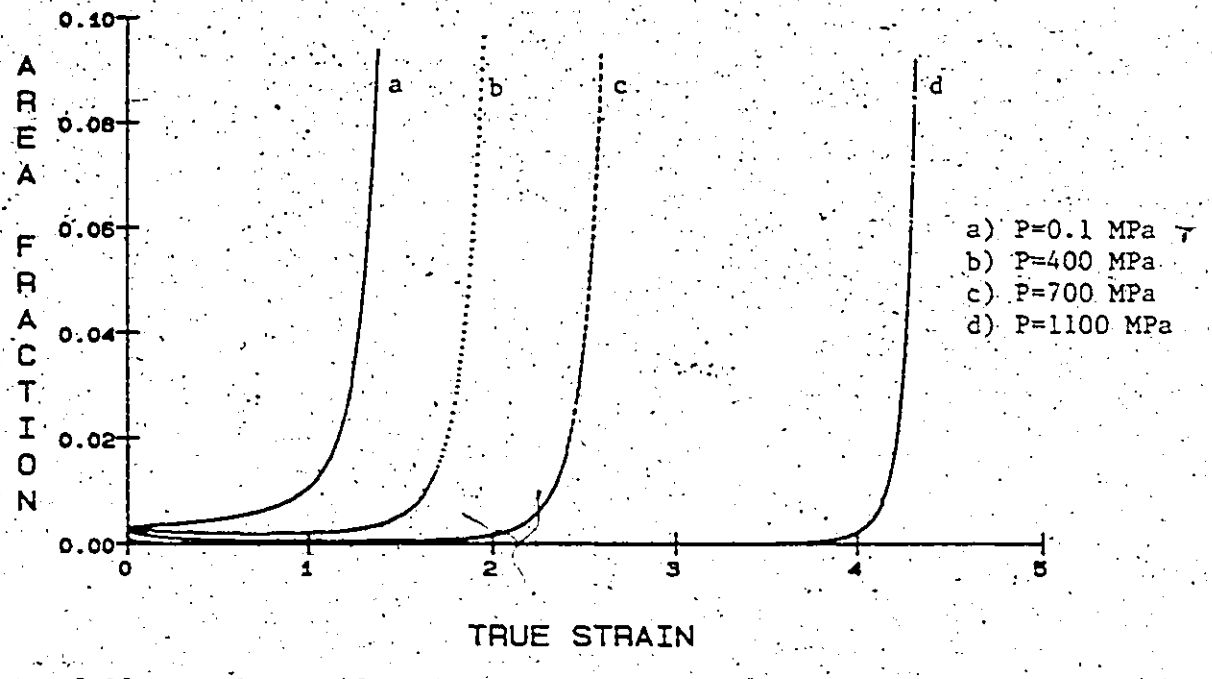

Fig. 3.18: Void area fraction vs. strain, employing the r_1 criterion. The influence of an imposed pressure P in retarding void growth and coalescence is illustrated. (f_v = 0.002, γ = 0.3)

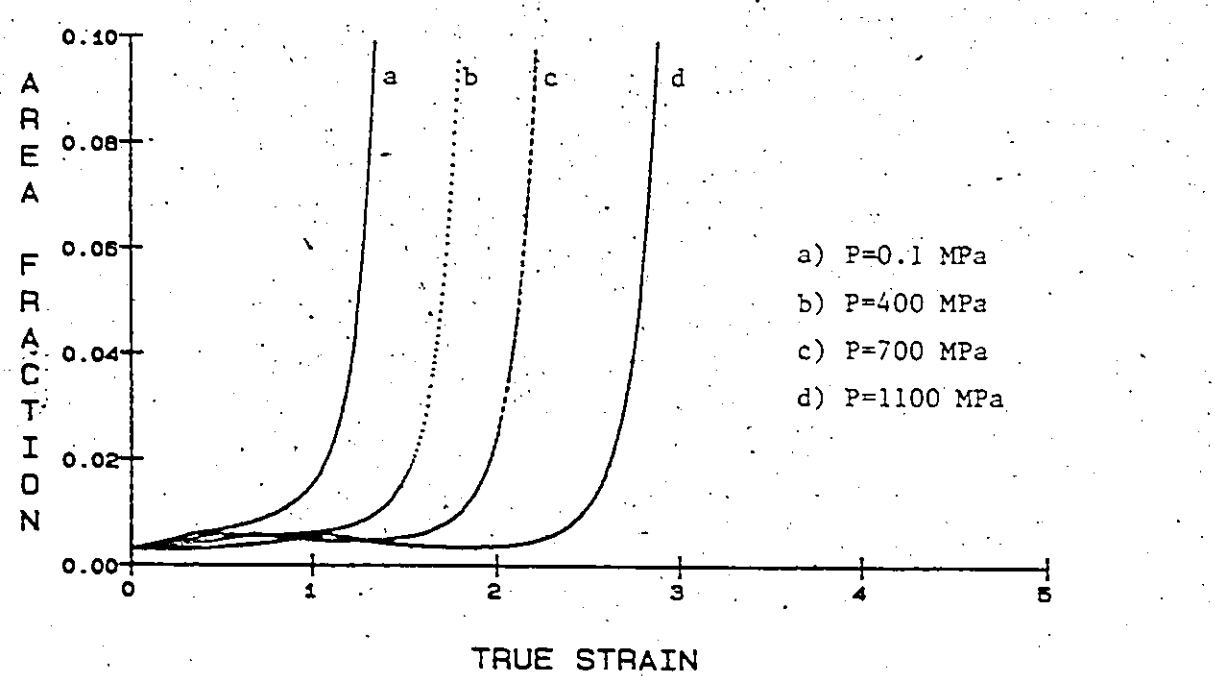

Fig. 3.19: Void area fraction vs. strain, employing the r_1 criterion. The combined influence of imposed pressure and constraint to void contraction (for ϕ = 2) on damage accumulation is illustrated. (f_v = 0.002, γ = 0.3)

an artificial scheme. This was done to overcome the problem of treating a distribution of void sizes with a single global damage parameter f_A, and to maintain the number of voids constant. However, if the fracture criterion is governed by a critical void or flaw size resulting from coalescence rather than an average damage level, predictions of fracture lie outside the scope of the model presented here.

The following section presents a simulation of the accumulation of damage due to void growth and coalescence in a random distribution of voids. The criterion for void coalescence is based upon the r_2 criterion previously given. The distribution of void sizes is followed and updated with each strain increment, so that the development of extremes in the distribution of void sizes may be predicted, thus giving an expected maximum flaw size at fracture in a randomly voided material. This approach differs from the previous model which assumed a critical flaw size δV, and then calculated the probability that a region with the appropriate local volume fraction existed.

3.4 Simulation of the Development of the Distribution of Void Sizes

The result of void coalescence is to produce a distribution of void sizes. In this section we will outline the computer simulation procedure and present preliminary results for the development of the size distribution resulting from an initial random distribution of voids of uniform size. The stress path followed is that of the 1045 steel

given previously, in uniaxial tension with the effect of the neck accounted for. After each strain increment the probabilities of coalescence between each void size interval are calculated, and the void number densities for the coalescing and resulting coalesced voids updated accordingly.

It should be emphasized that the simulation presented here of coalescence effects in ductile fracture is not of the type of approach considered by Melander (1979). Melander has considered an explicitly defined (although randomly generated) distribution of voids, and has simulated the fracture process along a defined fracture path. Here, we predict the development of a void size distribution, based on the approach given previously for determining probabilities of coalescence.

3.4.1 Simulation Procedure

The simulation begins at zero strain with a given number of voids per unit volume of identical size, and a given volume fraction. The void number densities for each size interval are stored in a two-dimensional matrix, where the row number corresponds to an interval in the distribution of r_1 dimensions of the voids, and the column number corresponds to a given size interval in the distribution of r_2 values. The voids are always assumed to be axisymmetric. Thus, at zero strain, there is only one non-zero element in the void number density matrix, corresponding to the void size at nucleation.

The calculation of the number of voids of one size interval which coalesce with those of another size interval after a strain increment of $\Delta\varepsilon$ is accomplished as follows. We utilize the r_2 criterion to define the coalescence condition.

Let us assume a strain ε. At this point we consider voids from two size intervals, say the i^{th} and j^{th}, having void dimensions (r_1^i, r_2^i) and (r_1^j, r_2^j) respectively. These dimensions correspond to the centres of the appropriate size intervals. Note that the superscript only denotes a void with a given r_1 and r_2 dimension. At strain ε, the number volume densities of voids in the selected i^{th} and j^{th} intevals are N_v^i and N_v^j respectively. Now we impose an incremental strain $\Delta\varepsilon$, and void growth results in voids from the i^{th} size interval moving into the k^{th} size interval, and voids from the j^{th} interval into the m^{th}. The void growth equations 3.8 are used here. To calculate the probability that voids from these two size intervals coalesce, we first note that the interaction zone, or excluded region, in the section plane about voids from the k^{th} interval is a circle of radius αr_2^k, and about voids from the m^{th} interval is a circle of radius αr_2^m, centred about the respective voids. Thus, for voids from the k^{th} interval to coalesce with those from the m^{th}, the region about the centre of a void from either size interval in which the centre of a void from the other interval must lie is a circle of radius $\alpha(r_2^k + r_2^m)$. This is illustrated in Figure 3.20.

The probability that a void from the m^{th} interval will coalesce with a given void from the k^{th} interval <u>over the strain increment $\Delta\varepsilon$</u> is then

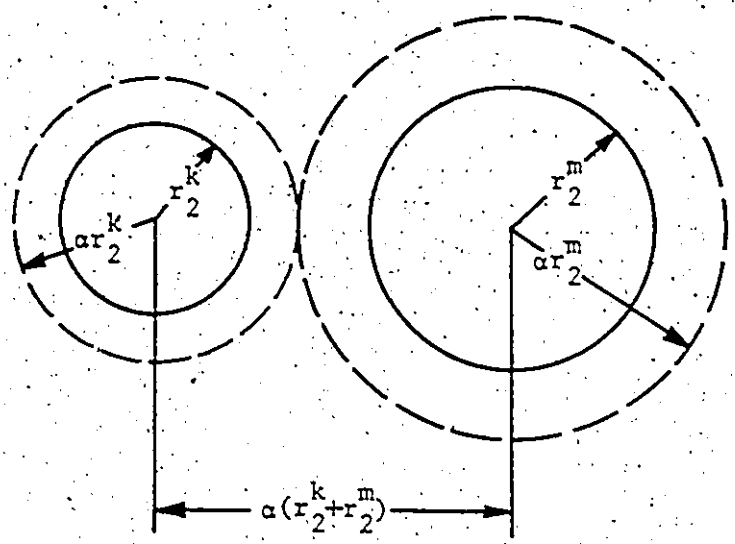

Fig. 3.20: View onto the section plane, in which the coalescence condition is defined between two voids having radii r_2^k and r_2^m in the section plane. The r_2 criterion is employed.

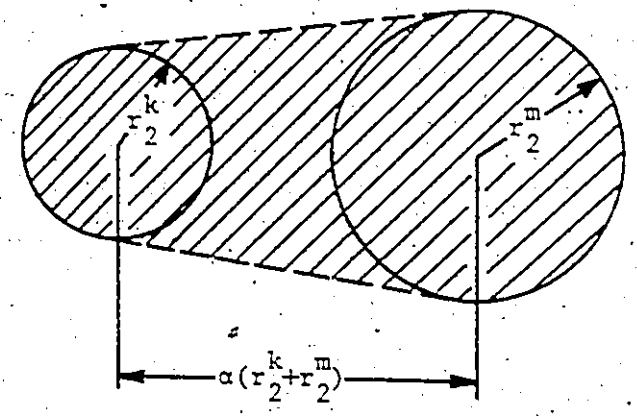

Fig. 3.21: View onto the section plane. The lateral dimension of the coalesced void, r_2^{coal}, is given by the radius of a circle with area equal to that of the shaded region. (Refer to Figure 3.20.)

$$P^{k,m} = \pi \left[\alpha(r_2^k + r_2^m)\right]^2 \cdot \Delta N_A^m \qquad (3.20)$$

where ΔN_A^m is the number of voids of size (r_1^m, r_2^m) which have been added to the section plane, the result of void growth taking voids of size (r_1^j, r_2^j) to size (r_1^m, r_2^m) over $\Delta\varepsilon$. We note here that only two-void clusters are considered, and that equation 3.20 is an overestimate of the number of two-void clusters (Roach, 1968). However, as higher-order clusters are not considered, the use of 3.20 should contribute to a conservative estimate of the damage which develops.

With the above assumption, the change in number density of voids in the k^{th} interval due to coalescence with voids in the m^{th} interval, in moving through the strain increment $\Delta\varepsilon$ is thus

$$\Delta N_V^{k,m} = -\frac{N_A^k \cdot P^{k,m}}{(r_1^k + r_1^m)} = -N_A^k \pi \left[\alpha(r_2^k + r_2^m)\right]^2 \cdot \frac{\Delta N_A^m}{(r_1^k + r_1^m)} \qquad (3.21)$$

where N_A^k is the number of voids per unit area in the k^{th} interval intersected by the section plane at the strain $(\varepsilon + \Delta\varepsilon)$. The denominator $(r_1^k + r_1^m)$ denotes the thickness of the region normal to the section plane over which voids from both the k^{th} and m^{th} size intervals will be intersected by the section plane. Note that the overlap factor δ is taken as zero in this development.

We now use $N_A^k = 2r_1^k N_V^k$

and $\Delta N_A^m = 2 \cdot \Delta(r_1^j N_V^m) = 2(r_1^j \Delta N_V^m + N_V^m \Delta r_1^j)$

where N_V^k and N_V^m are the number densities (per unit volume) of voids in the k^{th} and m^{th} size intervals respectively. Note here that we use the values r_1^j and Δr_1^j in calculating ΔN_A^m, where $r_1^m = r_1^j + \Delta r_1^j$. Thus we obtain, finally,

$$\Delta N_V^{k,m} = -4\pi\alpha^2 r_1^k N_V^k \frac{(r_2^k + r_2^m)^2}{(r_1^k + r_1^m)} \cdot (r_1^j \Delta N_V^m + N_V^m \Delta r_1^j) \qquad (3.22)$$

Similarly, the change in number density of voids in the m^{th} size interval due to coalescence with voids in the k^{th} size interval is

$$\Delta N_V^{m,k} = -4\pi\alpha^2 r_1^m N_V^m \frac{(r_2^k + r_2^m)^2}{(r_1^k + r_1^m)} \cdot (r_1^i \Delta N_V^k + N_V^k \Delta r_1^i) \qquad (3.23)$$

where $\Delta N_V^{k,m}$ must equal $\Delta N_V^{m,k}$.

After each strain increment, the number of voids (per unit volume) which coalesce between every combination of pairs of void sizes is calculated.

The number of voids which coalesce is subtracted from the current number density of each of the void sizes in the pair under consideration, and then this number of coalescing voids is added to the number density element in the matrix corresponding to the coalesced void size. This procedure properly accounts for the change in the number of voids due to coalescence.

The dimension of the coalesced void, assumed to be an axisymmetric ellipsoid, was determined as follows. The r_1 dimension after

coalescence was set to the larger of the two coalescing voids. The r_2 dimension was calculated to give a circle of approximately the same cross-sectional area (in the section plane) as the smallest envelope about the two voids, as shown in Figure 3.21. This is a reasonable estimate for the increase in void volume due to coalescence. The r_2 dimension of the coalesced void was thus determined as

$$r_2{}^{coal} = \left[\left(\frac{1}{2} + \frac{\alpha}{\pi}\right) \cdot \left(r_2^k + r_2^m\right) - r_2^k r_2^m \right]^{\frac{1}{2}} \qquad (3.24)$$

In equations 3.22 and 3.23, the terms ΔN_V^m and ΔN_V^k are the <u>total</u> changes in number density of voids in the m^{th} and k^{th} size intervals respectively, due to coalescence with <u>all</u> other voids in the size distribution in going through the strain increment $\Delta\varepsilon$. These values, however, are not known in the course of calculating the coalescence interactions between any two size intervals in the void size distribution. To calculate the interactions $\Delta N_V^{k,m}$ between all void size intervals using correct values of ΔN_V^m would require an iterative procedure to obtain a self-consistent solution to all of the $\Delta N_V^{k,m}$. This would require an unreasonable amount of computer time. The following scheme of continually updating the void number density matrix was used to include, at least in part, the effect of the $r_1^j \Delta N_V^m$ term in calculating $\Delta N_V^{k,m}$. This term was explicitly left out of the calculation of $\Delta N_V^{k,m}$ however, so that the equation used to obtain $\Delta N_V^{k,m}$ was

$$\Delta N_V^{k,m} = -4\pi\alpha^2 r_1^k N_V^k \frac{\left(r_2^k + r_2^m\right)^2}{\left(r_1^k + r_1^m\right)} \cdot N_V^m \Delta r_1^j \qquad (3.25)$$

With each $\Delta N_V^{k,m}$ interaction calculated, the value of $\Delta N_V^{k,m}$ was added (note $\Delta N_V^{k,m} < 0$) to each of N_V^k and N_V^m before the next pair of void sizes was considered, so that the number densities were updated during the course of the coalescence calculations for a given strain increment. This would in part compensate for the approximation made in equation 3.25, however the absolute value of $\Delta N_V^{k,m}$ would always be overestimated, resulting in an accelerated development of large voids in the distribution. Because of the magnitude of the strain increments required in the computation, however, it was usually the case that $\frac{\Delta r_l^j}{r_l^j} >> \frac{\Delta N_V^m}{N_V^m}$, i.e., $N_V^m \Delta r_l^j >> r_l^j \Delta N_V^m$, so that the above approximation should not be grossly in error.

The value $\Delta N_V^{k,m}$ was added to the element in the current number density matrix corresponding to the size of the coalesced void, so that these voids resulting from coalescence could be included for further interaction with other voids in the size distribution, within the same strain increment. This is a real effect. However, the manner in which coalescence interactions were calculated did not allow the interaction of the added $\Delta N_V^{k,m}$ term with voids in the distribution which had already been considered in the matrix update.

Thus, the computational scheme imposes a strain increment, calculates the void growth for each size interval in the void number density matrix, and shifts the density numbers into their new locations in the matrix. The density number matrix was then updated due to coalescence

between voids in the current size distribution, in order to obtain a new size distribution. A further strain increment was applied, and the process repeated. The evolution of the void size distribution could thus be followed in this simulation. A listing of the program used is given in Appendix A.

3.4.2 Results and Discussion

The limitation of available CPU time allowed only one simulation run, which was terminated at a strain of 0.65. The initial void volume fraction at zero strain was 0.002, with $\alpha = 2$. The size of the interval width separating elements in the number density matrix for both the r_1 and r_2 dimensions was set at a fraction 0.2 of the initial void dimensions r_{01} and r_{02} respectively (with $r_{01} = r_{02}$). The array size used was 180 x 240, so that voids with an r_1 dimension greater than 36 times the initial value r_{01}, or an r_2 dimension greater than 48 times r_{02} were excluded from the analysis. However, at the strain attained in this simulation, the number densities at the extremes of the matrix were of the order 10^{-3} to 10^{-5}, so that a cut-off at this point in the size distribution did not significantly affect its development with strain.

The initial void number density was selected as 2×10^6 mm^{-3}, a reasonable value observed by Teirlinck (1983) in a spheroidized 1045 steel. The flow stress and necking behaviour used were values obtained for this same steel.

Figure 3.22 presents the development of the average area fraction of voids in a plane normal to the tensile axis. This value was calculated incrementally, taking into account the possibility of voids in one size interval occluding those in another size interval as they grow into the section plane and coalesce. Comparison with the results of Figure 3.9 (with $\alpha = \beta = 2$), however, indicate a more rapid increase in void area fraction predicted by the simulation.

It is germane at this stage to point out that the r_2 dimension we give to the coalesced void is an upper limit. A void of dimensions (r_1^m, r_2^m) growing into a plane section on which a void of dimensions (r_1^k, r_2^k) is intersected, may be closer than the critical separation $\alpha(r_2^k + r_2^m)$ required for coalescence. This would result in the r_2 dimension of the coalesced void being less than the value we ascribe to it. The value to which the r_1 dimension of the coalesced void is set to, however, is a lower limit.

Figure 3.23 indicates the lowest strain at which the number per unit volume of a void of a given r_2 dimension (regardless of its r_1 dimension) will exceed unity. When its number per unit volume is greater than 1, then a void of the given dimension can exist in the volume of material specified. The r_2 dimension has been normalized by the r_2 dimension of a void which has grown in isolation from nucleation to the current strain. Thus, at a strain of 0.65, in a cubic mm of the given material, there exists a void with an r_2 dimension six times that of an isolated void.

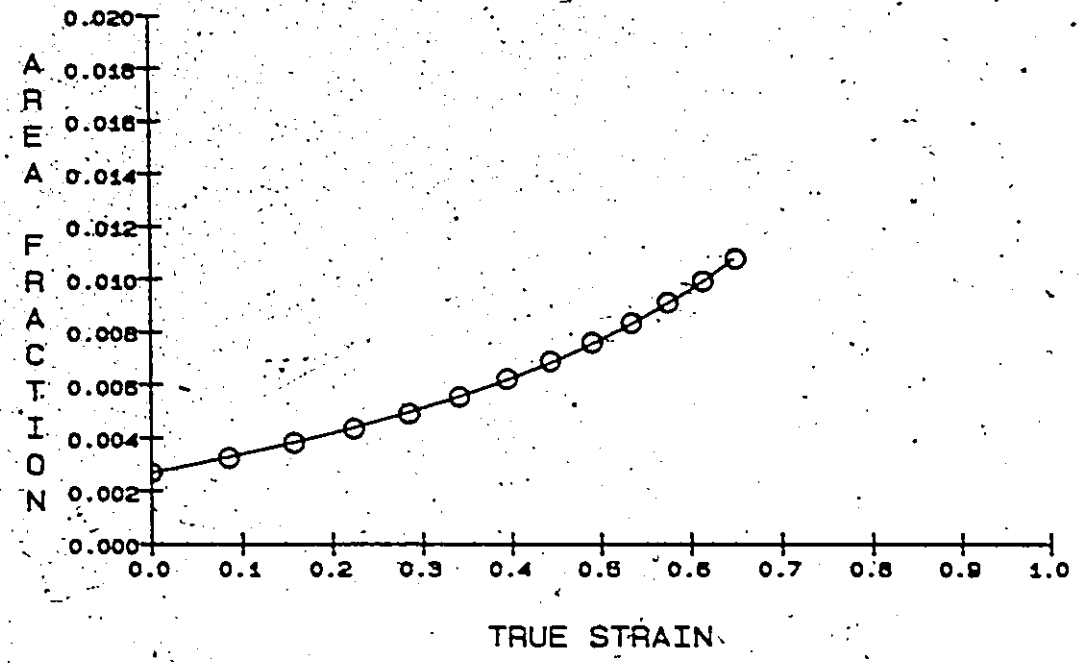

Fig. 3.22: Void area fraction vs. strain, obtained in the simulation. (f_v = 10.002, γ = 2)

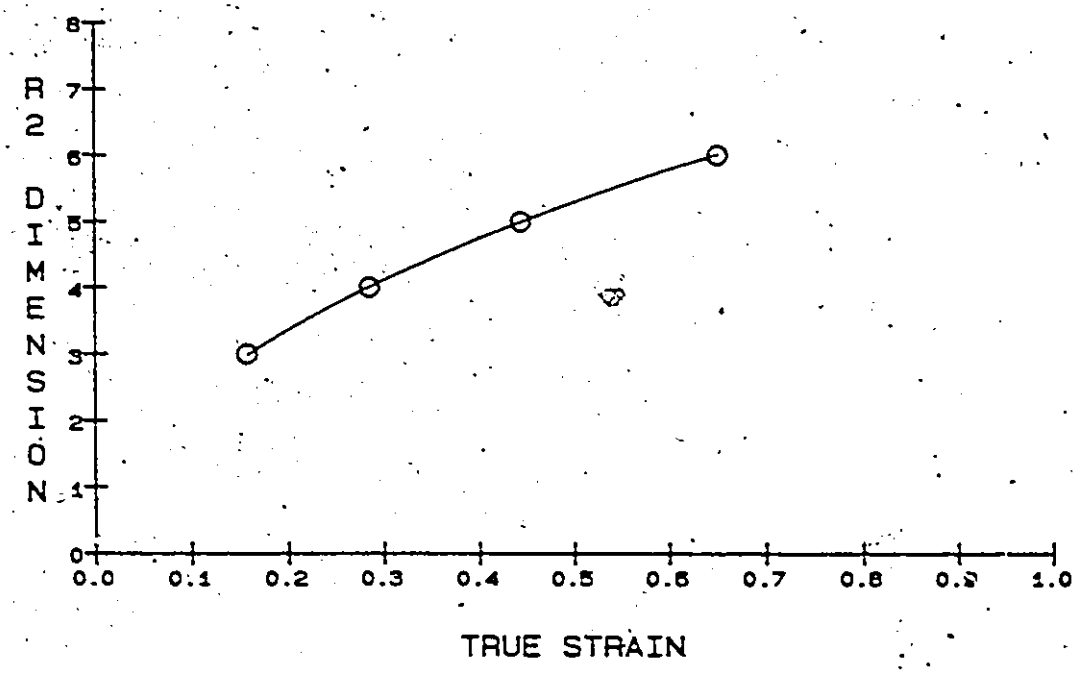

Fig. 3.23: Plot of the strain at which the number density of a void of given lateral (r_2) dimension is at least unity, so that the void can exist. The r_2 dimension has been normalized by that of a void which has grown in isolation to the given level of strain.

A plot of this type is thus a prediction of the largest defect which can exist at a given strain, in a random distribution of voids. One should note that the development of the tail end of the size distribution, at large void sizes, is dependent upon the volume of material sampled, for a random distribution. The present simulation could thus predict the effect of sample size on the extreme character of the void size distribution.

Figure 3.24 presents the size distribution of voids with respect to the r_2 dimension, at a strain of 0.65. It is actually the envelope of the values of the size distribution histogram, for an interval width of $0.2r_{02}$. The value for a particular interval was obtained by summing up the number densities of each element in the column of the void density matrix. This result, however, should not be interpreted as an actual distribution of the number densities of voids vs. the r_2 dimension. The distribution of number densities in the void size distribution is the result of a probability calculation, and is over both the r_1 and r_2 dimensions, so that both of these values have to be specified in the prediction of a number density.

3.5 Conclusions

A probabilistic model has been presented here which predicts the effect of void coalescence on the accumulation of damage in a dilute random distribution of voids. The criterion for linkage was given by the separation of voids in a plane normal to the tensile axis, which was

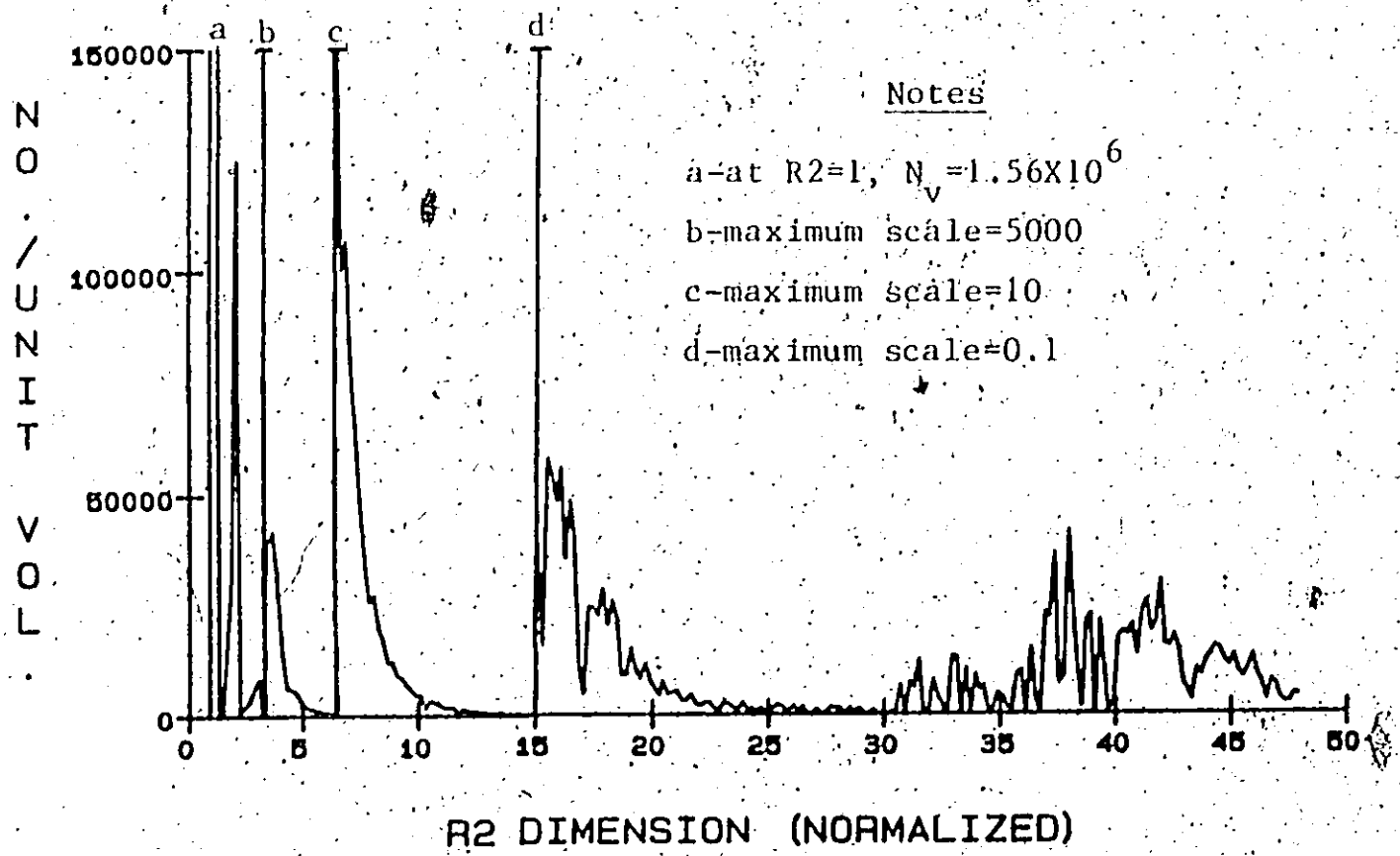

Fig. 3.24: This distribution represents the envelope of a histogram, obtained by summing up elements in the columns of the void size-number density matrix. Note that a given column corresponds to a certain r_2 dimension. The r_2 dimension here has been normalized by the initial void size. The result was evaluated at ε = 0.65, when the simulation was terminated. Note that this is strictly not a distribution of number densities over the r_2 dimension.

assumed to be a function of the void size only. This led to an expression for an average damage parameter, the area fraction of voids, which was a sigmoidal exponential curve.

Assuming fracture to occur at a critical area fraction, the r_2 criterion led to an expression giving the influence of initial void volume fraction and stress state on the fracture strain. The dependence of the fracture strain on volume fraction was stronger than that predicted by the Brown and Embury (1973) criterion.

Two different functions of the void dimensions defining the coalescence condition were considered. Then for each of these cases the dependence of the onset of rapid damage accumulation upon volume fraction, pressure, void spacing, and the influence of altering void growth was illustrated.

The results from the simulation provide a useful indication of the dimensions of the maximum flaw one may expect to develop in a (dilute) random distribution of voids. Many approximations were necessary to maintain reasonable computation time. However, the results obtained do suggest that the number of large flaws which develop at intermediate strains in a random distribution are few. If the initial distribution of voids exhibits a degree of clustering greater than that inherent in a random distribution, then a large flaw may develop at lower stains, and this could control final fracture. It is not possible, however, to introduce the effects of non-random clustering into the simulation outlined here.

CHAPTER 4

THE USE OF THE DIRICHLET TESSELLATION IN CHARACTERIZING POINT/PARTICLE DISPERSIONS

4.1 Introduction

An approach to the characterization of dispersions of points or particles which employs the Dirichlet tessellation has been presented in the literature review. However, to date there is no data in the literature which uses this method to assess the degree of clustering or periodicity. A knowledge of the level of clustering or periodicity and the limit to which significant differences between dispersions can be given represents the goals of this characterization procedure.

This chapter begins with an analysis of a series of point dispersions which have been computer-generated, ranging from strongly periodic to strongly clustered. Several properties of the tessellations for these dispersions are evaluated and compared as indicators of deviation from randomness. The approach taken here is not statistically rigorous, as no tests of statistical significance were done in the comparison of results.

Several examples of microstructures with different characteristic particle distributions are then analyzed. These include an analysis of the inclusion distribution in a structural HSLA steel, followed by several materials with higher volume fractions of second phase.

4.2 Method of Computation of Tessellation

Several algorithms for the analytic computation of Dirichlet tessellations have been discussed in the literature (Rhynsburger, 1973; Crain, 1978; Browstow et. al., 1978; Hinde and Miles, 1980; Shehata, 1985). A particularly efficient method has been developed by Green and Sibson (1978), in which the computing time required scales as $N^{3/2}$, where N is the total number of points in the array.

The approach taken in this study was to construct the Dirichlet cells individually. Although this algorithm was not highly efficient, programming and debugging were straightforward. The program ran on a DEC Micro PDP-11 under RT11-SJ.

Consider Figure 4.1, in which a cell is being constructed about point O. First the nearest-neighbour, point A is determined. The nearest-neighbour of point O must be associated with one of the sides, say S1, of its cell. Then, for each line joining point O to another point in the array, the equation of the perpendicular bisector is determined. From this set of bisectors, the smallest envelope about point O (which defines its associated cell) is developed, starting with the bisector B1 forming side S1. To find the two vertices associated with this side the intersection points of all the perpendicular bisectors with B1 are calculated. Since point A is the nearest-neighbour of point O, the two vertices at the ends of side S1 must lie on opposite sides of the point M. Note that if point A was not the nearest-neighbour, this would not necessarily be true. Thus, the first two vertices calculated

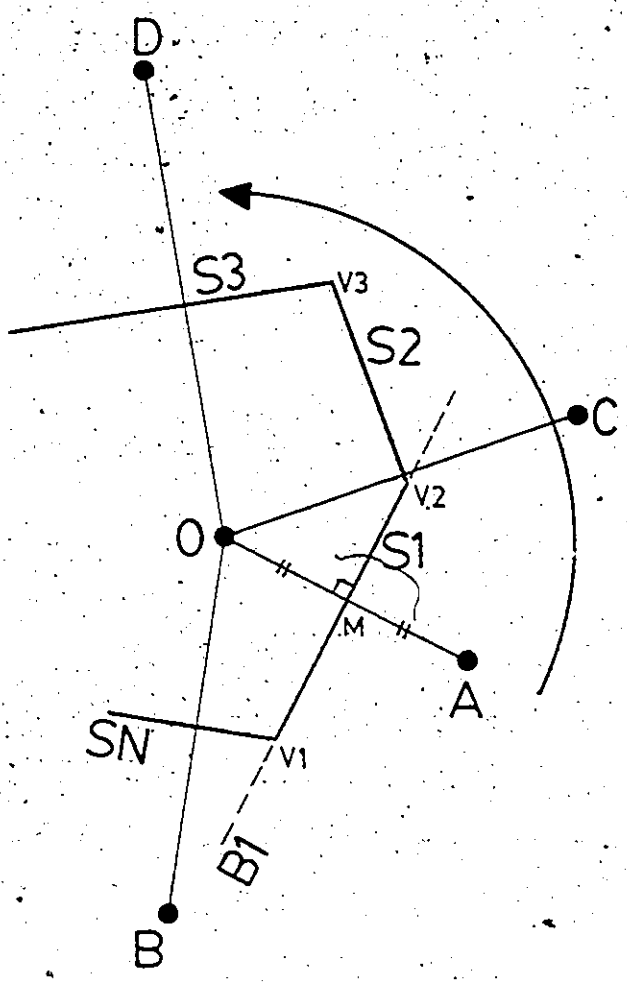

Fig. 4.1: Illustration of the method of construction of the Dirichlet cell about point 0. Point A is the nearest neighbour. The cell is constructed by "walking around" point 0 in the direction indicated by the arrow.

(V1 and V2) are those intersection points on B1 which are closest to point M, one on either side of this point. The points in the dispersion associated with these intersecting bisectors, points B and C, are near-neighbours of point 0.

The cell is then completed by "walking around" point 0, along S2 in the direction indicated by the arrow. The next vertex, on side S2, is the point of intersection of another bisector with S2, which is closest to the vertex V2. This intersection point must also lie on the same side of S1 as point 0. The point D associated with the next side S3 is then checked against near-neighbour B. If they are the same point, then the cell is complete, and it is a triangle. If they are not, the next vertex on side S3 is determined (checking that it lies on the same side of S2 as point 0). The cell is finally constructed when the near-neighbour point B is once again found.

The program also checks for the situation where two different bisector lines intersect a given side at exactly the same point. As the Dirichlet cell about 0 is the smallest envelope of these bisector lines, the bisector which passes closest to point 0 is chosen as the correct side. Thus the (square) cells for the degenerate case of a square lattice can also be constructed.

In a finite field of points, those at the periphery will have cell sides extending to infinity - their associated cells cannot be computed. Often periodic boundary conditions are applied in constructing these cells. In the present program, however, the boundaries of the field were used as sides to complete the cells along the field

edge. These were not true Dirichlet cells, and as such, were not included in any subsequent cell analyses. Points along the periphery were included in the clustering analyses, however. The portions of the periphery cells which were the results of the Dirichlet tessellation were then used to define near-neighbours of these points.

4.3 Generation of Test Dispersions

A series of planar point arrays were computer-generated with varying degrees of clustering or periodicity. The random and the clustered arrays contained 1032 points, and the more periodic arrays contained 1024 points. Schwartz and Exner (1983) (see also references therein) estimate that, for a random array, the actual average nearest-neighbour distance can be given to within 5% by analyzing a distribution of approximately 1000 points. The error is due to the effect of finite boundaries, which remove any point lying on or outside the field. The above array sizes were chosen with this in mind, and also due to the memory limitations of the computer. To minimize the boundary effect, the field was defined as a square. It is important to note that this sample size may not be adequate in eliminating boundary effects for dispersions which deviate from randomness towards clustering. This arises due to the manner in which the clustered dispersions were generated. However, this problem was not analyzed in the current work.

The random point arrays were generated using a pseudo-random number generating routine, generating consecutively the x- and y-coordinates for each point. The random array was then used as a basis for

generating the clustered dispersions by the following method. First, a critical distance $\alpha\lambda^{-\frac{1}{2}}$ was chosen, where λ is the average point density and α is between 0 and 1. The point distribution was then analyzed, and any point which did not have any other point within $\alpha\lambda^{-\frac{1}{2}}$ was removed. After all these "isolated" points were removed an equivalent number were added randomly, so that every point was within $\alpha\lambda^{-\frac{1}{2}}$ of at least one other point. These distributions were thus related to the clustering characteristics inherent in a random distribution (Wray et. al., 1983). For this study, distributions were generated and analyzed with α values of 0.7, 0.5 and 0.3.

The point distributions with periodic characteristics were generated as deviations from a periodic hexagonal array with point spacing d. To obtain a given distribution each point was displaced a distance of $\beta\gamma d$ in a random direction, where β was a pseudo-random number between 0 and 1. Since β is uniformly distributed on this interval, the average point displacement was $\frac{1}{2}\gamma d$. γ was a selected constant, and as it was increased the distribution tended more towards randomness. In this study dispersions were generated for γ values of 0.3, 0.5, 0.7, 0.9 and 2.0.

In order to gain an indication of the scatter, or the reproducibility of the results of the analyses, two separate series of the above dispersions were investigated. Several more series of such distributions would have to be analyzed before any statistical significance could be given to these results, and they could be used as a standard base to evaluate other distributions. Nonetheless, the results to date appear to indicate that such standards could be obtained.

4.4 Computer-Generated Point Dispersions

Results and Discussion

The computed tessellations for one of the series of dispersions analyzed are given in Figures 4.2a-i, where the value of α or γ used in the generation of each distribution is indicated.

As a comparison with later analyses, let us first consider the results obtained from a simple grid count method. Here the entire sample field was gridded with squares having area $\frac{1}{\lambda}$, where λ is the average areal point density. The results for the random distribution and the least two periodic and clustered distributions are presented in Figures 4.3a-d (note that each figure contains the analyses of the dispersions from both series). The grid count frequencies are presented as the deviation from the expected frequencies for a random distribution. The expected fraction of grid squares containing n points is given by $P_n = \frac{(\lambda A)^n \exp(-\lambda A)}{n!}$, where A is the area of the grid square. For a sample area equal to the average area per point; $\lambda A = 1$ and $P_n = \frac{1}{en!}$. The results in Figures 4.3a-d plot $(P_n - f_n)$ vs. n, where f_n is the observed fraction of grid squares containing n points. Differences between all the dispersions are detected by this method. In particular, the dispersion generated by displacing the hexagonal lattice with γ equal to 2 still shows a slight tendency to periodic behaviour in this analysis. This character is not evident in viewing the distribution.

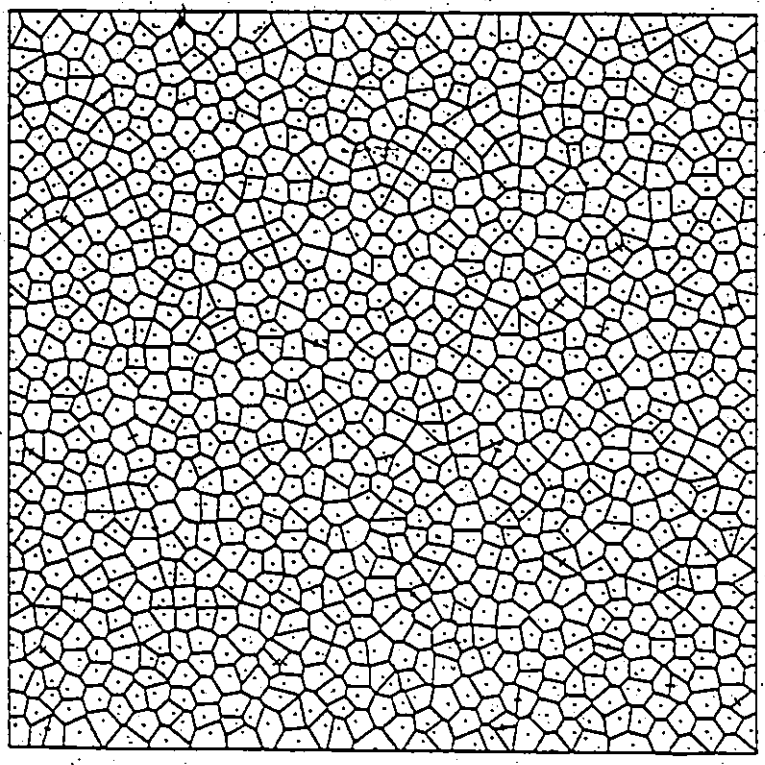

Fig. 4.2b: ^{1}P, $\gamma = 0.5$

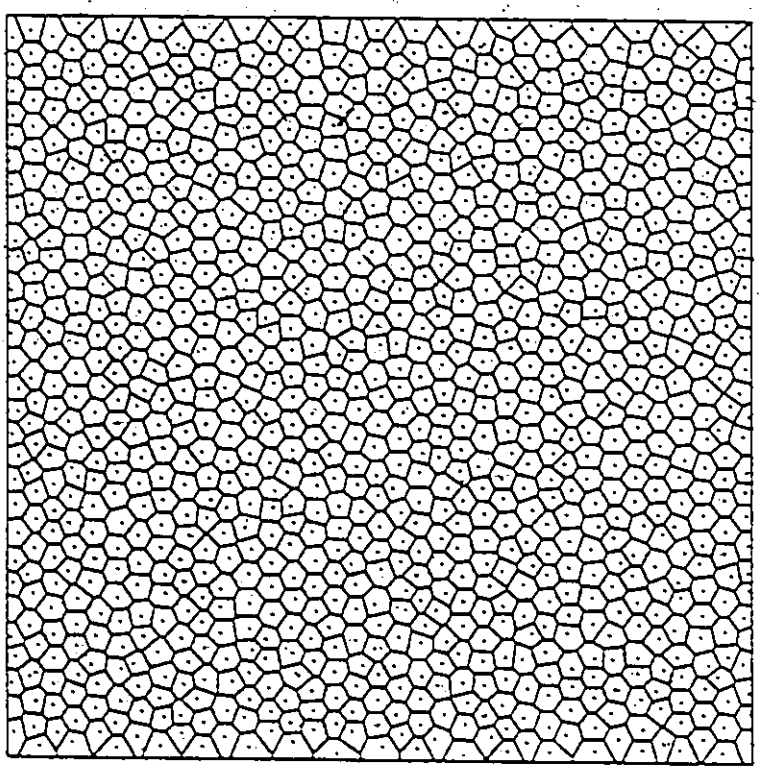

Fig. 4.2a: P, $\gamma = 0.3$

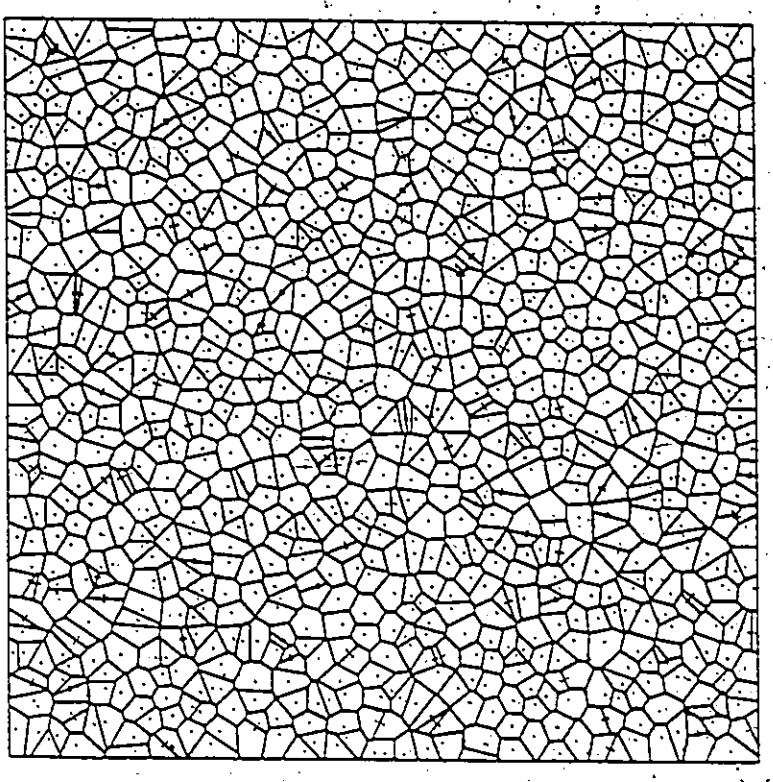

Fig. 4.2d; P, γ = 0.9

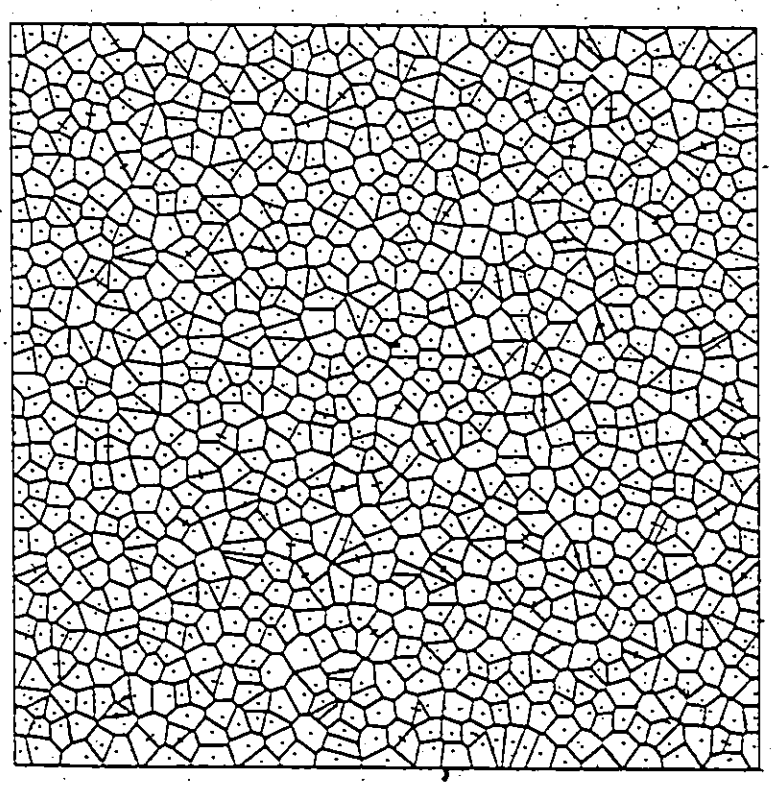

Fig. 4.2c; P, γ = 0.7

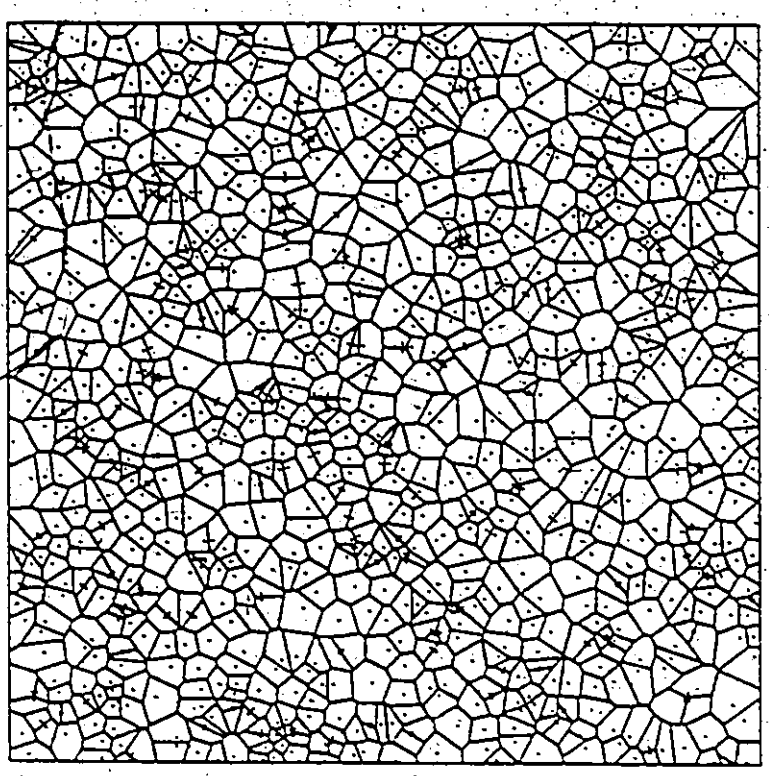

Fig. 4.2f: Random

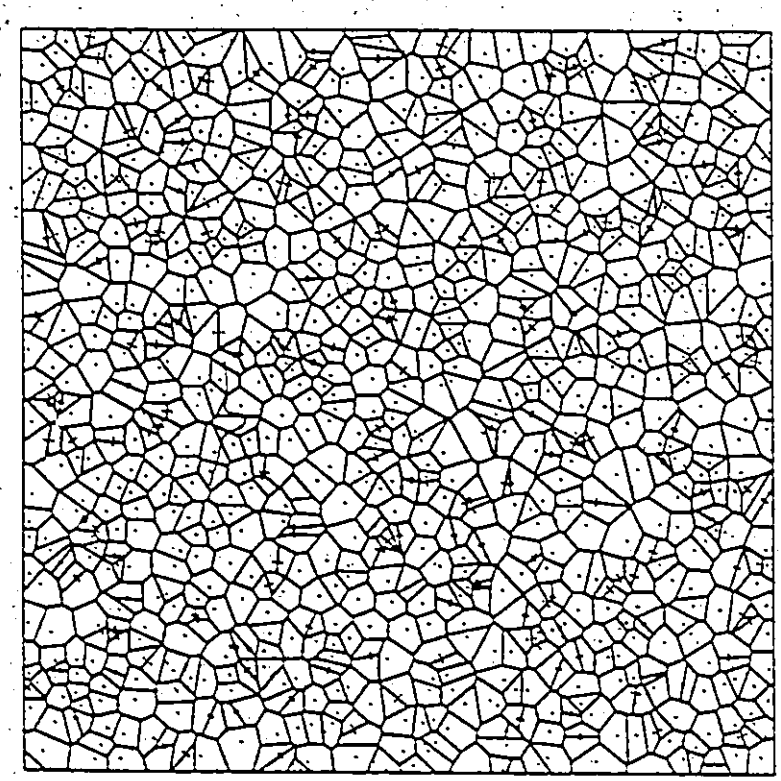

Fig. 4.2e: P, Y = 2.0

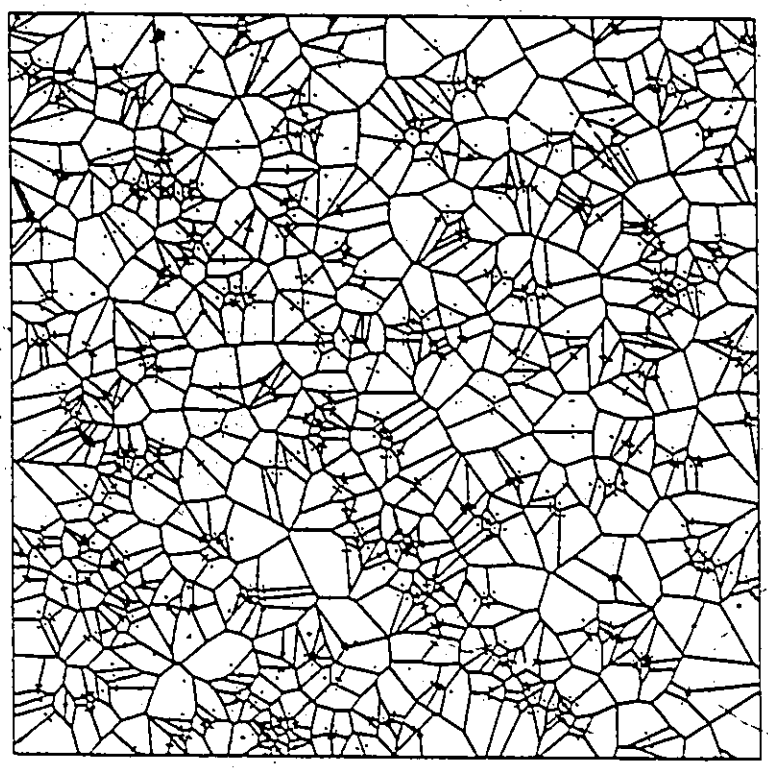

Fig. 4.2h: C, α = 0.5

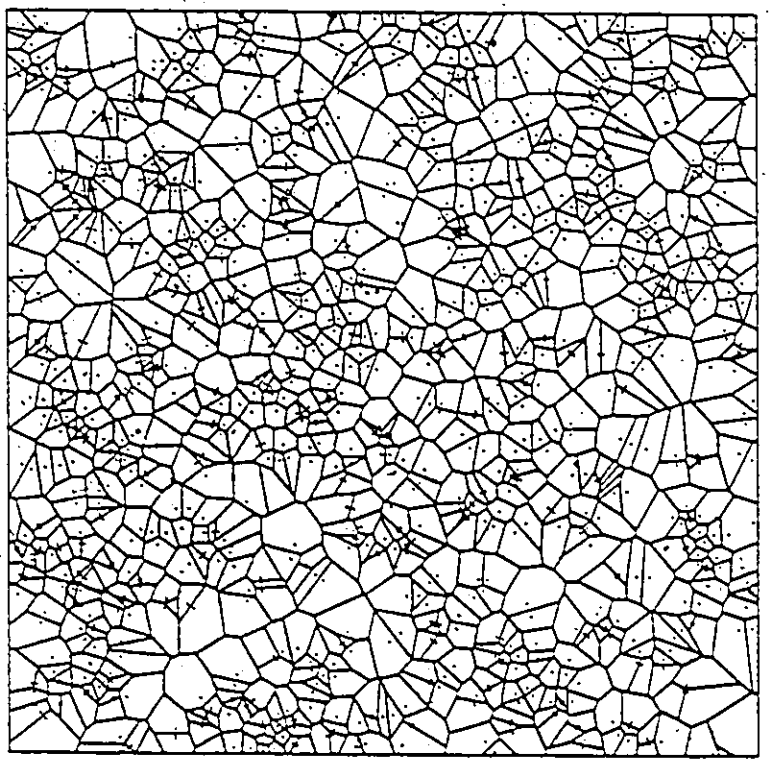

Fig. 4.2g: C, α = 0.7

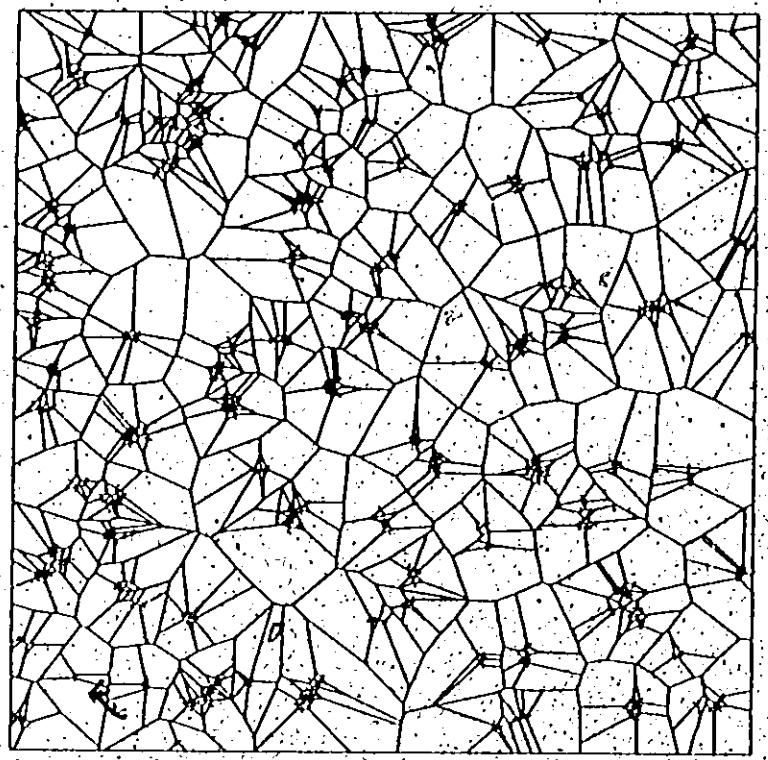

Fig. 4.21: C, α = 0.3

Fig. 4.2: Tessellations for one of the series of point dispersions analyzed. P denotes a dispersion generated from a hexagonal periodic array, and C denotes a clustered dispersion generated from a pseudo-random dispersion. The value of γ or α used in generating the dispersions are indicated.

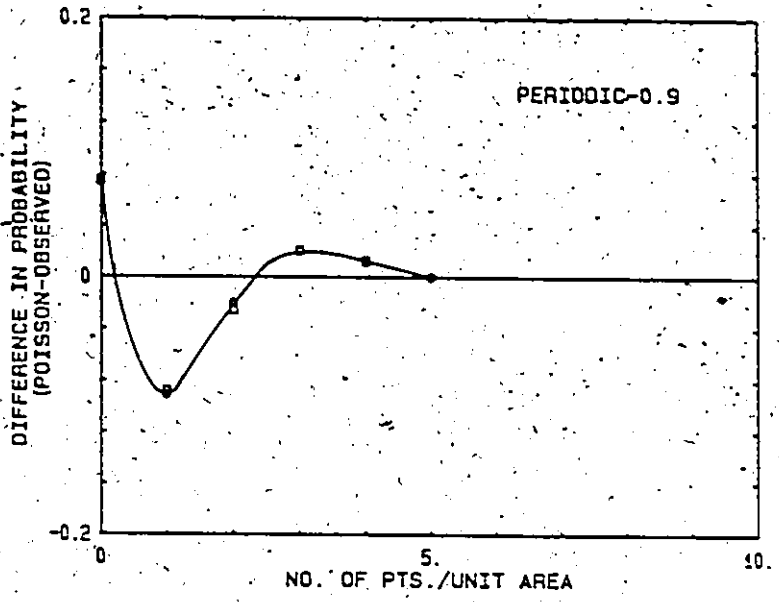

Fig. 4.3a: P, γ = 0.9

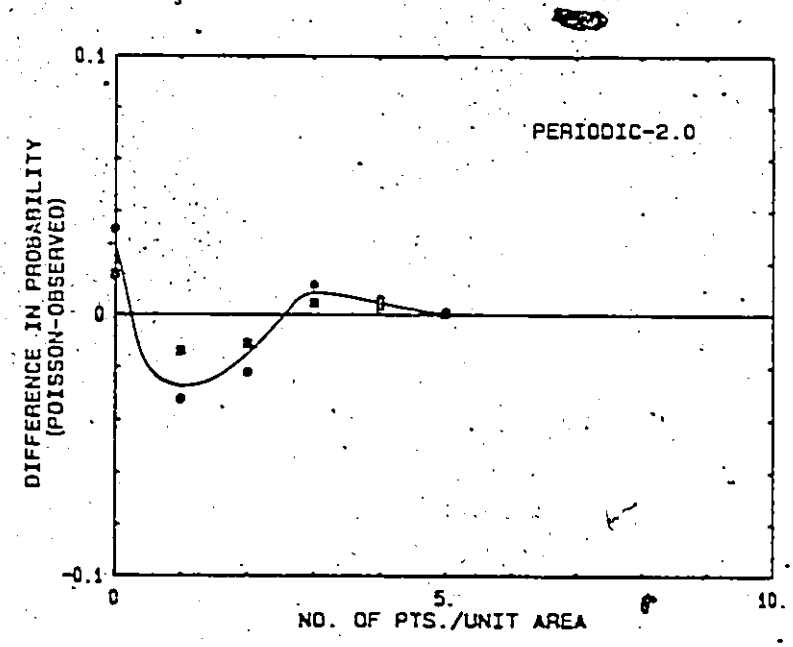

Fig. 4.3b: P, γ = 2.0

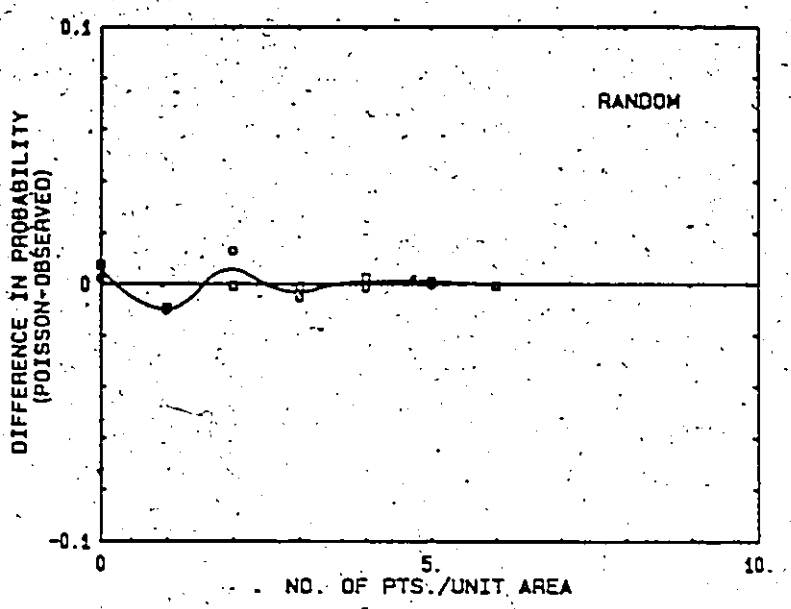

Fig. 4.3c: Random

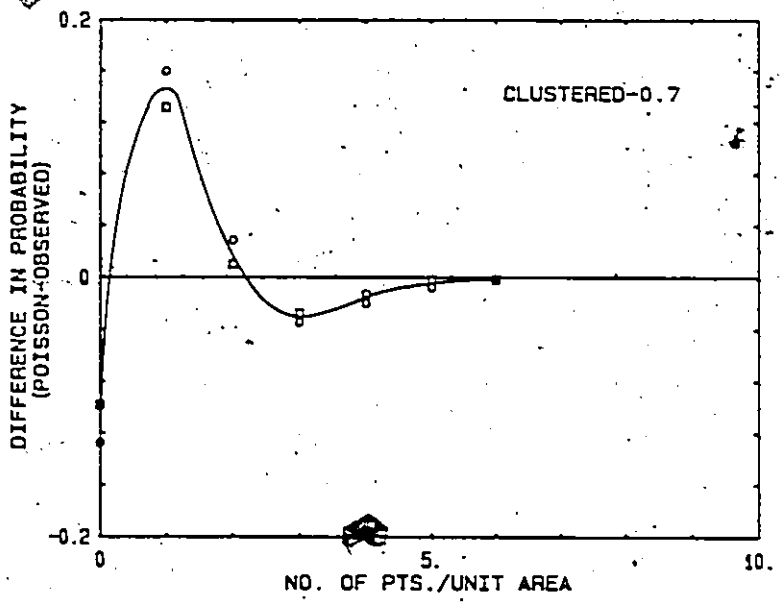

Fig. 4.3d: C, α = 0.7

Fig. 4.3: Results obtained from grid count analyses of four of the point dispersions, as identified in the appropriate figures. A square sample grid was used, with a sampling area equal to λ^{-1}, where λ is the average areal point density. The results are presented as the difference between the observed and the random point count frequency. Note that results for two dispersions are given in each figure.

Table 4.1 presents the results of the nearest-neighbour distance analyses, presented as the average value and standard deviation for each of the dispersions. These have been normalized by the factor $\lambda^{-\frac{1}{2}}$, so that distributions of different scale may be compared. Examples of the histograms of these distributions for one of the periodic ($\gamma = 0.9$), the random and one of the clustered ($\alpha = 0.5$) dispersions are seen in Figures 4.4a-c. The expected (normalized) nearest-neighbour distance should be 0.5 for a random dispersion, as the results illustrate. Also, the standard deviations indicate that the distribution of nearest-neighbour distances is broadest for the random dispersion. The results suggest that the nearest-neighbour distance is a statistic which is sensitive enough to be useful in characterizing differences between dispersions. It is not obvious from these results, however, whether it is numerically more sensitive to deviations from randomness towards clustering or periodicity.

In Table 4.2 the results from the analyses of the near-neighbour distance distributions are given, normalized by $\lambda^{-\frac{1}{2}}$. There is only a small variation in the average value. The largest standard deviation was obtained for the most strongly clustered dispersion. The effect could be due in part to the boundaries, however, no estimate of the effect of finite sample size was attempted. The standard deviation in the distribution of near-neighbour distances is sensitive to departures from randomness, and could thus provide a useful parameter in characterization. Examples of the histograms for three of the dispersions are given in Figures 4.5a-c. These distributions become more skewed as the level of clustering increases.

TABLE 4.1

ANALYSIS OF NEAREST-NEIGHBOUR DISTANCE DISTRIBUTIONS

POINT DISPERSION	AVERAGE NEAREST-NEIGHBOUR DISTANCE $\bar{d}_n$ (NORMALIZED)	STANDARD DEVIATION OF $\bar{d}_n$
P, γ = 0.3	0.8514	0.1184
P, γ = 0.3	0.8537	0.1121
P, γ = 0.5	0.7171	0.1934
P, γ = 0.5	0.7369	0.1742
P, γ = 0.7	0.6341	0.2285
P, γ = 0.7	0.6289	0.2314
P, γ = 0.9	0.5678	0.2448
P, γ = 0.9	0.5702	0.2421
P, γ = 2.0	0.5089	0.2626
P, γ = 2.0	0.5281	0.2693
Random	0.4966	0.2540
Random	0.5067	0.2692
C, γ = 0.7	0.3658	0.1669
C, γ = 0.7	0.3640	0.1630
C, γ = 0.5	0.2642	0.1148
C, γ = 0.5	0.2552	0.1226
C, γ = 0.3	0.1404	0.0699
C, γ = 0.3	0.1394	0.0698

P denotes a dispersion with a degree of periodicity, generated from a hexagonal periodic array.

C denotes a clustered dispersion, generated from a pseudo-random dispersion.

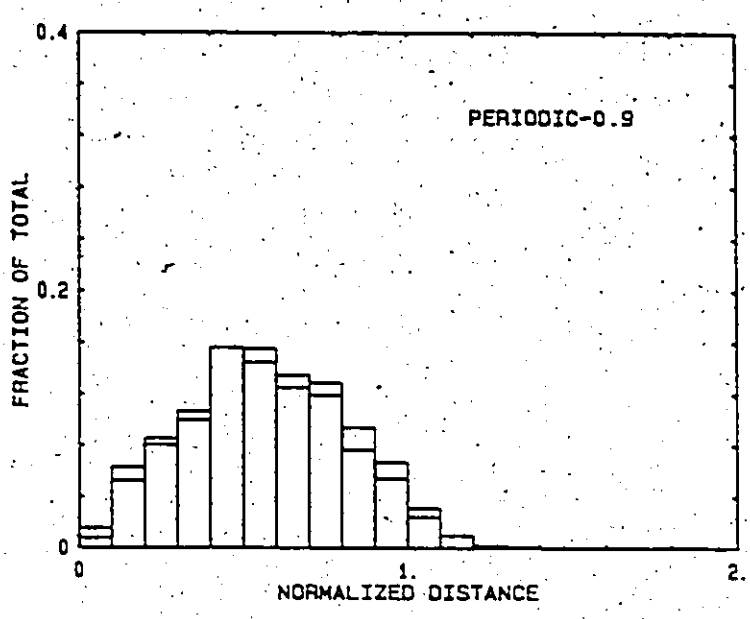

Fig. 4.4a: P, γ = 0.9

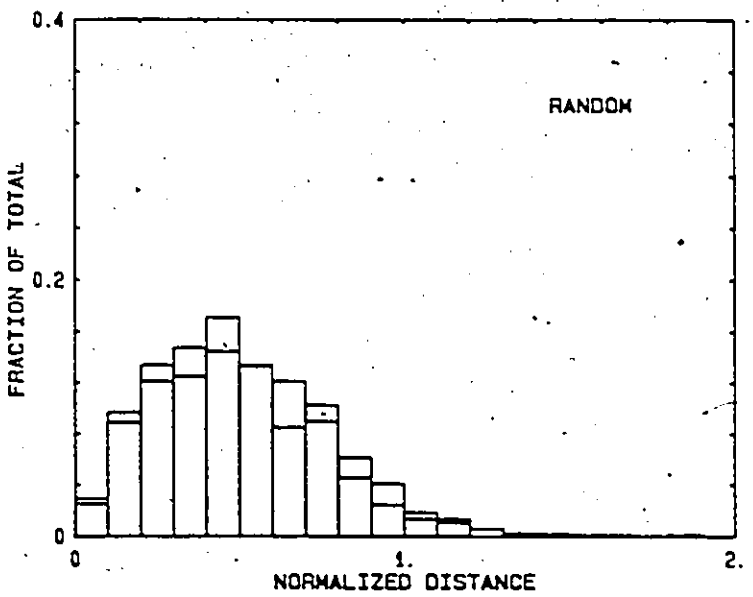

Fig. 4.4b: Random

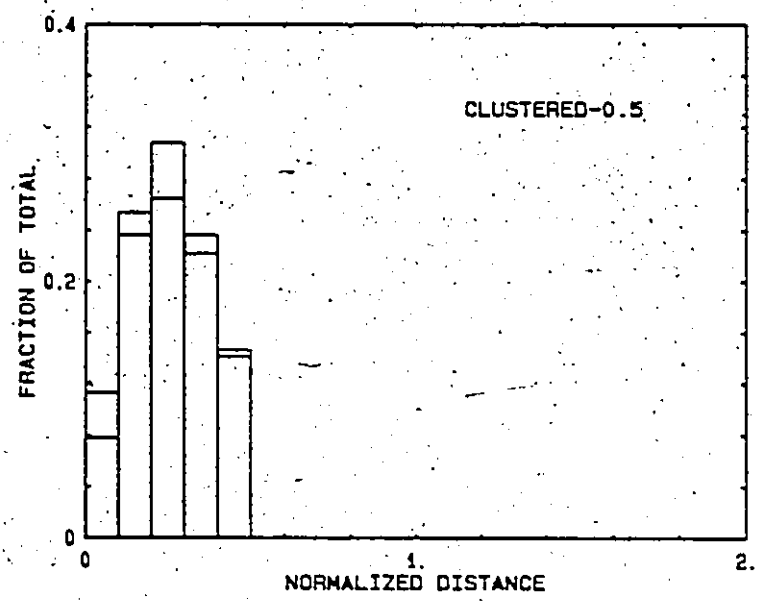

Fig. 4.4c: C, $\alpha = 0.5$

Fig. 4.4: Histograms of the distribution of nearest-neighbour distances for three of the point dispersions, as identified on the appropriate figures. Distances have been normalized by $\lambda^{-\frac{1}{2}}$. Results are given as the fraction of the total number of nearest-neighbours counted in the distribution. Note that results for two dispersions are given in each figure.

TABLE 4.2

ANALYSIS OF NEAR-NEIGHBOUR DISTANCE DISTRIBUTIONS

POINT DISPERSION	AVERAGE NEAR-NEIGHBOUR DISTANCE $\bar{d}_{nn}$ (NORMALIZED)	STANDARD DEVIATION OF $\bar{d}_{nn}$
P, γ = 0.3	1.094	0.1961
P, γ = 0.3	1.093	0.1901
P, γ = 0.5	1.119	0.3113
P, γ = 0.5	1.117	0.2991
P, γ = 0.7	1.139	0.3854
P, γ = 0.7	1.142	0.3909
P, γ = 0.9	1.147	0.4517
P, γ = 0.9	1.142	0.4420
P, γ = 2.0	1.135	0.5351
P, γ = 2.0	1.137	0.5117
Random	1.128	0.5618
Random	1.123	0.5635
C, γ = 0.7	1.107	0.7401
C, γ = 0.7	1.092	0.7687
C, γ = 0.5	1.045	0.9276
C, γ = 0.5	1.042	0.9592
C, γ = 0.3	0.8829	1.262
C, γ = 0.3	0.8792	1.274

P denotes a dispersion with a degree of periodicity, generated from a hexagonal periodic array.

C denotes a clustered dispersion, generated from a pseudo-random dispersion.

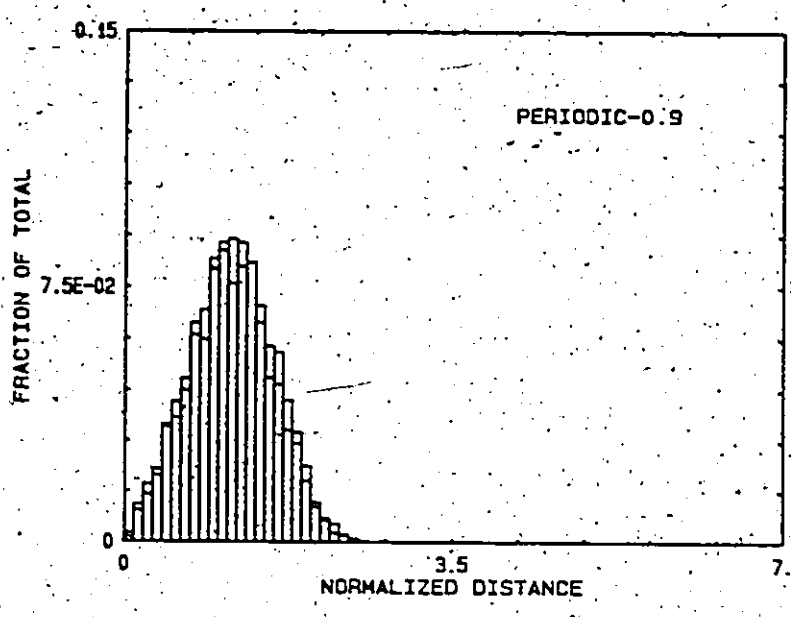

Fig. 4.5a: P, $\gamma = 0.9$

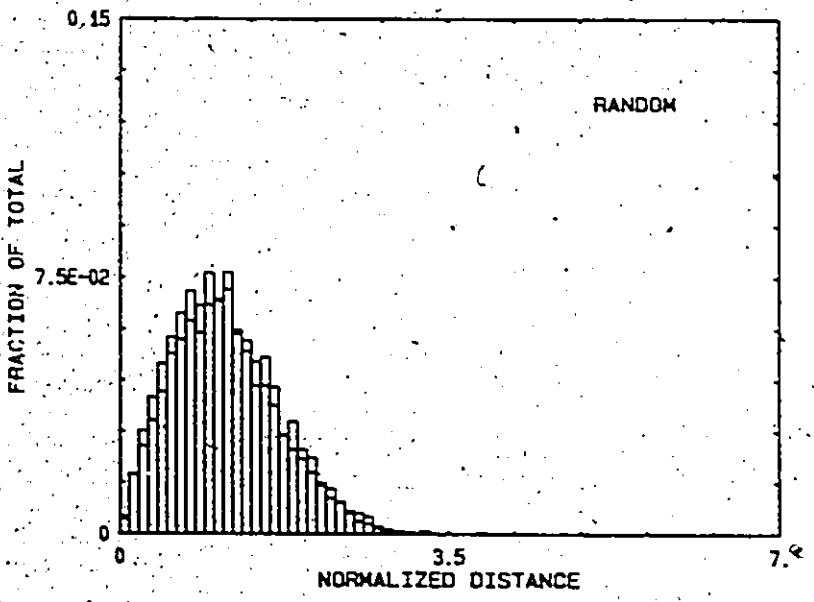

Fig. 4.5b: Random

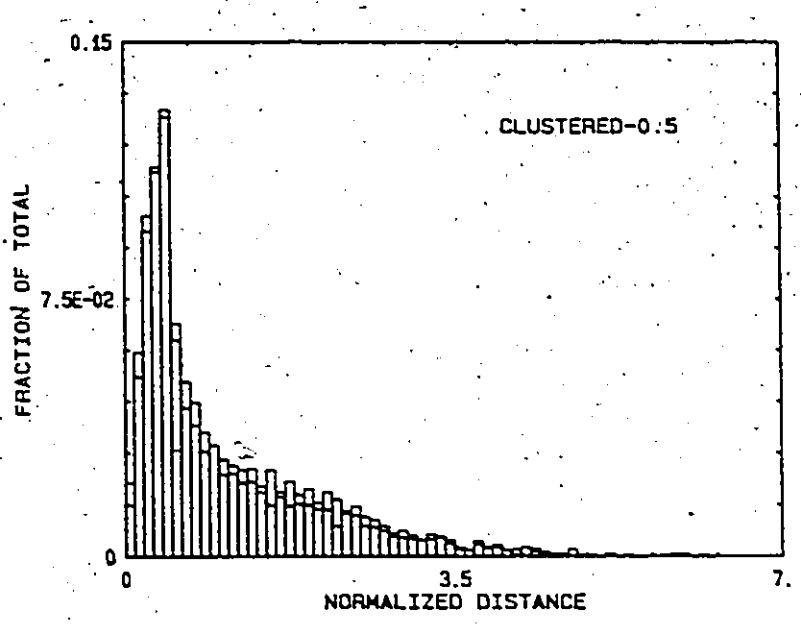

Fig. 4.5c: C, α = 0.5

Fig.4.5: Histograms of the distribution of near-neighbour distances for three of the point dispersions, as identified on the appropriate figures. Distances have been normalized by $\lambda^{-\frac{1}{2}}$. Results are given as the fraction of the total number of near-neighbours counted in the distribution. Note that results for two dispersions are given in each figure.

The distribution in the number of near-neighbours (equal to the number of sides on the cell about a given point) were investigated next, and the results are given in Table 4.3. Only those points whose cells did not lie on the field boundaries were considered in the analysis. This excluded from 9% to 12% of the points from this analysis. The average value is close to 6, although it decreases slightly as the nature of the dispersion moves from periodic to clustered. The standard deviation is seen to be quite sensitive to deviations from randomness. It is especially sensitive to departures from periodicity. The results for the dispersion generated from the periodic lattice with $\gamma = 2.0$, however, suggest that this array may be slightly clustered. This result could not be explained.

The distribution in cell areas was determined for each of the dispersions, with the results given as the average and standard deviation in Table 4.4. The areas have been normalized by λ^{-1}, the average area per point. The decrease in average value as the dispersion character moves from periodic to clustered must be a boundary effect, because the average cell area in an infinite-sized dispersion must be unity. It appears that the spread in the distribution of cell areas is more sensitive to the degree of clustering than to periodicity. The histograms of cell area distributions for three of the dispersions given in Figures 4.6a-c illustrate the skewness and the tail which develops as the level of clustering increases. (Note that Figure 4.6c, for the clustered dispersion has been truncated. A very sparse amount of data extends to a normalized cell area of approximately 9).

TABLE 4.3

ANALYSIS OF DISTRIBUTIONS OF NUMBER OF SIDES PER CELL

POINT DISPERSION	AVERAGE NUMBER OF SIDES PER CELL $\bar{N}$	STANDARD DEVIATION OF $\bar{N}$
P, γ = 0.3	5.98	0.179
P, γ = 0.3	5.99	0.154
P, γ = 0.5	5.98	0.729
P, γ = 0.5	5.98	0.657
P, γ = 0.7	5.97	1.09
P, γ = 0.7	5.97	1.09
P, γ = 0.9	5.97	1.21
P, γ = 0.9	5.98	1.22
P, γ = 2.0	5.95	1.34
P, γ = 2.0	5.95	1.34
Random	5.95	1.28
Random	5.95	1.31
C, γ = 0.7	5.94	1.44
C, γ = 0.7	5.95	1.44
C, γ = 0.5	5.92	1.50
C, γ = 0.5	5.92	1.60
C, γ = 0.3	5.90	1.70
C, γ = 0.3	5.91	1.68

P denotes a dispersion with a degree of periodicity, generated from a hexagonal periodic array.

C denotes a clustered dispersion, generated from a pseudo-random dispersion.

TABLE 4.4

ANALYSIS OF CELL AREA DISTRIBUTIONS

POINT DISPERSION	AVERAGE CELL AREA $\bar{A}_c$ (NORMALIZED)	STANDARD DEVIATION OF $\bar{A}_c$
P, γ = 0.3	0.9988	0.1075
P, γ = 0.3	1.000	0.1054
P, γ = 0.5	0.9988	0.1911
P, γ = 0.5	0.9995	0.1816
P, γ = 0.7	0.9964	0.2560
P, γ = 0.7	0.9955	0.2536
P, γ = 0.9	0.9946	0.3215
P, γ = 0.9	0.9970	0.3240
P, γ = 2.0	0.9783	0.4507
P, γ = 2.0	0.9845	0.4290
Random	0.9889	0.4968
Random	0.9899	0.5365
C, γ = 0.7	0.9682	0.6623
C, γ = 0.7	0.9671	0.7232
C, γ = 0.5	0.9336	0.8846
C, γ = 0.5	0.9562	1.015
C, γ = 0.3	0.9160	1.464
C, γ = 0.3	0.8965	1.550

P denotes a dispersion with a degree of periodicity, generated from a hexagonal periodic array.

C denotes a clustered dispersion, generated from a pseudo-random dispersion.

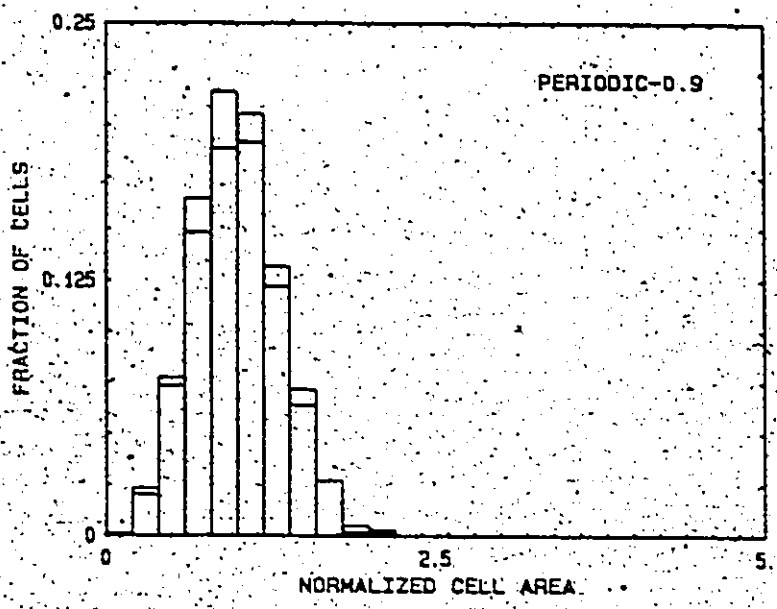

Fig. 4.6a: P, γ = 0.9

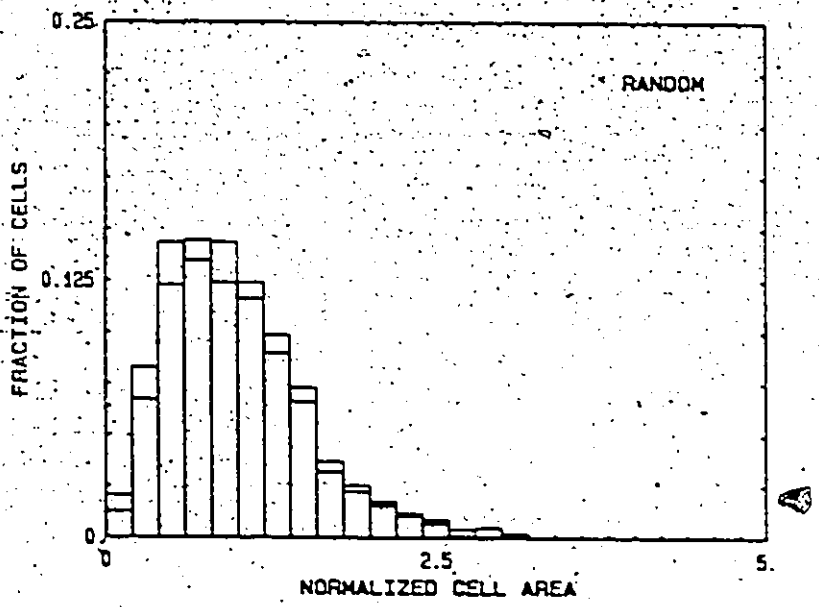

Fig. 4.6b: Random

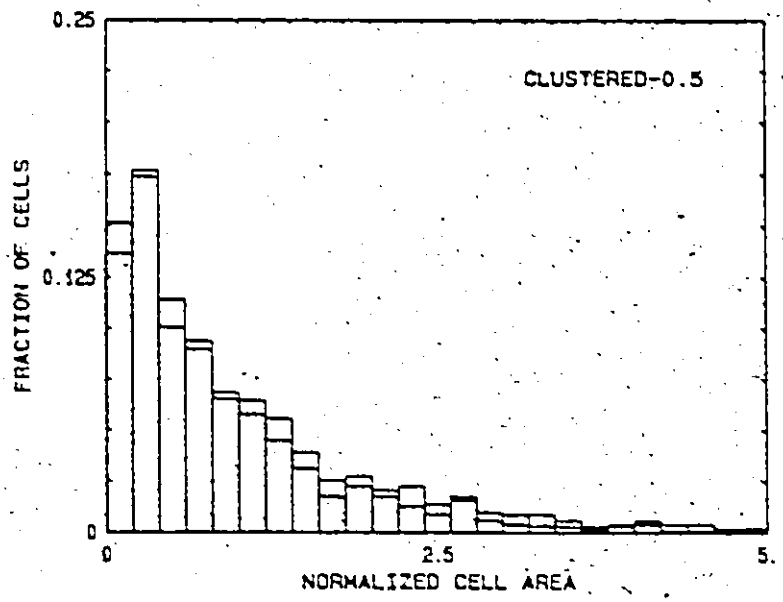

Fig. 4.6c: C, α = 0.5

Fig. 4.6: Histograms of the distribution of cell areas obtained from the tessellation from three of the point dispersions, as identified on the appropriate figures. Cell areas have been normalized by λ^{-1}. Results are given as the fraction of the number of cells in the tessellation, excluding cells which lie on the field boundaries. Note that results for two dispersions are given in each figure.

The behaviour of the extreme end of a distribution may be very sensitive to the level of clustering. In samples of finite size, however, the data in this tail end region will be sparse. The comparison of two distributions based on such a small amount of data in the extremes of the distribution cannot indicate differences with a high degree of confidence. If we weight the tail end of the cell area frequency distribution more heavily by multiplying the frequency by the cell area, the distribution of the fraction of the field area covered by cells (excluding cells on the boundaries) of a given size is obtained. Differences in the extreme characteristics then become more obvious, as seen in Figures 4.7a-d. Periodicity in a dispersion results in a rather symmetric distribution, which becomes skewed and eventually evenly distributed as the dispersion tends toward strong clustering. As measures of the mean and the spread in these distributions we will use the first moment and the square root of the second moment respectively, where the second moment has been evaluated about the first. These values are given in Table 4.5 for each of the distributions. The sensitivity of both of these parameters to the degree of clustering is very high, however, the same sensitivity towards periodicity is not displayed.

Many of the cells in a clustered dispersion are not equiaxed. This suggests the cell aspect ratio as an indicator of the level of clustering in a dispersion. Here, the aspect ratio of a cell was defined by the ratio of the maximum distance between any two of its vertices to the dimension of the cell perpendicular to the direction of this maximum dimension. Results for these frequency distributions are

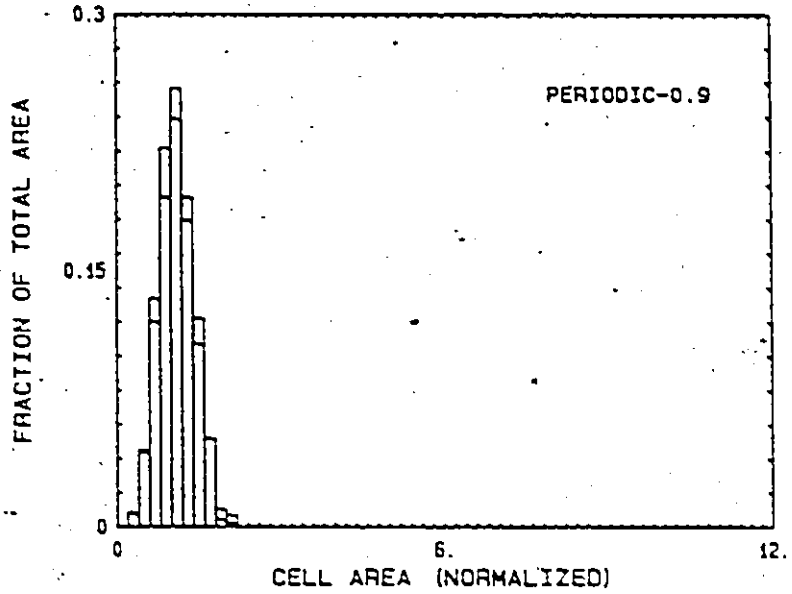

Fig. 4.7a: P, γ = 0.9

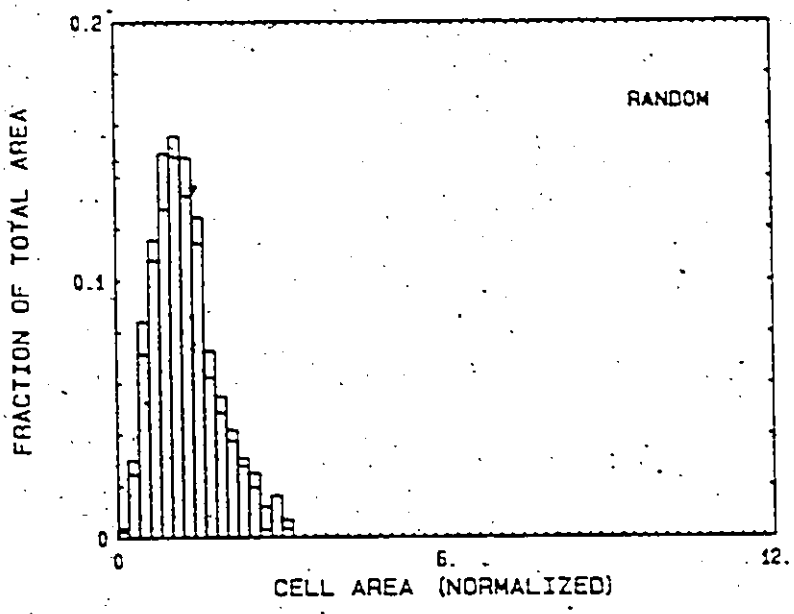

Fig. 4.7b: Random

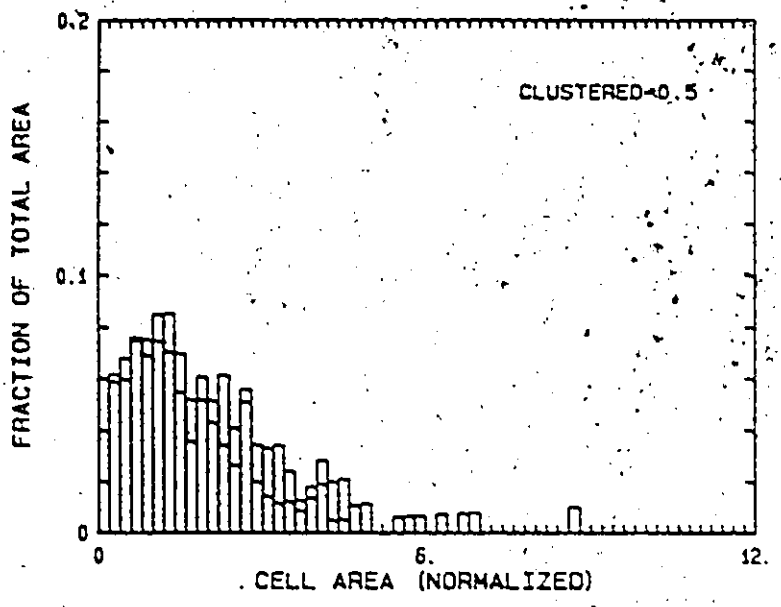

Fig. 4.7c: C, α = 0.5

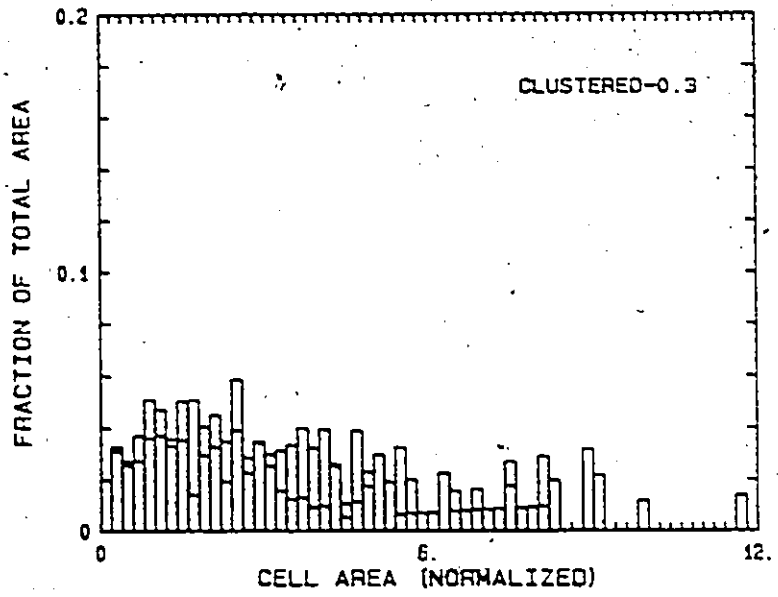

Fig. 4.7d: C, α = 0.3

Fig. 4.7: Distributions of the fraction of the total field area covered by cells of a given area. The dispersions are identified on the appropriate figures. Cell areas have been normalized by λ^{-1}. Note that cells lying on the field boundaries have been excluded from the analysis, and that in each figure results for two dispersions are indicated.

TABLE 4.5

ANALYSIS OF THE DISTRIBUTIONS OF FRACTION OF TOTAL FIELD AREA VS CELL AREA

POINT DISPERSION	FIRST MOMENT $\bar{A}_F$ OF DISTRIBUTION OF FRACTION OF TOTAL AREA VS CELL AREA (NORMALIZED)	(SECOND MOMENT OF DISTRIBUTION ABOUT $\bar{A}_F$)$^{1/2}$
P, γ = 0.3	1.011	0.1075
P, γ = 0.3	1.011	0.1053
P, γ = 0.5	1.035	0.1880
P, γ = 0.5	1.033	0.1810
P, γ = 0.7	1.062	0.2536
P, γ = 0.7	1.060	0.2522
P, γ = 0.9	1.098	0.3132
P, γ = 0.9	1.102	0.3192
P, γ = 2.0	1.186	0.4605
P, γ = 2.0	1.171	0.4457
Random	1.238	0.5252
Random	1.280	0.5971
C, γ = 0.7	1.421	0.7949
C, γ = 0.7	1.507	0.9171
C, γ = 0.5	1.771	1.147
C, γ = 0.5	2.033	1.576
C, γ = 0.3	3.254	2.330
C, γ = 0.3	3.574	2.704

P denotes a dispersion with a degree of periodicity, generated from a hexagonal periodic array.

C denotes a clustered dispersion, generated from a pseudo-random dispersion.

presented in Table 4.6, and the corresponding histograms for three of the dispersions given in Figures 4.8a-c. It is seen that, although this statistic displays sensitivity to both the degree of periodicity and clustering, it is much more sensitive to the latter. It should be noted that this result is obtained for an isotropic dispersion, and is not due to any anisotropy in the distribution.

The neighbour distances and properties of the individual cells in the tessellation have thus all been shown to be potentially useful statistics in characterizing the surroundings of points in a dispersion. As the character of a dispersion on a larger scale is related at least in part to the character of the local surroundings of its points, general differences between dispersions can be identified, i.e., whether they tend towards clustering or regularity. In particular, the standard deviation in the distribution of number of sides per cell appears to be quite sensitive to deviations from periodicity, and the cell area and aspect ratio distributions are useful indicators of the level of clustering.

An alternative presentation of the nearest-neighbour distance distribution would be to analyze the dispersion for all those points which have at least one other point within a certain distance of it. This critical distance would then be the criterion used to define whether two given points are clustered, with a value based on a physical or mechanical parameter. The fraction of points in the dispersion which are clustered in this manner at a given critical clustering separation, and the variation of the fraction clustered with separation distance would yield information on the character of the dispersion.

TABLE 4.6

ANALYSIS OF CELL ASPECT RATIO DISTRIBUTIONS

POINT DISPERSION	AVERAGE CELL ASPECT RATIO $\bar{R}$	STANDARD DEVIATION OF $\bar{R}$
P, γ = 0.3	1.184	0.0989
P, γ = 0.3	1.184	0.0973
P, γ = 0.5	1.261	0.1907
P, γ = 0.5	1.260	0.1805
P, γ = 0.7	1.416	0.3479
P, γ = 0.7	1.403	0.3224
P, γ = 0.9	1.506	0.4499
P, γ = 0.9	1.461	0.3795
P, γ = 2.0	1.613	0.5271
P, γ = 2.0	1.574	0.5327
Random	1.566	0.4615
Random	1.595	0.5220
C, γ = 0.7	1.760	0.6606
C, γ = 0.7	1.813	0.7564
C, γ = 0.5	2.004	0.8502
C, γ = 0.5	2.074	0.9361
C, γ = 0.3	2.333	1.330
C, γ = 0.3	2.471	1.613

P denotes a dispersion with a degree of periodicity, generated from a hexagonal periodic array.

C denotes a clustered dispersion, generated from a pseudo-random dispersion.

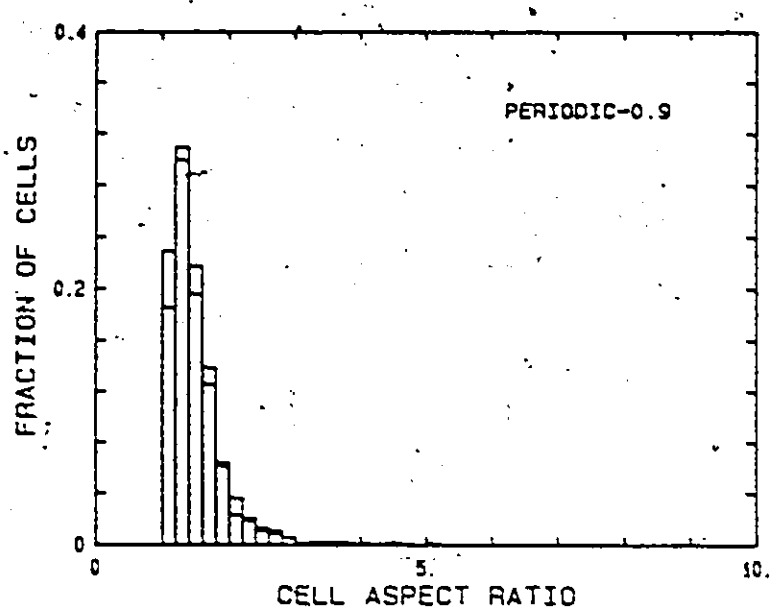

Fig. 4.8a: P, γ = 0.9

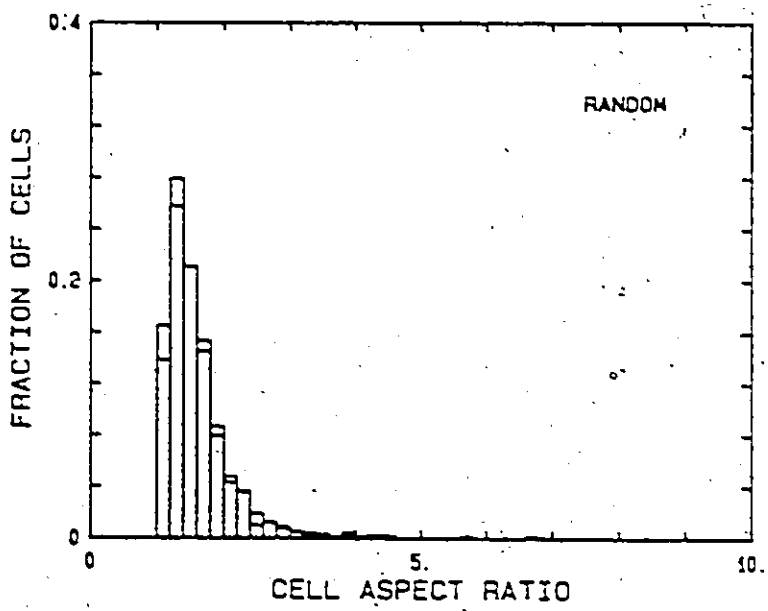

Fig. 4.8b: Random

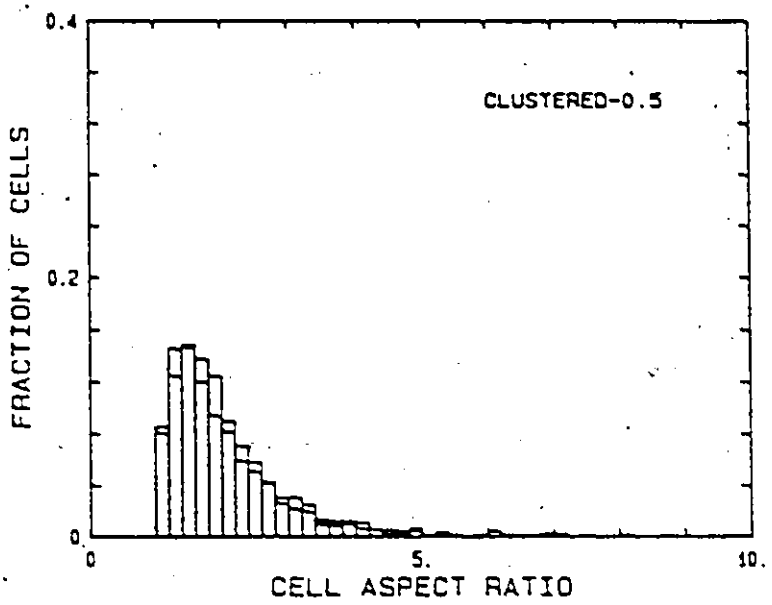

Fig. 4.8c: C, α = 0.5

Fig. 4.8: Histograms of distribution of cell aspect ratios in tessellations constructed about the dispersions indicated. Results are given as the fraction of the total number of cells in the tessellation, excluding those lying on the field boundaries. Note that results for two dispersions are given in each figure.

The results of this analysis for the generated point dispersions are shown in Figures 4.9 and 4.10. Note that the clustering interaction distance has been normalized by $\lambda^{-\frac{1}{2}}$. The presentation of results in this form illustrates very clearly the differences between the dispersions. The more strongly clustered arrays have a steeper initial rise in the curve. An array with a strong degree of periodicity would display a sharp rise in its curve at a normalized spacing close to unity, as illustrated in Figure 4.10. A different characteristic present in the banded dispersion of Figure 4.11 may also be illustrated in this form of plot. The results for this dispersion given in Figure 4.12 suggest that, although it is evidently clustered, there is a degree of periodicity within the clusters.

In using the plots of Figures 4.9 and 4.10 as a basis for evaluating another dispersion, care should be used. First, they have been developed using a distance criterion for clustering, and thus will not provide information regarding any anisotropy in the dispersion. Also, since they are based upon the separation between only pairs of points, they will not necessarily be dependent upon the scale of any fluctuation in the local point density. Indeed, the scale of clustering in the generated clustered dispersions analyzed here was dependent upon the spatial distribution of regions in a random dispersion which, locally, contained a higher-than-average point density.

The application of the Dirichlet tessellation to the characterization of a dispersion of particles in a material should employ a geometrical statistic which relates to the physics of the phenomenon

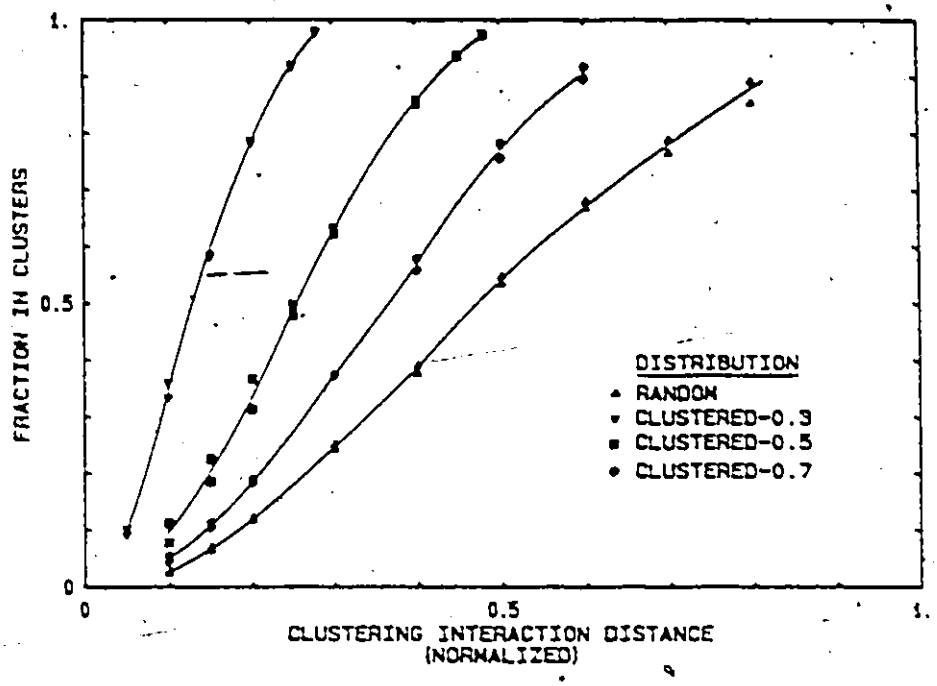

Fig. 4.9: Analysis of clustering in the random and clustered dispersions. Note that, in each case, two dispersions were analyzed. Results are given as the fraction of points in the dispersion which have at least one point within a distance given by the indicated clustering interaction distance. Distances have been normalized by λ^{-1}.

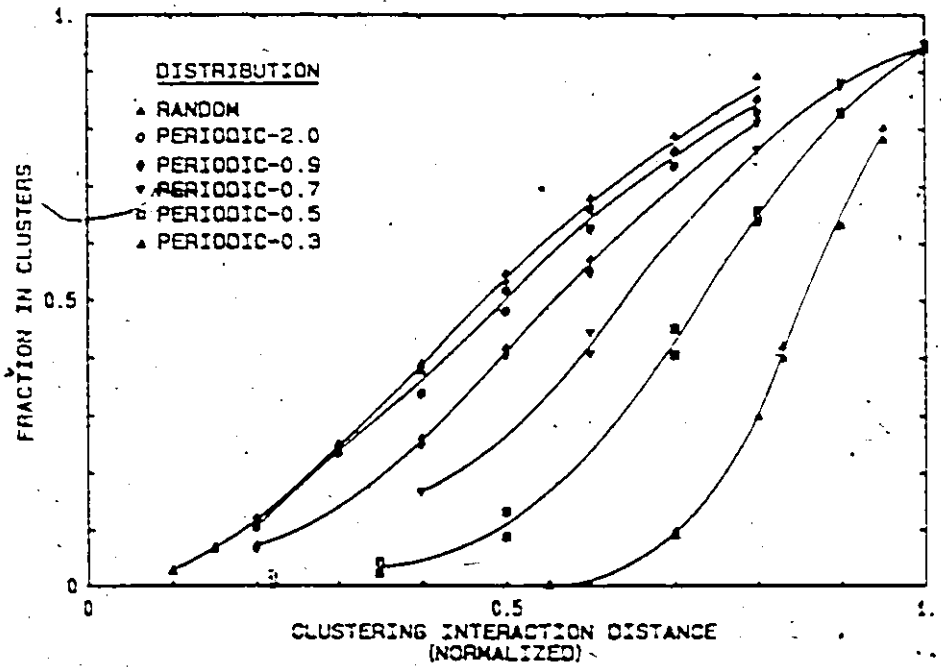

Fig. 4.10: Analysis of clustering in the random and characteristically periodic distributions. Results are presented as in Figure 4.9.

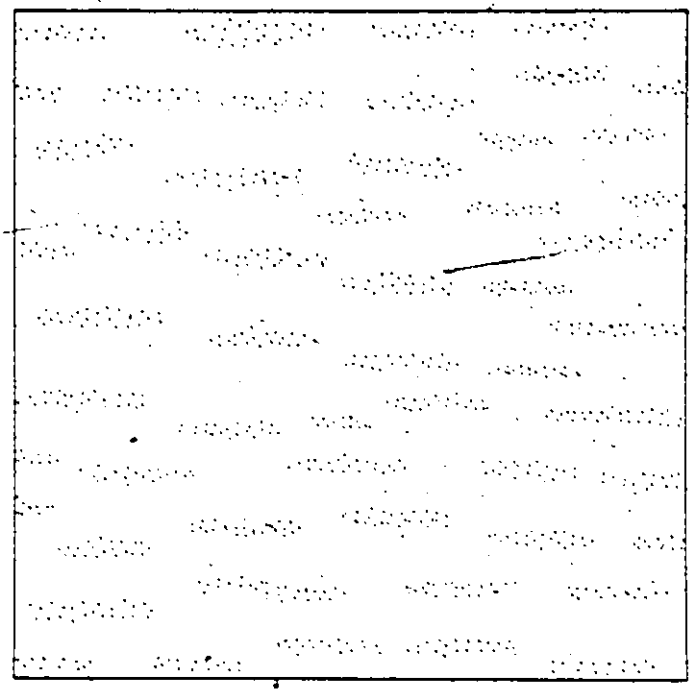

Fig. 4.11: A banded dispersion exhibiting clustering.

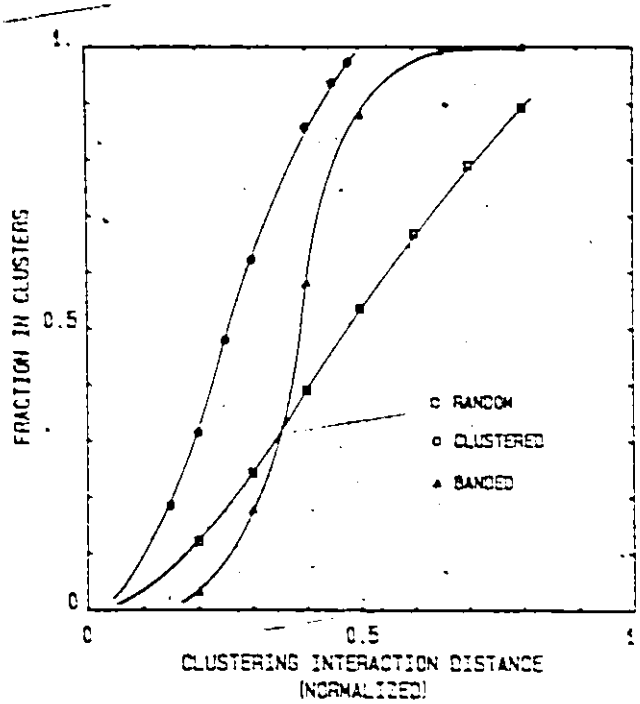

Fig. 4.12: Comparison of results of clustering analysis of the banded distribution in Figure 4.11 with a random and a clustered (α = 0.5) dispersion. The banded dispersion displays periodic characteristics on a local scale, and clustered characteristics on a larger scale.

under consideration. For example, if the tessellation was constructed about a point distribution defined by the centroids of a dispersion of (small) growing precipitates which have nucleated simultaneously, each cell then defines the (two-dimensional) diffusion field about its associated particle. The cell boundaries then give the iso-activity lines. Parameters which define the mechanical interaction between hard particles or inclusions during deformation relate to nearest-neighbour or near-neighbour particle spacings.

The method of analysis presented above does not necessarily require the computation of tessellations for the dispersions. However, the results of the tessellation are useful in further analyzing the nature and scale of clustering. This will be discussed in the following section, where several characteristically different particle dispersions are analyzed.

4.5 Application to the Analysis of Microstructures

In this section the tessellation construction will be applied in the examination of particle distributions in several microstructures. Consideration will be given first to the distribution of sulphide inclusions in a continuously-cast structural HSLA steel, and then to several microstructures with higher volume fractions of second phase particles.

4.5.1 HSLA Steel

The composition of the HSLA steel is given in Table 4.7. Sections were examined in two orientations, looking along the rolling direction on a plane normal to the rolling plane containing the rolling

TABLE 4.7

COMPOSITION OF HSLA STEEL
USED IN INCLUSION CLUSTERING ANALYSIS

	%
C	0.044
Mn	1.99
P	0.002
S	0.005
Si	0.21
Cr	0.26
Mo	0.26
Ti	0.005
N	0.007

direction, and looking along the rolling direction on a plane normal to both the rolling plane and the rolling direction. Two different sections for the first case were analyzed for comparison.

The tessellations for the inclusion distributions in these sections are presented in Figures 4.13a-c. The cells were constructed about points located at the centroids of the inclusions. Figure 4.14 presents the clustering analysis of the three inclusion distributions as the variation of the fraction of inclusions clustered with normalized inclusion spacing. This analysis was discussed in the previous section, and the result for the random point dispersion is included in Figure 4.14 for comparison. The curves indicate a degree of clustering in the inclusion dispersions, and that the inclusion distribution is more strongly clustered in sections containing the rolling direction. The curves for the inclusion distributions tend toward the curve for the random point distribution at higher clustering interaction spacings, suggesting that the deviation in the spatial distribution of inclusions from randomness (based on a distance criterion) is not very significant.

The output from the tessellation construction allows the individual clusters of inclusions to be determined very efficiently. The clusters are then mapped as groups of points, and thus the scale of clustering can be investigated. For the inclusion distribution in Figure 4.13a, viewed along the rolling direction, if we choose a (normalized) clustering spacing of 0.4, the separate clusters may be identified and boundaries constructed around the clustered regions, as illustrated in Figure 4.15. The periphery of a given cluster is given here

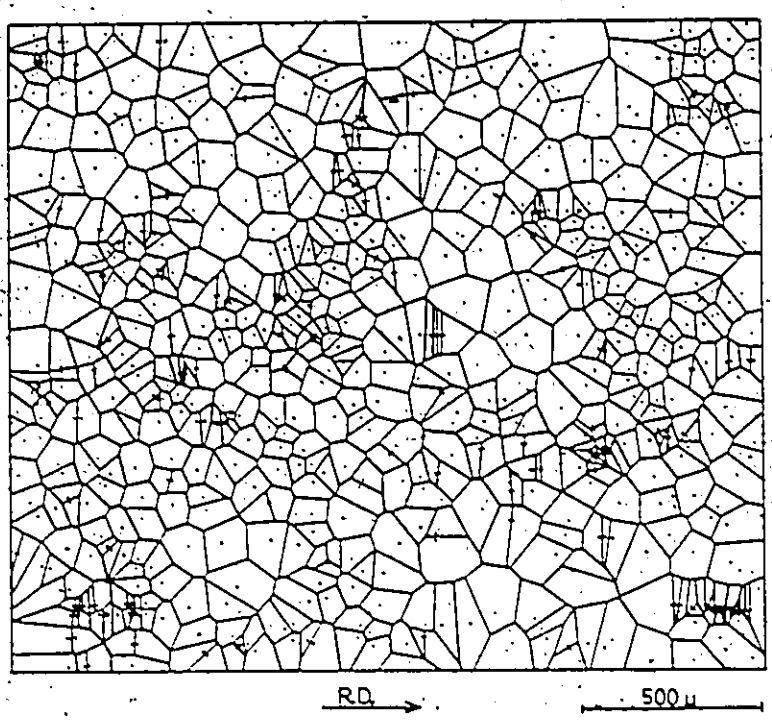

Fig. 4.13a: Section plane along rolling direction - #1.

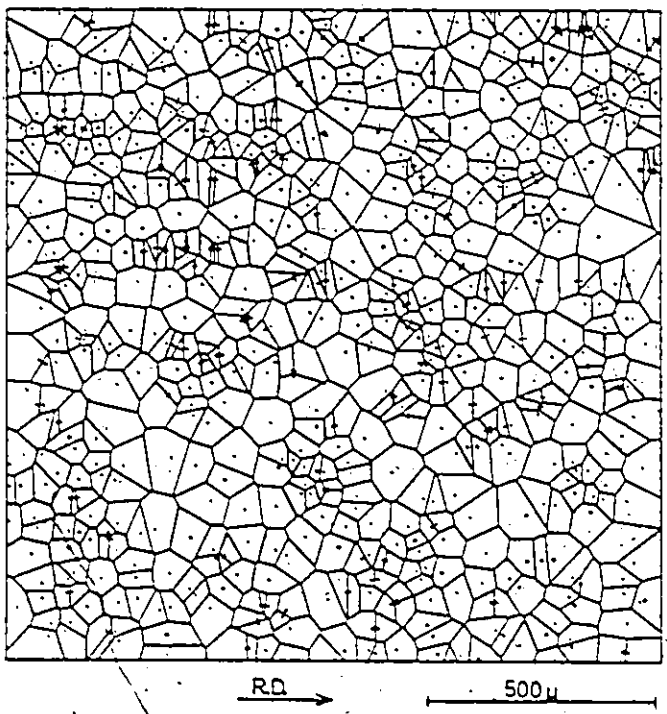

Fig. 4.13b: Section plane along rolling direction - #2.

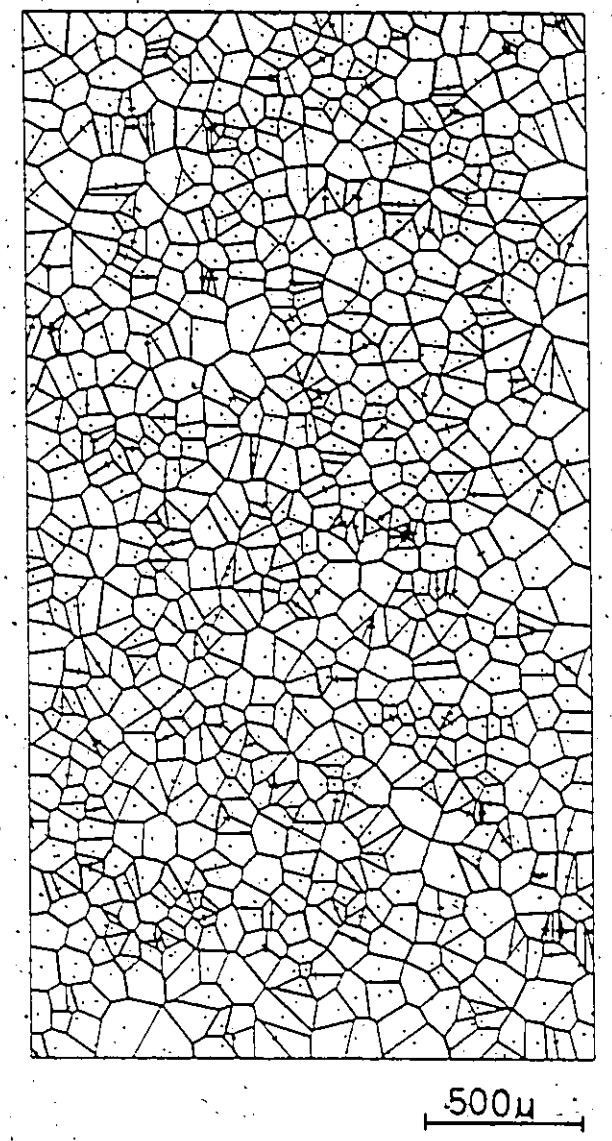

Fig. 4.13c: Section plane normal to rolling direction, so that the view is <u>in</u> the rolling direction.

Fig. 4.13: Tessellations constructed about the inclusion distribution in a continuously-cast HSLA steel. The orientation of the section plane is given on the appropriate figure.

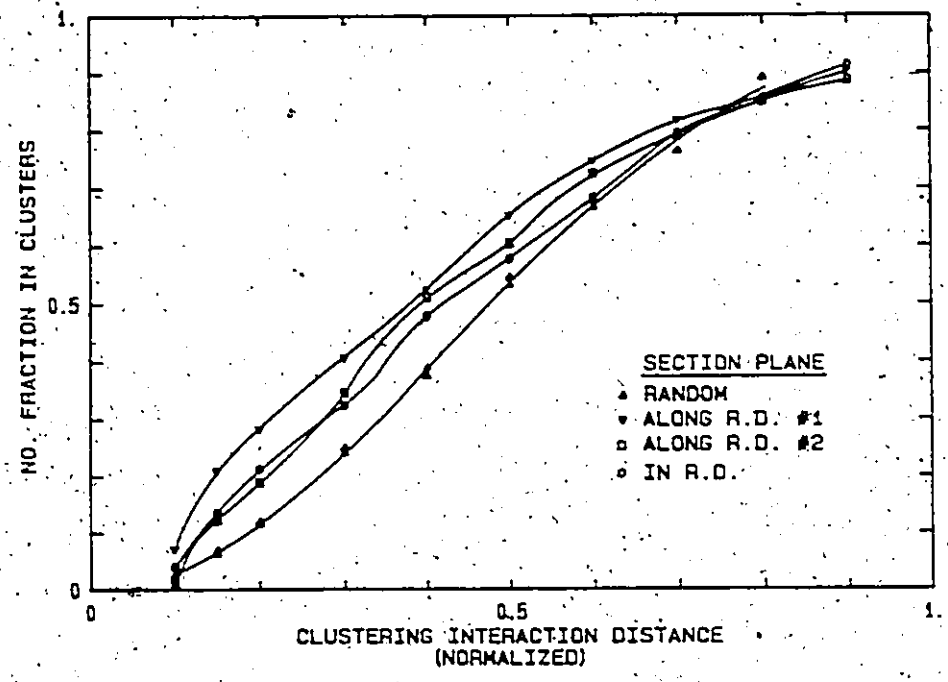

Fig. 4.14: Results of clustering analyses of the inclusion distributions given in Figures 4.13a-c, based on a critical clustering interaction distance (see Figure 4.9). The result for the pseudo-random point dispersion is given for comparison.

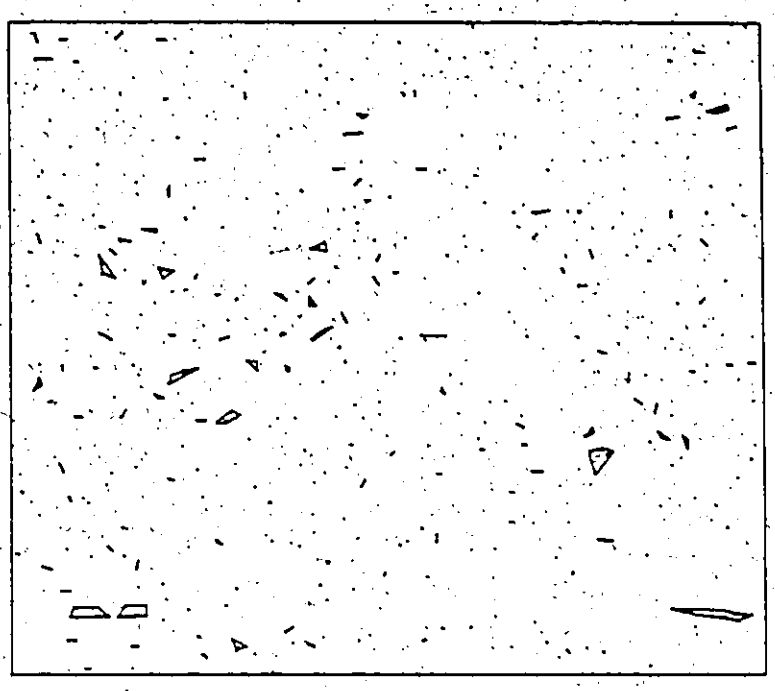

Fig. 4.15: Construction of boundaries about the peripheries of the clustered regions, for the inclusion distribution given in Figure 4.13a. The normalized clustering interaction distance used was 0.4.

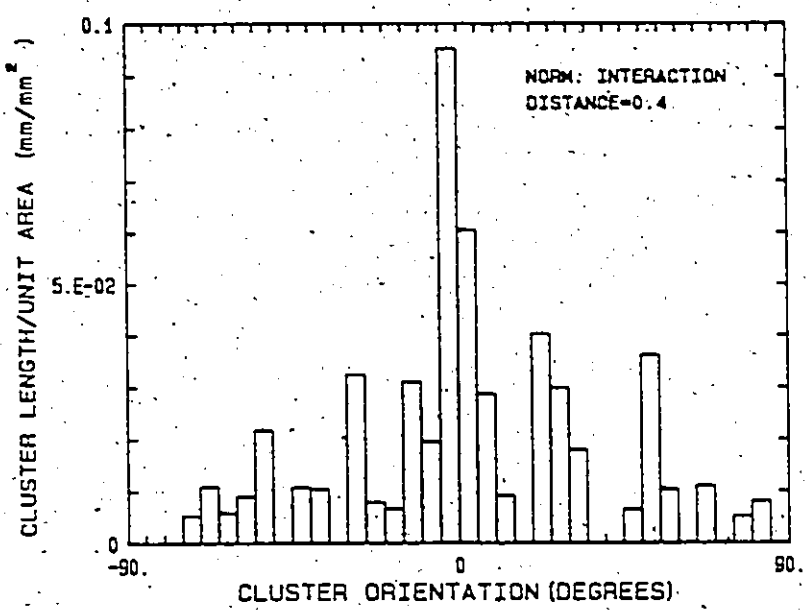

Fig. 4.16: Distribution of total cluster length vs. orientation relative to the rolling plane, for the clustered regions defined in Figure 4.15. The peak near 0 degrees indicates the anisotropy in the inclusion distribution.

as the smallest convex polygon which encloses all of the inclusions in the cluster. The clusters of inclusions thus identified are regions which will develop a high local level of damage during deformation.

The measure used to give the size of a cluster should consider its shape. If the clustered regions tend to be elongated, depending upon the imposed strain the maximum dimension of a clustered region may be a more useful description of the inclusion cluster than its area, with respect to the damage it contributes to the material. If we use this maximum dimension description and note the orientation it is measured in, a practical technique for evaluating anisotropy in the distribution results. Figure 4.16 thus gives the distribution of the total length of clusters for Figure 4.15, oriented in angular intervals of 5 degrees from the rolling plane. The peak at 0 degrees clearly indicates the inclusion stringering in the rolling direction. If we construct the boundaries of the clustered regions for the inclusion distribution in Figure 4.13c (from a section perpendicular to the rolling direction), again for a normalized clustering spacing of 0.4, the result is seen in Figure 4.17. A similar total cluster length vs. orientation distribution for this dispersion, given in Figure 4.18, indicates that the distribution of inclusions is more isotropic when the material is sectioned normal to the rolling direction. An analysis of the anisotropy of a dispersion based on a single orientation of the section plane thus does not necessarily offer an adequate description.

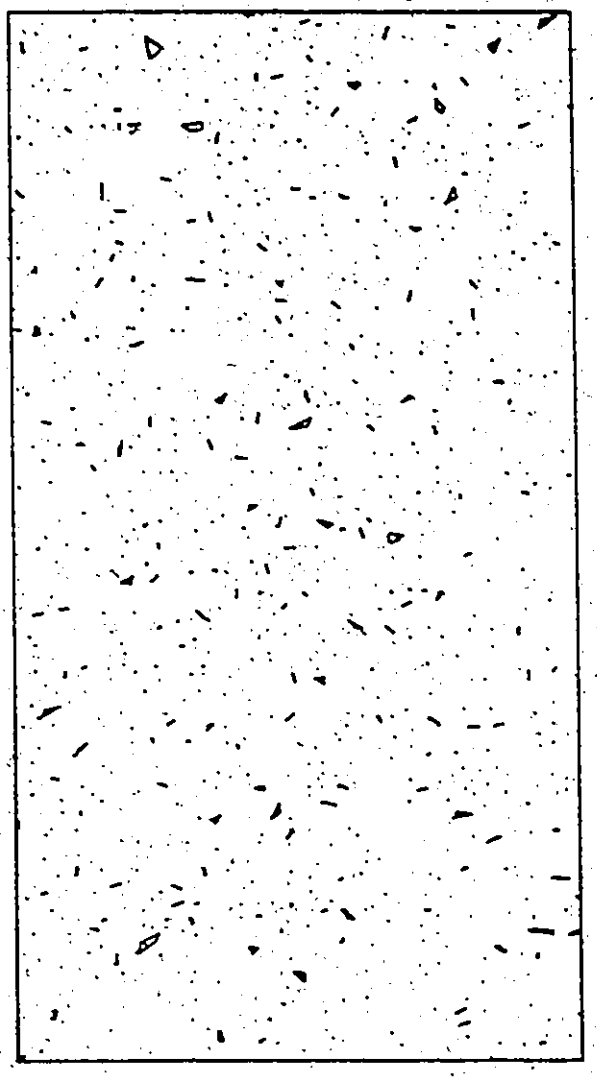

Fig. 4.17: Construction of boundaries about the peripheries of the clustered regions, for the inclusion distribution given in Figure 4.13c. The normalized clustering interaction distance used was 0.4.

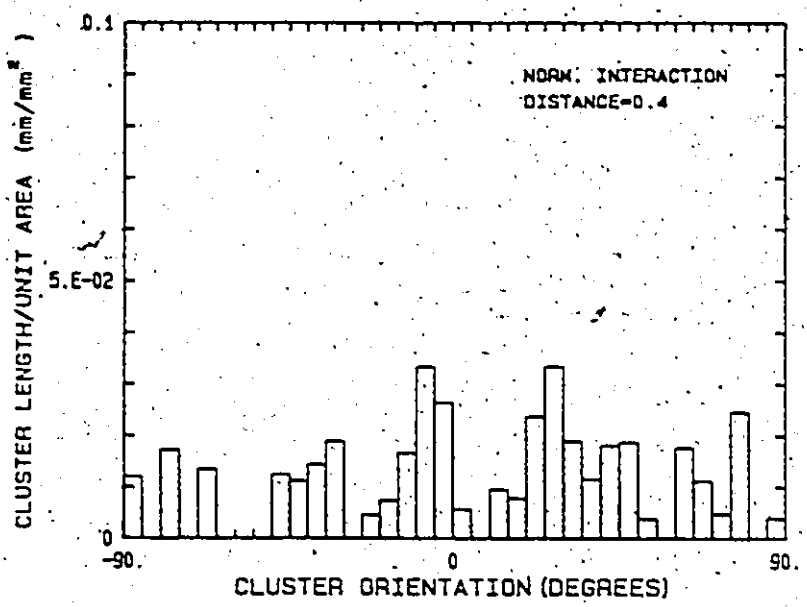

Fig. 4.18: Distribution of total cluster length vs. orientation relative to the rolling plane, for the clustered regions defined in Figure 4.17. The results do not indicate a strong degree of anisotropy in inclusion distribution in the plane normal to the rolling direction.

The results of an inclusion analysis such as that presented here could be useful in correlating crack opening displacement measurements with crack orientation and inclusion distribution in structural steels. This would provide a valuable extension of the work of Luo et. al. (1985) on the events occurring at a crack tip.

4.5.2 Particle Distributions with Higher Volume Fractions

The volume fraction of sulphide inclusions in the HSLA steel was of the order 0.002 to 0.003, so that in the spatial analysis of the distribution of inclusions they could be considered reasonably as a distribution of points. For particle dispersions with higher volume fractions, where the particle size-to-spacing ratio is significant, the tessellation about points located at the centroids of particles would give no consideration to particle size in the construction of the associated cells. One expects in deformation however, that a larger particle would influence a larger region of the matrix surrounding it. It would be useful if the particles defined as near-neighbours of a given particle (i.e., those particles which were used in the construction of the cell sides about that particle) were those which it would interact with in deformation and fracture processes, at least in the approximation that the interaction between any two particles was independent of the others. The complete analysis of particle interactions and the dependence upon particle size and spacing in inelastic deformation processes, however, does not yield analytic expressions. Thus, it is difficult to obtain an exact relationship for the mechanical interaction

between two particles, which could be used in the construction of the cell about a given particle. Note that this approach to delineating cell boundaries can result in a tessellation which is quite different from the Dirichlet tessellation.

A purely geometric approach to the tessellation construction could construct the cell wall between two particles as the locus of points which are equidistant from the particle surfaces. However, the cell wall would then be a portion of a hyperbola, and the computation of the tessellation would involve considerable time. The method employed in this study considered only the geometry of the dispersion in the tessellation construction. The cell boundary between two neighbouring particles was thus defined by the perpendicular bisector of the portion of the line joining the particle centroids which lay between the particle surfaces. Particles were approximated as circles of equivalent area for this construction. Note that the cells formed in this way do not completely fill space, as a given vertex on a cell is not located exactly at the vertices of the cells of the two neighbouring particles associated with that vertex. The construction is an approximate tessellation, unless all of the particles have equal intercepted areas in the metallographic section.

Four microstructures possessing different characteristic second-phase dispersions were analyzed using the above construction. They were:

(a) A 1045 carbon steel, spheroidized (volume fraction of carbides = 0.078).

(b) A nodular cast iron (volume fraction of graphite = 0.031)

(c) A Mn-Sb rod-eutectic, in which the MnSb rods were viewed end-on (volume fraction of MnSb = 0.278)

(d) A Fe-3.5% Ni-1.0% Al-3.4% Ti alloy, in the early stages of precipitation (volume fraction of precipitates = 0.026). The micrograph used was from an extraction replica.

The microstructures and their associated tessellations are given in Figures 4.19 to 4.22.

A clustering criterion used to discern whether two particles interact mechanically during deformation in these larger volume fraction materials must include geometrical factors such as the particle spacing and size. However, the criterion should also consider properties of the matrix, such as diffusion coefficients or the matrix work-hardening rate. The particle centroid spacing alone does not provide sufficient information to serve as an adequate clustering parameter in this application.

Here again we will employ a simple geometrical criterion to define the clustering condition between two particles, suggested by the approximate analysis of Argon and Im (1975) for the interaction between two closely-spaced hard particles in a plastically deforming matrix. We define the clustering parameter as the ratio of the sum of the radii of the two neighbouring particles to the spacing between their

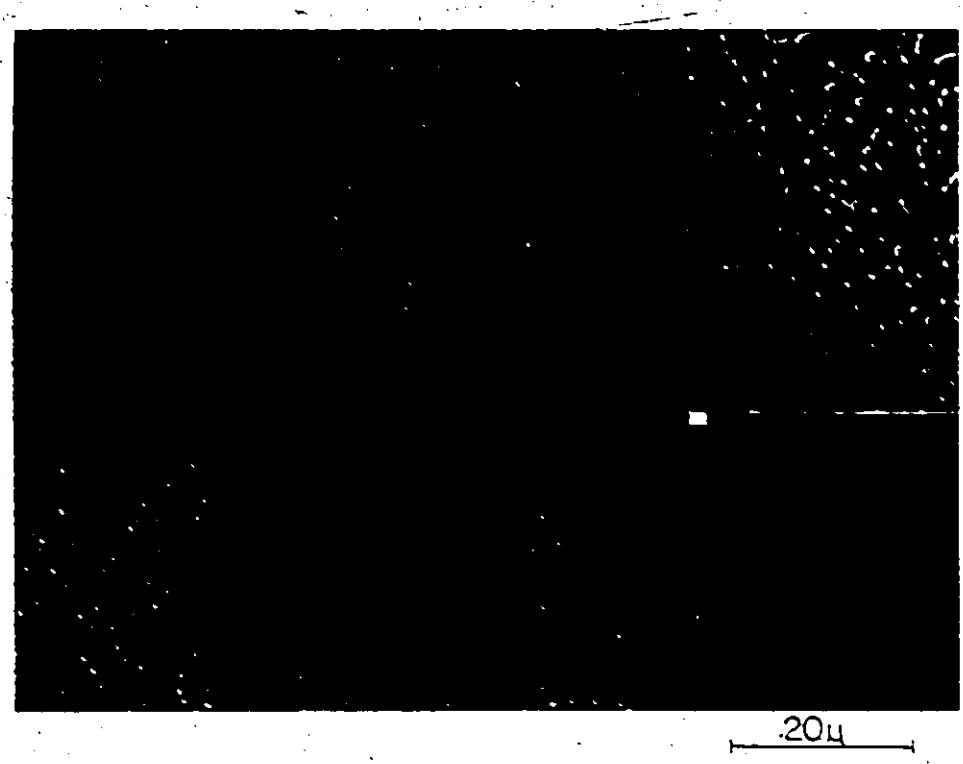

Fig. 4.19a:

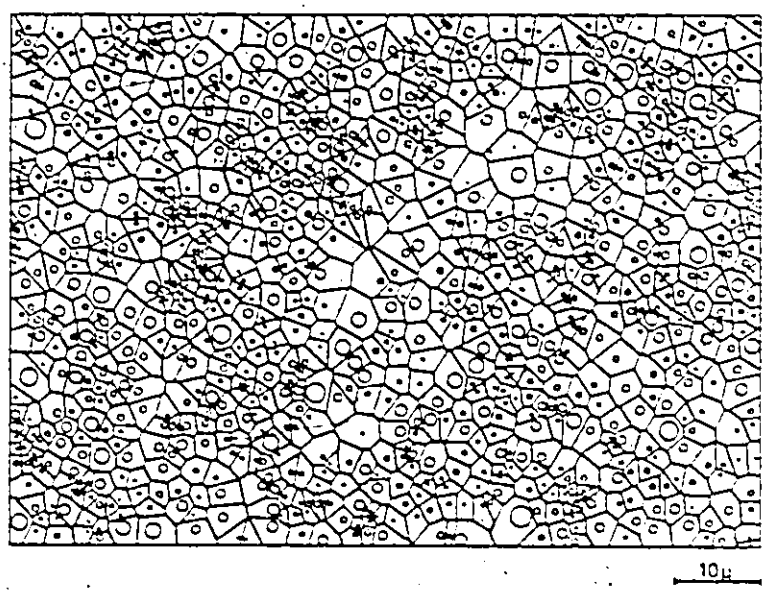

Fig. 4.19b:

Fig. 4.19: SEM micrograph of the carbide distribution in a spheroidized 1045 steel, and the associated tessellation constructed about carbides in a portion of the region.

Fig. 4.20a:

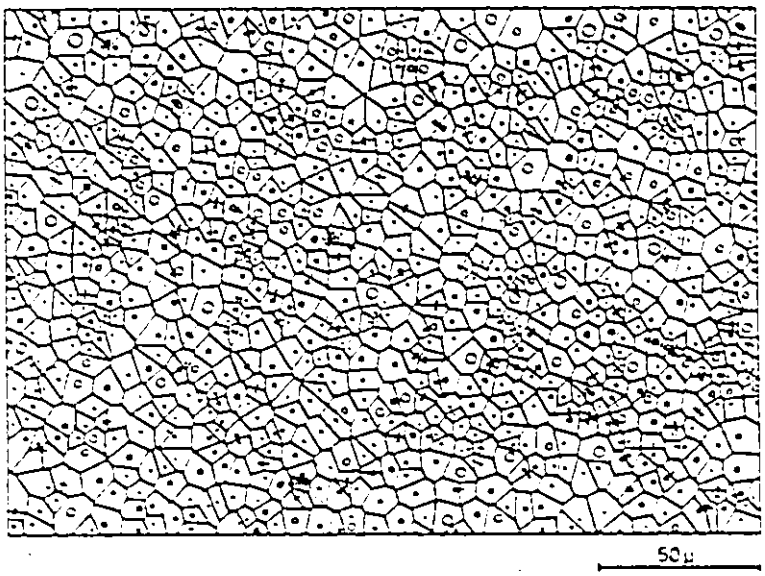

Fig. 4.20b:

Fig. 4.20: Optical micrograph of the distribution of graphite nodules in a nodular cast Iron, and the associated tessellation.

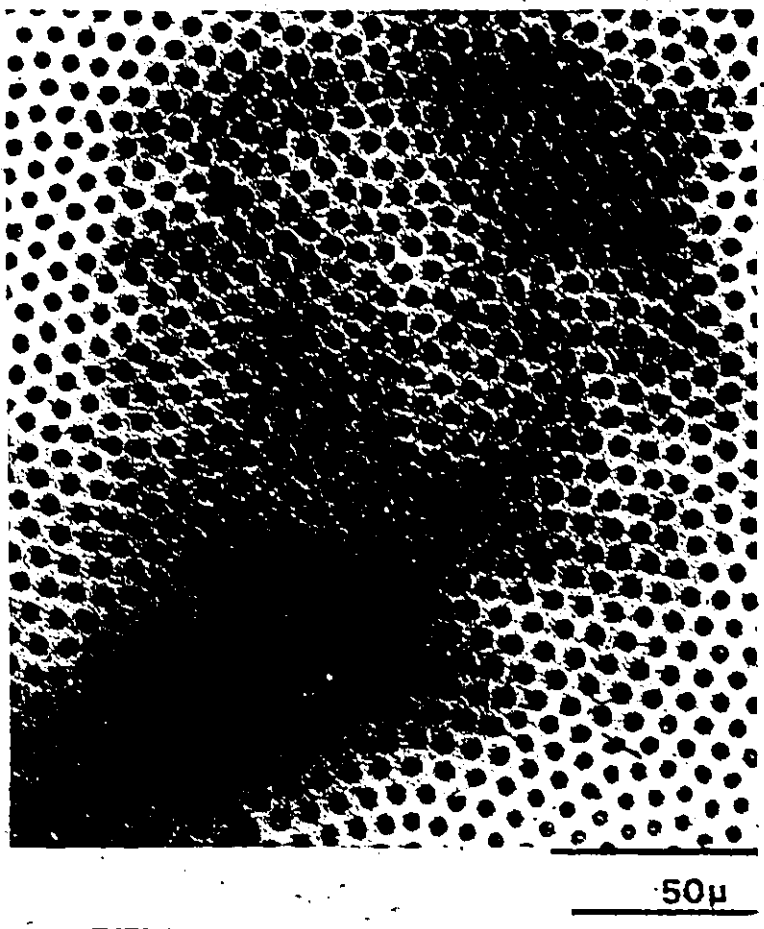

Fig. 4.21a:

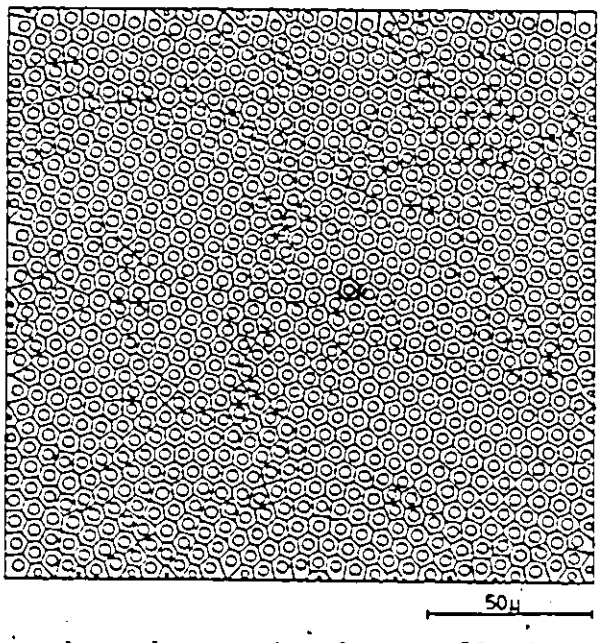

Fig. 4.21b:

Fig. 4.21: Micrograph and associated tessellation for a Mn-Sb rod eutectic microstructure, viewing the rods end-on.

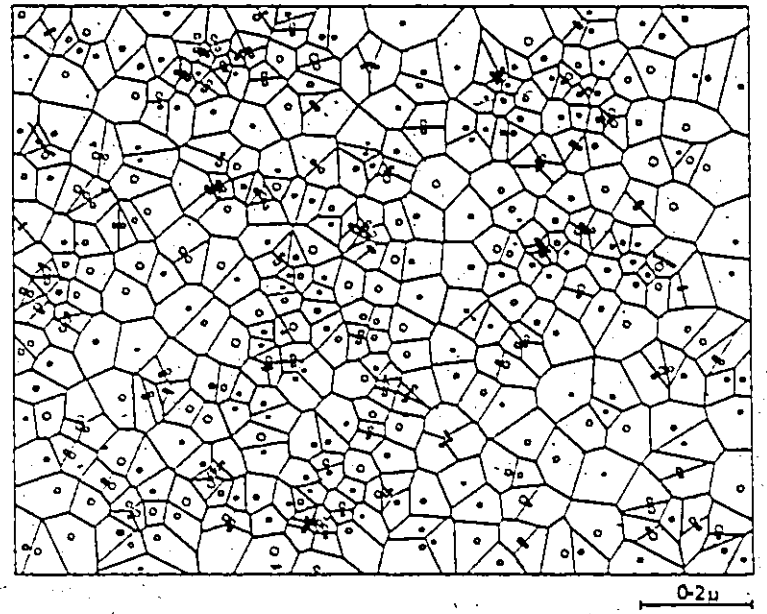

Fig. 4.22: Tessellation constructed about the distribution of precipitates in a Fe-Ni-Al-Ti alloy, in the early stages of precipitation. The particle distribution was obtained from an extraction replica.

centroids. A high value suggests a strong mechanical interaction between the two particles.

The clustering characteristics of the four microstructures were analyzed using this clustering parameter. The results are given in Figure 4.23 as the variation of the fraction of particles which are clustered (i.e., those particles which have at least one near-neighbour for which the radius/spacing ratio is greater than the critical value defining clustering) with the value chosen for the clustering parameter. In determining these curves, the clustering parameter for each microstructure has been normalized by the average radius/spacing ratio so that the results for the individual microstructures may be compared directly.

The curve for the rod eutectic rises steeply near a normalized value of one. This is to be expected for a highly periodic microstructure with little variation in the size of the second phase constituent. The Fe-Ni-Al-Ti alloy, with its clustered particle distribution, results in a curve which is not as steep and extends to much higher values of the clustering parameter. These two materials represent extremes in the character of particle dispersions. The behaviour of the 1045 carbon steel and the nodular cast iron lay in between these extremes. Spitzig et. al. (1985) have concluded that the distribution of carbides in carbon steels is close to random. Whether or not the distribution of graphite nodules could be accepted as random by the same analysis was not determined, but the curves of Figure 4.23 suggest a difference between the cast iron and 1045 steel. The 1045 steel appears to have a larger fraction of particles which are strongly clustered.

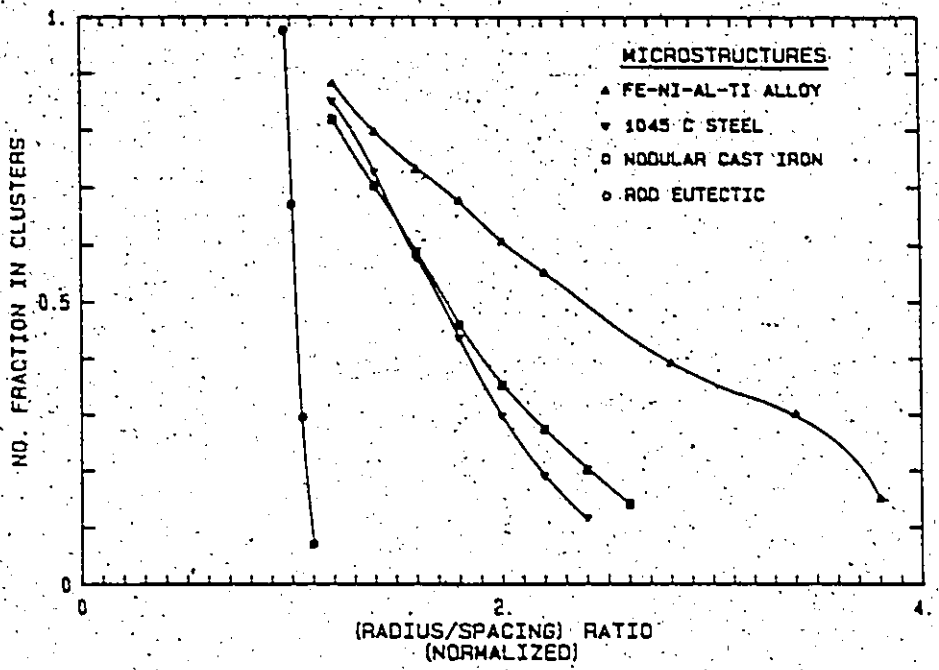

Fig. 4.23: Results of particle clustering analyses for the four microstructures, given as the number fraction of particles which are clustered with at least one other particle, at a given particle radius/spacing ratio. This parameter has been normalized by the average value, for each microstructure.

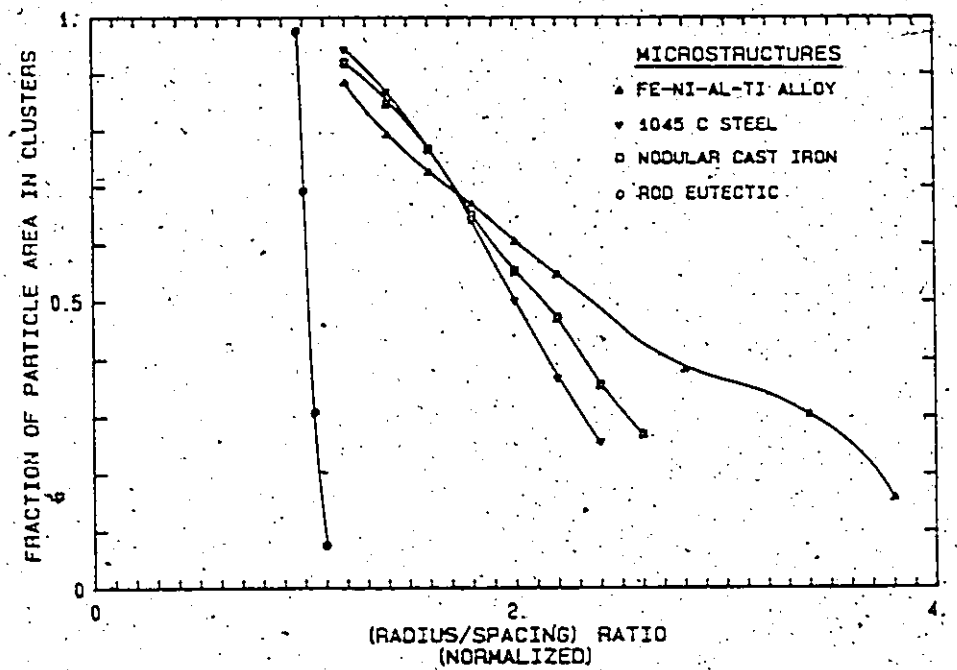

Fig. 4.24: Results of the particle clustering analyses given in Figure 4.23, however, here the result is given as the fraction of the total particle area in the field associated with particles which are clustered.

If we plot the fraction of the total particle area associated with clustered particles, instead of the number fraction, the curves in Figure 4.24 are obtained. It is seen that the curves for the nodular cast iron and 1045 steel remain unchanged relative to each other, but are moved upward. This indicates that it is the larger particles in these two microstructures which are clustered. In the carbon steel, the coarsening process has thus not produced the expected distribution of isolated large carbides.

4.6 Conclusions

The Dirichlet tessellation has been shown to be a useful method in the characterization of spatial distributions of particles in plane sections. In addition to providing near-neighbour distances, the characteristics of the cells in the tessellation may be analyzed to provide information on the local surroundings of the particles in a dispersion. These results in turn can be used to indicate differences between dispersions with respect to both periodicity and clustering. The tessellation procedure may be altered to include an effect of particle size in determining the boundaries of cells, so that the spatial analysis of dispersions with large volume fractions of a second phase may be accomplished.

The criterion for discerning whether two particles interact mechanically, and are thus clustered in a mechanical sense, should consider the size and spacing of the particles, as well as the properties

of the matrix. However, it has been illustrated here that simple geometrical clustering parameters can give useful descriptions of particle dispersions.

A basis for analyzing the spatial distribution of clusters has been outlined in this chapter. The output from the tessellation computations provides for an efficient method of grouping particles in individual clusters according to the clustering criterion chosen. These regions of clustering can be identified, and their use in analyzing for anisotropy in the distribution was demonstrated. The approach to the analysis of spatial relationships between clustered regions, however, requires further work, and the development of additional software.

If one considers the fracture behaviour of materials in which damage is associated with inclusions or other second-phase particles, the extremes in the behaviour of the dispersion can influence the overall fracture properties. However, to characterize these extremes, a large base of microstructural data is required, and the analysis of this data requires techniques which can be implemented on a computer. The tessellation and clustering procedures outlined in this chapter are examples of such methods which can be used in analyzing dispersions, allowing further improvements in the prediction of fracture properties to be made.

CHAPTER 5

THE EFFECTS OF MICROSTRUCTURE AND INCLUSIONS ON THE FRACTURE OF CONTINUOUSLY-CAST HSLA STEELS

5.1 Introduction

Continuously-cast HSLA steels often display marked variations in local microstructure, which result from their complex processing history. Variations in grain size, distribution and nature of non-ferritic transformation products, and in the inclusion distribution are often observed. Extremes in the distribution of microstructural features can significantly alter the local operative states of stress and the allowable strain levels. If they are controlled by a local criterion or event rather than a global one, then the initiation of flow localization or final fracture may be promoted at lower macroscopic levels of stress and/or strain in heterogeneous microstructures than would be expected for a more homogeneous structure.

Thus, HSLA steels offer a microstructure in which the effects of inhomogeneity may dominate both the macroscopic fracture condition and the resulting fracture mode. The dimensions and distribution of microstructural features affect the development of damage and can thus alter the competition between these damage processes in attaining a critical condition for fracture. The influence of variations in applied stress state on the development of damage (for example, through tests done

under an applied hydrostatic pressure) could be used to provide information on the critical local conditions involved in various damage processes, and on the criterion for fracture associated with the dominant damage process. Local states of stress and strain could also be altered by increasing the flow stress of the ferrite in deformation at low temperatures. Data for the increase in flow stress with decreasing temperature in bainite (Kotilainen, 1980a; Kotilainen et. al., 1982) suggest that the temperature variation of the flow stress of ferrite is stronger than that of the non-ferritic transformation products. This effect would also contribute to variations in local stress and strain conditions produced by temperature changes.

The result of the casting and rolling operations is to produce inhomogeneity in both the nature of microstructural features and their spatial distributions. The non-ferritic components are often banded, and clusters of inclusions become elongated in the rolling direction. The influence of the orientation of the applied principal stress axes relative to these oriented microstructural features would yield useful information for the prediction of fracture behaviour under complex stress states.

In this chapter the influence of microstructure on damage accumulation and fracture behaviour was investigated in several continuously-cast hot-rolled HSLA steels. Tests were conducted on tensile samples at low temperatures, under superimposed hydrostatic pressures, and on samples taken from various orientations in the rolled plate.

5.2 Materials

In this investigation, four different heats of continuously-cast HSLA steels were considered. Their chemical compositions are given in Table 5.1. Note that subsequent figures and micrographs will refer to these materials by their heat number. However, for convenience, in the text we will refer to these materials by a letter designation. The four heat numbers and their corresponding letter designations are given below:

HEAT NUMBER	STEEL
NJ1239	A
NJ4034	B
G1338	C
14867	D

The low sulphur levels in these steels indicate that, on average, they should contain low sulphide volume fractions. Two of the steels, C and D, were calcium-treated. The thermo-mechanical histories of all the steels were very similar, with the final rolling pass above the Ar_3 temperature in the austenite region. However, the final plate thickness of the calcium-treated steels was 0.404 in., while for the untreated steels A and B, reduction was only to 0.539 in. The subsequent cooling rates after the final rolling pass were not available for comparison.

The microstructures of the four steels near the plate centre-line are given in Figures 5.1a-d. They are essentially ferrite-pearlite steels, but they differ in the amount and type of non-ferritic transformation products present. Steels G1338 and 14867 are seen to have a

TABLE 5.1

CHEMICAL ANALYSES OF THE HSLA STEELS STUDIED
(in wt %)

HEAT NO.	C	Mn	P	S	Si	V	Cb	Cu	Ni	O_2* (ppm)	Ca	ASA ACID SOLUBLE ALUMINUM
NJ1239 (steel A)	0.087	1.57	0.018	0.004	0.28	0.064	0.030	---	---	21/22	---	0.024
NJ4034 (steel B)	0.079	1.62	0.014	0.002	0.26	0.063	0.024	---	---	12/18	---	0.027
G1338 (steel C)	0.093	1.62	0.020	0.002	0.25	0.064	0.034	---	---	34/21	0.030	0.023
14867 (steel D)	0.091	1.43	0.009	0.001	0.31	0.044	0.024	0.17	0.15	49/28	0.022	0.037

* The results of two separate analyses are given

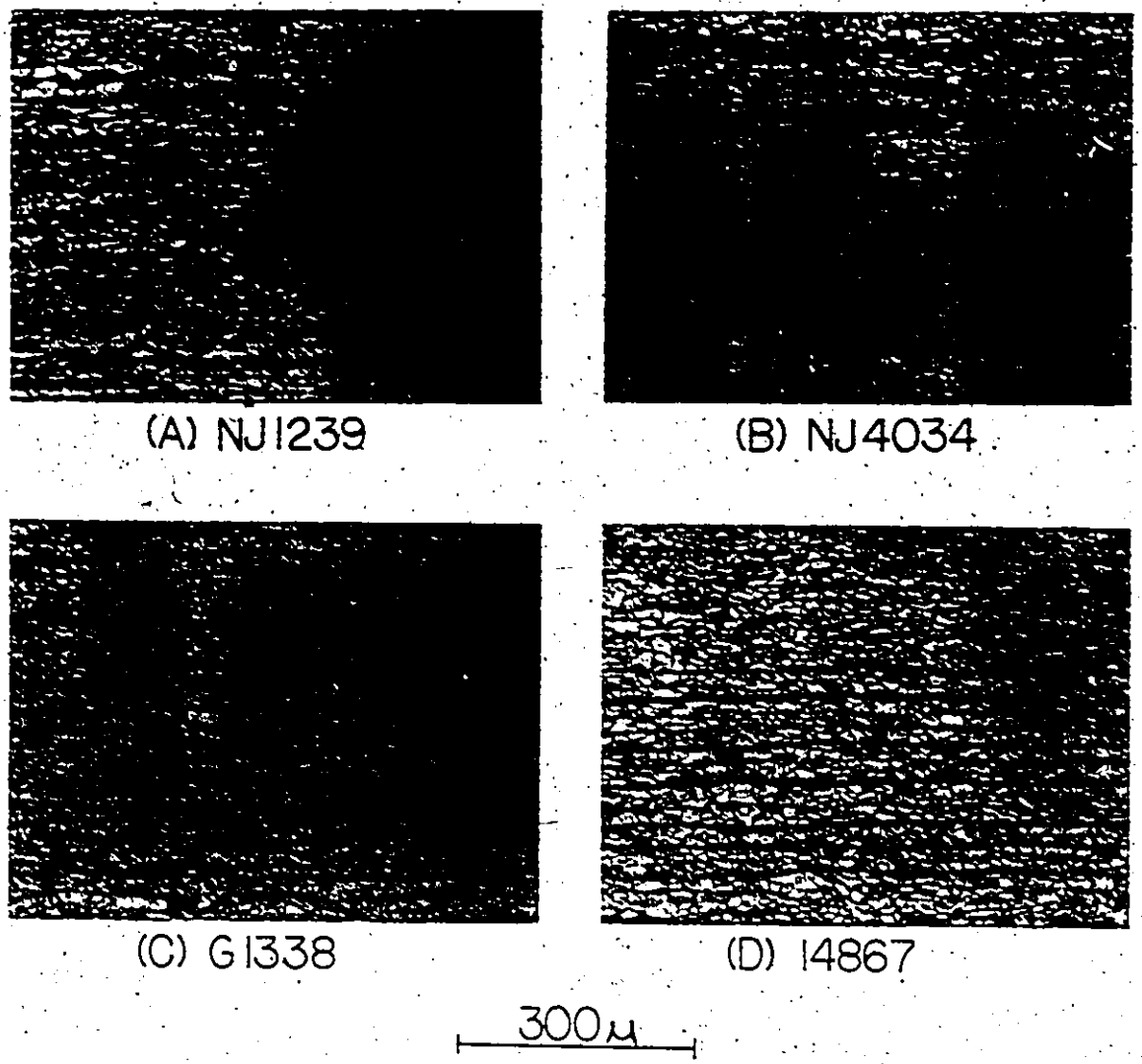

Fig. 5.1: Microstructures of hot-rolled HSLA steels in the centre-line region of the plate. They have essentially banded ferrite-pearlite microstructures, with other transformation products present. (a) steel A, (b) steel B, (c) steel C, (d) steel D.

finer and more continuous degree of banding, however, whether this was due to a difference in the thermo-mechanical history or due to differences in cooling rate after rolling is not known. In addition, the continuity of banding in steel A was significantly less than that in steel B.

Figures 5.2a-c clearly illustrate the higher levels of bainite and/or martensite-austenite phase present in steels A and B, which occurred predominantly along the centre-line region of the plate. Although in the present work the microstructural component in Figure 5.2a will be referred to as bainite, no transmission electron microscopy was done to determine whether any martensite was present in this phase.

In general, steel A was observed to have the highest level of bainite along the centre line. Bainite was present in steels C and D however, but with much lower volume fraction than in the other two steels. It should be noted that the presence of bainite along the centre-line was not continuous and the level of bainite varied considerably between different samples taken from the same plate. Figures 5.2a-c also indicate the non-uniformity in ferrite grain size in steels A and B, which was most prominant along the centre-line.

The results of inclusion analyses on the steels are given in Table 5.2, where they are presented as the total projected lengths in the rolling direction. The calcium-treated steels do not have any sulphide content indicated due to the use of an oxalic acid etch to darken the sulphides. Manganese sulphides are much darker than oxides after etching with oxalic acid, however, calcium sulphides do not darken. The automatic image analyzer would include these in the oxide

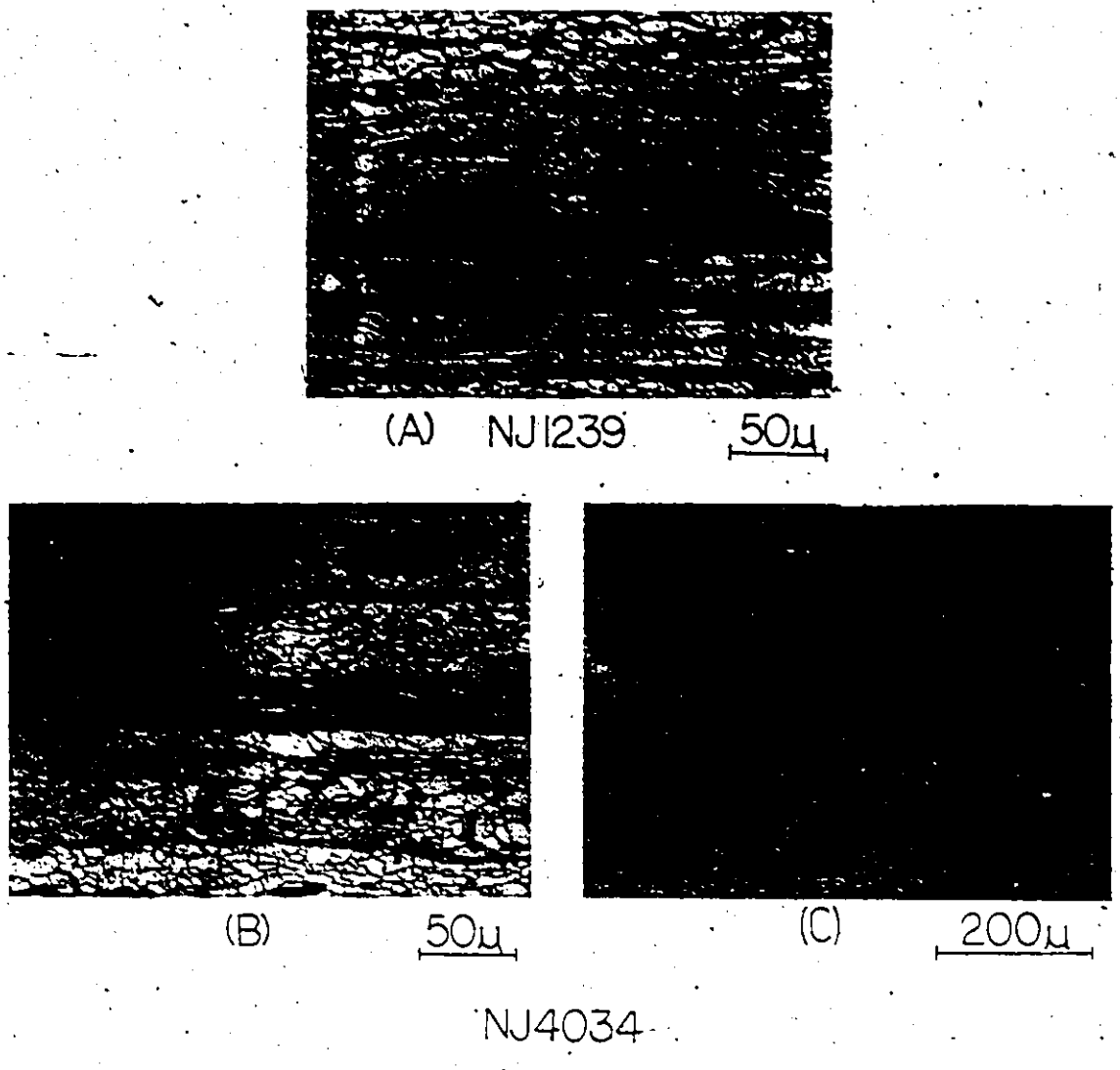

Fig. 5.2: Microstructures of steels A (Figure a) and B (Figures b,c) at the plate centre line. The inhomogeneity in ferrite grain size is illustrated, along with the presence of brittle transformation products containing bainite and/or martensite.

TABLE 5.2

LENGTH OF INCLUSIONS PARALLEL TO ROLLING DIRECTION

(mm/mm^2)

HEAT NO.	SULPHIDES	OXIDES	TOTAL
NJ1239 (steel A)	0.2369	0.1832	0.4201
NJ4034 (steel B)	0.1096	0.1100	0.2196
G1338 (steel C)	0	0.2424	0.2502
14867 (steel D)	0	0.2111	0.2158

Note that the sulphide population was determined through an oxalic acid etch, which does not darken calcium sulphide. Also note that these inclusion analyses were performed at the centre region of the plate.

grey level range. In the calcium-treated steels the sulphur was often associated with calcium aluminate inclusions, however, a duplex structure with the sulphide on the periphery of a calcium aluminate was not observed (Wilson, 1984).

Examples of some of the inclusions observed are shown in Figures 5.3a-e. In general, all the steels possessed elongated silicate inclusions, however, they occurred in a relatively low volume fraction. The non-treated steels, A and B, contained primarily elongated manganese sulphides (Figure 5.3a) and alumina inclusions (Figures 5.3b,c). Figure 5.3b indicates an elongated silicate trailing from the alumina inclusion. The longest sulphide inclusions, up to approximately 100 μ long, were usually associated with the bainitic phase present along the plate centre-line, as seen in Figure 5.3a. The sulphide content in the centre-line region was significantly higher than in the rest of the plate in the non-treated steels.

The calcium-treated steels contained calcium aluminate inclusions, seen in Figures 5.3d and e. EDAX analysis often indicated these to contain sulphur. These equiaxed inclusions were observed (in cross-sections) up to approximately 8 μ in diameter. Their distribution throughout the plate thickness was much more uniform than the distribution of sulphides in the non-treated steels.

To summarize, there are several distinct differences between the steels which have been calcium-treated, and those which have not. The effect of center-line segregation in the continuous-casting process is more evident in the microstructures of the non-treated steels, altering

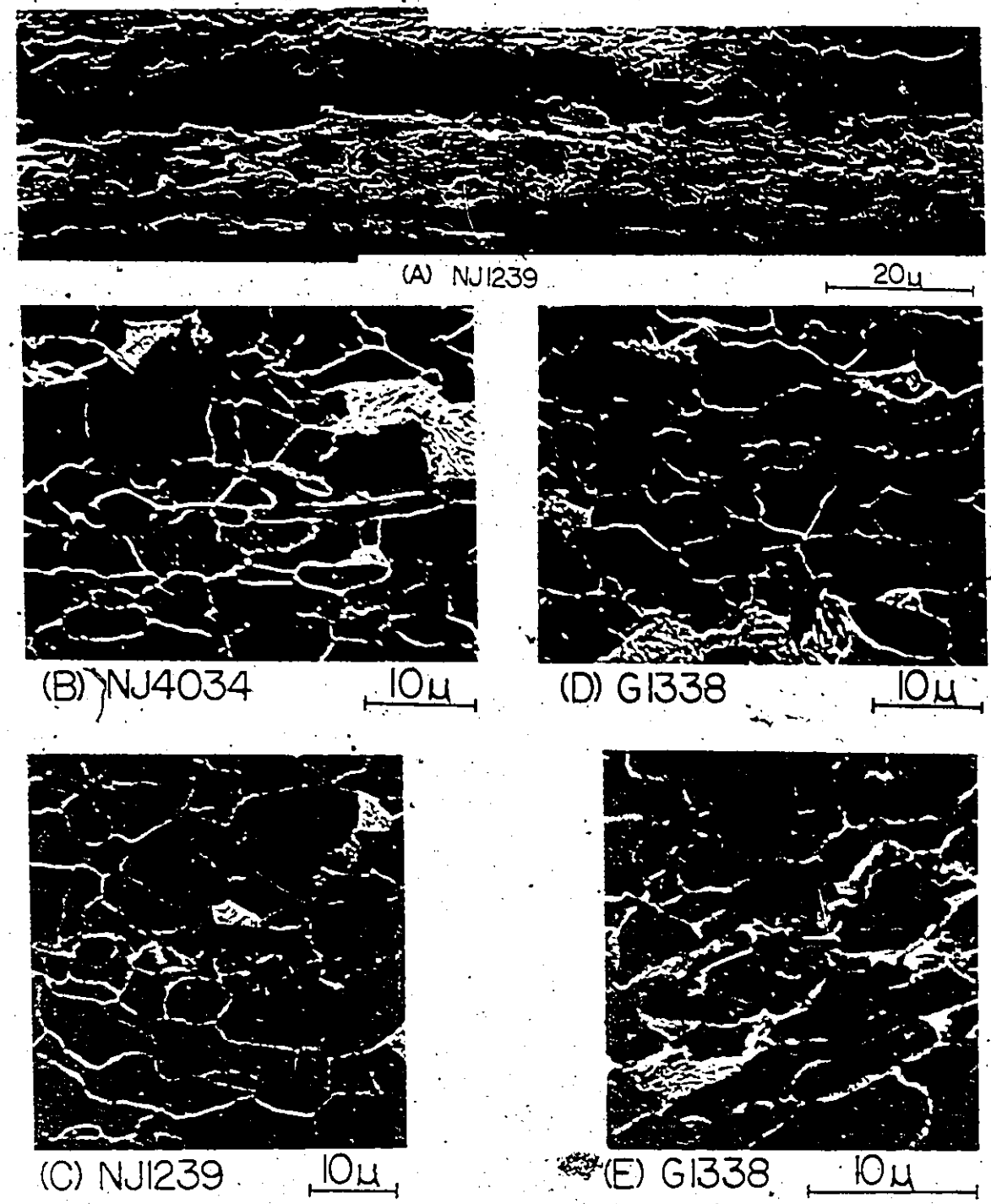

Fig. 5.3: Inclusions observed in the steels. (a) Elongated manganese sulphides associated with centre-line transformation products in steel A. (b) Elongated silicate trailing from alumina inclusion in steel B. (c) Alumina inclusions in steels A. (d and e) Calcium aluminate inclusions in steel C, which an EDAX analysis indicated to contain sulphur.

the transformation products so that significant amounts of bainitic or martensitic constituents are present along the centre of the plate. This is most prominent in steel A. Also, with no calcium additions to promote the formation of sulphides earlier in the solidification process, this has resulted in very large elongated sulphides, predominantly along the centre-line region. The nature of the banded non-ferritic components was observed to be more coarse and irregular, and the ferrite grain size more non-uniform in the untreated steels.

These hot-rolled microstructures were heat-treated for some of the low temperature tests to modify the non-ferritic phases, to produce a spheroidized structure. This was achieved by austenitizing for one hour at 900°C in vacuum, oil quenching, and then spheroidizing the samples for 70 hours at 675°C. The distribution of carbides, however, retained the banded character of the non-ferritic components of the hot-rolled structure.

5.3 Experimental Procedure

Tensile testing was performed on axisymmetric tensile samples which, except for the through-thickness samples, were 5 mm in diameter with a 25 mm gauge length. These specimens, taken in the rolling direction and transverse to the rolling direction, were machined from the centre of the plate so that the axis of the tensile samples was along the plate centre-line. The through-thickness samples were fabricated by friction welding end pieces onto a $\frac{1}{2}$-inch diameter stud machined from the plate. A reduced section 0.375 inch in diameter was machined down

between the weld lines, as indicated in Figure 5.4, to produce a final gauge length of approximately 0.3 inches for steels C and D, and approximately 0.4 inches for steels A and B. Scanning electron and optical microscopy observations revealed no microstructural changes a very small distance away from the weld line, so that the as-received microstructure was not altered in the centre-line region, where fracture occurred.

Tensile testing at ambient pressure was conducted on a screw-driven Instron testing machine, with an initial strain rate of 0.02 sec^{-1}. Tests under superimposed pressures of 690 MPa and 1100 MPa were carried out in a Harwood hydrostatic pressure unit, at the same strain rate. This pressure unit was described by Teirlinck (1983).

Low temperature tensile tests were conducted at -196°C in a liquid nitrogen bath, again with an initial strain rate of 0.02 sec^{-1}. The sample was immersed in the bath for 10 minutes prior to the test start, to ensure that its temperature had equilibrated to that of the liquid nitrogen.

Due to the marked anisotropy in deformation behaviour between orientations lying in and out of the rolling plane, an elliptical cross-section developed. This was observed even prior tc the initiation of necking, and prevented the evaluation of true stress-strain behaviour at large strains through photographs of the necked region of the tensile samples.

Compression testing was performed on cylindrical samples, with the compression axis along the plate rolling direction. The test samples had an initial height-to-diameter ratio of 1.5. The loading

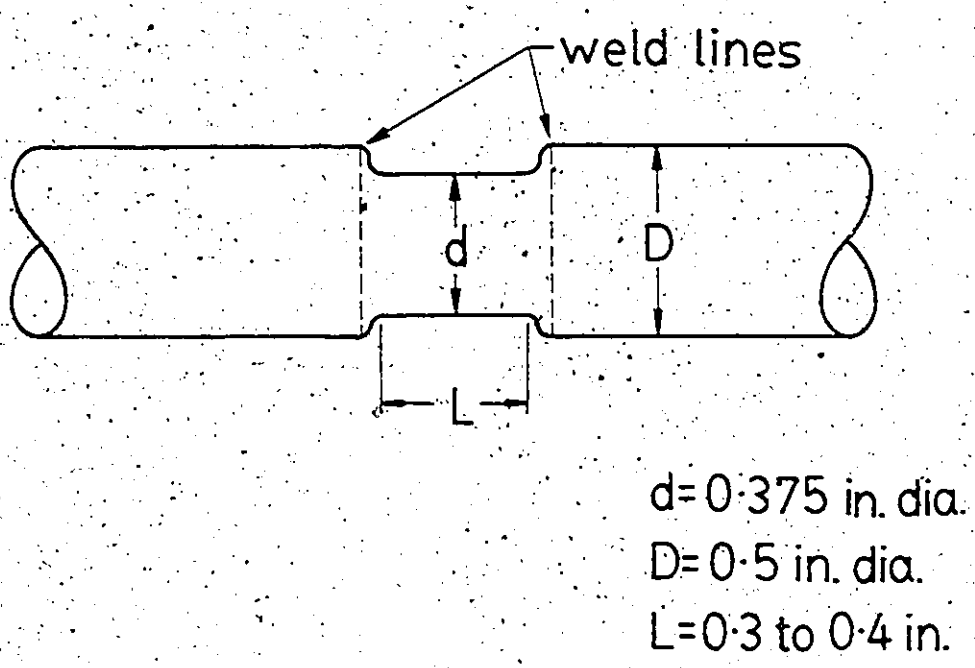

Fig. 5.4: Geometry and dimensions of through-thickness samples.

rate during testing was selected so that the strain rate was similar to that used in the tensile tests. Teflon tape was used to minimize friction effects at the sample ends, and the Teflon was replaced at 10% strain intervals to maintain low friction levels.

Metallographic examination was performed on sections taken along the tensile or compression axes, on a plane which passed through the minor axis of the elliptical cross-section in the tensile samples, and through the major axis in the compression samples. This section plane is a plane of symmetry, so that the shear strain in a plane perpendicular to the section plane is zero. The samples were ground down close to the mid-plane on 220 grit silicon carbide grinding paper using light hand pressure, to minimize sub-surface deformation introduced through grinding. Subsequent grinding steps to 1200 grit and diamond polishing resulted in the section plane lying along the central axis of the specimen. The etchant used was 2% nital.

5.4 Experimental Results

5.4.1 The Influence of Microstructural Anisotropy

The effects of directionality in the microstructure of the rolled plate on the room temperature mechanical properties were investigated in tensile tests on specimens taken from three perpendicular orientations in the plate: in the rolling direction, transverse to the rolling direction, and in the through-thickness direction.

5.4.1.1 Mechanical Properties

The mechanical properties obtained from the tensile tests and the macroscopic fracture strains are summarized in Table 5.3.

The yield stress in the transverse orientation was less than that in the rolling direction in all four steels, by approximately 1 to 2%. Although this difference was small, it was a consistent observation. The yield stress was a maximum in the through-thickness orientation, however, this result could be affected by a degree of plastic constraint, due to the gauge length being approximately equal to the diameter of the reduced section.

The anisotropy in deformation behaviour resulted in an approximately elliptical cross-section, with the strain in the cross-section of the tensile sample a maximum in the direction normal to the plate rolling plane and a minimum in the direction in the rolling plane. This maximum strain is denoted by $\varepsilon_{\perp}$ and the minimum strain by ε_{11} in Table 5.3. In all of the steels the reduction in area (RA) was a maximum when tested in the rolling direction and a minimum in the through-thickness orientation. However, the relative decrease in ductility for orientations away from the rolling direction was considerably greater for steels A and B which were not calcium-treated.

Although there was an observed effect of orientation on ductility in the calcium-treated steels C and D, no significant effect on the fracture stress was measured. The non-calcium treated steels, however, showed a marked dependence of fracture stress on orientation, most notably in the through-thickness direction.

TABLE 5.3

MECHANICAL PROPERTIES OF STEELS TESTED AT AMBIENT PRESSURE AND TEMPERATURE

STEEL	ORIENTATION*	LOWER YIELD STRESS (MPa)	FRACTURE STRESS (MPa)	FRACTION REDUCTION IN AREA	$\varepsilon_{\perp}$	ε_{11}
A (NJ1239)	1	470	1350	0.715	0.88	0.37
A	2	465	1150	0.658	0.68	0.38
A	3	507	754	0.288	--	--
A	4	573	---	---	--	--
B (NJ4034)	1	483	1460	0.734	0.94	0.33
B	2	476	1060	0.644	0.47	0.29
B	3	522	897	0.411	--	-
C (G1338)	1	461	1330	0.700	0.76	0.42
C	2	455	1210	0.675	0.64	0.45
C	3	565	1270	0.513	--	--
D (14867)	1	509	1390	0.721	0.83	0.45
D	2	491	1320	0.698	0.69	0.46
D	3	571	1360	0.547	--	--

* 1 - tensile axis oriented in the rolling direction.
2 - tensile axis oriented transverse to the rolling direction.
3 - tensile axis oriented in the plate through-thickness direction.
4 - compression axis oriented in the rolling direction.

5.4.1.2 Metallographic and Fractographic Observations

At ambient temperature and pressure, all steels displayed a ductile fracture mode, as seen in the fracture surfaces in Figure 5.5. In these one can distinguish macroscopic lines or bands of damage running across the fracture surface in the region corresponding to the centre-line of the plate. More detailed observations indicate a degree of splitting in steels A and B, seen in Figure 5.6. This splitting tendency was not as strong in the calcium-treated steels, whose fracture surfaces were marked with many large voids associated with calcium aluminate/sulphide inclusions, evidenced in Figure 5.7. Final fracture on the outer shear region of the fracture surface was associated with the development of small voids, as seen in Figure 5.8.

Metallographic examination revealed that the dominant source of damage was initiated through the fracture of the banded non-ferritic transformation products, illustrated in Figures 5.9a-c. Note that all metallographic sections are in a plane normal to the rolling plane. Although there was occasional evidence that fracture in the non-ferritic components was initiated at inclusions present within these phases, for samples tested in the rolling direction inclusions were not predominantly associated with these local fracture events. Thus, for this orientation the low inclusion content led to the non-ferritic transformation phases acting as the dominant component controlling damage, most significantly the bainite but also, to a lesser extent, pearlite. Damage was observed predominantly along the central axis of test specimens where the volume fraction of bainite and/or pearlite was greatest.

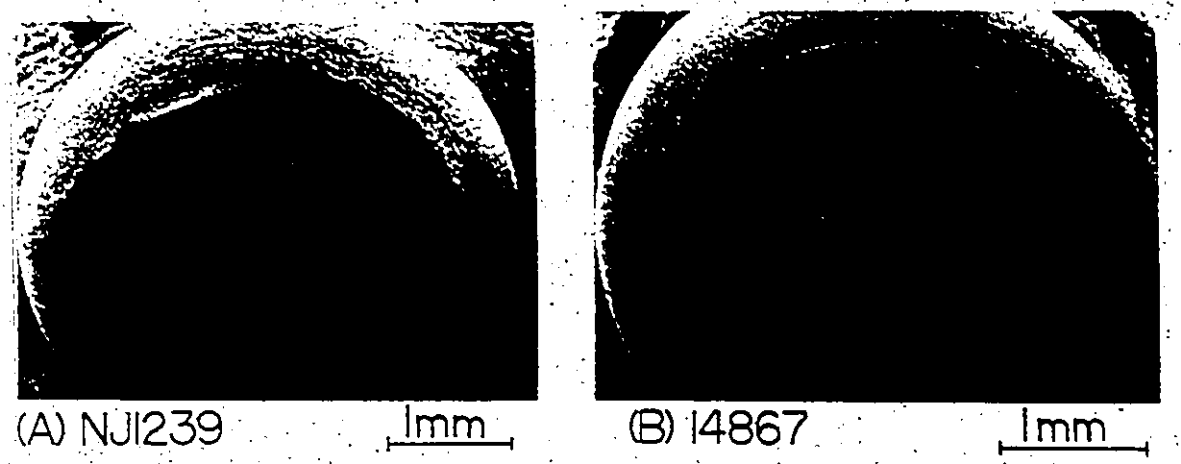

Fig. 5.5: Macroscopic fracture surface appearance of steel A (Figure a) and steel D (Figure b), tested at ambient temperature and pressure, in the rolling direction. Note bands of damage across the fracture surfaces.

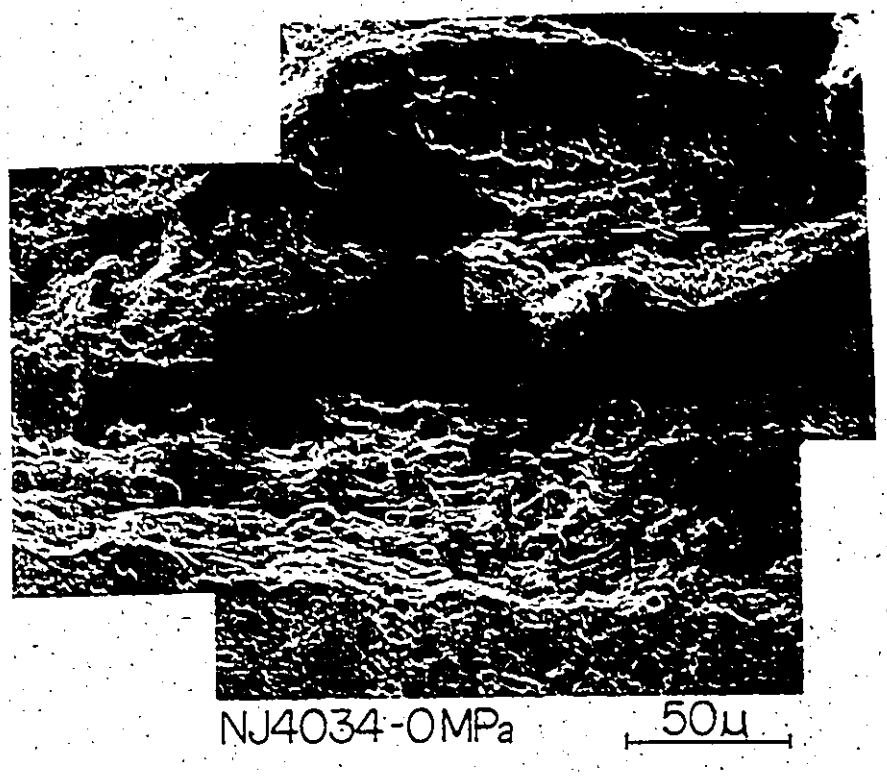

Fig. 5.6: Splitting observed on fracture surface of steel B tested at ambient temperature and pressure, in the rolling direction. Photograph was taken at the centre of the sample, corresponding to the plate centre line.

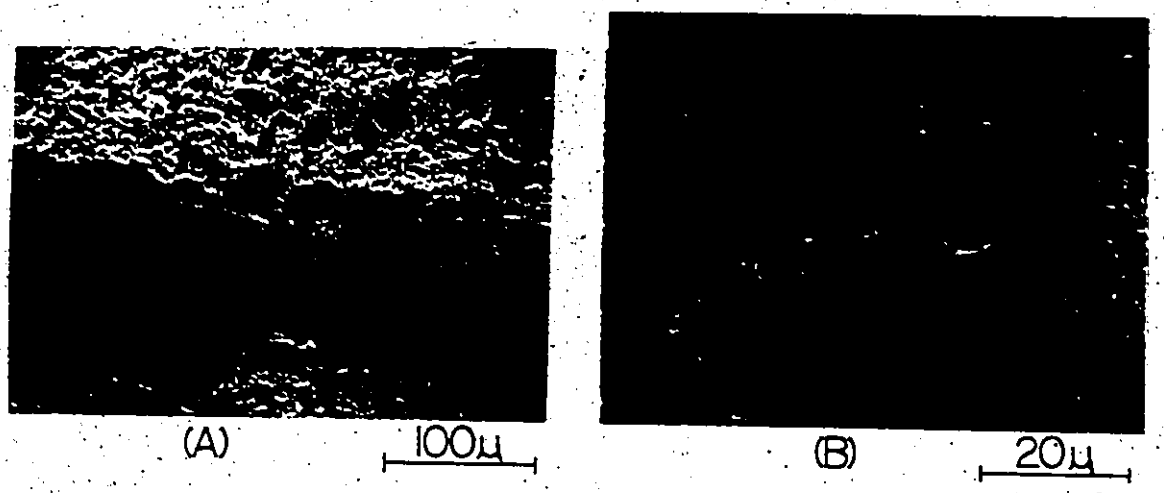

Fig. 5.7: Fracture surface of steel C, tested at ambient temperature and pressure, illustrating a bimodal dimple size. Figure b shows the large voids to be associated with calcium aluminate/sulphide inclusions.

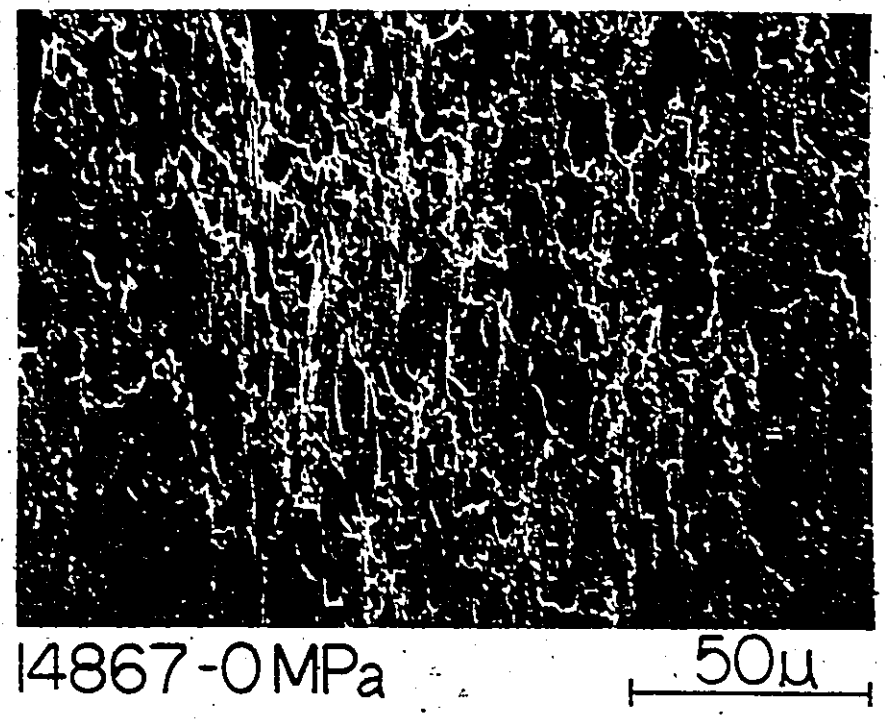

Fig. 5.8: Void-sheeting mechanism involved in the outer shear portion of the fracture surface in steel D. Test at ambient temperature and pressure, in rolling direction.

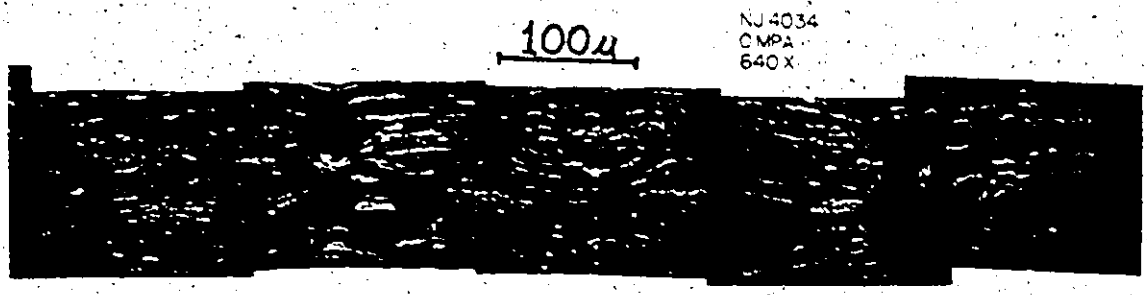

Fig. 5.9a: Steel B

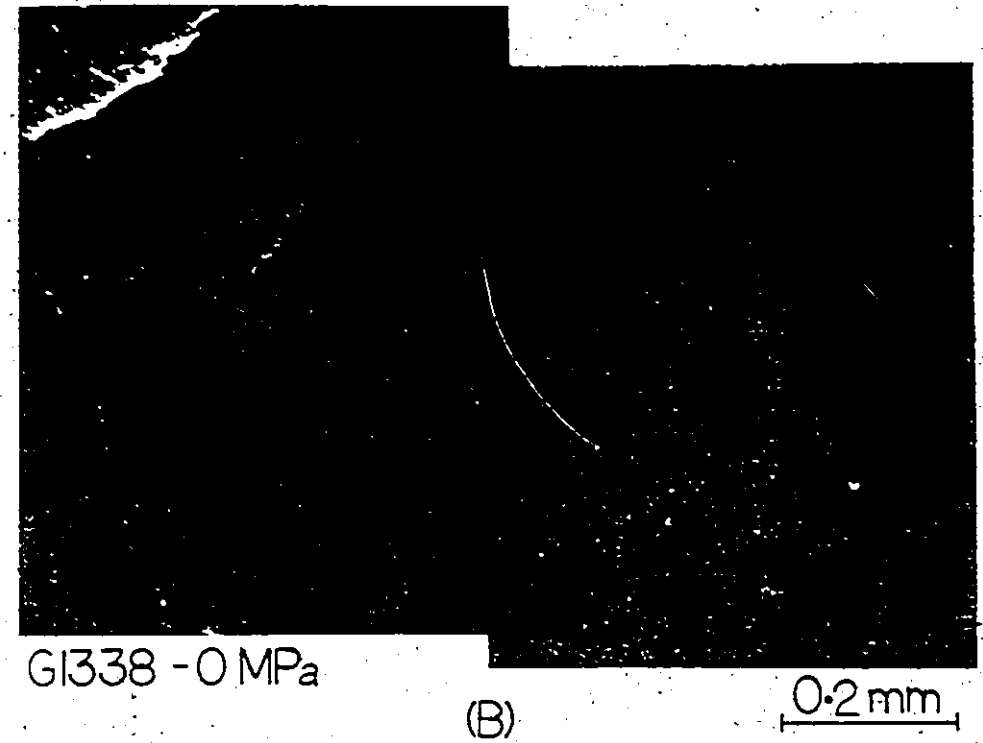

Fig. 5.9b: Steel C

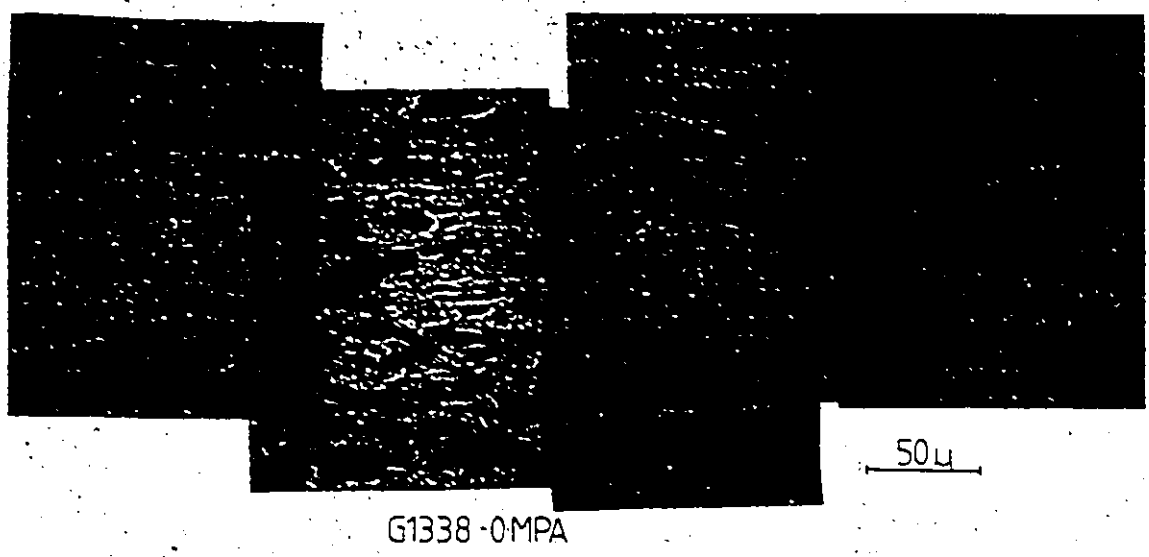

Fig. 5.9c: Steel C

Fig. 5.9: SEM micrographs of samples tested at ambient temperature and pressure, in rolling direction. The dominant source of damage was the banded non-ferritic transformation products, which was most evident in the region corresponding to the plate centre line.

The extent of the damaged region was noted back from the fracture surface to approximately the periphery of the necked region. Although the distribution of voids along the non-ferritic bands was not ideally regular, a degree of regularity in the spacing between local fractures was often observed, as seen in Figure 5.10. This was most frequently observed in bainite when the thickness and morphology of the band was uniform. Irregular void spacing was usually associated with non-uniformity of the banded phase, or could have been due to the presence of inclusions. This observation of a regular distribution of damage along the "harder" bainite or pearlite bands suggests a composite mode of loading with a characteristic transfer length in the bainite, equal to the void spacing.

Fracture surface observations suggested that these large voids were elongated in the direction normal to the tensile axis. Their coalescence resulted in the lines of ridges which developed on the fracture surface, seen in cross-section in Figure 5.11. The void linkage process in the central region of the sample did not necessarily occur through the accumulation of significant damage levels in the shear zones between voids, as seen in Figure 5.12, and on the fracture surface in Figure 5.13. The orientations of these sheared zones made an angle of 37° ± 2° with the tensile axis.

In steels A and B, the fracture stress and reduction in area obtained in tests in the transverse orientation were lower than in the rolling direction. Fracture surface observations indicated elongated MnS inclusions normal to the tensile axis which were associated with large voids and splitting features along the centre of the samples.

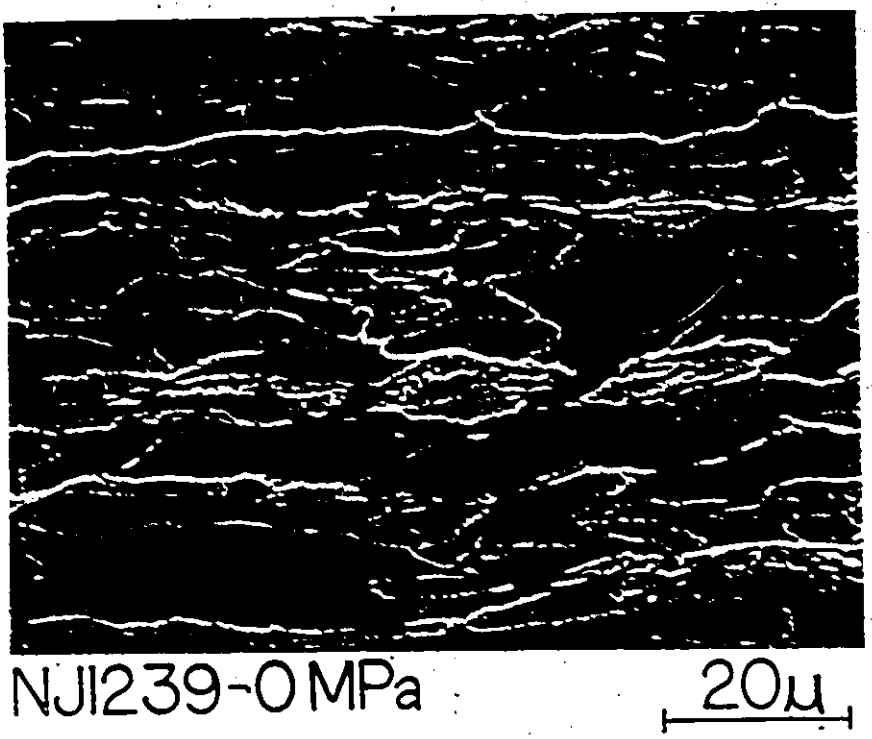

Fig. 5.10: SEM micrograph of steel A, tested at ambient temperature and pressure, in rolling direction. Where the bainite morphology was uniform, a regular spacing between fracture sites was observed.

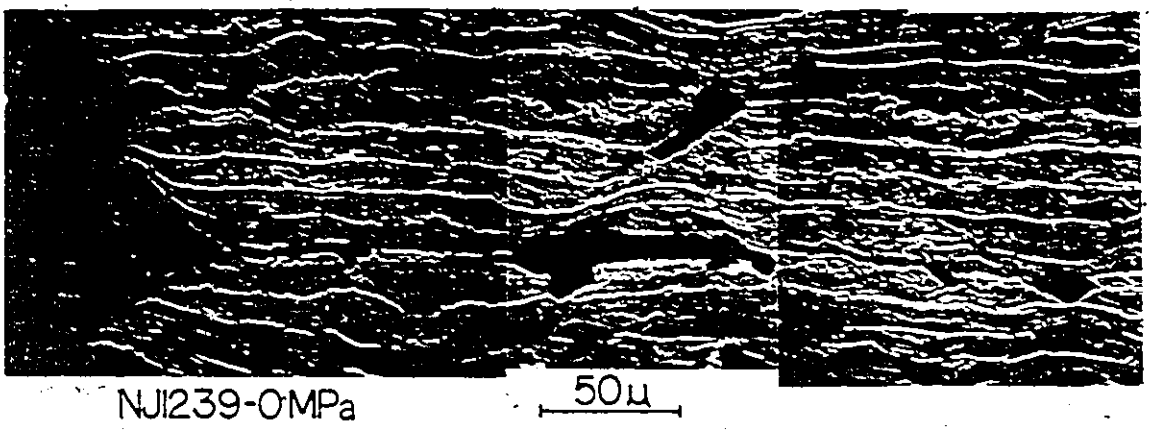

Fig. 5.11: SEM micrograph of steel A, tested at ambient temperature and pressure. The linkage of voids initiated at the banded transformation products produces ridges across the fracture surface, illustrated here in cross-section.

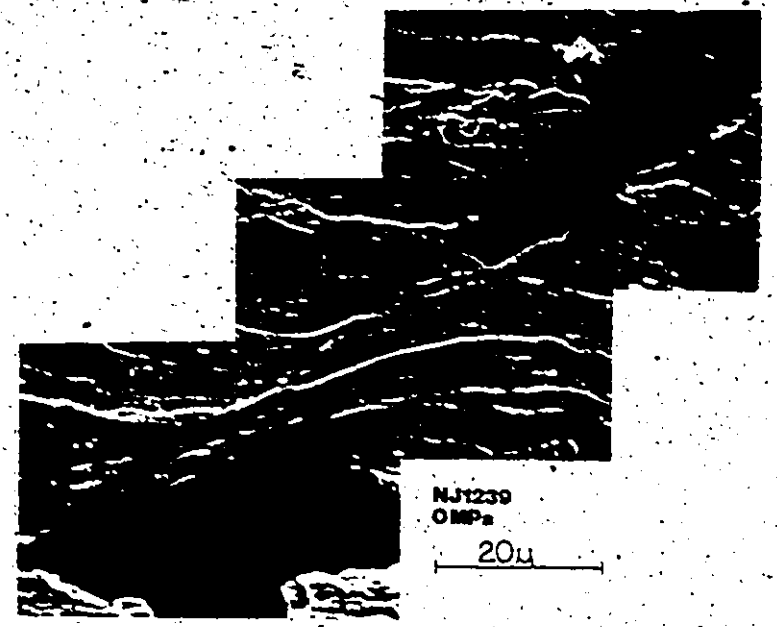

Fig. 5.12: Steel A, tested at ambient temperature and pressure. the linkage process between large voids is seen to occur through localized shear, involving a minor amount of damage within the shear zone.

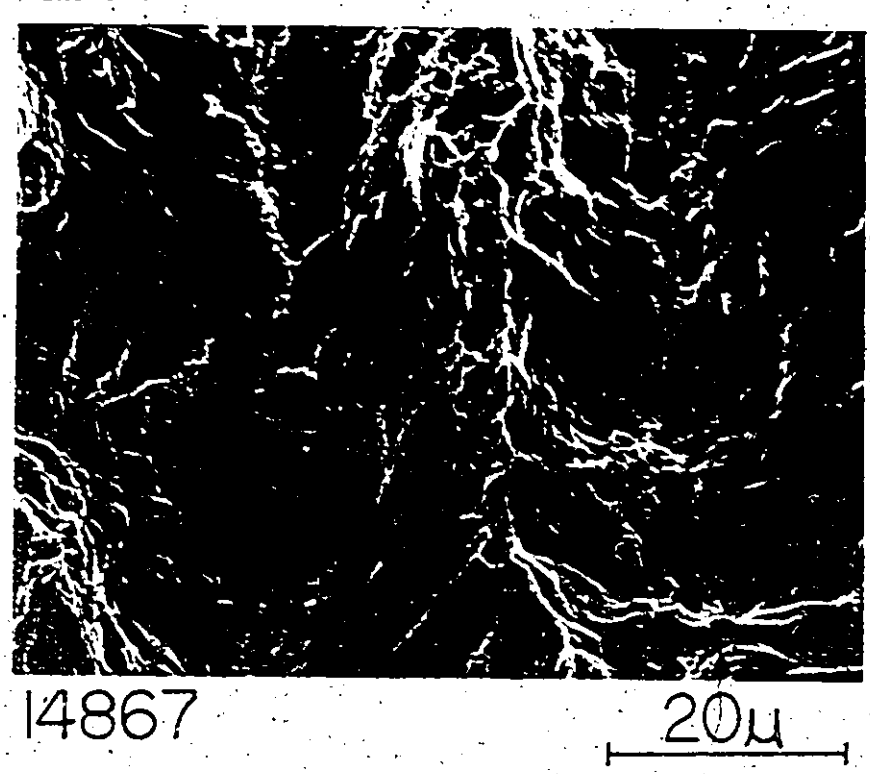

Fig. 5.13: Fracture surface of steel D, tested at ambient temperature and pressure. The absence of dimples on the shear portions illustrates that little damage accumulated in the void shear linkage process.

This is seen in Figure 5.14. The decrease in fracture properties of the calcium-treated steels, when tested in the transverse orientation, was not as large.

Testing in the through-thickness orientation indicated the most significant differences between the calcium-treated and non-treated steels. The fracture surfaces of the calcium-treated steels were characterized by a dimple size associated with the spacing of the calcium aluminate/sulphide inclusions, as seen in Figures 5.15a-b. Features on the fracture surfaces of the non-treated steels, however, were related to the dimensions of the clusters of alumina inclusions or manganese sulphides which were extensively elongated in the rolling direction, seen in Figures 5.16a-d. The largest clusters of elongated sulphides observed were 200 to 300 μ in length. These severely limited the ductility and fracture stress of the material in the through-thickness orientation.

Figure 5.17 illustrates that the fine pearlitic component, in the absence of inclusions, did not initiate a significant level of damage in the untreated steels. The fracture path was largely through the bainitic phase in these materials along the plate centre-line. Figure 5.18 indicates that fracture in the bainite was initiated at the elongated sulphides present within it. The fracture surfaces showed a complex topography, as seen in Figures 5.19a,b. Flat regions approximately normal to the tensile axis are separated by regions of the fracture surface oriented away from these planes toward the tensile axis. In the non-treated steels, the initially planar banded structure was deformed

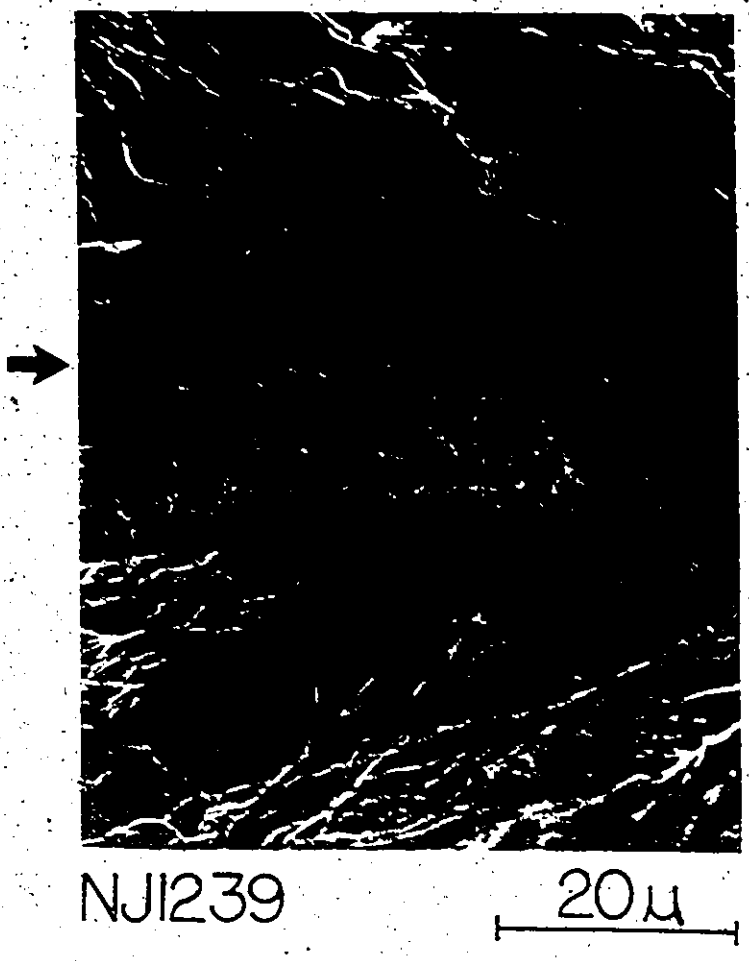

Fig. 5.14: Fracture surface of steel A, tested at ambient temperature and pressure, in transverse orientation. Elongated MnS inclusions (indicated by arrow), oriented normal to the tensile axis, were associated with splitting features.

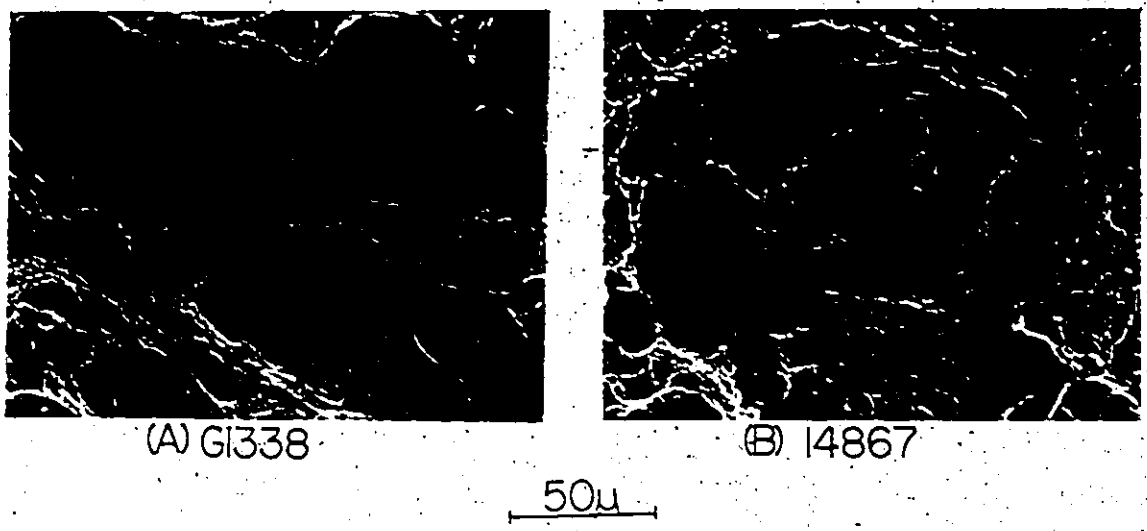

Fig. 5.15: Fracture surfaces of steel C (Figure a) and D (Figure b), tested at ambient pressure and temperature in the through-thickness orientation. The large dimple size was associated with the spacing of the calcium aluminate/sulphide inclusions, as shown.

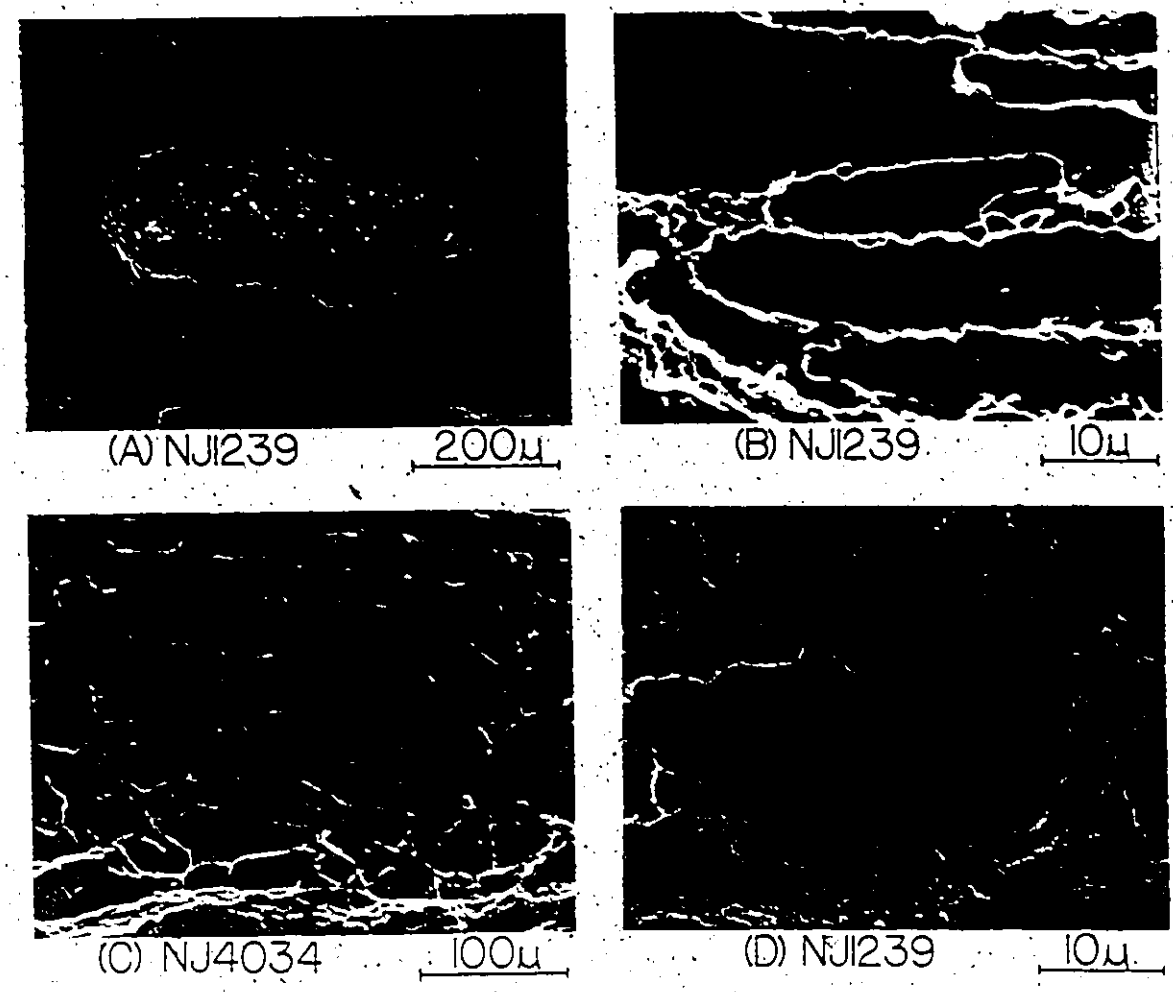

Fig. 5.16: Fracture surface observations of steel A (Figures a, b and d) and steel B (Figure c) tested in the through-thickness orientation. A very large cluster of alumina inclusions is indicated in Figure a, and elongated manganese sulphides in Figures b, c and d.

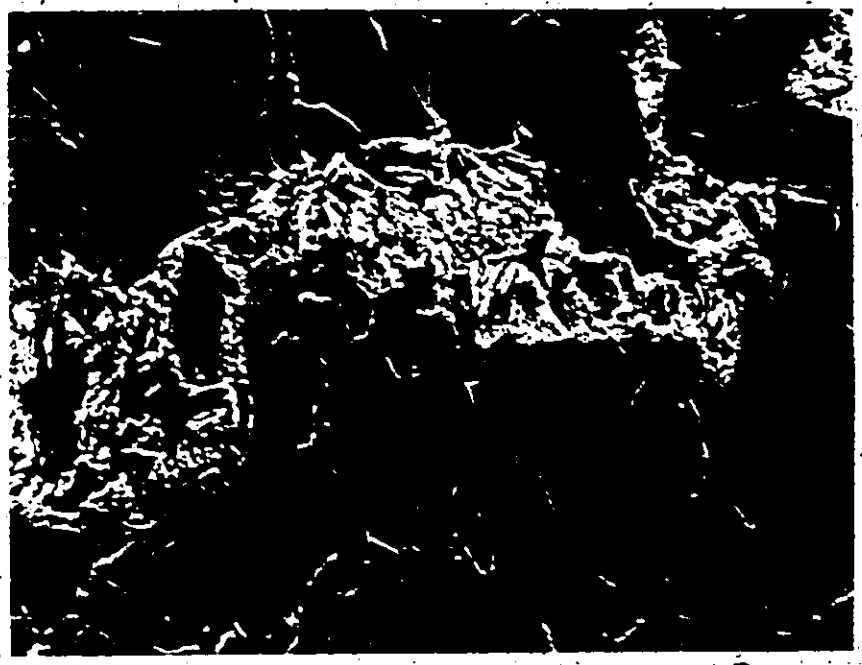

Fig. 5.17: SEM micrograph near fracture surface in steel C, tested in through-thickness orientation. Damage levels associated with pearlite were low.

Fig. 5.18: SEM micrograph of steel A, tested in through-thickness orientation. Fracture surface is at top. Elongated sulphides (indicated by arrows) present within bainite can initiate damage resulting in fracture.

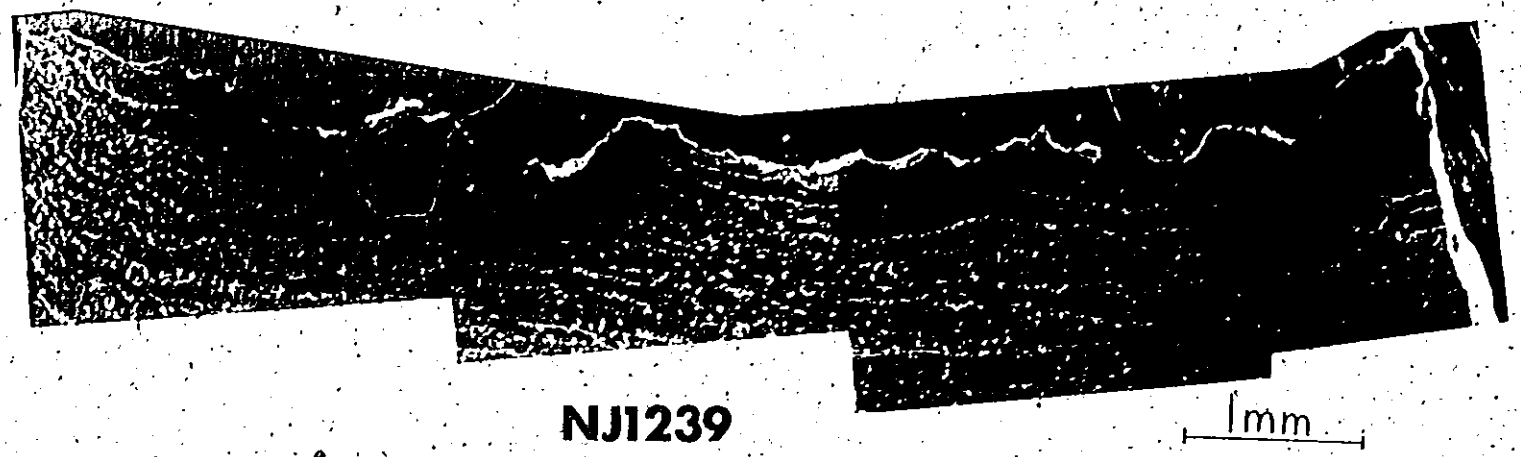

Fig. 5.19a: Steel A

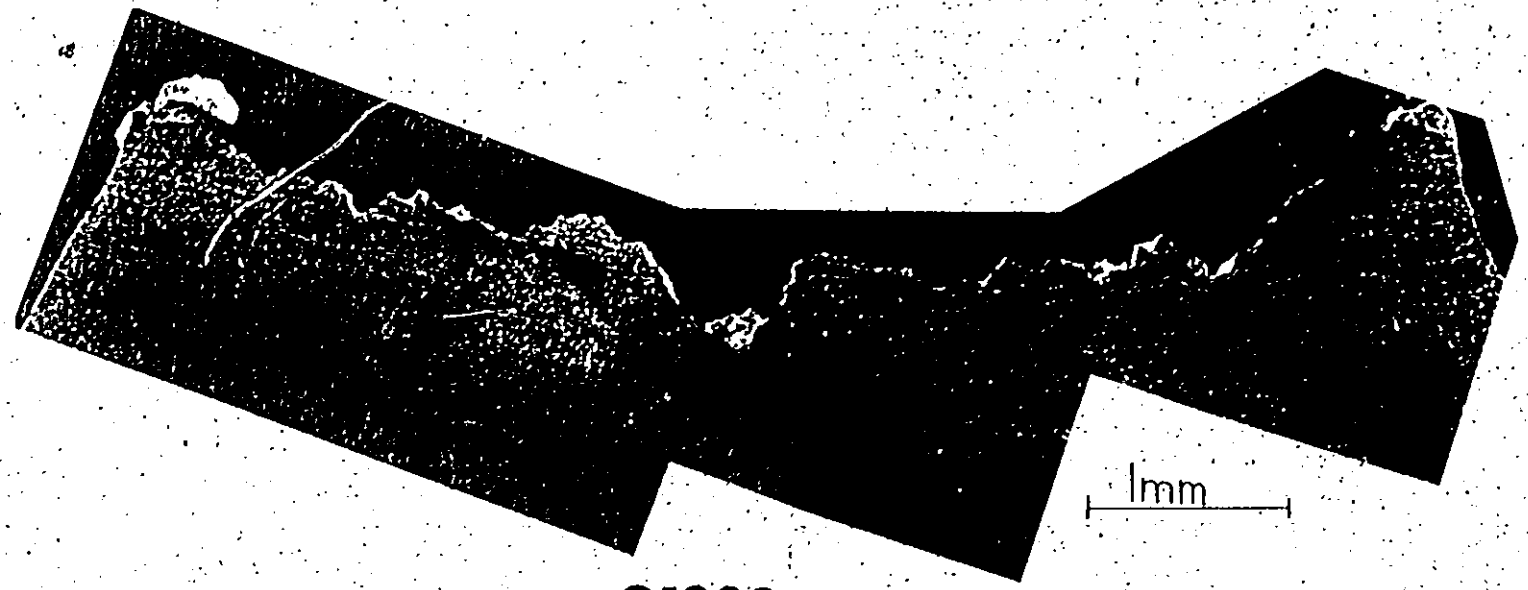

Fig. 5.19b: Steel C

Fig. 5.19: Cross-section illustrating topography of fracture surfaces in through-thickness tests. The deformation behind the fracture surface is indicated by the banded structure.

to follow the local perturbations in the fracture surface (Figure 5.19a). Near the fracture surface in the calium-treated steels, however, the non-ferritic bands remained planar, as seen in Figure 5.19b.

The tensile tests carried out did not provide conclusive evidence of whether or not the bainite deforms prior to fracture. The disruption of the banded structure in the through-thickness tests must involve some deformation, however, for the observed curvatures developed in the banded regions, this only involves small strains. Compression testing with the compression axis in the rolling direction did indicate that the bainite is capable of undergoing quite large plastic strains without fracturing. Figure 5.20 illustrates this in steel A, in a test interrupted at a strain of 1.04. The macroscopic flow stress at this point was 1680 MPa. The bainite in Figures 5.20a and b has buckled under the compressive strains. In the regions where it has buckled, the local strains in the bainite are estimated from the local curvature to be approximately 0.3 to 0.7. This assumes that the bainite did not plastically deform other than at the buckling points. In Figures 5.20c and d, the elongated inclusions contained within the bainite have not promoted fracture of this component in compression.

5.4.2 The Effects of an Imposed Hydrostatic Pressure

Tensile tests were performed on samples oriented in the rolling direction, under imposed pressures of 0.1, 690, and 1100 MPa.

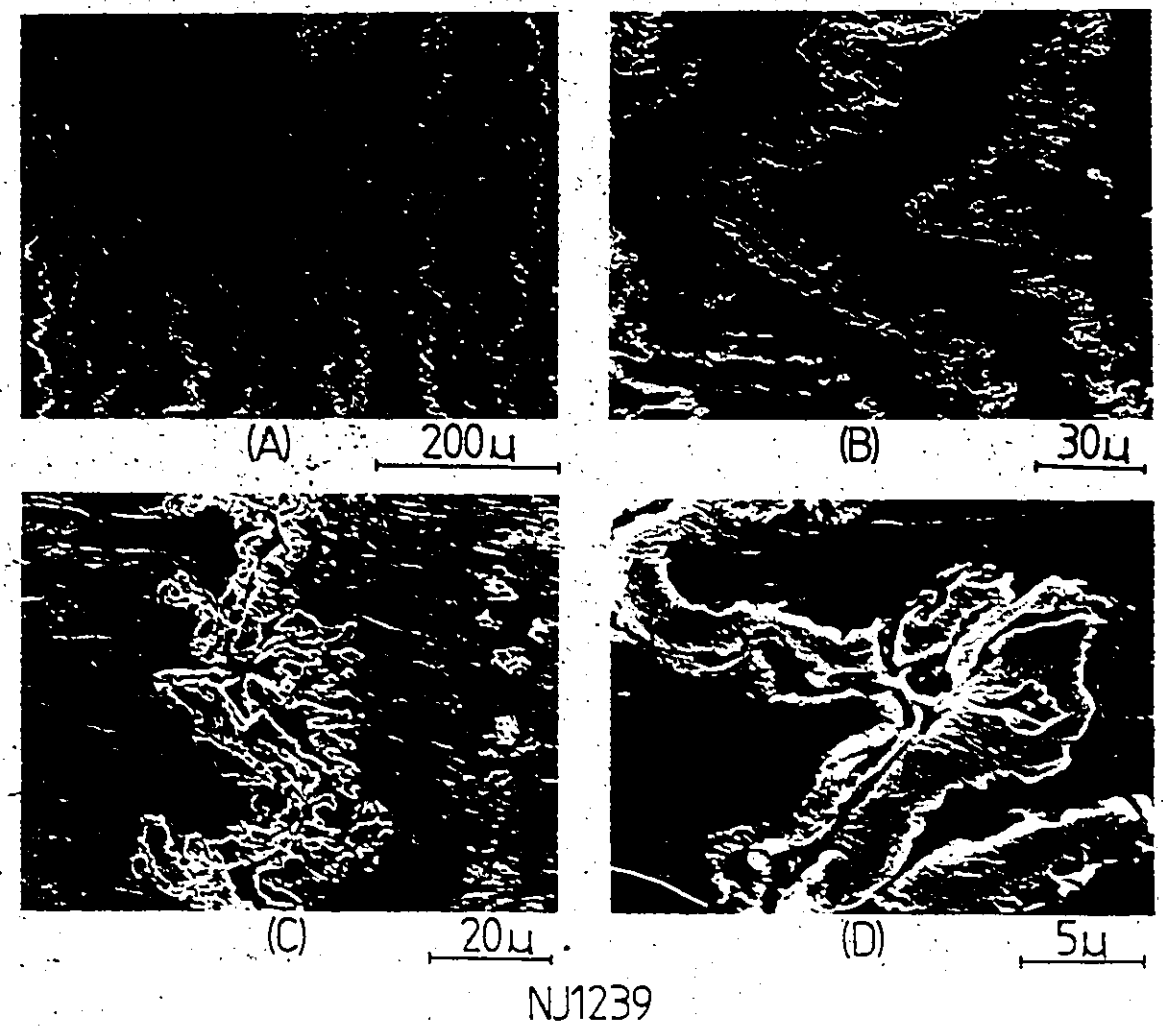

Fig. 5.20: SEM micrographs of steel A, tested in compression (compression axis vertical). The bands of bainite have buckled. Figures c and d indicate a sulphide contained within the bainite which has not resulted in bainite fracture.

5.4.2.1 Mechanical Properties

The results obtained from tests under pressure are tabulated in Table 5.4, along with those at 0.1 MPa already given in the previous section. The influence of hydrostatic pressure on the lower yield stress is plotted in Figure 5.21, indicating a linear increase in yield stress with pressure. If we assume the form for this relationship as $\sigma_y = \sigma_y^o (1 + 3\alpha P)$, where σ_y is the yield stress under pressure P and σ_y^o the yield stress with zero applied pressure (Richmond and Spitzig, 1980; Teirlinck, 1983), a least squares fit gives the following values of α for the four steels:

STEEL	α (10^{-6}MPa^{-1})
A (NJ1239)	9.98
B (NJ4034)	9.90
C (G1338)	26.6
D (14867)	14.1

The influence of pressure on the yield stress is stronger for steels C and D, which were calcium-treated and possess a finer, more continuous degree of banding than the non-treated steels.

The effect of pressure on the tensile fracture stress is plotted in Figure 5.22. At ambient pressure there is relatively little difference in the fracture stress between the four steels, however, with increasing pressure they display different behaviour. The dependence of fracture stress upon applied pressure is least sensitive in steel A and most sensitive in steel B, the two non-calcium treated steels.

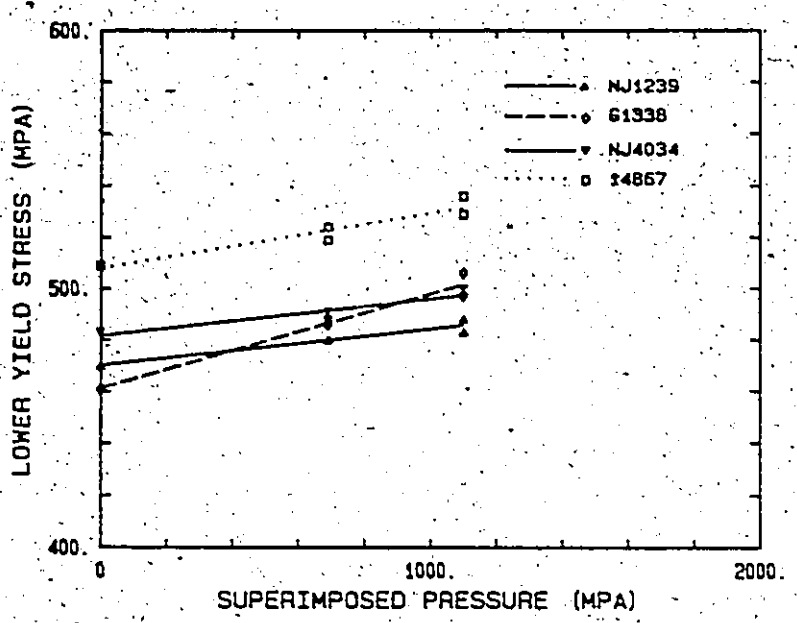

Fig. 5.21: Plot of lower yield stress vs. superimposed pressure for the four steels.

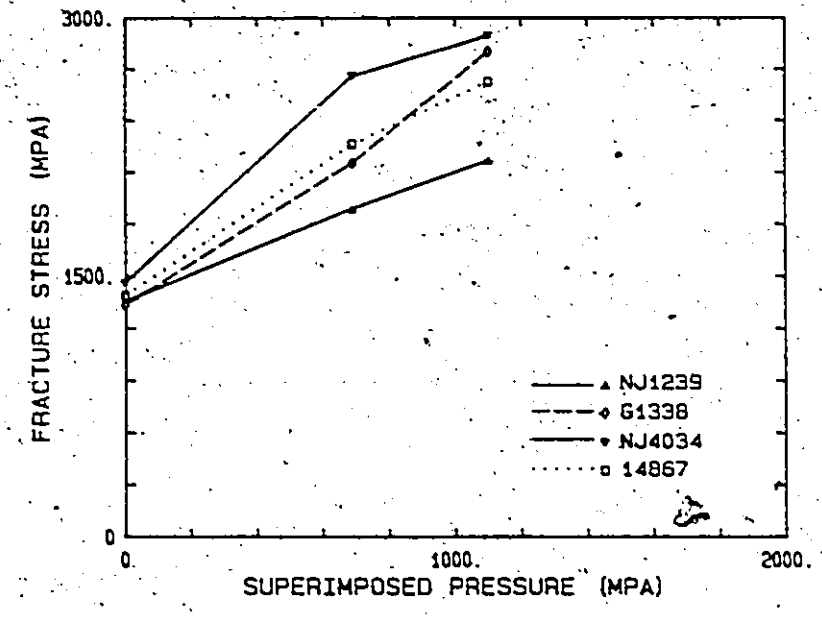

Fig. 5.22: Plot of fracture stress vs. superimposed pressure for the four steels.

TABLE 5.4

MECHANICAL PROPERTIES OF STEELS TESTED UNDER HYDROSTATIC PRESSURE (TENSILE AXIS ORIENTED IN THE ROLLING DIRECTION)

STEEL	IMPOSED PRESSURE (MPa)	LOWER YIELD STRESS (MPa)	FRACTURE STRESS (MPa)	FRACTION REDUCTION IN AREA	ε_1	ε_{11}
A (NJ1239)	0.1	470	1350	0.715	0.88	0.37
A	690	480	1890	0.897	1.49	0.56
A*	690	480	---	---	---	---
A	1100	488	2170	0.942	2.00	0.65
A*	1100	483	---	---	---	---
B (NJ4034)	0.1	483	1460	0.734	0.94	0.33
B	690	491	2660	0.933	2.11	0.56
B*	690	488	---	---	---	---
B	1100	500	2900	0.957	2.47	0.62
B*	1100	497	---	---	---	---
C (G1338)	0.1	461	1330	0.700	0.76	0.42
C	690	487	2150	0.912	1.41	0.84
C*	690	486	---	---	---	---
C	1100	506	2800	0.952	2.17	0.86
C*	1100	497	---	---	---	---
D (14867)	0.1	509	1390	0.721	0.83	0.45
D	690	524	2260	0.909	1.85	0.58
D*	690	519	---	---	---	---
D	1100	536	2630	0.948	1.97	0.83
D*	1100	529	---	---	---	---

* denotes a test which was interrupted prior to failure.

The variation of fracture stress with pressure appears to be reasonably linear for a given steel. The pressure dependence of the reduction in area is not linear, as seen in Figure 5.23. Reduction in area was used to quantify ductility, as the strains were not uniform across the elliptical cross-section. At higher pressures the increase in RA with pressure is not as great. Steel A displayed the lowest increase in RA with pressure and steel B the greatest, with the calcium-treated steels exhibiting intermediate behaviour.

Figure 5.24 plots the principal fracture strains ε_{11} and $\varepsilon_{\perp}$ measured in directions along the major and minor axes of the elliptical fracture surface respectively, as a function of imposed pressure. It has already been noted that at 0.1 MPa the tensile yield stress in the through-thickness orientation (corresponding to the minor axis in the current tensile samples) was greater than that in the transverse orientation (the major axis). However, the large strain behaviour resulted in much higher strains in the current samples along the direction corresponding to the plate through-thickness direction. An increase in applied pressure had little influence on the strains which developed in the transverse direction; it was the strain to failure along the through-thickness direction which was promoted to higher levels. In comparing the ellipticity of the cross-section of samples which were interrupted prior to failure with the fractured samples, it was noted that the deformation behaviour tended increasingly towards a plane strain condition with increasing strain, in the plane defined by the rolling and through-thickness orientations. Figure 5.24 indicates that the high ductility of steel B arises due to the high strains developed

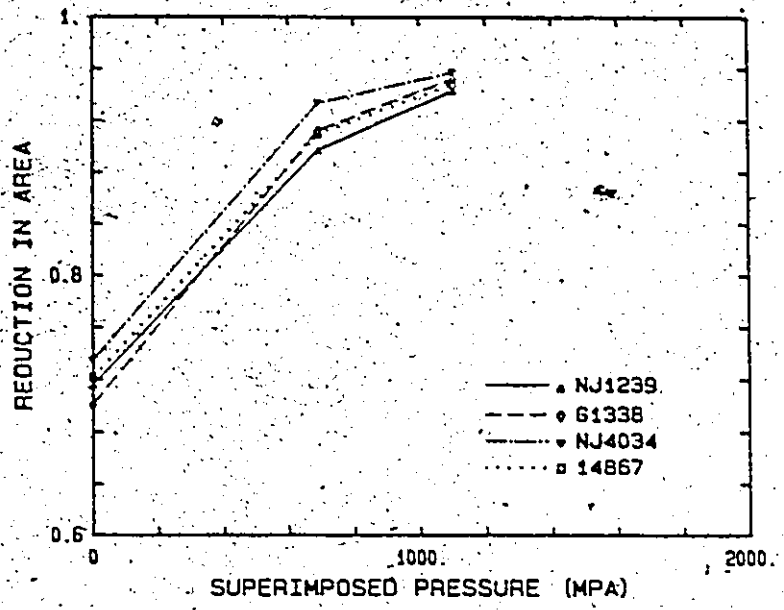

Fig. 5.23: Plot of reduction in area vs. superimposed pressure for the four steels.

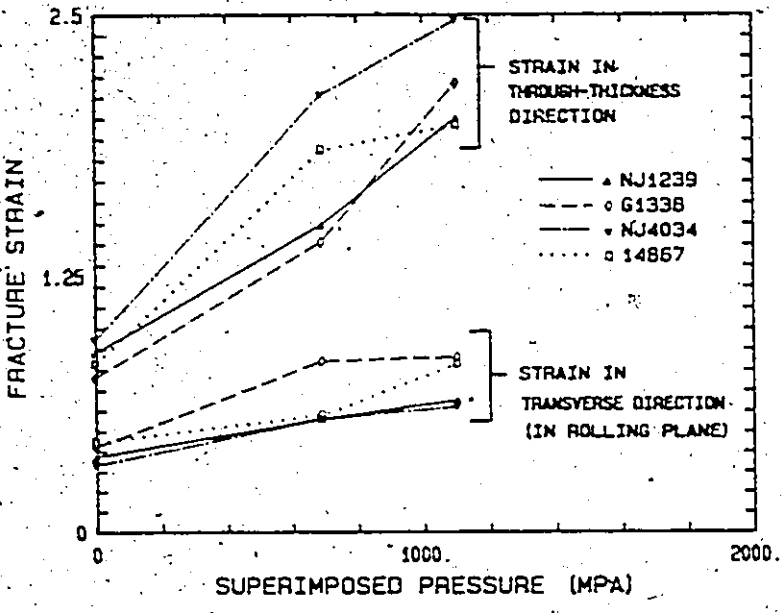

Fig. 5.24: Plot of fracture strains measured in directions along the major and minor axes of the elliptical fracture surface vs. superimposed pressure. The major axis corresponds to the transverse plate direction, and the minor axis to the plate through-thickness direction.

in the direction normal to the rolling plane of the plate. However, the fracture strain in the transverse direction is very low in this material.

Richmond and Spitzig (1980) have proposed that the influence of an applied hydrostatic pressure P on the flow stress behaviour of a material which follows the Ludwig equation $\bar{\sigma} = k\bar{\varepsilon}^{n}$, where $\bar{\sigma}$ and $\bar{\varepsilon}$ are effective stress and strain respectively, is adequately given by $\bar{\sigma} = k\bar{\varepsilon}^{n}\ (1 + 3\alpha P)$, where α is a material constant. The values of k and n are pressure-independent. They effectively assume that an applied pressure influences only the elastic modulus, and not the nature of the development of dislocation substructure with strain. With this constitutive equation consideration of the rate-independent Considère criterion for necking gives the dependence of the necking stress σ_n upon pressure as $\sigma_n = \sigma_n^{o}\ (1 + 3\alpha P)$, where σ_n^{o} is the necking stress under zero pressure (Teirlinck, 1983).

The stress at which necking initiates is plotted in Figure 5.25 as a function of pressure. Although there is considerable scatter in the data the increase with pressure appears significant. In keeping with the assumption of a linear elastic effect of pressure on the work-hardening rate, we may normalize the necking stress under pressure P by $(1 + 3\alpha P)$ to obtain the corresponding value of the flow stress at zero pressure. This is done in Figure 5.26, using values of α evaluated through the pressure dependence of the lower yield stress, rather than by fitting the entire flow curve. These values are consistent with the assumption of a linear effect of pressure on the flow curve.

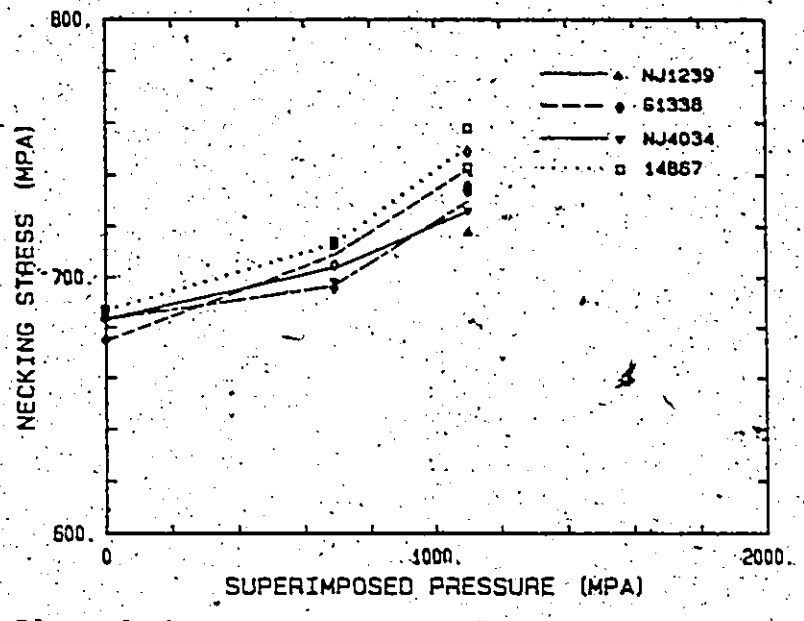

Fig. 5.25: Plot of the stress at which necking initiates vs. superimposed pressure, for the four steels.

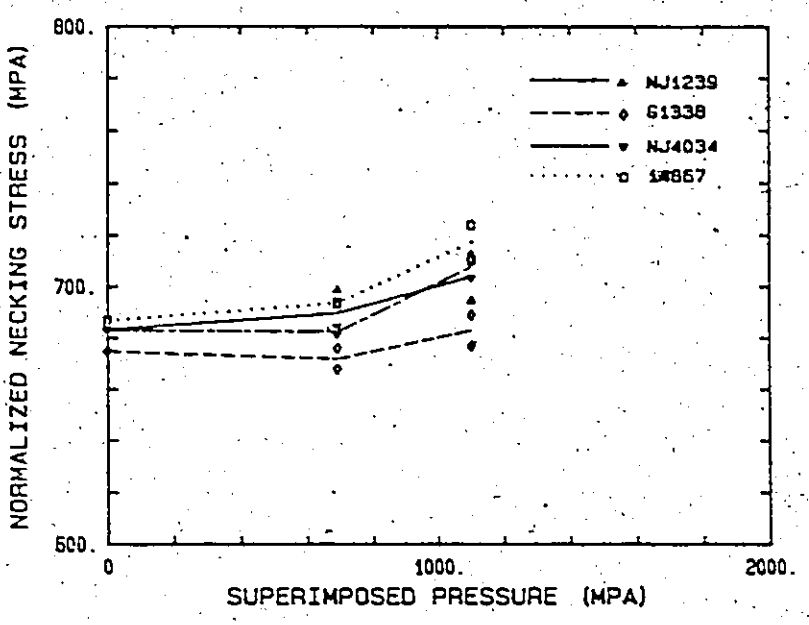

Fig. 5.26: Plot of normalized necking stress vs. superimposed pressure. The necking stress has been normalized to give the flow stress at zero imposed pressure, assuming a linear effect of pressure on the flow stress.

If the effect of pressure on the necking condition arises solely due to the influence on the flow stress behaviour, we would expect the data in Figure 5.26 to lie on a horizontal line. At imposed pressures of 690 MPa, which was approximately the necking stress at 0.1 MPa, the scatter in the data suggest that this is so. The increase in normalized necking stress above that at 0.1 MPa was 2 MPa, averaged over all four steels. At 1100 MPa however, there is a significant increase of 21 MPa in the average value of the normalized necking stress.

Figure 5.27 plots the strain at which necking initiates against imposed pressure. Again, the scatter at 690 MPa indicates little significant effect on the necking strain at this pressure. If the pressure influence on the flow stress was linear, this result would be implied by the results for the normalized necking stress. However, the necking strain is significantly increased under an applied pressure of 1100 MPa. If a linear influence of pressure on the flow stress and work-hardening rate is maintained at high strains, then the necking strain should remain constant with pressure. Thus, under applied pressures somewhat greater than the necking stress at ambient pressure, the necking condition appears to be altered.

5.4.2.2 Metallography and Fractographic Observations

The application of a hydrostatic pressure affected both the initiation of damage through fracture of the non-ferritic components, and the subsequent lateral growth of these voids. This resulted in fracture via a shear mode.

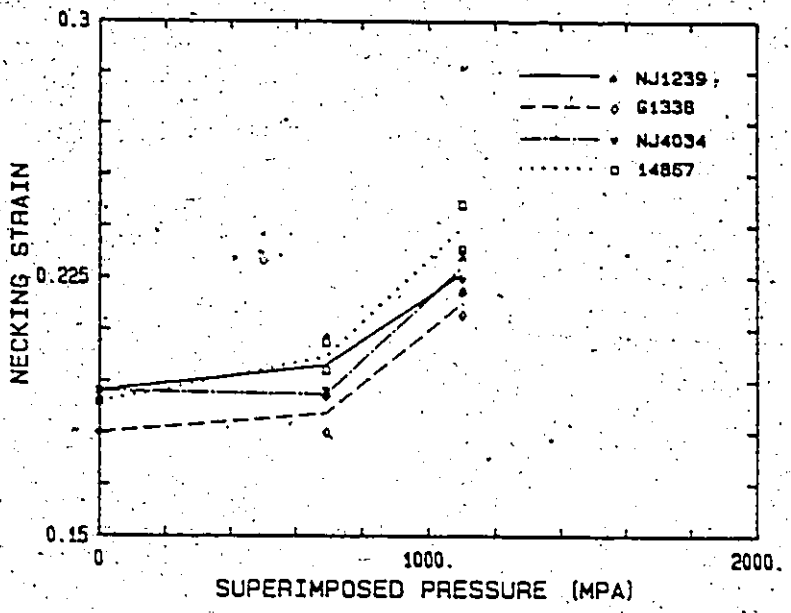

Fig. 5.27: Plot of the strain at which necking initiates vs. superimposed pressure, for the four steels.

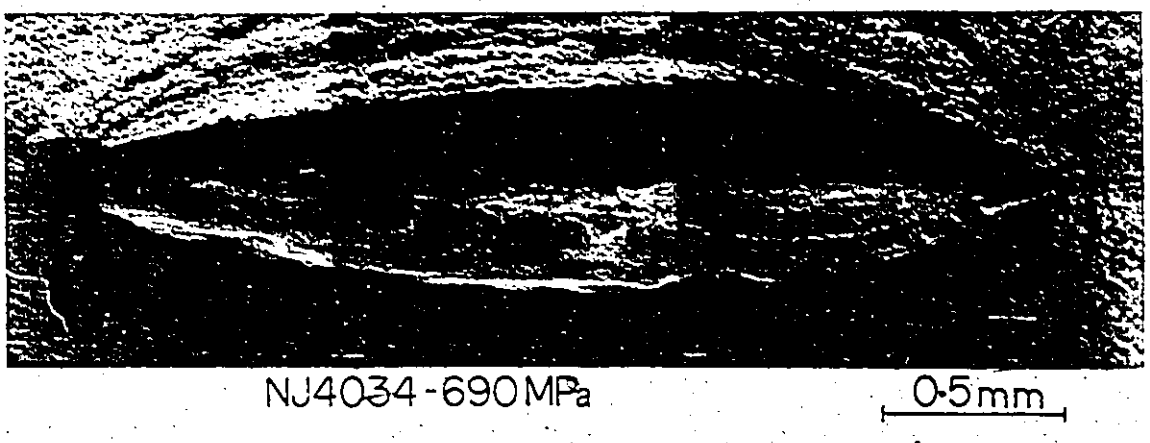

Fig. 5.28: Fracture surface of steel B, tested in tension under 690 MPa. Note the anisotropy of the sample cross-section.

The effect of pressure on the general appearance of the fracture surface is seen in Figure 5.28, where the large strains which are in the direction normal to the rolling plane are apparent. Some splitting along the centre-line region is evident, but the major portion of the fracture surface is associated with the shear mode. The fracture in the outer shear region (i.e., away from the centre-line) contains little evidence of damage associated with the final shear process, as seen in Figure 5.29. In this sample tested at 690 MPa, however, damage was associated with the local shear processes occurring in the centre-line region, as indicated in the upper portion of this figure. Voids in the shear zones appeared to nucleate at grain boundary carbides, within the grains at large carbides, and in the fine pearlite. The development of damage in association with shear in the central region was not always observed, as Figure 5.30a indicates. At a pressure of 1100 MPa the absence of dimples on the fracture surface was very apparent, as seen in Figure 5.30b.

Montages of the metallographic sections of several of the samples are given in Figures 5.31a-d and 5.32a-c for tests at 690 MPa and 1100 MPa respectively. The section plane is along the rolling direction normal to the rolling plane. The development of extensive shear bands is clearly seen, although they are more developed in the samples tested at 1100 MPa. The orientation of these large scale shear bands changes in going from the centre to the edge of the sample, due to large rotations involved in the final fracture process. However, the orientation of these shear bands, and of the shear fracture surface near the centre.

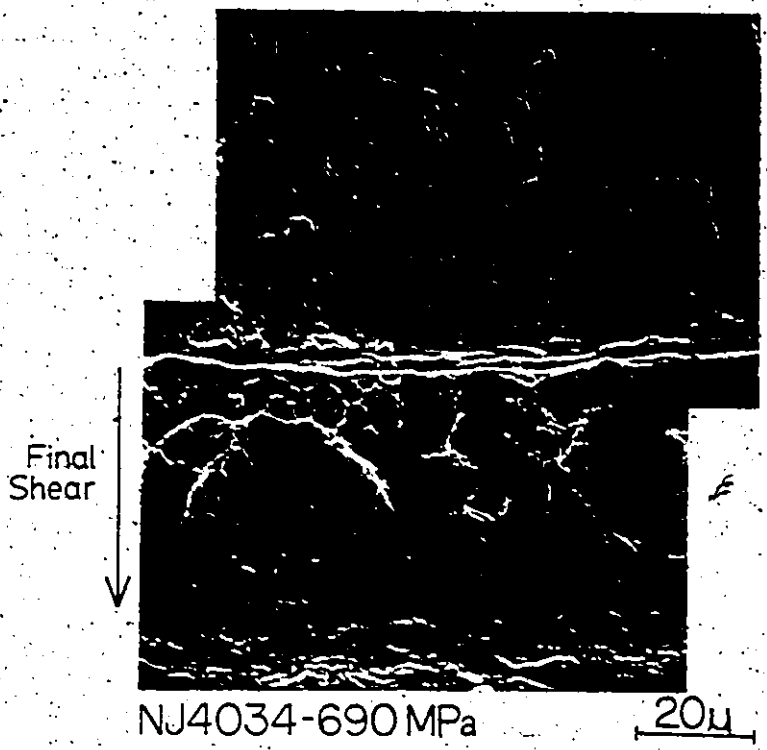

Fig. 5.29: Fracture surface observations for steel B tested in tension under 690 MPa. Fracture in the outer shear region (bottom portion) indicates little evidence of associated damage.

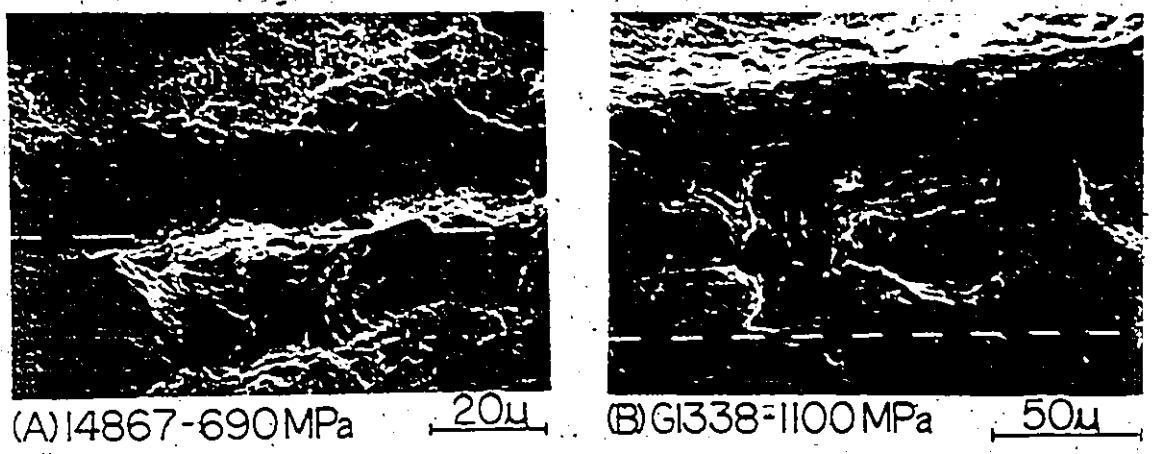

Fig. 5.30: Fracture surface observations of steel D (Figure a) and steel C (Figure b), near the centre of the sample. Figure b indicates that less damage is involved in void coalescence via localized shear in tests under 1100 MPa.

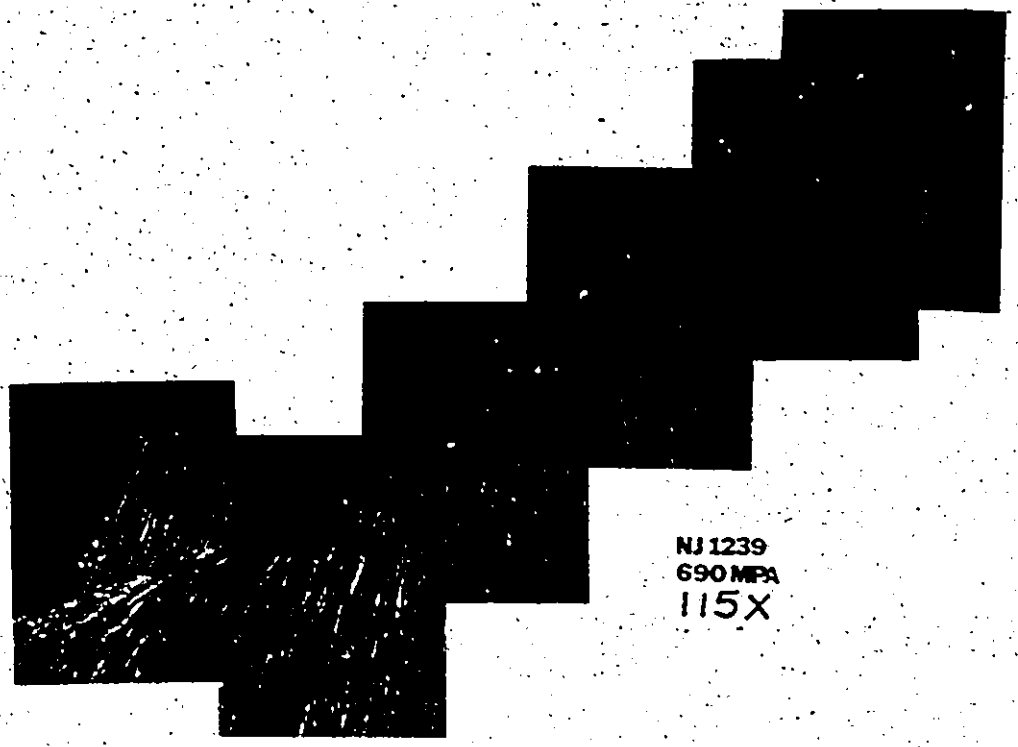

Fig. 5.31a: Steel A

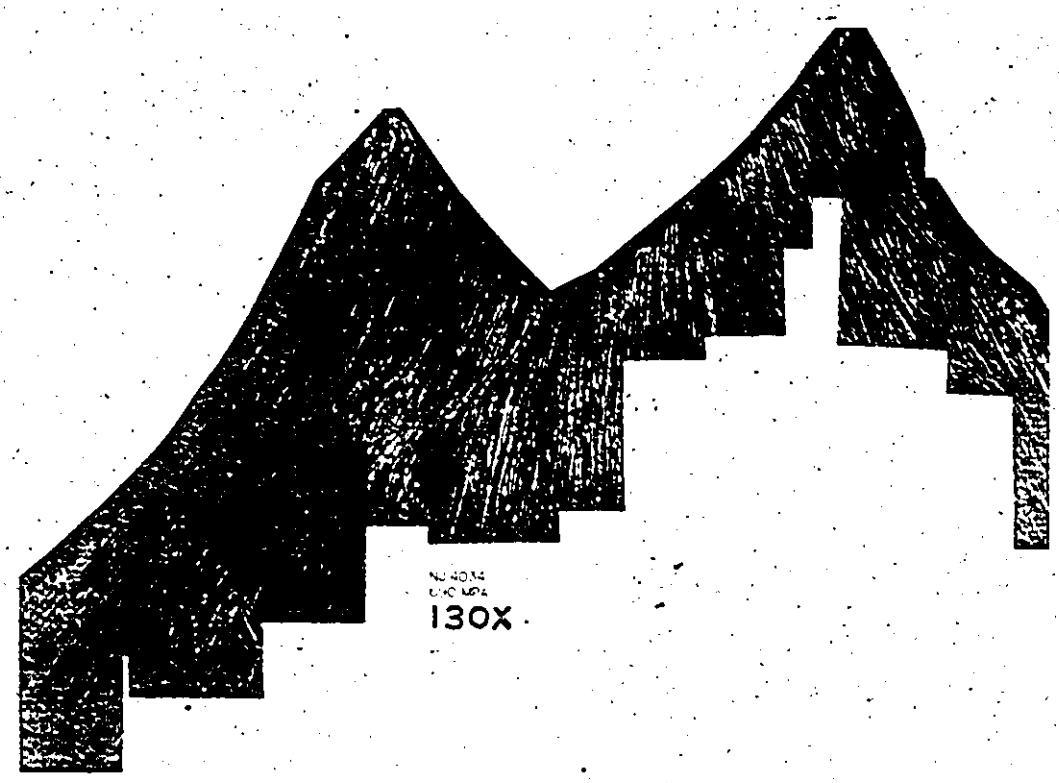

Fig. 5.31b: Steel B

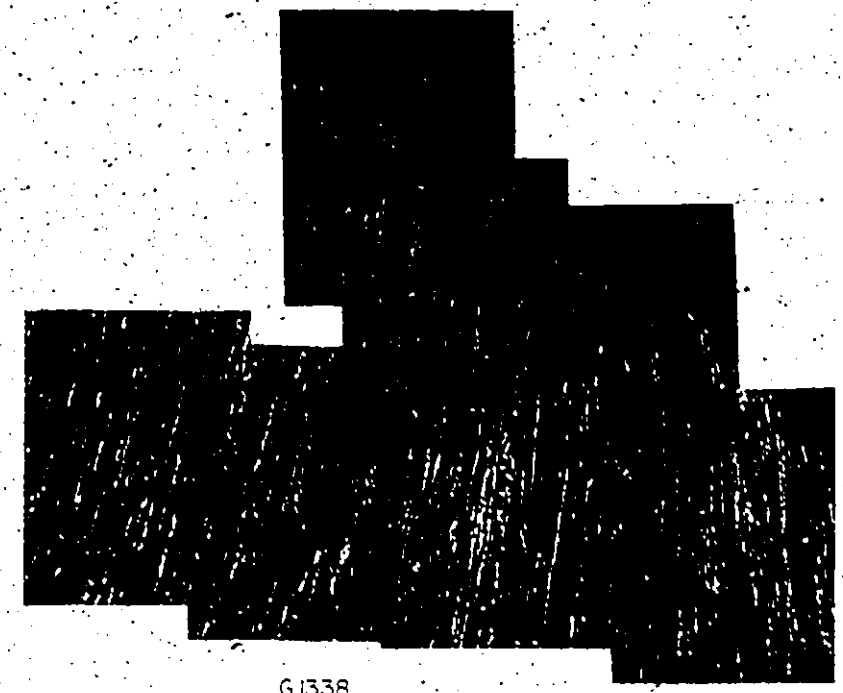

Fig. 5.31c: Steel C

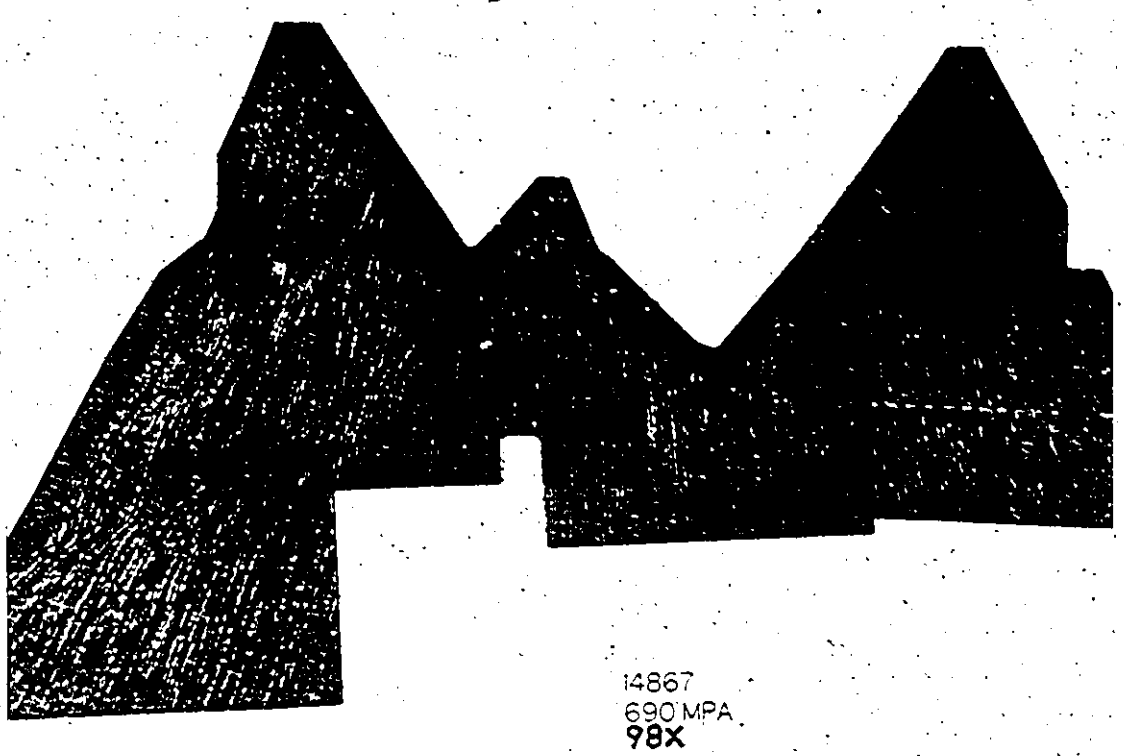

Fig. 5.31d: Steel D

Fig. 5.31: Montages of steels tested in tension under 690 MPa.

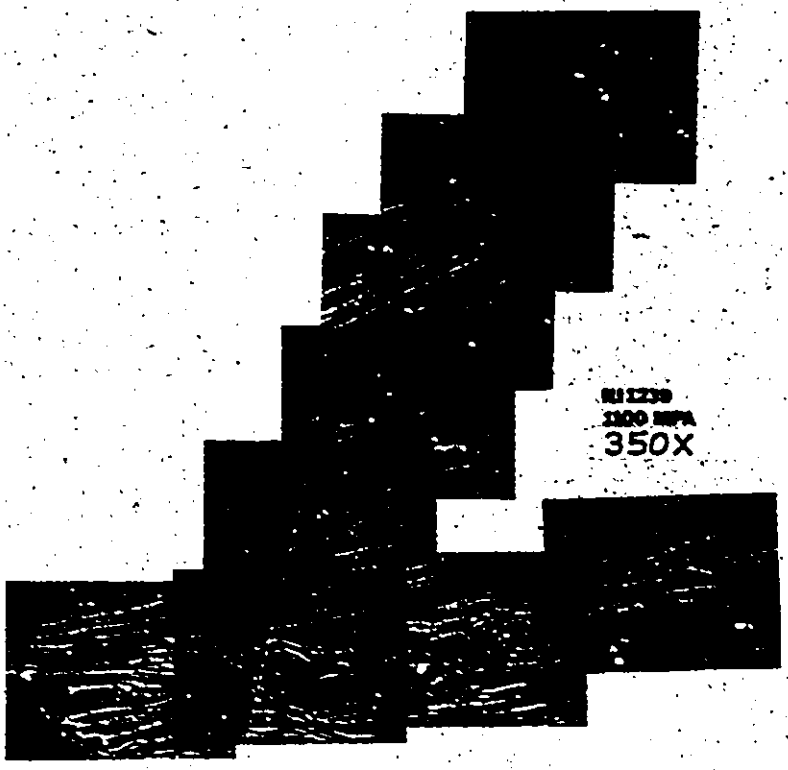

Fig. 5.32a: Steel A

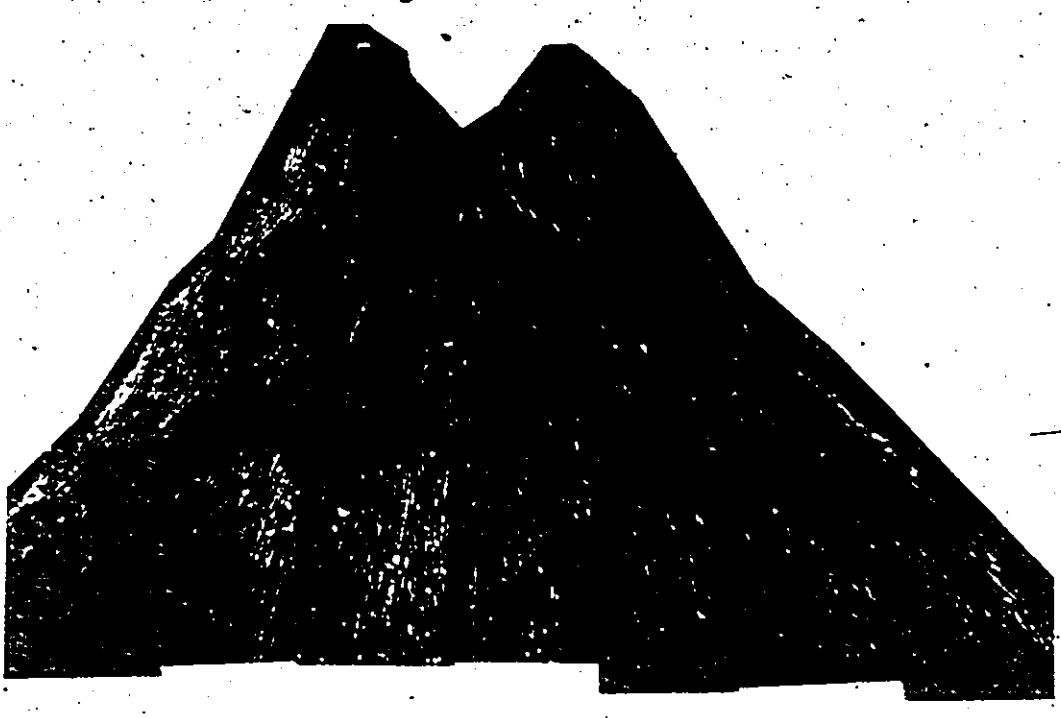

Fig. 5.32b: Steel B

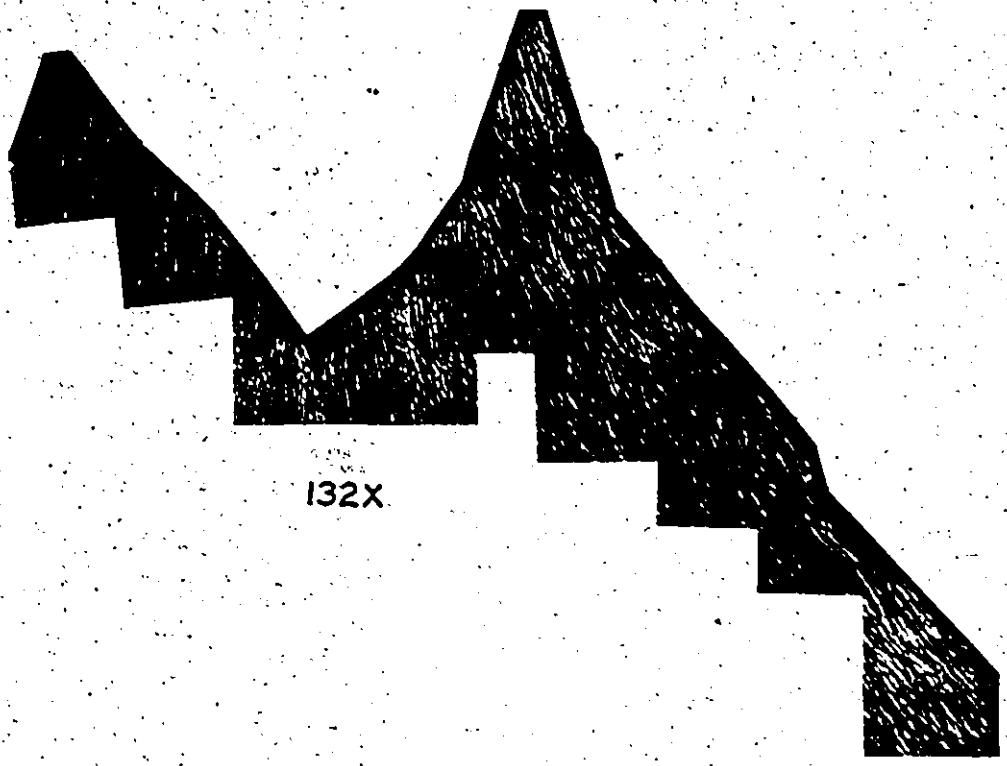

Fig. 5.32c: Steel C

Fig. 5.32: Montages of steels tested in tension under 1100 MPa.

of the sample was observed to make an angle of 47° ± 2° with the tensile axis.

The banded structure served as a set of markers indicating the shear strains which had developed in a shear band. Large strains developed in the shear bands, however, a more detailed examination near the fracture surface (Figure 5.33) reveals very little localized shear involved in the final fracture over portions of the fracture surface.

In Figure 5.32a, it appears that the shear band initiated at the damage which developed at the fractured bainite along the centre line of the specimen. This is suggested by the decrease in the shear strain in the band in moving away from the centre. The initiation of shear bands on a local scale (i.e., having dimensions of the non-ferritic band spacing) was observed to occur primarily through the fracture of bainite, however, damage development was also associated with the pearlitic regions. The fracture of the non-ferritic components is seen in Figures 5.34a,b from tests which were interrupted prior to failure. Although only a qualitative observation was made, an increase in applied pressure resulted in a decrease in the observed frequency of local fractures in bainite. However, an increase in applied pressure from ambient to 1100 MPa produced a decrease in number density of fracture sites in bainite which was certainly less than two. The development of damage observed in the pearlitic regions, on the other hand, was significantly reduced at 1100 MPa. The pattern of deformation in the ferrite around the bainite, seen in Figure 5.35, indicates that the level of deformation in the bainite is small relative to that in the ferrite. Here the

GI338 - 1100 MPa
640X
30° tilt

Fig. 5.33: SEM micrograph illustrating both fracture surface and polished and etched section behind fracture surface. Very little localized shear is involved near the fracture surface over those portions away from the shear bands.

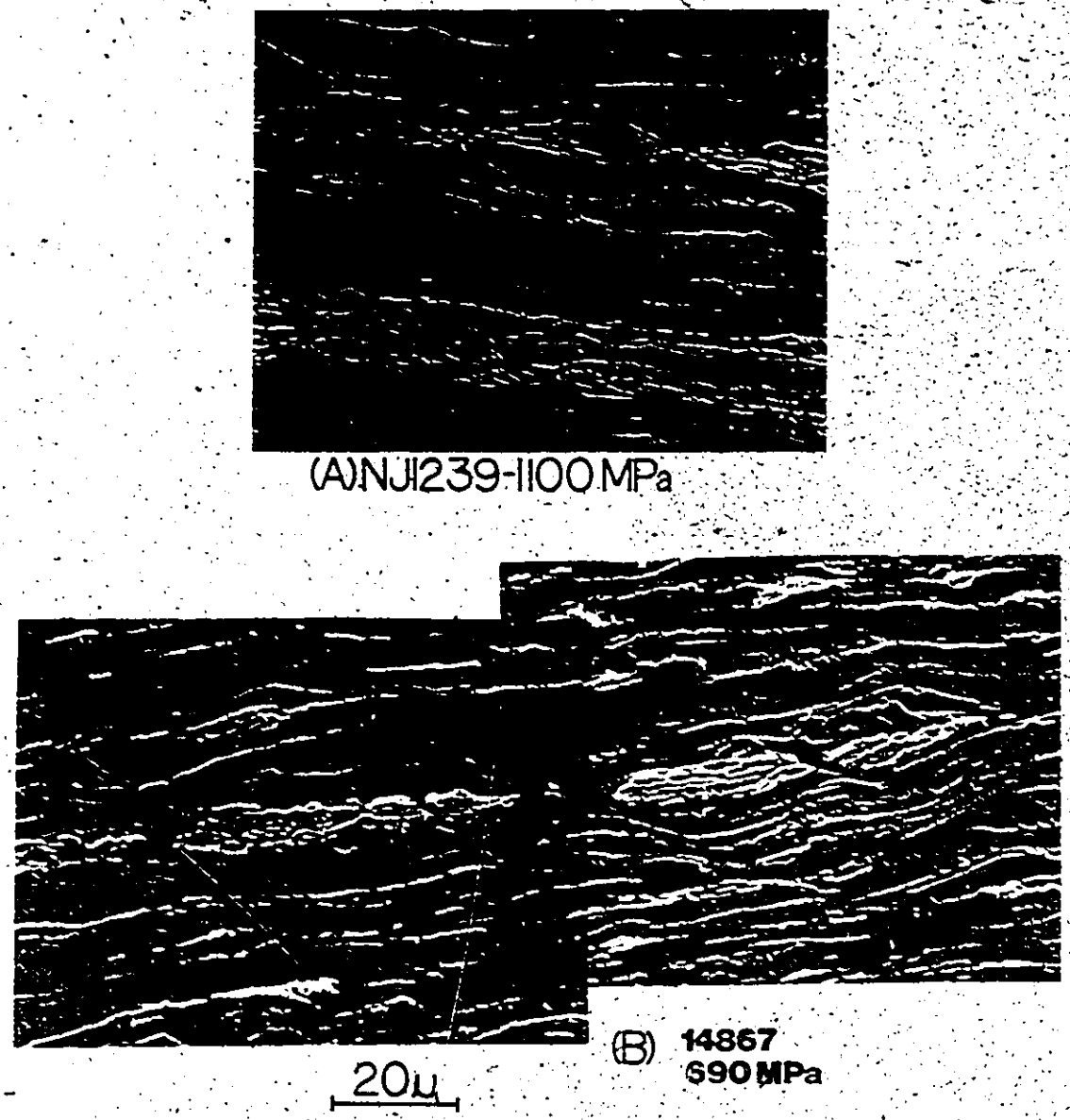

Fig. 5.34: SEM micrographs illustrating fracture of banded non-ferritic components in steel A (Figure a) and steel D (Figure b). In Figure b localized shear is seen to initiate at these local fracture sites.

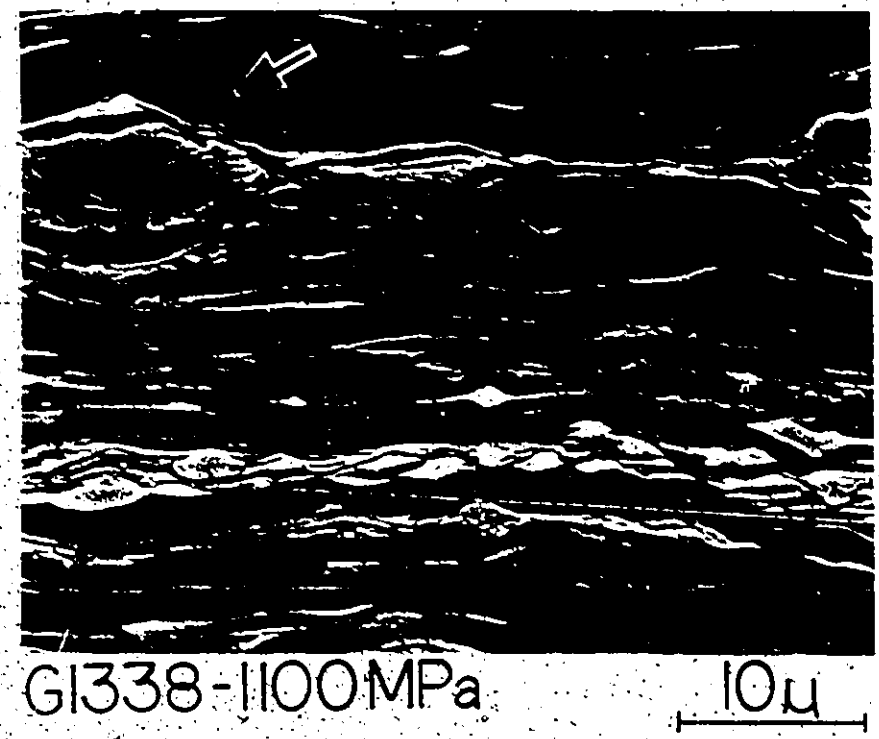

Fig. 5.35: SEM micrograph of steel C, tested under 1100 MPa. The pattern of deformation in the ferrite around the bainite, revealed by the grain boundaries (indicated by arrow) suggests that the deformability of the bainite relative to ferrite is low.

bainite is accommodated in the deformation process through the locally high strains which develop in the ferrite.

Shear bands were observed to initiate from fracture sites in the bainite in tests under imposed pressures, although the extent to which they developed (i.e., their dimensions, and the correlation and interaction with other local shear bands) was greater at the higher strains attained at 1100 MPa. This is seen in comparing Figures 5.36 and 5.37. Figure 5.38 illustrates the pattern of damage and the shear bands which developed in steel A at 1100 MPa in an interrupted test. The average tensile stress supported by the material at this point was approximately 1450 MPa. The extensive development of shear banding in this material is due to the large volume fraction of bainite occurring along the plate centre-line in this steel.

The orientation of the microcracks in the bainite component was frequently not normal to the tensile axis, as seen in Figure 5.38. Local fracture perpendicular to the tensile axis is illustrated for comparison in Figure 5.39. Whether the orientation of the fracture in bainite influences that of the shear band which develops is not clear, however, the angle at which a shear band develops, local to the bainite fracture, was observed to be quite invariant. These shear bands made an angle of 37° ± 1° with the local orientation of the band of bainite. Along the centre line the bainite was oriented along the tensile axis, however, the orientation of any band of bainite existing away from the centre line followed the pattern of deformation in the neck of the sample. The angle measured between the local shear band and the

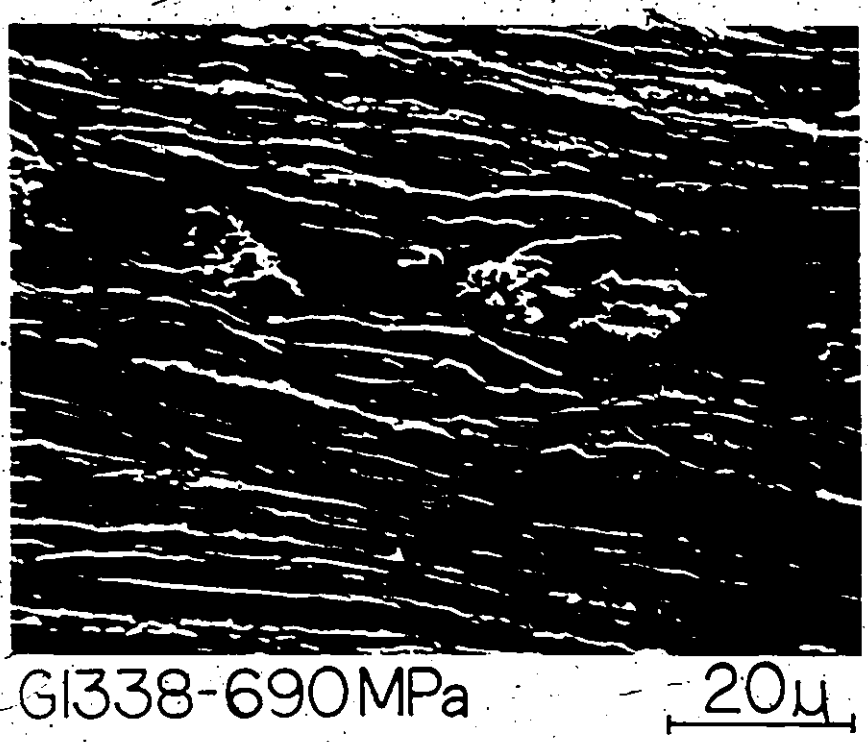

Fig. 5.36: SEM observations of shear bands initiating from fracture sites in the banded transformation products. Steel C, tested under 690 MPa.

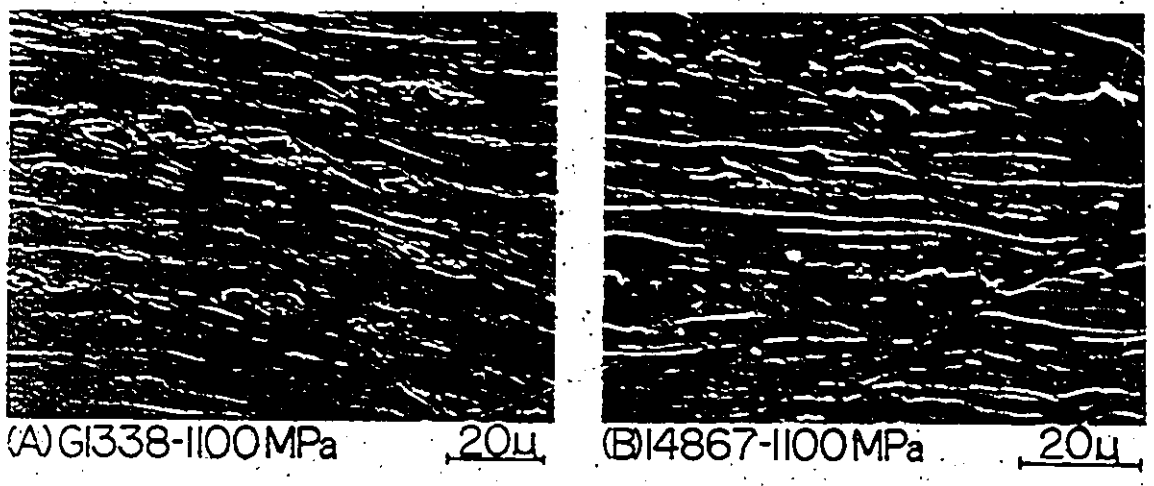

Fig. 5.37: SEM observations of shear bands in steel C (Figure a) and steel D (Figure b) tested under 1100 MPa. Shear bands were extensive and more developed in tests under 1100 MPa (compare with Figure 5.36).

Fig. 5.38: SEM micrograph illustrating the pattern of damage and the shear bands which developed in steel A, tested under 1100 MPa.

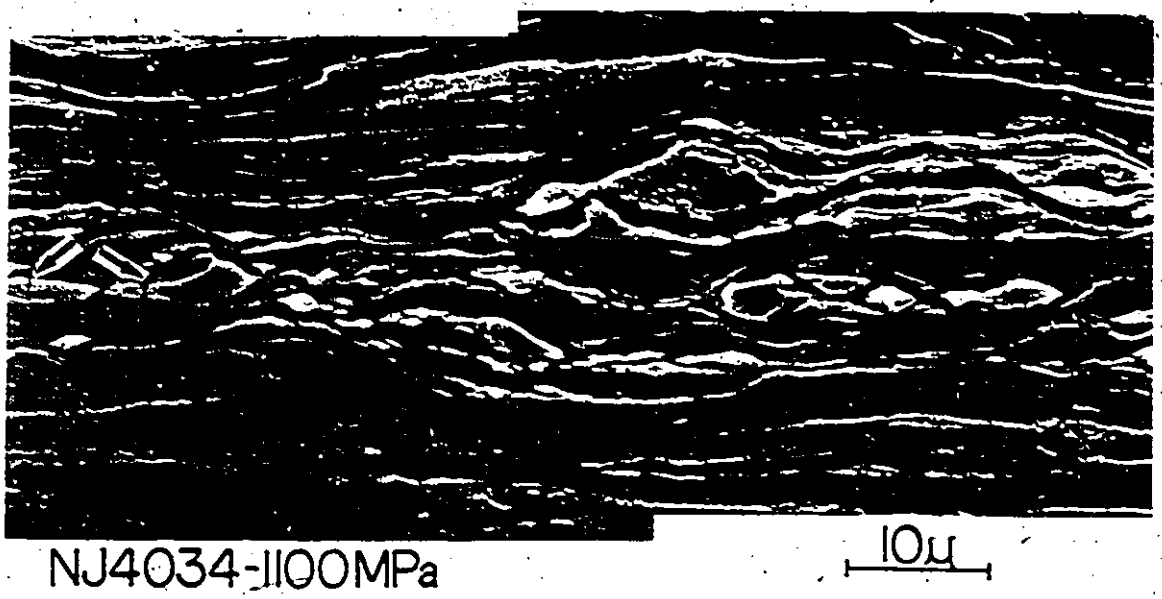

Fig. 5.39: SEM micrograph of steel B, tested under 1100 MPa. Arrows indicate fracture in the bainite normal to the tensile axis (horizontal).

bainite, however, was still approximately 37°, i.e., the orientation of the local shear bands was dependent upon the orientation of the bainite, not the tensile axis. As bainite was located primarily in the region close to the centre line, the maximum angle observed between the bainite and tensile axis was approximately 8°.

Thus an important observation made was that the orientation (relative to the tensile axis) of the small-scale shear bands which initiated and developed local to the microcracks in the bainite was different from the orientation of any macroscopic shear band which subsequently developed.

The presence of inclusions was not observed to influence the development of localized shear. In Figure 5.40, an elongated MnS inclusion in steel NJ1239 tested under 1100 MPa did not affect the initiation of shear banding.

In several of the samples, the initiation of localized shear was observed at the sample surface in the neck region. This is suggested in Figure 5.41, where the strains in the shear band continuously decrease as one moves away from the specimen surface.

5.4.3 The Influence of Increased Flow Stress of the Ferrite Matrix: Testing at -196°C

Tests were conducted at -196°C in liquid nitrogen on tensile samples taken from the as-received plate in the rolling and transverse orientations, and on the spheroidized samples which had been taken from the rolling direction.

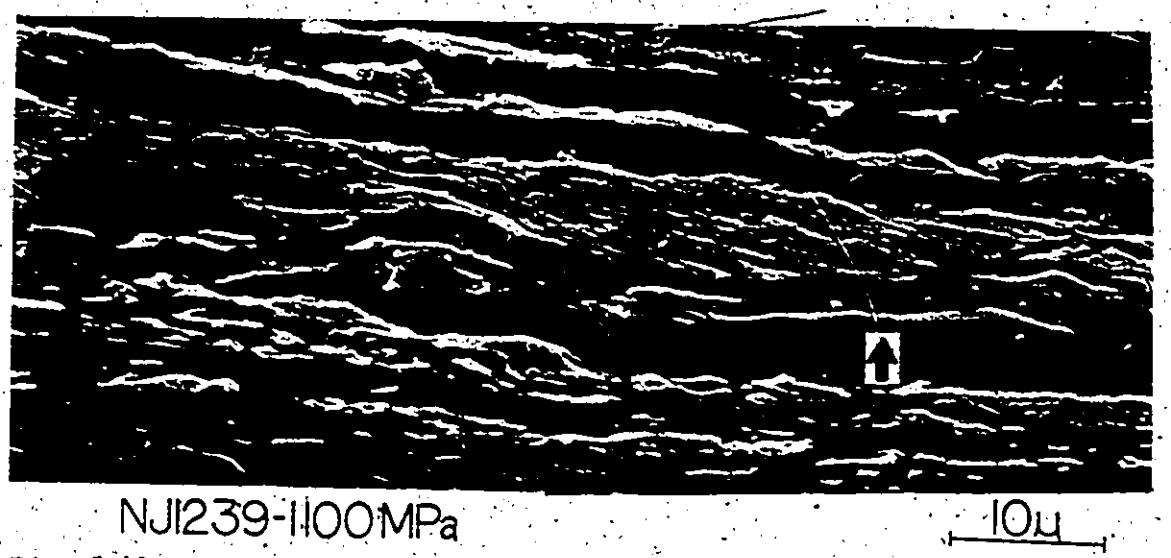

Fig. 5.40: SEM micrograph of steel A, tested under 1100 MPa. The elongated sulphide (indicated by arrow) has not promoted localized shear.

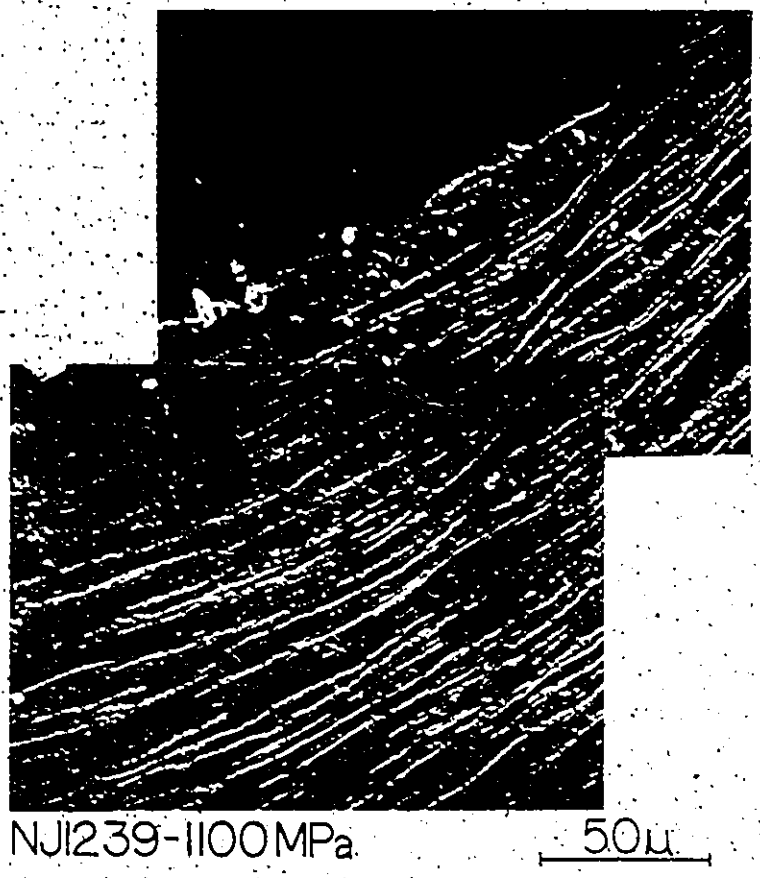

Fig. 5.41: SEM micrograph of localized shear in steel A which initiated at specimen surface. Note the decreasing shear strains in from the surface.

5.4.3.1 Mechanical Properties

The results of the tensile tests are summarized in Table 5.5. The steels all possessed considerable ductility at -196°C, with reductions in area of the order of 50%.

Contrary to the behaviour at ambient temperature, the yield stress at -196°C in the transverse orientation was higher than that in the rolling direction for all four steels, by an average of 6%. There was considerable scatter in the fracture stresses, however, the data does indicate that in the rolling direction fracture stresses of the calcium-treated steels were higher, more significantly in comparison with steel A than steel B. In the transverse orientation considerably higher fracture stresses and reductions in area were obtained in the calcium-treated steels. The reduction in area in the calcium-treated steels was not influenced by the testing orientation, however, in the non-treated steels the RA in the transverse orientation was lower. The anisotropy in fracture properties in these steels was more significant at lower temperatures than at room temperature.

The effect of the spheroidization treatment generally resulted in a decrease in yield stress, as expected. The anisotropy in deformation behaviour which resulted in an elliptical cross-section was still present, however, in steel B, which had the highest degree of anisotropy, the ellipticity of the fracture cross-section was significantly reduced. Spheroidization of the microstructure produced an increase in ductility and fracture stress in steels A and B, so that the fracture properties of the non-treated steels were superior to those of the calcium-treated

TABLE 5.5

MECHANICAL PROPERTIES OF STEELS TESTED AT -196°C

STEEL	ORIENTATION*	LOWER YIELD STRESS (MPa)	FRACTURE STRESS (MPa)	FRACTION REDUCTION IN AREA	$\varepsilon_{\perp}$	ε_{11}
A (NJ1239)	1	940	1550	0.499	0.36	0.27
A	1	915	1450	0.493	0.49	0.21
A	2	993	1560	0.425	0.34	0.21
A (spheroidized)	1	938	1830	0.610	0.57	0.38
B (NJ4034)	1	943	1700	0.561	0.56	0.26
B	1	943	1580	0.525	0.55	0.25
B	2	1010	1470	0.332	0.27	0.15
B (spheroidized)	1	914	1800	0.610	0.57	0.37
C (G1338)	1	926	1620	0.496	0.40	0.28
C	1	923	1700	0.555	0.48	0.31
C	2	975	1710	0.533	0.42	0.35
C (spheroidized)	1	856	1460	0.424	0.30	0.24
D (14867)	1	929	1740	0.577	0.52	0.33
D	1	927	1670	0.571	0.54	0.30
D	2	970	1770	0.552	0.45	0.38
D (spheroidized)	1	810	1710	0.602	0.52	0.39

* 1 - tensile axis oriented in the rolling direction.
2 - tensile axis oriented transverse to the rolling direction.

steels. Although the properties obtained for steel C were poor (due to an above-average inclusion content in the given sample), those for steel D suggested that the fracture properties of the calcium-treated steels were influenced little by the spheroidization treatment.

5.4.3.2. Metallographic and Fractographic Observations

In the tests performed at low temperatures several damage processes were observed to operate in a given material, associated with the local microstructure and its influence on local conditions. Void growth through plastic flow, cleavage cracking and intergranular cracking could all be observed in a given sample.

The repeated tests on samples from the rolling direction indicated scatter in the macroscopic fracture stresses and strains, but the characteristic microstructural damage and fracture surface features were qualitatively similar between repeat tests in a given material. However, although all the steels were quite ductile, there were considerable differences between them in their fracture characteristics. Steels A and B, which were not calcium-treated, delaminated along the plate centre-line when tested in the rolling direction orientation, shown in Figure 5.42. The delamination plane in these steels indicated that the delamination involved a brittle fracture mode, as seen in Figure 5.43. Figure 5.43 illustrates the micro-cracking which developed normal to the tensile axis, observed as cracks perpendicular to the delamination surface. Microscopic examination of the delamination surfaces did not reveal any large inclusions or inclusion clusters which

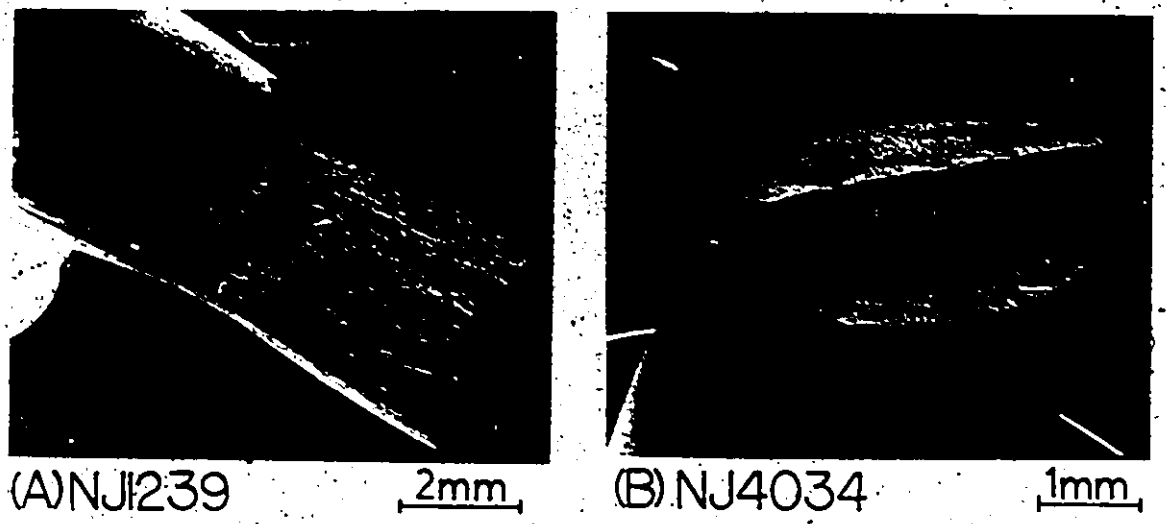

Fig. 5.42: Tensile samples of untreated steels A (Figure a) and B (Figure b) which delaminated in testing at -196°C in the rolling direction. The delamination plane corresponded to the plate centre line.

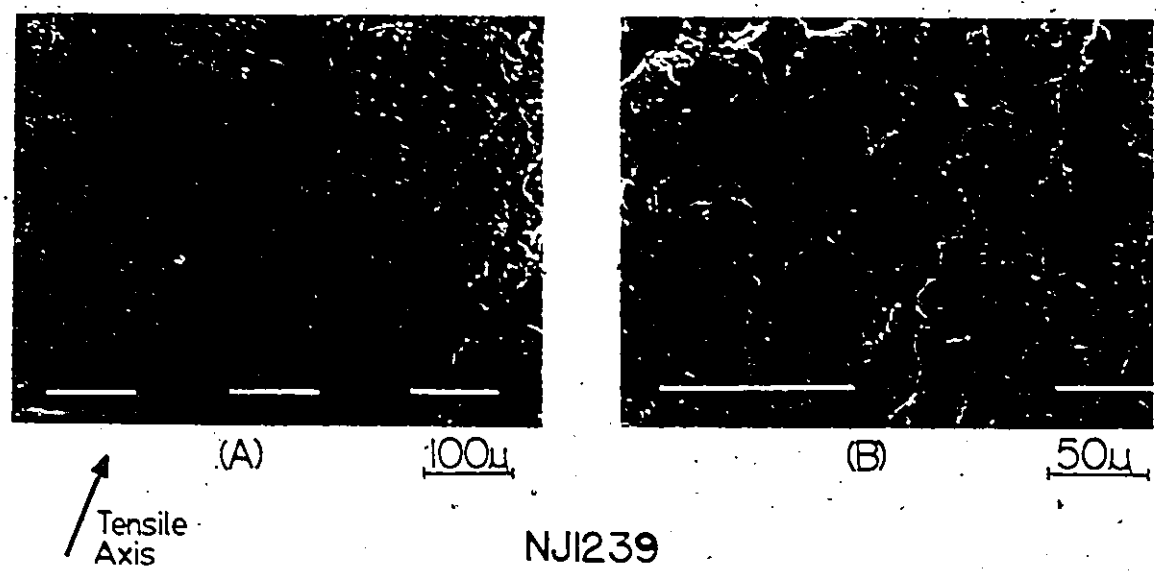

Fig. 5.43: Delamination surface in steel A, indicating a brittle mode of fracture. In Figure a, microcracking normal to the tensile axis is observed.

may have served to initiate the delamination fracture. The possibility of decoherence from the fracture surface during fracture, however, would be quite likely at the stresses attained in low temperature tests.

The fracture surfaces in steels A and B along which final fracture occurred were markedly different. In steel A, this fracture surface was normal to the tensile axis, and indicated cleavage as the dominant fracture mode (Figure 5.44a). Banded regions oriented with the rolling plane were observed near the centre, in which a ductile fibrous mode was observed. In steel B, however, the plane along which final fracture occurred contained the plate transverse direction, and made an angle of approximately 48° with the tensile axis. Figure 5.44b indicates that the final fracture in this material occurred through a ductile mode involving a void-sheeting mechanism. The large shear strains involved adjacent to the fracture surface are seen in Figure 5.45. Outside of this shear zone the average level of damage was observed to be very small.

In steel A, the mode of fracture along the intersection of the delamination surface and the final fracture surface was observed to change, in moving from the centre to the outer edge of the sample. Figure 5.46a indicates a ductile fibrous mode near the centre, leading to a cleavage mode. In Figure 5.46b, at a position approximately midway between the centre and the surface of the sample, the fracture mode was predominantly cleavage, exhibiting only minor levels of local fibrous fracture. It should be noted that this observation was not the result of variations in the microstructure, as both micrographs were taken at locations along the plate centre line.

Fig. 5.44: Surfaces along which final fracture occurred in steels A (Figute a) and B (Figure b), tested at -196°C in the rolling direction. In steel A, final fracture occurred in predominantly a cleavage mode. In steel B, a ductile mode was observed, involving a void-sheeting mechanism.

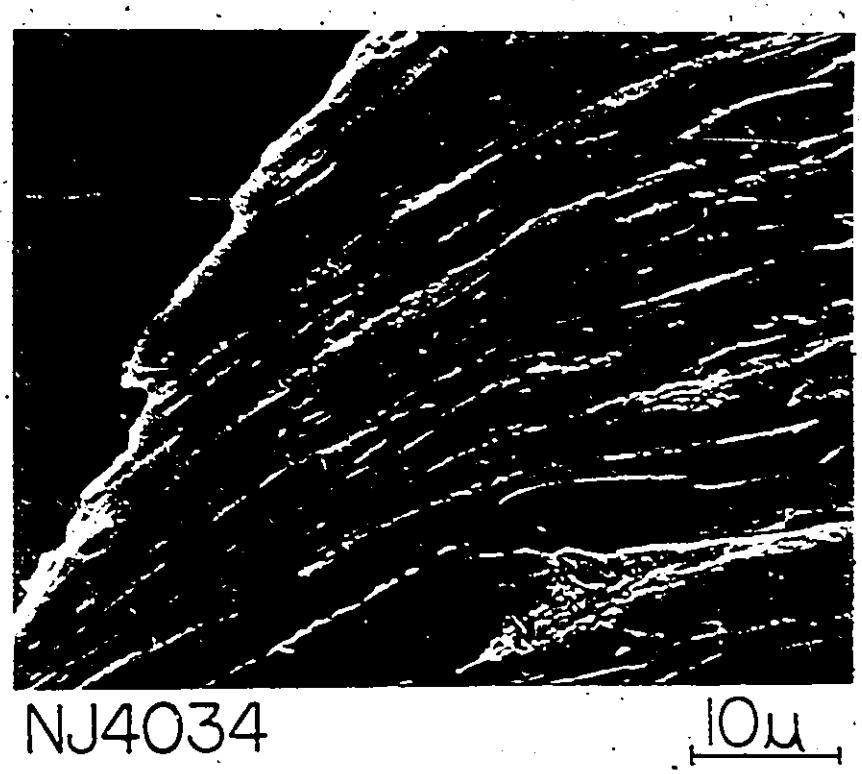

Fig. 5.45: SEM micrograph of region adjacent to final fracture surface in steel B, tested at -196°C in the rolling direction. Outside of the sheared region adjacent to the fracture surface, average damage levels were significantly lower.

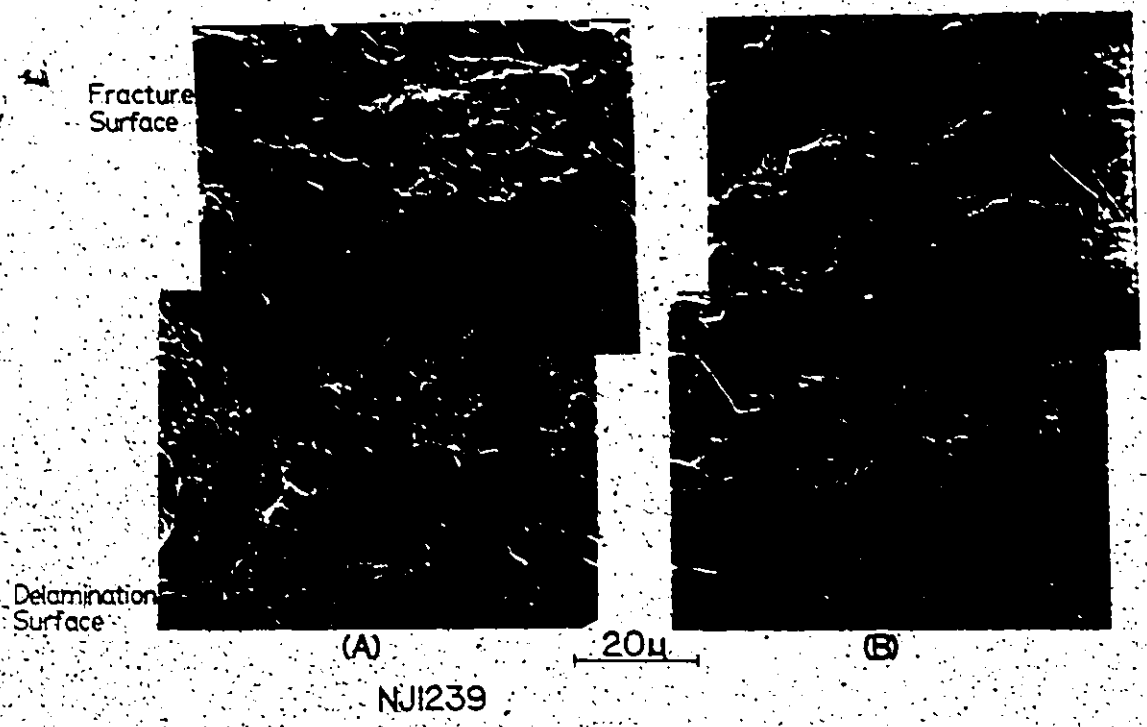

Fig. 5.46: Intersection of the delamination—surface and the final fracture surface in steel A, tested at -196°C, in the rolling direction. In Figure a, near the centre, the fracture involves a ductile fibrous mode, while in Figure b, away from the centre, the mode has become predominantly cleavage.

Propagation of the delamination crack extended beyond the necked region of the sample, where it was observed to branch. The secondary crack which resulted was oriented normal to the tensile axis. In steel A, however, the propagation of this secondary crack did not necessarily control final fracture; in some instances the terminal fracture process occurred at the minimum cross-section in the neck region. The branching and/or continuation of a delamination crack normal to the tensile axis (horizontal) is observed in Figures 5.47a and b. The delamination crack followed a path predominantly through the bainite, as seen in Figure 5.47c, however, propagation through ferrite was also observed, either in an intergranular or transgranular mode. Figure 5.47d illustrates the secondary cracking in ferrite parallel to the main delamination crack which was frequently observed. Splitting observed on the fracture surface was related in some cases to fracture in the ferrite, which lay between two closely-spaced bands of bainite or pearlite. This is shown in Figure 5.48.

In steel A, observations beneath the delamination surface indicated significant damage levels involving large plastic strains, as shown in Figures 5.49a and b. Here voids have initiated though fracture in the bainite, and are in the process of coalescing via a shear mode. Fracture in the bainite, along the tensile axis, is seen to be related to the presence of elongated inclusions, indicated by the arrows.

Figure 5.50a illustrates the damage in steel A associated with the bainite present along the centre of the sample. Figure 5.50b shows the local delamination in the bainite to arise due to the elongated

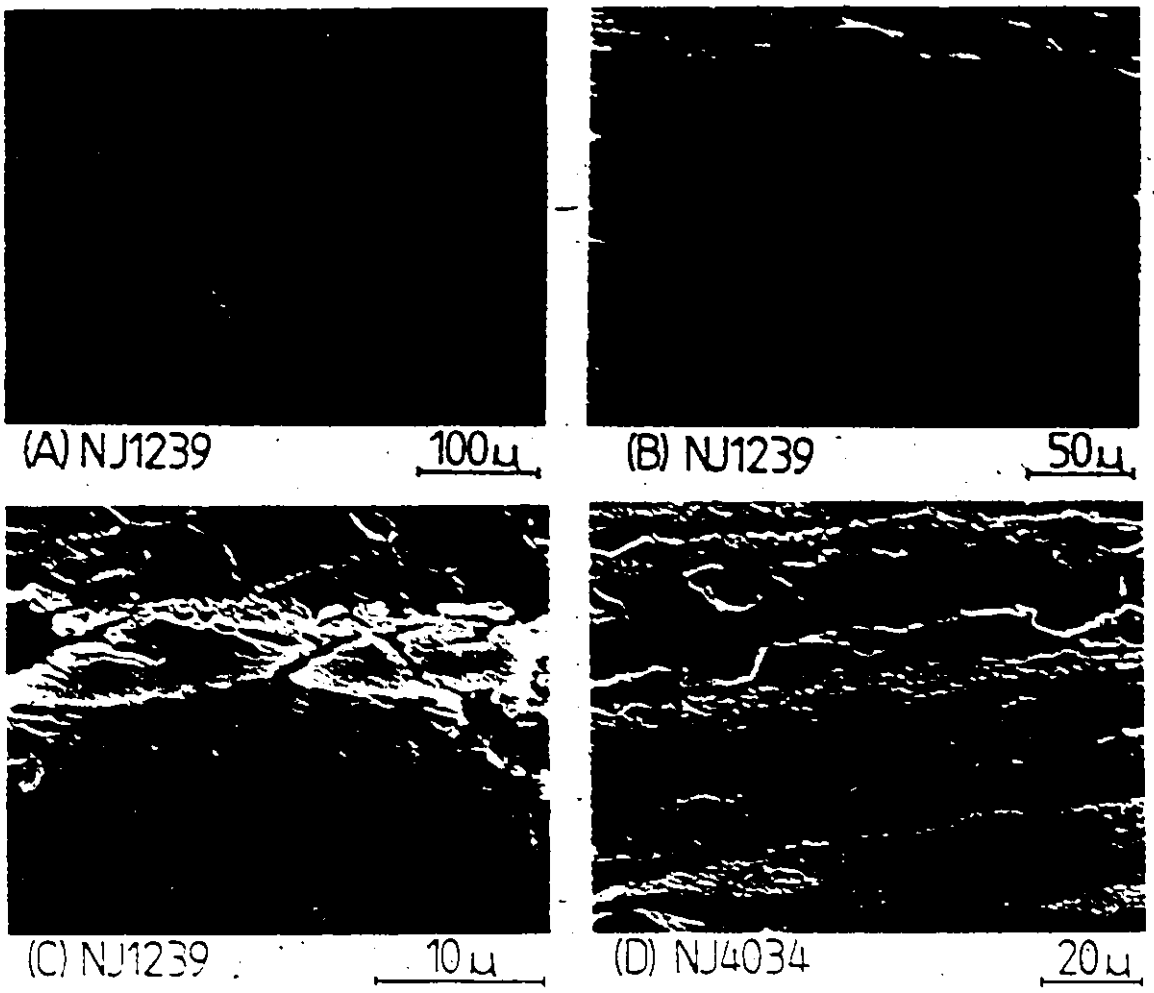

Fig. 5.47: SEM micrographs of the mode of propagation and branching of the delamination crack in steels A (Figures a, b and c) and B (Figure b). Note that the propagation path may be along the bainite (Figures b, c), or through ferrite, either in a transgranular or intergranular mode (Figure d).

Fig. 5.48: SEM micrograph adjacent to fracture surface in steel A, tested at -196°C in the rolling direction. Intergranular splitting was promoted in regions between closely-spaced bands of pearlite or bainite. Material in crack is mounting compound.

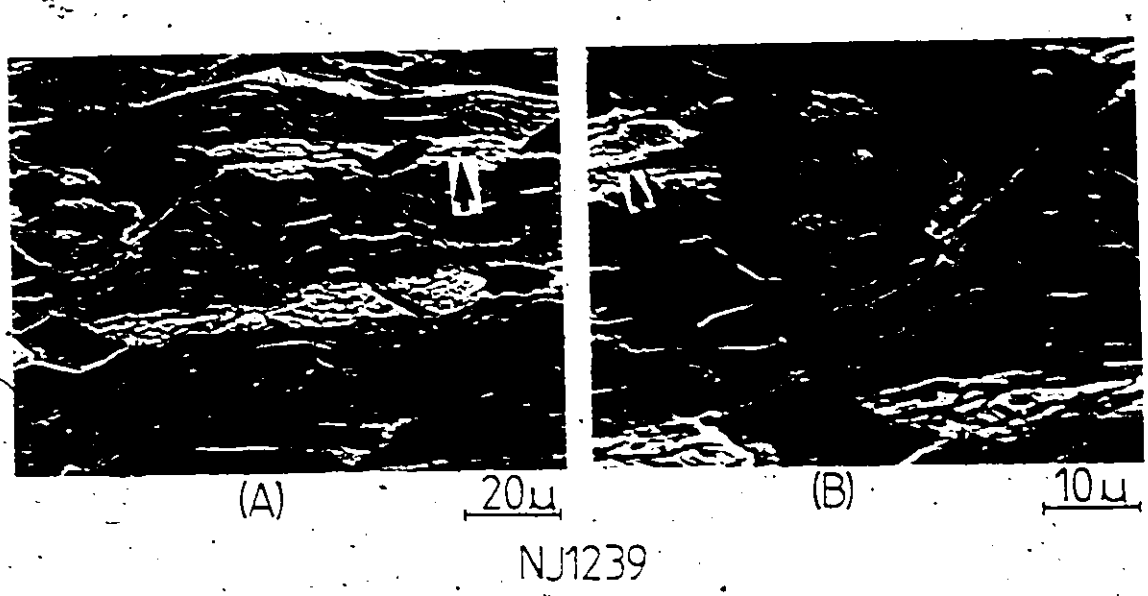

Fig. 5.49: SEM micrographs of damage which developed adjacent to the delamination surface in steel A, at -196°C. Arrows indicate inclusions as damage sites within the bainite. In Figure b, the void linkage process via localized shear was observed.

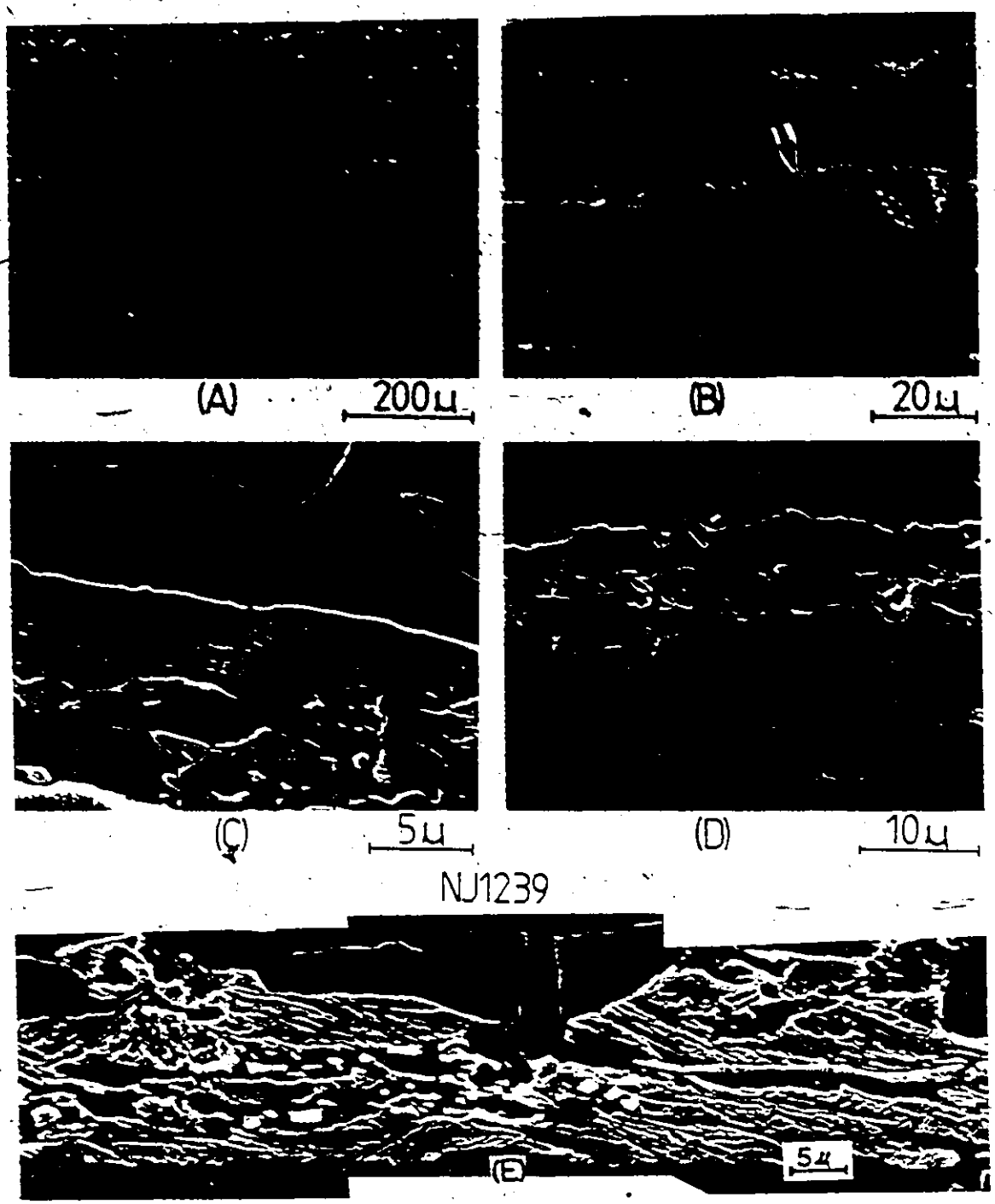

Fig. 5.50: SEM micrographs of damage in steel A along centre of sample, at -196°C. In Figure b, the arrow indicates a sulphide inclusion, which promoted local delamination. In Figures c and d (from transverse samples), sulphides elongated normal to the tensile axis promote bainite fracture. In Figure e, cleavage in ferrite was initiated at a sulphide.

manganese sulphides present within. Microcracks normal to the tensile axis were stabilized by the surrounding ferrite, as seen in Figures 5.50c and d. Here, inclusions were observed as initiation sites for cleavage in the bainite. Note that Figures 5.50c and d are observations made in samples tested in the transverse orientation, where cracking across the width of the bands of bainite was more frequently seen. Figure 5.50e illustrates cleavage in ferrite which initiated at an inclusion.

Voids were also observed to nucleate at grain boundary carbides and in pearlite (Figure 5.51a). The damage associated with the carbides present along the grain boundaries relates to the frequent intergranular cracking observed near the fracture surface, seen in Figure 5.52. Still another source of damage was the boundary separating the pearlite and ferrite regions, which in Figure 5.51b has served as either a crack initiation site or an easy path for crack propagation. Although the damage associated with intergranular carbides and pearlite was observed throughout the neck region of the sample, these microstructural components provided a more prominent source of damage near the fracture surface at the minimum sample cross-section, where the macroscopic stress and strains were a maximum.

When tested in the transverse orientation, the non-calcium treated steels exhibited lower reductions in area. Splitting was frequently observed on the fracture surface, however, the significant delamination which occurred in the samples oriented in the rolling direction did not develop in these samples. In steel B, the ductile shear mode

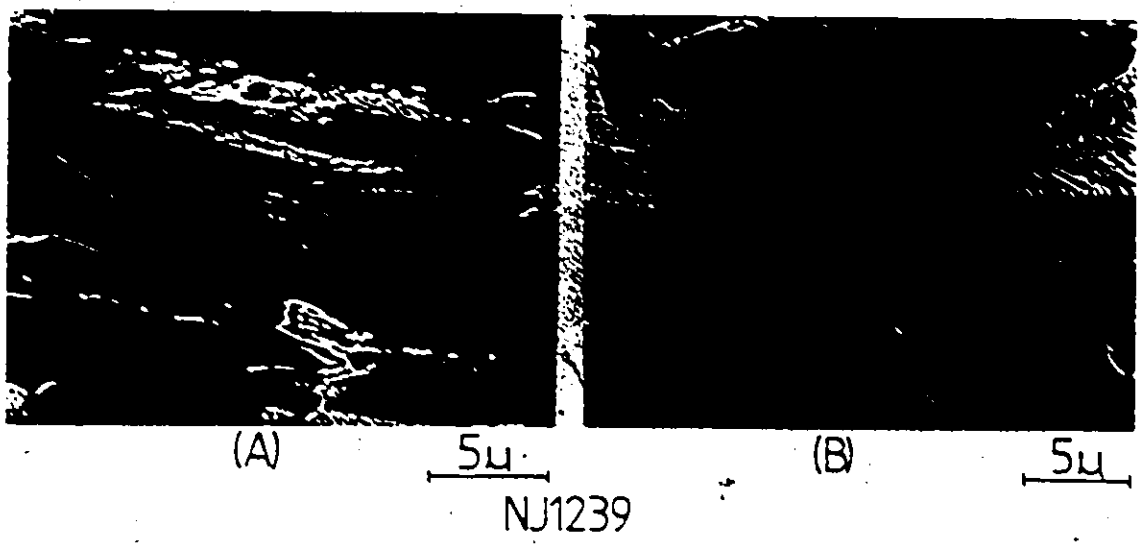

Fig. 5.51: SEM micrograph illustrating damage initiated in pearlite and at intergranular carbides (Figure a) and at the pearlite-ferrite boundary (Figure b) in steel A.

Fig. 5.52: Intergranular and transgranular cracking adjacent to fracture surface in steel A, at -196°C.

operative when tested in the rolling direction was not observed in samples oriented in the transverse direction. The fracture surface was predominantly cleavage, with the ductile mode evidenced only infrequently, usually between two closely-spaced cracks which were parallel to the tensile axis (Figure 5.53a). The high degree of splitting in this sample in the central region was related to elongated inclusions which lay normal to the tensile axis, as seen in Figure 5.53b.

The calcium-treated steels did not delaminate as the non-treated steels did. The fracture surface of steel C was almost entirely cleavage, with very little splitting evident in both rolling and transverse directions. Large calcium aluminate/sulphide inclusions, or the holes they occupied, were frequently observed, as seen in Figures 5.54a-c. In Figure 5.54a it appears that the inclusion has served as an initiation site for cleavage. Metallographic sectioning indicated damage associated with bainite cracking, shown in Figure 5.54d, however, as the amount of bainite in the calcium-treated steels was lower than in the non-treated steels, the level of damage associated with bainite was not as high in this material. The fracture surface of steel D exhibited frequent splitting when tested in the rolling direction, but relatively little in the transverse orientation. This result could be due to the lower degree of plastic anisotropy in the plane normal to the tensile axis in the transverse samples. The smaller strain in the plate through-thickness direction resulted in a less severe neck profile and thus lower tensile stresses in the neck normal to the plane of banding

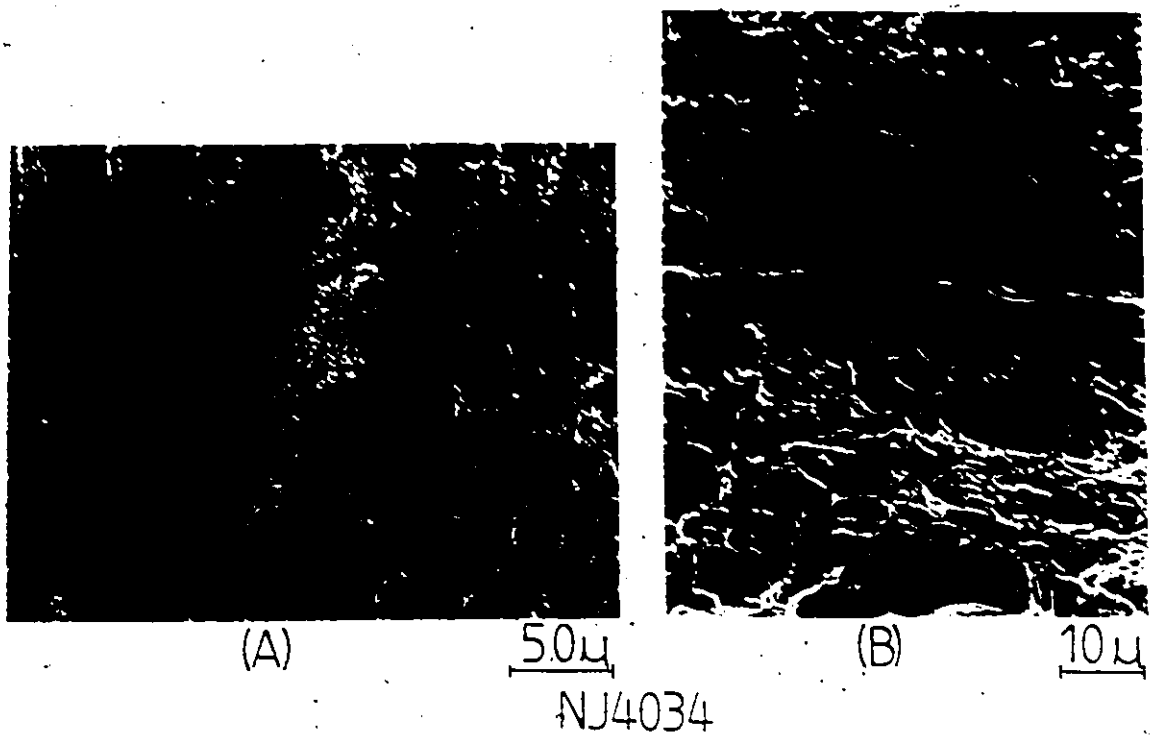

Fig. 5.53:- Fracture surface observations of splitting in steel B, tested in the transverse direction at -196°C. In Figure a, a ductile mode was promoted in the region between two closely-spaced splits. In Figure b, splitting is associated with elongated sulphide inclusions.

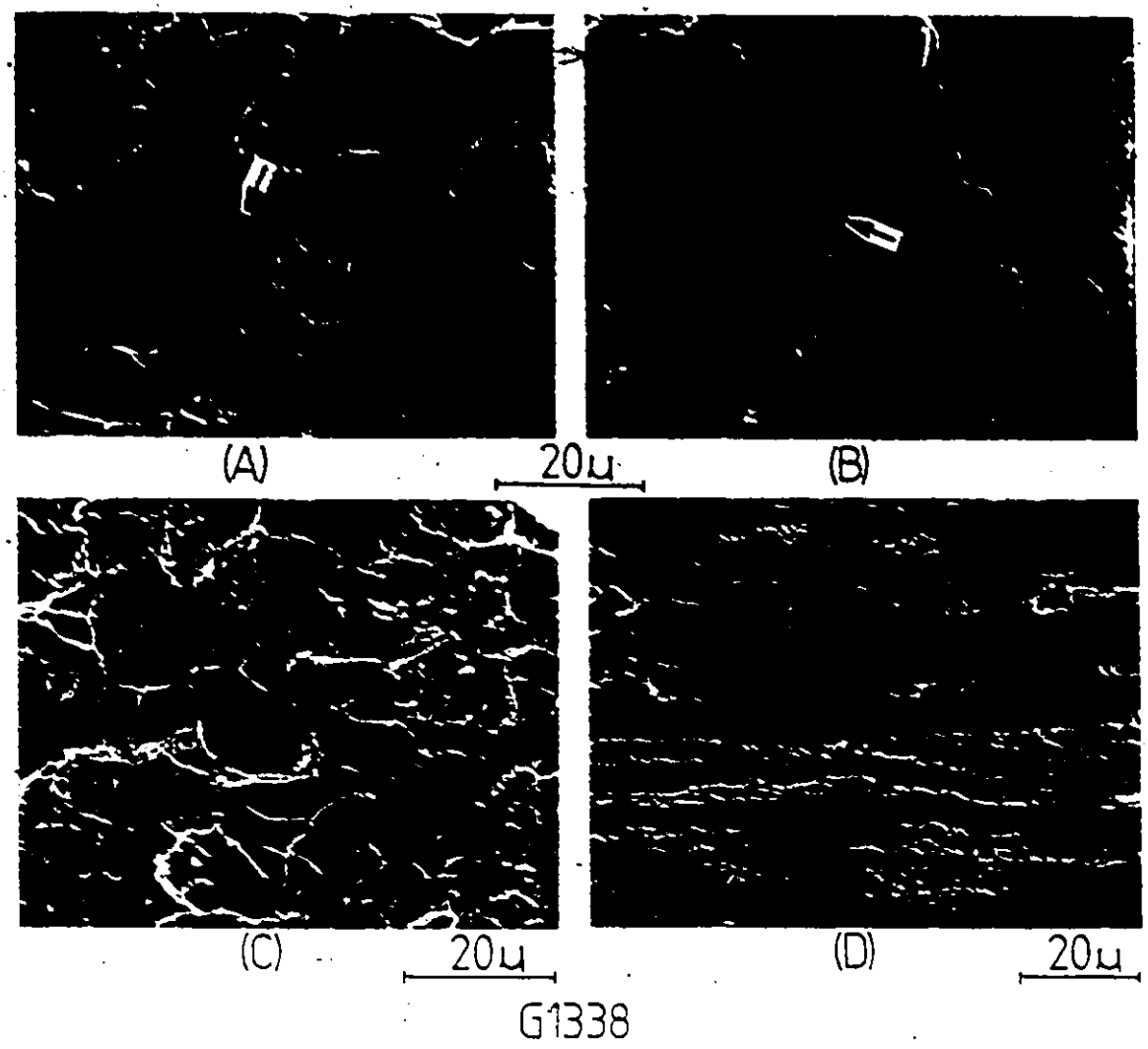

Fig. 5.54: Steel C, tested at -196°C. Fracture surface observations (Figures a, b and c) suggest that calcium aluminate/sulphide inclusions act as cleavage initiation sites. The metallographic section in Figure d illustrates the damage associated with bainite cracking.

developed. The fracture surfaces for either testing orientation in steel D, however, were mixed cleavage/fibrous. Evidence of plastic shear in the ferrite involved in the coalescence of damage associated with bainite is observed in Figure 5.55, indicating that the final fracture process in some regions was associated with considerable local deformation.

Spheroidization of the microstructure removed evidence of splitting in the calcium-treated steels, but not in steels A and B in the plate centre-line region, as seen in Figure 5.56a. The fracture surfaces of these non-treated steels were a mixture of cleavage and fibrous near the centre (Figure 5.56b), and predominantly cleavage outside the centre-line region. Close to the fracture surface, damage was observed as voids associated with the carbides, initiated at the particle interface or through particle fracture. Cleavage cracks were also present, some of which were associated with carbides. These features are seen in Figure 5.57(a) and (b). Figure 5.58 illustrates the distribution of damage which accumulated in steel A along the centre of the sample, within the banded regions of spheroidal carbides. Microcracks have developed across the width of the band as a result of the damage initiated at the carbides. These microcracks have been stabilized by the surrounding ferrite which contains a low volume fraction of second phase. Also, cracks parallel to the tensile axis are evident, which are associated with the elongated sulphides present at the plate center line.

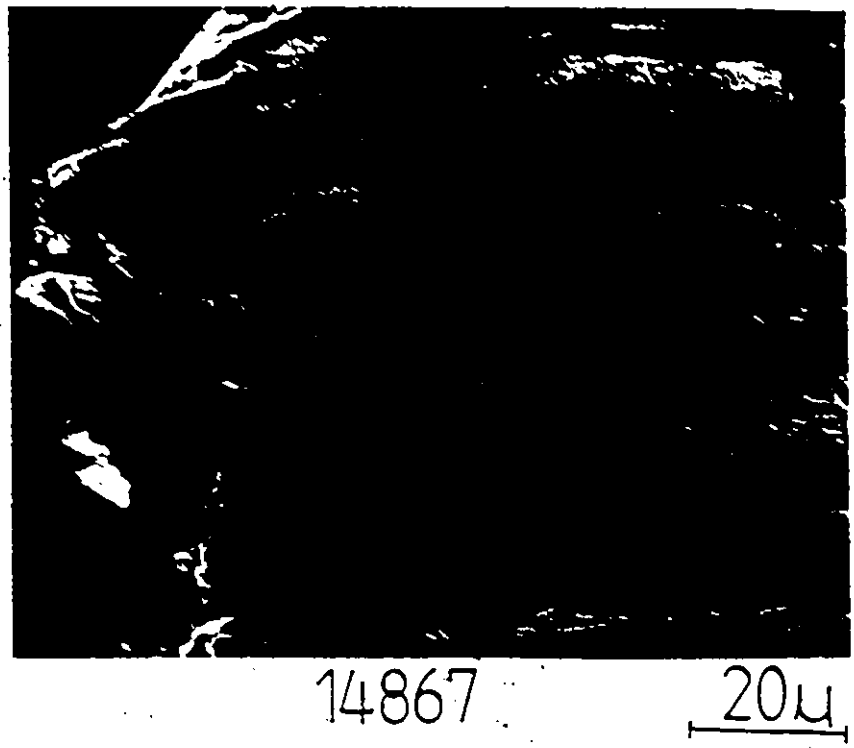

Fig. 5.55: SEM micrograph of region adjacent to fracture surface in steel D, tested at −196°C in the transverse orientation. Coalescence of the damage initiated at the bainite has involved considerable local ductility.

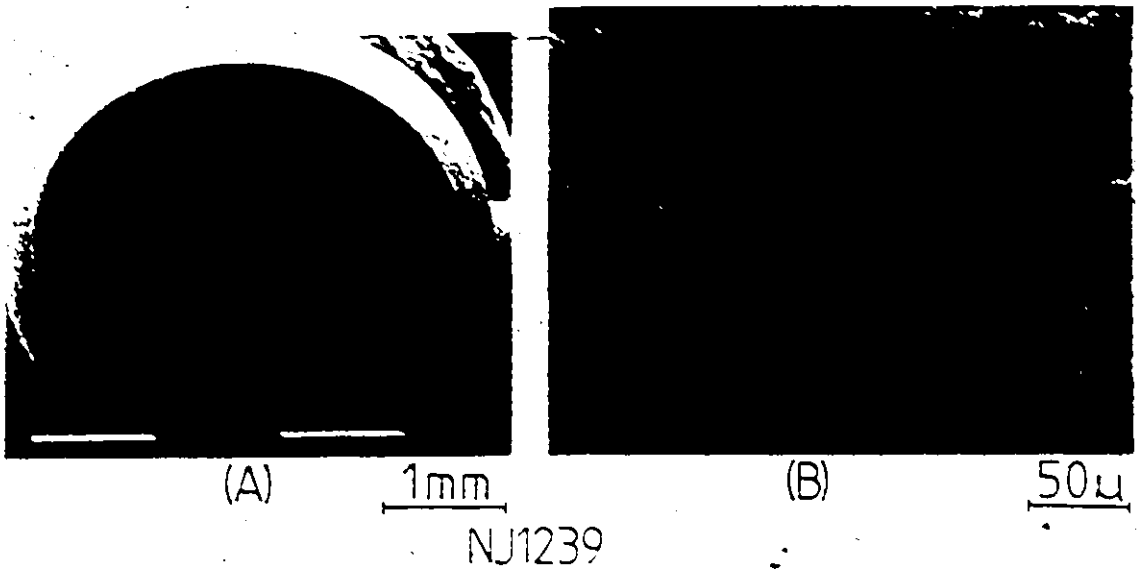

Fig. 5.56: Fracture surface of steel A in spheroidized condition, tested at -196°C. Delamination was eliminated through spheroidization, however, splitting was still evident. The fracture mode was mixed cleavage-fibrous.

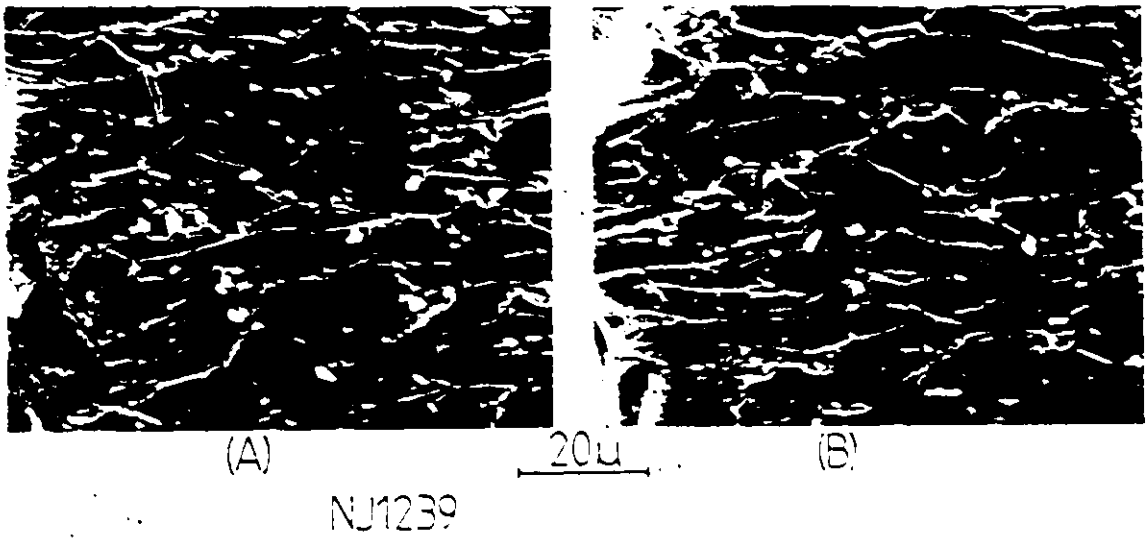

Fig. 5.57: SEM micrograph of region adjacent to the fracture surface in steel A, spheroidized, tested at -196°C. Carbides were associated with both void development and cleavage initiation.

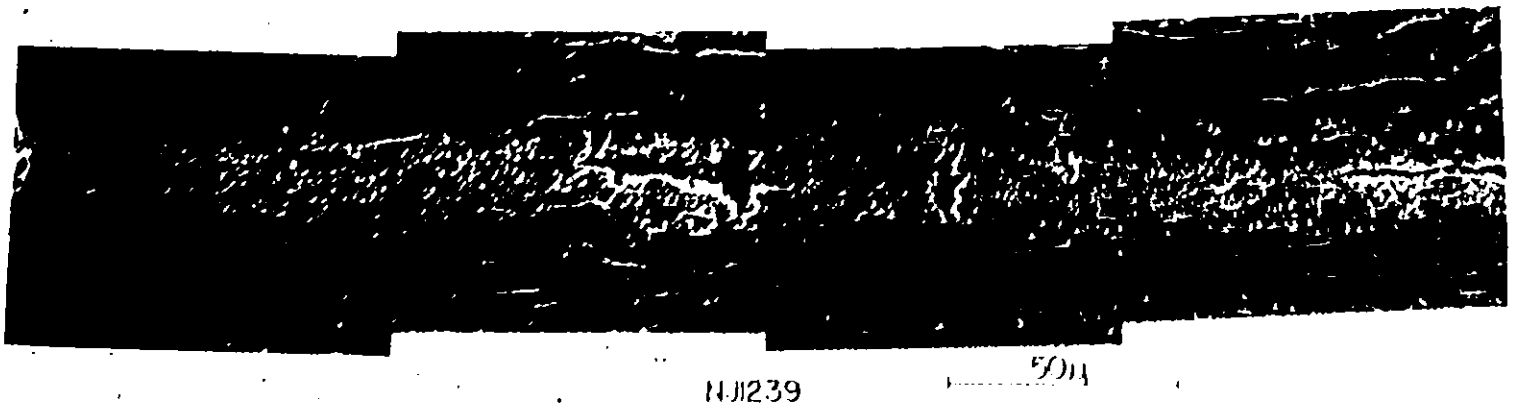

Fig. 5.58: SEM micrograph illustrating the damage which developed within the banded regions of carbides in steel A, in the spheroidized condition. The tensile axis is horizontal. Microcracks parallel to the tensile axis were associated with elongated sulphide inclusions. Note the cracks normal to the tensile axis, which have been stabilized in the ferrite regions.

The spheroidization treatment removed completely any evidence of splitting on the fracture surface of steel D, however, the fracture mode remained mixed cleavage/fibrous. Cavitation associated with carbides was the predominant form of damage, however, a relatively a minor amount of cleavage cracking was observed in the region just behind (i.e., within a distance of a few grains) the fracture surface. The fracture surface of steel C, which had relatively low ductility, was entirely cleavage. The behaviour of this sample appeared to be limited by the presence of large calcium aluminate/sulphide inclusions. These were frequently observed on the fracture surface, and may have influenced the initiation of cleavage cracking.

5.4.4 Summary of Experimental Results

Prior to discussing the foregoing results it is of value to put the current work into perspective in regard to advances in steelmaking technology. In the past decade, major advances have been made in the control of both the morphology and global levels of inclusions in steels. However, in products which are continuously-cast and control-rolled two major problems can arise. Segregation can occur at the centre-line due to the form of the liquid-solid interface and the flow of material in the mushy zone. On subsequent rolling both inclusions and transformation products can be aligned parallel to the rolling

plane. It is thus important to consider the role of the segregated inclusions in association with transformation products in fracture.

In the present study, the following salient features were observed:

(i) With the exception of the tensile tests performed at room temperature in the rolling direction, the fracture behaviour in the current steels was controlled by the inclusions present. Their effect was due either to a large spherical size or their association with the brittle transformation products along the centre-line. The orientation of the elongated sulphides with respect to the tensile axis markedly influenced delamination behaviour in the non-calcium treated steels at low temperatures.

(ii) At low temperatures, the increase in flow stress resulted in several operative sources of damage, associated with the different microstructural components. Intergranular carbides and the pearlitic component contributed more significantly to the overall damage level observed. It was also evident that closely-spaced microstructural components having a higher flow stress than the surrounding ferrite could influence the local conditions of stress and/or strain. This effect promoted the local level of damage in the ferrite in the region between the harder components. However, the inclusions and centre-line transformation products continued to dominate the overall fracture behaviour.

(iii) The bainitic phase present along the centre-line was the dominant source of damage in deformation at room temperature, for tests performed in the rolling direction. The distribution of microcracks in this semi-continuous phase suggested a composite mode of load transfer from the surrounding ferrite. This observation allows the estimation of the fracture stress of the bainite.

Observation suggested that the deformability of bainite relative to the ferrite was low. In tests performed under superimposed pressure, the shear mode of fracture was promoted. The effect of the applied pressure was to alter the deformation pattern in the ferrite in relation to the microcracks which crossed the width of the band of relatively non-deformable bainite. Local shear bands developed in the ferrite adjacent to these microcracks, extending across the region between bands of the non-ferritic components. These were observed to make an angle of $37° \pm 2°$ with the plane of the bainite. The angle which the macroscopic shear bands made with the tensile axis was different from this, which was closer to the direction of maximum shear stress, on a macroscopic scale.

The transition from the ductile fibrous to ductile shear mode of fracture was not distinct. This broad transition in fracture mode was apparently influenced by the effect of pressure on the accumulation of damage within the shear bands, allowing higher strains to develop locally within the bands prior to final fracture.

An influence of pressure on tensile instability was also noted.

5.5. Discussion

This study has identified several microstructural components which are involved individually or interactively in damage accumulation processes. Their relative importance in controlling the mode and conditions of fracture was observed to depend upon temperature, stress and the stress state with respect to the microstructure.

Despite the low average inclusion content of these steels, the size, morphology and/or distribution of inclusions resulted in a direct or indirect controlling influence on fracture behaviour, particularly at low temperatures and in the through-thickness orientation. At low temperatures, fracture surface observations indicated that the large spherical inclusions in the calcium-treated steels served as cleavage initiation sites. Steel C, with a larger volume fraction of inclusions than steel D, and whose average inclusion size was also larger, exhibited a predominantly cleavage mode of fracture. The fracture surface of steel D was mixed cleavage/fibrous. The reduction in area and fracture stress of steel D, however, were only slightly greater. This suggests that the critical conditions for either cleavage or ductile fracture in the pearlitic regions, whether or not they are significantly different within this component, are not separated by large differences in macroscopic conditions of stress and/or strain. (Note that no significant differences in pearlite morphology were evident between these two steels.)

At low temperatures the fracture behaviour of the non-calcium treated-steels was controlled by the elongated manganese sulphide inclusions contained within the bainite located along the plate centre-line. The evidence of only minor splitting in the spheroidized sampled isolated the effect of inclusions on splitting. Thus the presence of the brittle bainitic phase is also required in the delamination process as a low-toughness path for crack propagation. The tensile stresses developed in the neck can cause the initiation of a crack which can propagate in an unstable manner through the bainite along the tensile axis, resulting in the delamination observed. Cracks were observed to develop across the bainite bands normal to the tensile axis, occasionally associated with inclusions, but these cracks were arrested and blunted by deformation in the ferrite. The possible influence of an enhanced crack tip stress field due to the transfer of load from ferrite to bainite was not sufficient to overcome crack arrest in the ferrite.

The absence of gross delamination in samples tested in the transverse orientation could be explained by the orientation of the elongated sulphides relative to the stress axes, and by the elliptical shape of the planar clusters of inclusions, whose major axis is oriented in the rolling direction. In the transverse orientation, the elongated inclusions were observed to promote cracking in the bainite normal to the tensile axis, which propagated across the thickness of the individual bands of bainite. This increase in damage level led to lower fracture strains. Thus, the neck in the tensile sample did not develop as fully

in the transverse orientation samples, and the tensile stresses normal to the plane of the inclusion clusters and the bands of bainite was not as high.

The following point is argued on the assumption that we may consider the clusters of inclusions as planar elliptical flaws, or cracks in a brittle material (the bainite). The plane of these cracks is parallel to the tensile axis, so that the tensile stresses normal to the plane arise due to the development of the neck. The stresses around an elliptical flaw in tension normal to the crack face are greatest at the minor axis (Sih, 1973). However, the stress in the neck normal to the tensile axis is a maximum at the minimum sample cross-section (Argon, Im, and Needleman, 1975). When the maximum dimension of the inclusion cluster (i.e., the flaw) is oriented normal to the tensile axis, in the transverse samples, we might expect that the fracture stress in bainite normal to the plane of the clusters would be attained at a lower level of stress in the neck, normal to the tensile axis. Thus the neck need not develop as fully before the fracture condition is attained, and a lower reduction in area would be predicted. This, of course, assumes that final fracture is controlled by unstable fracture in the bainite in a plane parallel to the tensile axis. The observations of cracks in bainite normal to the tensile axis, and splitting on the fracture surface, however, suggest that both these sources of damage influence final fracture. In the tensile samples taken from the rolling direction, cracking normal to the tensile axis was not as frequently observed. This allowed the neck to develop further, and the higher

transverse tensile stresses which resulted, combined with the larger flaw dimension along the tensile axis, could produce higher stresses at the cluster periphery. This could have promoted the initiation and propagation of an unstable crack along the tensile axis and the resulting delamination.

At -196°C, data from Kotilainen (1980a) and Hahn (1984) give the K_{IC} for a bainitic steel between 30 and 40 MPa-$m^{-\frac{1}{2}}$. Assuming this value for the centre-line transformation products in steel A, we can estimate the critical flaw size. Although the development of the neck was not followed during deformation, the neck profile of the fractured sample gave an (upper limit) estimate of the transverse tensile stress at the minimum cross-section as 0.25 of the average section stress. This value was obtained using the neck radius of the sample profile in a view parallel to the major axis of the cross-section. The Bridgman correction for a neck in plane strain in an isotropic material was employed. Taking the average net section stress as 1500 MPa, and assuming a Poisson ratio of 0.3, Irwin's (1962) result for a circular crack in an infinite medium yields an estimated critical crack size at the given fracture condition of 1 to 2 mm in diameter.

The largest inclusion clusters observed, however, were approximately 300 μ. It is noted that these are not ideal cracks, and the stresses at the periphery of a cluster will not be as high as that given by crack analyses. Several factors could contribute to the apparent brittleness of the centre-line transformation product with respect to the

above analysis. First, as stated, it was not determined whether martensite was present along the centre-line. The low toughness of this material would not support large flaws. Secondly, the ratio of sample dimension to inclusion cluster size was approximately 10, so that the stress intensity at the periphery of a cluster would be somewhat higher than in an infinite solid, the assumed geometry in Irwin's analysis. However, the dominant effect is likely due to the presence of several inclusion clusters within the region of the neck. Thus, fracture results not from the action of an isolated flaw of critical size, but rather due to a critical level of damage in the plane of the centre-line phase. The results of ambient temperature tests in the through-thickness orientation yielded very low reductions in area and fracture stresses. Fracture surface observations indicated a high area fraction of elongated inclusions, so that the centre-line plane is indeed a very heavily damaged region in this material, and that this damage occurs at low stress levels.

At low temperatures, the intergranular cracking associated with grain boundary carbides and the damage (both microcracking and void growth) which developed in the fine pearlitic regions provided other sources of damage. These processes operated concurrently with those involving inclusions and bainite, offering alternative, and possibly competitive modes of damage accumulation. The damage levels which these carbides and pearlite contributed were relatively low however, and thus they did not control final fracture. Data from Lewandowski and Thompson (1985) indicate that the fracture stress for fine pearlite at -196°C is

at or above the observed fracture stresses in these steels. Thus the influence of the pearlitic component in controlling fracture is precluded by fracture in bainite.

In regions where the local stress state is likely to be altered by the local microstructure, the occurrence of intergranular cracking was intensified. Evidence of this was seen in Figure 5.48, where two closely-spaced non-ferritic bands, with a higher flow stress than the surrounding ferrite, could have exerted a degree of plastic constraint, intensifying the local stress in the ferrite to promote intergranular fracture. The influence of local microstructural parameters on the local stress state should thus be recognized in determining the conditions under which the processes involved in damage occur.

It should be noted that if the large inclusions and brittle transformation products were not present, fracture might then be controlled by the intergranular carbides or pearlite. It has been suggested (Hero et. al., 1975; Bramfitt and Marder, 1979) that intergranular carbides or a banded distribution of pearlite may act as a source of delamination fracture in some HSLA plate steels at low temperatures.

Further evidence suggesting the influence of local stress state on the operative fracture mode and on the competition between fracture and further deformation was observed. Beneath the delamination surface, the stress triaxiality was lowered due to the free surface created. This allowed continued plastic flow, and large local strains developed in the shear zone involved in the void coalescence process. This

observation suggests that there may have been plastic deformation during or after the delamination process, and that delamination was not an unstable process resulting in immediate final fracture.

Fracture surface observations also illustrated a possible influence of local triaxiality on the mode of crack propagation. Near the centre of the fracture surface, closer to the region of crack initiation, the flaw size was small and the local stress triaxiality low, and a ductile mode of crack propagation was observed. However, further away from the centre, at a point where the flaw size and crack tip triaxiality were large, the mode of crack propagation was predominantly via brittle cleavage. Hahn (1984) has discussed the influence of crack propagation rate on the transition from ductile to cleavage behaviour, and it is possible that the brittle mode arises due to the high strain rates inherent in rapid crack advance.

The observation of plastic shear involved in void coalescence occurred at lower strains in deformation at low temperatures than at ambient temperature. The level of stress operating in this process at low temperature, however, was considerably higher. Thus, one must consider both the stress and the strain level, and most likely the work-hardening rate in attaining the conditions at which shear processes can operate. However, one must also consider the magnitude and triaxility of the stress state, so that a fracture mechanism such as cleavage does not interrupt continued plastic flow.

The influence of stress state could explain the marked difference in final fracture behaviour between steels A and B at -196°C when tested in the rolling direction. Both steels delaminated, however, the lateral-strain in the direction normal to the rolling plane was higher in steel B. This was due to a smaller inclusion cluster size and lower volume fraction of centre-line bainite in steel B, allowing continued necking before delamination occurred. Delamination through the major axis of the elliptical section in these specimens would more effectively relieve the triaxial stresses in the neck, because the dimension of the minor axis is considerably smaller. The thin section and plane stress condition could allow the ductile shear failure observed in steel B to occur without the intervention of a competitive cleavage process. The neck in steel A did not develop as fully, and in particular strains in a direction normal to the rolling plane (ε_1 in Table 5.5) were not as high, so that the fracture events following delamination could have been influenced by a remaining triaxiality in the stress conditions.

The deformation and fracture characteristics of these steels at ambient temperatures were qualitatively similar to those observed in laminated composites. At large strains in the tensile samples the strain normal to the rolling plane was significantly greater than that in the rolling plane, normal to the tensile axis. This anisotropy in deformation behaviour allowed reductions in area with a minimum of deformation of the bainite. The resistance of bainite to deformation,

relative to ferrite, was observed in compression (Figure 5.20) where locally inhomogeneous deformation patterns developed due to the inhomogeneity in bainite deformation. This increase in deformation of bainite for a given macroscopic strain and the additional redundant plastic deformation in the ferrite to accommodate the buckled pattern of bainite could explain the higher flow stress in compression than in tension.

The banded bainitic structure along the centre-line region provided the predominant microstructural component initiating damage in room temperature deformation. Where the morphology of the bainite was uniform, the regular spacing of fractures along the bainite suggested a composite mode of load transfer from the ferrite to bainite. The transfer length is then equal to the spacing between the fracture sites, and is associated with the fracture stress of the bainite. To estimate the fracture stress we note the observation that the width of a band of bainite in the rolling plane normal to the rolling direction was much greater than the thickness of the band. For this geometry the distance from the end of the bainite plate (assumed to be rigid) at which the tensile stress is equal to the fracture stress is given by (Kelly, 1972; Piggott, 1980),

$$\ell_t = \tfrac{1}{2} \frac{\sigma^b_{frac}}{\tau^\alpha_{flow}} t = \frac{\sqrt{3}}{2} \frac{\sigma^b_{frac}}{\sigma^\alpha_{flow}} t \qquad (5.1)$$

where t is the thickness of the bainite, σ^{b}_{frac} the tensile fracture stress of bainite, and σ^{α}_{flow} and τ^{α}_{flow} the flow stress in tension and in shear, respectively, for ferrite. ℓ_t is then the spacing between fracture locations in the bainite.

Fracture in the bainite was observed over the extent of the necked region of the sample. This suggests a reasonable overall stress at which bainite fractures as the stress at which necking initiates, which for steel A was 694 MPa. The most frequently observed values of $\frac{\ell_t}{t}$ were between 2.5 and 3. Assuming the flow stress of the ferrite as the average, or macroscopic flow stress at necking, the fracture stress for bainite obtained through equation 5.1 is between 1990 and 2370 MPa. This is an agreement with Kotilainen's (1980a, 1982) values of 2000 to 2200 MPa at room temperature. The thickness of the bainite bands was commonly of the order of 10-15 μ, so that this dimension was equal to the characteristic dimension for cleavage processes in bainite determined by Kotilainen (1982). Thus a direct comparison can be made between the two results.

The two assumptions made in estimating the fracture stress for bainite should be considered further. The bainite was assumed to be rigid, however, data from Brozzo et. al. (1977) and Kotilainen (1980a) give the room temperature yield stress for various bainitic structures as between 600 and 720 MPa, dependent upon the bainite packet size and lath substructure. If the bainite does deform, then the stress level in

less than that given by the rigid laminate model. However, observations made in the current steel on the pattern of deformation of ferrite, as indicated by the ferrite grain boundaries, suggest that the deformability of the bainite relative to ferrite at applied stresses greater than the necking stress is very low.

The investigation of Kotilainen considered a fully bainitic structure, with a packet size of 3 μ. The bainite packet size was not determined in the present steels, or indeed, if any martensite was present along the centre-line. The metallographic observations suggest that the flow stress of the centre-line transformation products in these steels was considerably different from that of the bulk bainitic structure studied in Kotilainen's (1980a,b) work, and that the microstructures may not be directly comparable.

The second assumption in estimating the fracture stress of bainite was in the use of the average section stress as the flow stress of the ferrite matrix. The matrix flow stress is lower than the average stress, the result of the load borne by the bainitic and pearlitic components. The average volume fraction of the non-ferritic components was approximately 15%, and the higher flow stress in compression suggests that the flow stress in the ferrite is less than the average stress (the increase in flow stress due to an increase in bainite deformation for a given overall deformation, in compression, rather than fracturing, as in tension, suggests a significant influence of the deformation properties of the non-ferritic component on the overall behaviour), however, one should note that this increase in flow stress

(~ 20%) also reflects the enhanced work-hardening in the ferrite matrix due to the redundant deformation which accomodates the buckling in the bainitic structure.

Under compression at room temperature, the ferrite grain boundaries indicated very high strains adjacent to the bainite. No evidence of shear banding was observed. This suggests that the shear bands observed in tensile tests under superimposed hydrostatic pressure were not the onset of some substructural instability in a homogeneous deformation mode, that is, they did not occur solely due to the high strains involved. In addition, shear band development was not associated with the inclusions observed in the neck region, so that damage associated with voids, or free surface effects were not the primary site for the initiation of localized shear. The development of localized shear appears to require damage due to the fracture of bainite, but involves the local stress state and the low deformability of bainite relative to ferrite, and the laminate geometry. Observations suggested the sequence of events in the development of localized shear which are illustrated in Figure 5.59. Fracture across the thickness of a band of bainite and the subsequent separation of the broken faces with continued strain opens up a void, however, the lateral pressure $P-\sigma_{neck}$ (where P is the applied hydrostatic pressure, and σ_{neck} the transverse stress due to the neck geometry) and the relative hardness of the bainite results in the extrusion of ferrite into the void.

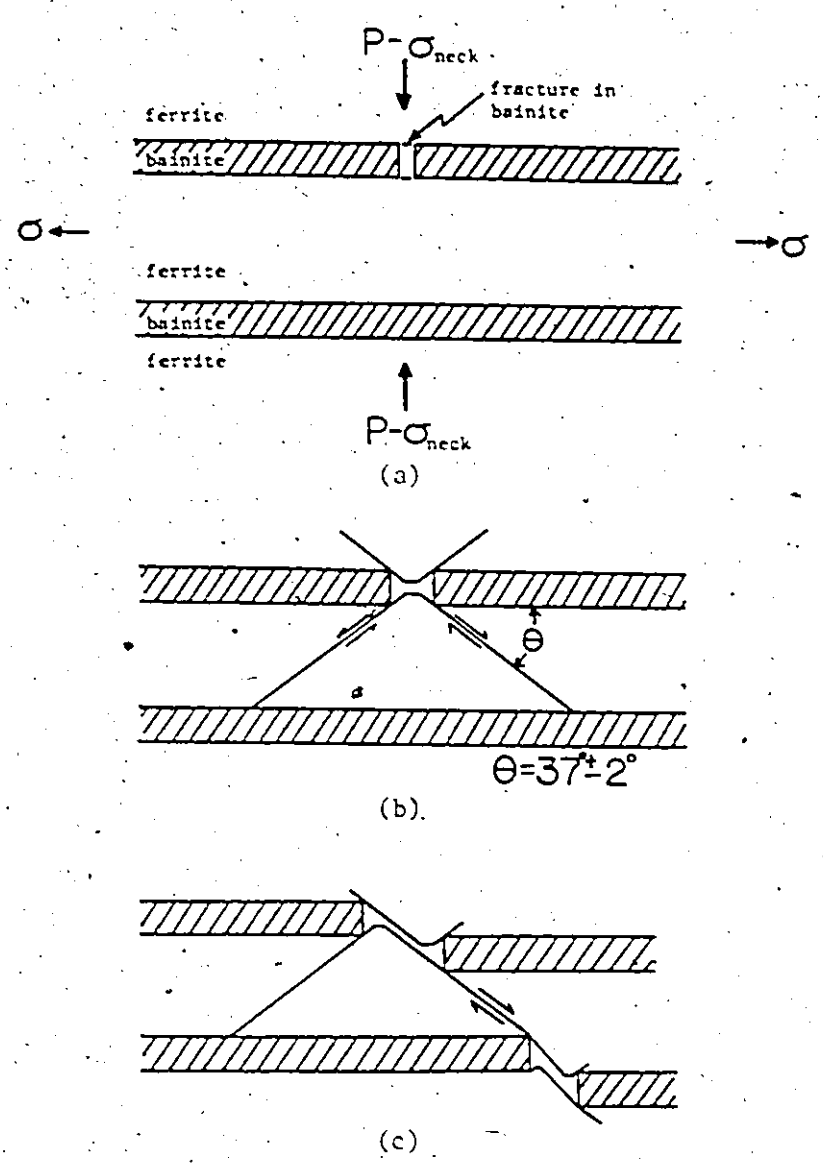

Fig. 5.59: Schematic illustration of the sequence of events in the development of bands of localized shear. (a) Fracture in bainite. (b) Ferrite is "extruded" into the void which opens up at the local fracture site, under the influence of the stress $P-\sigma_{neck}$. This leads to the development of a shear band which extends to the adjacent band of bainite. (c) Fracture in the adjacent bainite allows continued propagation of shear band. Tensile axis is horizontal. The normal to the page corresponds to the plate transverse direction.

At the strains at which these processes are occurring, the incremental strains in the rolling plane normal to the tensile axis (corresponding to the direction out of the plane of the page in Figure 5.59) are small relative to those normal to the rolling plane. Thus, an analogy might be drawn between the local damage process occurring here and a plane strain punch or extrusion problem. The geometry and boundary conditions involved in this problem, however, would not be amenable to a simple analysis.

With a shear stress along the bainite/ferrite interface due to the difference in flow stress between the two phases, the direction of maximum shear stress local to the bainite must rotate towards the tensile axis, away from the 45° orientation. If the orientation of the shear bands local to the bainite were determined by the direction of maximum shear stress, they would be expected to make an angle of less than 45° with the tensile axis. The observed angle of 37° ± 2° supports this. It is suggested here that, although the initiation of localized shear is in a region of stress and strain concentration near the end of the fractured bainite, the subsequent propagation of the shear band which develops is along the direction of local maximum shear stress. The propagation of a local shear band from the initiation point to a neighbouring band of bainite (depicted in Figures 5.59b and c) and beyond, however, is likely to be a very complex instability.

Anand and Spitzig (1980, 1982) have noted that, in metals, the orientation of any shear bands which develop are often observed to make angles of less than 45° with the tensile axis. In an aged maraging

steel in plane strain tension they observed shear bands which were 38° ± 2° to the tensile axis. The development of a macroscopic shear band was through the growth and interaction of smaller shear bands, so that the orientations of the micro- macro-shear bands were the same. Anand and Spitzig (1982) were able to reasonably predict the onset and orientation of the micro-shear bands based on the continuum bifurcation analysis of Rudnicki and Rice (1975) for pressure-sensitive, plastically dilatant elastic-plastic materials. However, they did not investigate the source of shear band initiation. In this study we have identified their origin in the steels studied as the result of both damage and the pattern of local deformation which develops in a heterogeneous microstructure with a relatively hard phase.

In the steels studied, the spatial correlation of the micro-shear bands local to the bainite to produce a macroscopic shear band, and the subsequent propagation of this macro-shear band did not follow the orientation of the micro-shear bands. This is contrary to the observations of Anand and Spitzig. Although on a local scale between the bands of bainite the orientation of maximum shear stress may be rotated away from the 45° orientation towards the tensile axis, on a macroscopic level the maximum shear direction is at 45°. This orientation is very close to that observed here for the macroscopic shear bands. Thus, in the present materials investigated, the orientation of the macroscopic shear bands appears also to be controlled by the maximum shear stress direction. The discrepancy between this observation and that of Anand and Spitzig could be due to a difference in the density of micro-shear

bands which develop. They appeared to occur with a much higher density in the maraging steels, so that macroscopic shear band formation was due to the coalescence of growing micro-shear bands. In the present HSLA steels, however, the orientation of the macro-shear bands appeared to arise through the propagation of a few micro-shear bands originating in the centre-line region.

Although at 690 MPa, the operative fracture mode was shear, the development of the shear bands (i.e., the dimensions of the shear bands and the shear strains within) at failure was much more pronounced in tests at 1100 MPa. At 1100 MPa, some shear bands which were 37° to the tensile axis were observed to extend over a region of several band spacings. This evidence suggests that the transition from the ductile to the shear mode of fracture with increasing pressure is not sharply delineated, but rather occurs over a range of imposed pressure. This transition is seen as a more fully developed shear band structure and arrangement of shear bands, on both a local and a macroscopic scale. The shear portion of the fracture surfaces of specimens tested at 690 MPa exhibited more frequent dimpling than those of specimens tested at 1100 MPa. The imposed hydrostatic pressure thus suppresses the development of damage (with an associated dilatancy) in the shear bands, allowing greater shear strains to accumulate within the shear bands prior to failure. This observation has been made quite convincingly in a 7075 aluminum alloy by Teirlinck (1983).

It was observed that pressures of 690 MPa could significantly suppress the development of damage in the pearlitic regions. However,

over the range of pressure investigated the influence in retarding fracture in the bainite was not as effective. This evidence suggests that the flow stress of the bainite is very near to its fracture stress, and the fracture strains are low. If we consider the centre-line region as a discontinuous laminated composite, the tensile stresses in the bainite are dependent upon the shear stress acting at the interface, assumed to be given by the flow stress of the ferrite matrix. Thus, if the bainite is brittle in the sense that the fracture condition is given by a maximum tensile stress criterion, an applied pressure should not have a significant effect in suppressing fracture in the bainite. If the bainite does deform, the amount of deformation prior to fracture would be expected to increase somewhat prior to fracture. However, the assumption regarding the strength of the bainite/ferrite interface should be questioned. If the interface strength in shear is less than the shear flow stress of ferrite, and if it were pressure-dependent such that it increased with pressure on the interface, an increase in load transfer to the bainite with pressure would result. This would contribute to a negative effect of pressure on ductility of the bainite component, so that the net effect of applied pressure on the fracture behaviour of bainite in these steels could be small. These effects could explain the observed insensitivity of fracture in bainite to imposed pressure.

There appeared to be a real influence of pressure on the condition of tensile instability, beyond the effect of pressure on the flow stress. As damage was observed at approximately the level of strain at

which necking initiated, the strain-rate independent Considère criterion for tensile instability should be modified to include the influence of damage. Assuming that the reduction in flow stress due to damage is given simply by the reduction in cross-sectional area, the instability condition is given by

$$\frac{1}{\sigma}\frac{d\sigma}{d\varepsilon} = 1 - \frac{df_v}{d\varepsilon} \qquad (5.2)$$

where f_v is the volume fraction of voids, assumed to be uniformly distributed, σ is the average section stress over the dimension of the sample (the stress in the material is greater than σ), and ε is the macroscopic tensile strain, which includes the dilation due to the accumulation of damage. The influence of a superimposed pressure in suppressing the development of damage in the pearlitic regions and around inclusions and the growth of damage initiated through fracture of the bainite could thus explain the shift in the necking condition to higher stresses and strains. The applicability of equation 5.2 to the present steels, however, is questionable, as the damage distribution in these materials was confined predominantly to the region near the centre-line , with a higher volume fraction of inclusions and non-ferritic components. The effect of a non-uniform distribution of damage on tensile instability may require additional information regarding the spatial distribution of damage, so that the influence of variations in local stresses and damage accumulation rate may be appreciated.

To conclude this discussion, it is useful to consider the approaches existing in the literature which attempt to map the observed fracture modes into regions of space defined by variables related to stress state, strain and temperature. These defined spaces include

(i) - $\bar{\sigma}$ - P space (Ashby et. al., 1985), where $\bar{\sigma}$ is the effective stress, and P the applied pressure.

(ii) σ_{max} - $\bar{\varepsilon}$ space (Otsuka et. al., 1979), where σ_{max} is the maximum tensile stress, and ε the effective strain. Results at different temperatures may be given in this form of map.

(iii) $\frac{\bar{\sigma}_{mean}}{\bar{\sigma}}$ - T space (Shimura and Saito, 1980), where σ_{mean} is the mean hydrostatic tensile stress component, and T the temperature.

It has been observed (Shimura and Saito, 1980) that the positions of boundaries separating the different fracture modes are sensitive to microstructure. In the present HSLA steels, however, a variety of microstructural components and associated damage processes were observed. These local fracture processes are expected to be influenced differently by changes in the conditions under which deformation is occurring, for example, through the application of hydrostatic pressure. The transitions in fracture mode in such materials in a given space thus cannot be exactly defined. This was illustrated in the current work in

the suppression of damage accumulation in the shear bands (associated with pearlite and the larger carbides) with increasing hydrostatic pressure, allowing the shear bands to develop more extensively. At lower pressures, the transition to this shear mode is thus not expected to be an abrupt change with pressure. The lines on these fracture maps which separate different modes in materials with complex microstructures should be replaced with transition regions, in which various features of the microstructure contribute to the mode (or local modes) of fracture observed. This is illustrated in Figure 5.60.

5.6 Conclusions

This chapter has investigated the role of microstructure in various fracture modes in several hot-rolled HSLA plate steels, affected by the conditions of temperature and stress state. Although many observations were reported, several general conclusions can be made:

(i) The influence of centre-line segregation in the continuous casting of HSLA steels can lead to significant limitations in the mechanical properties, even in low sulphur steels with low average inclusion contents. The centre-line microstructure can then control the mechanical properties of plate material, due to the poor through-thickness properties. This is especially the case when the steels have not been calcium-treated, so that the sulphides precipitate in the last region to solidify, along the centre line, where the manganese level is also high. The transformation products in the centre-line region are thus affected,

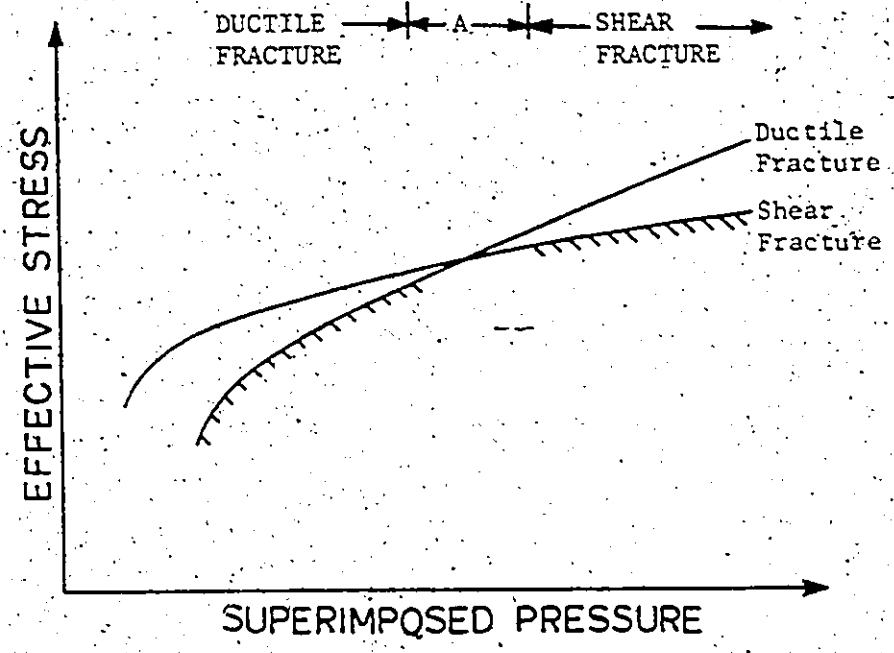

Fig. 5.60: Schematic illustration of a fracture map in effective stress-pressure space, for heterogeneous material. The interval A represents a transition region between well-defined ductile and shear modes of fracture. In this interval, different microstructural components, or variations in the distribution of components, can alter the local mode of fracture and/or the local level of damage at failure.

and the interaction between the resulting elongated sulphides and the brittle phase they are contained within controls the overall mechanical properties. The practice of placing squeeze rolls just beneath the mold has reduced the level of centre-line segregation (Ushijima et. al., 1984).

(ii) At low temperatures, where the flow stress was high, several sources of damage were identified, associated with various components of the microstructure. These different local damage components could, under certain ranges of conditions, compete with each other in controlling final fracture. However, under the low temperature conditions studied here, it appeared that in the calcium-treated steels the large spheroidal inclusions controlled or initiated final fracture through cleavage, while in the non-treated steels the association of the elongated sulphides with the brittle bainitic phase present along the centre-line controlled fracture. It was noted that the centre-line transformation product was not identified with respect to the presence of martensite.

(iii) The presence of a hard phase, or several microstructural components in close proximity which have a higher flow stress than the surrounding matrix, can significantly influence the local pattern of deformation or damage development. This can also lead to a

change in fracture mode. Evidence of this was seen in the initiation of shear bands at the sites of fracture in the bainite in tests under superimposed pressure. At low temperatures, intergranular cracking in the ferrite was enhanced due to the local influence of closely-spaced bands of transformation products.

Thus, it has been observed that, in addition to the microstructural components present in the HSLA steels investigated here, the distribution of these features in the material is also an important factor in the accumulation of damage and control of fracture.

CHAPTER 6

THE EFFECT OF SOLUTE DISTRIBUTION ON CREEP FRACTURE IN A Ni-Sn ALLOY

6.1 Introduction

Many alloys used in high temperature service are inhomogeneous in both chemistry and microstructure on a scale greater than the grain size. The accumulation of intergranular damage in creep, however, is sensitive to variations in microstructural features such as grain size or intergranular precipitation (Ashby et. al., 1979a), and to local chemistry effects, such as grain boundary segregation (Wilkinson et. al., 1980; Briant and Banerji, 1978). Inhomogeneity results in deformation and damage accumulation characteristics which vary throughout the material. The comparison of fracture behaviour between such non-uniform materials and models based on average chemical composition or grain size may not yield a consistent correlation.

In this chapter, the creep deformation, damage accumulation, and fracture behaviour of a Ni-Sn solid solution alloy is described. Here, damage takes the form of intergranular voids and cracks. A parameter giving the level of damage in the material should be dependent upon a quantitative measure of the amount of cavitation and cracking. In addition, it must correlate with the fracture behaviour, relating the applied stress with either failure time or strain. It is shown here

that quantitative measures of damage based on an average level, given here by the cavity number density and the fraction of the specimen diameter covered with voids, do not adequately describe the fracture condition.

Tin additions were made to enhance the intergranular creep damage, however, the segregation pattern of the tin was not removed through homogenization. Thus, the influence of the solute pattern on the resulting distribution of damage was quite marked. The results are compared with the work of White et. al., (1982, 1983) on a similar material with a more homogeneous solute distribution.

6.2 Material and Experimental Procedure

The material used in this study was a solid solution (at 600°C) of nickel alloyed with (nominally) 1% tin. The purity of the base nickel was 99.97% +, and its composition is given in Table 6.1. The tin additions were a high purity grade. The alloy was sand cast under vacuum into an ingot 4 inches square by 13 inches long. This ingot was then quartered down the axis, and the sections machined to 1 inch diameter. These were then swaged through a total reduction in area of 86%, with intermediate anneals at 800°C for one hour between passes. Cylindrical tensile samples were machined with a gauge length of 25.4 mm and 5 mm diameter. They were then annealed at 1000°C for one hour in high vacuum to produce an average grain size of 86 microns, which was stable during creep testing (White and Padgett, 1982).

TABLE 6.1

COMPOSITION OF BASE NICKEL*

ELEMENT	ppm
Al	6
As	3
Ca	4
C	25
Cr	1
Co	190
Cu	6
Fe	13
Mg	1
Si	4
S	6
Zn	1.6

* Analysis performed by Falconbridge Nickel Co.

The cast dendritic structure was not completely homogenized by this thermo-mechanical processing. The resulting microstructure contained elongated regions in which the grain size was considerably smaller than the average value of 86 μ. These are seen in Figure 6.1. The orientation of the regions of small grain size was along the tensile axis of the samples. Electron microprobe analysis revealed these small-grained clusters to be interdendritic regions of high solute concentration. It was estimated that the level of tin in these regions was higher than that in the neighbouring large-grained material by a factor of two to four. However, although the material was non-uniform on the scale of the interdendritic spacing, chemical analysis on several samples showed that the average composition between samples was constant with a tin content of 1.10 ± 0.1 wt %.

The creep tests were performed in a Dennison constant-load creep machine, in an atmosphere of Ar/5% H_2 at 5 psig. All tests were performed at 600°C, with a maximum variation of 2°C over the sample gauge length. During furnace heat-up the applied pre-load was 10 MPa. Full load was carefully applied at testing temperature.

Three different initial stress levels were investigated, which were nominally 113, 141, and 179 MPa. Tests at each stress were interrupted at various stages in the creep life, so that the damage accumulation process could be examined in detail. Specimens were sectioned through the centre along the tensile axis for metallographic examination. As the material is very soft, care was taken in minimizing

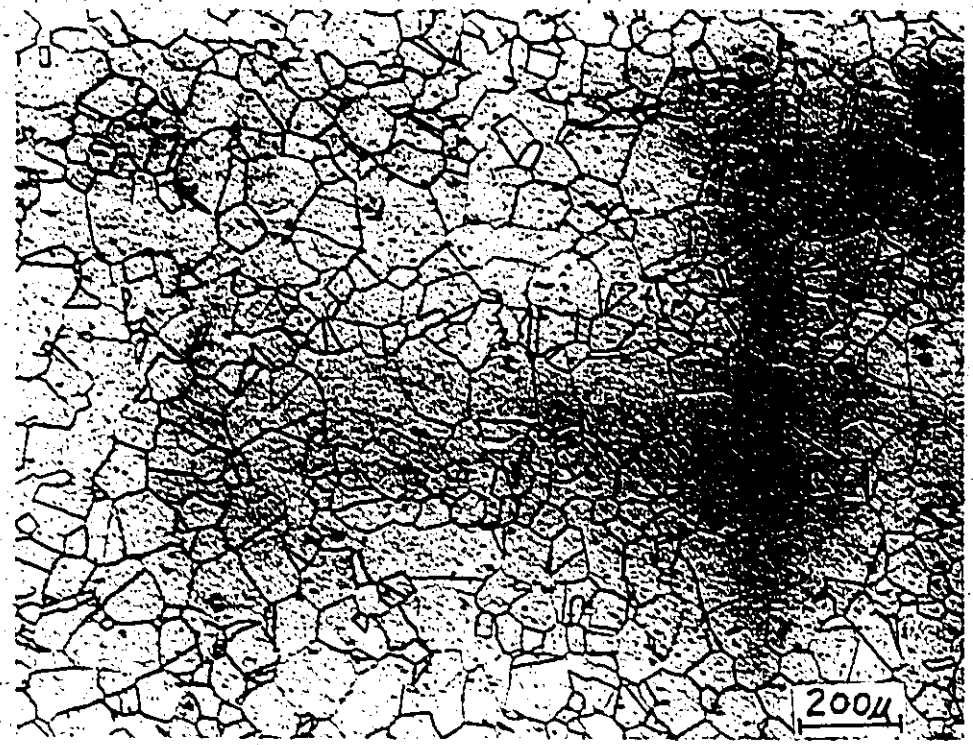

Fig. 6.1: Microstructure of Ni-Sn alloy. Note the small-grained regions elongated in the horizontal direction.

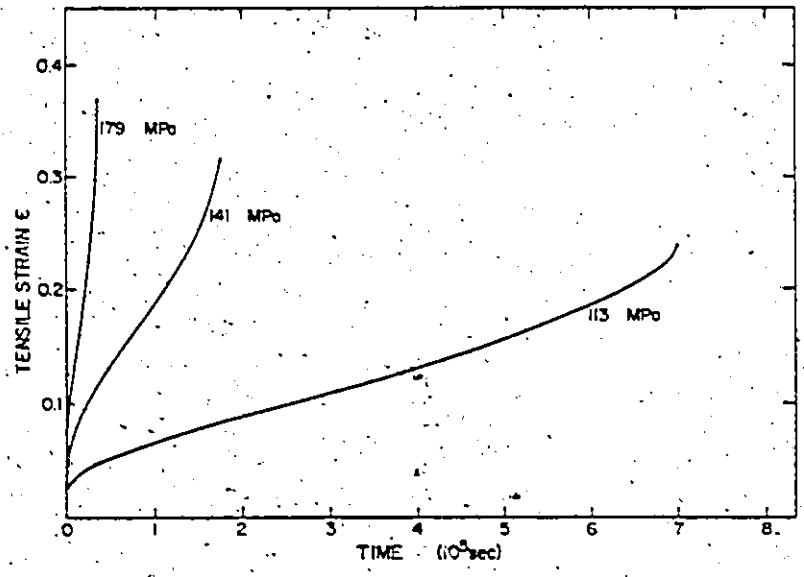

Fig. 6.2: Tensile creep strain vs. time curves at 600°C for the three initial stress levels indicated.

grinding pressure, so that the deformed layer of material beneath the surface would not be significant. The final stage of preparation employed an etch-polishing technique. This was required to remove the thin layer of material which had smeared over cavities in the previous grinding and polishing stages. The samples were polished on an automatic polisher using 0.3μ Al_2O_3 in an etching solution composed of nitric acid, glacial acetic acid and glycerol in the ratio 1:1:2 respectively. This composition was chosen to avoid the effects of passivation and surface pitting, while maintaining the viscosity of the etchant so that rounding of the cavity edges due to the nappe of the polishing cloth was minimized. Polishing times for the final stage were from 3 to 5 minutes.

Regions extending across the specimen diameter were photographed at a magnification of 160X and assembled to form a montage. Histograms of the cavity or microcrack size distributions were obtained through the use of a graphics tablet interfaced with an Apple II computer. The cavity or crack dimension was taken as the component of its length normal to the tensile axis. Consideration of the magnification at which the photos were taken and the resolution of the graphics tablet gave the lower limit to cavity size recorded as approximately 4 μ.

6.3 Experimental Results

6.3.1 Deformation and Fracture Behaviour

Representative creep curves for the three stress levels are given in Figure 6.2. It should be noted that there was a degree of scatter about the "average" behaviour given, which increased with stress.

However, this scatter was not significant relative to the differences indicated between these curves. Table 6.2 summarizes the results obtained from the tensile strain-time plots, along with those of White et. al. (1983), which will be discussed later.

Figure 6.3 illustrates the characteristic variation of strain rate with strain which was observed. This particular curve was obtained from a creep test at 113 MPa. Although the details of the curves varied between stress levels, and indeed between tests at a given stress, the characteristic shape was similar in all tests. Note that steady-state creep conditions were not attained due to the constant load conditions. However, the minimum creep rate $\dot{\varepsilon}_{mcr}$ (at point A in Figure 6.3) could be determined. Figure 6.4 shows that the strain at which the minimum creep rate occurs increases with stress.

The point labelled B in Figure 6.3 marks the onset of what is commonly referred to as the tertiary stage, in which the creep rate begins to rise rapidly. (The true tertiary stage, however, begins at the strain at which the minimum creep rate is attained, at which point the creep rate starts to increase.) This rapid increase in strain rate at a point beyond the minimum creep rate was observed in all tests performed. The increment in strain (beyond the strain at $\dot{\varepsilon}_{mcr}$) at which the transition to the final tertiary stage occurred increased with only a very weak dependence upon stress. However, there was considerable scatter between tests, so that correlation between this strain interval and stress was not considered significant.

TABLE 6.2

CREEP AND CREEP RUPTURE PROPERTIES OF Ni-Sn ALLOY EVALUATED AT 600°C

	σ (MPa)	FAILURE TIME t_f(sec)	LOG t_f	ELONGATION TO FAILURE ε_f	MINIMUM CREEP RATE $\dot{\varepsilon}_{mcr}$	MONKMAN-GRANT EXPRESSION $C_{MG} = \dot{\varepsilon}_{mcr} t_f$
Present work	113	6.75×10^5	5.83	0.234	2.12×10^{-7}	0.143
	113	7.66×10^5	5.88	$\simeq$ 0.24	2.03×10^{-7}	0.155
	141	1.77×10^5	5.25	0.32	1.09×10^{-6}	0.193
	179	3.26×10^4	4.51	0.360	6.30×10^{-6}	0.205
	179	3.14×10^4	4.50	0.338	6.06×10^{-6}	0.190
Data from White et. al. (1983)	34.5	7.4×10^6	6.9	0.065	5.8×10^{-9}	0.043
	69	5.7×10^5	5.8	0.071	9.9×10^{-8}	0.056
	103.5	7.0×10^4	4.8	0.078	5.9×10^{-7}	0.041

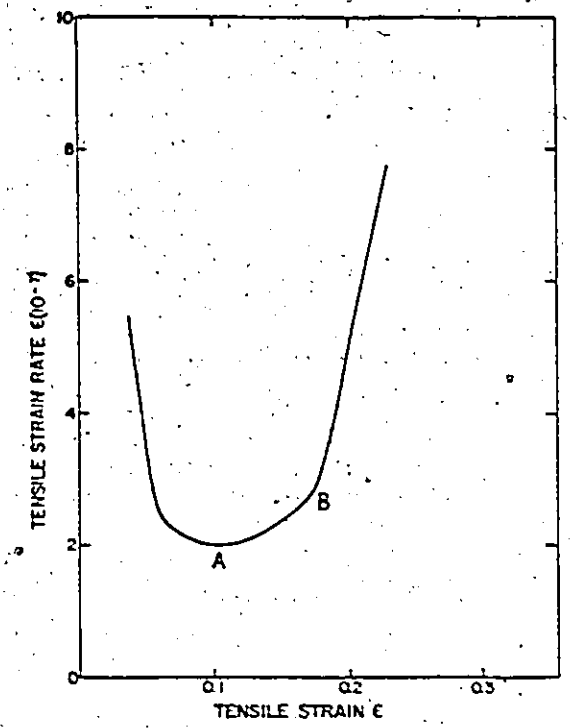

Fig. 6.3: Plot of tensile strain rate vs. tensile strain, for a given test at 113 MPa. Note point A, at which $\dot{\varepsilon} = \dot{\varepsilon}_{mcr}$, and point B, where the strain rate begins to increase rapidly.

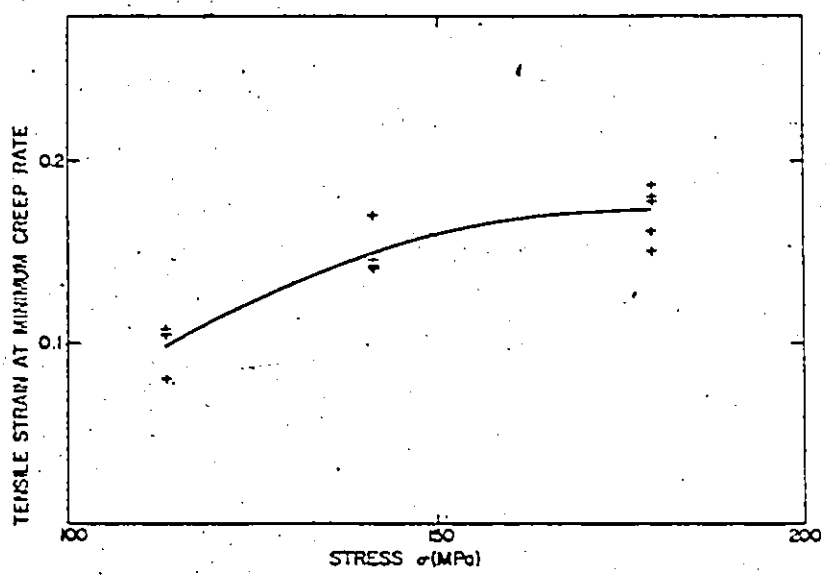

Fig. 6.4: Plot of the variation of the strain at $\dot{\varepsilon}_{mcr}$ with initial applied stress.

Figure 6.5 plots log $\dot{\varepsilon}_{mcr}$ vs. log σ to reveal a power-law relationship between the minimum creep rate and initial applied stress. A stress exponent of n = 7 was observed in the present material. Included in Figure 6.5 are the results from White et. al., for discussion in the following section.

The value of C_{MG} in Table 6.2, usually termed the Monkman-Grant constant, did not appear to be constant over the range of stress investigated here. Within experimental scatter, the value of $\dot{\varepsilon}_{mcr} t_f$ was the same for initial stress levels of 142 and 179 MPa, however, at 113 MPa a value was obtained which was significantly lower.

There was a degree of necking which accompanied the fracture process, which increased with applied stress. An estimate of the maximum increase in hydrostatic stress component attained due to the neck can be made assuming the Bridgman correction to apply. This was calculated using the neck profile of a fractured sample tested at 179 MPa (the fracture stress used was not this initial stress, but accounted for the decrease in cross-sectional area), to give the increase in hydrostatic stress at the centre of the neck at approximately 4 MPa. At lower stress levels the influence of the neck was considerably less than this. Although in a highly damaged material this additional hydrostatic stress may have significant effects, no further consideration was given here to its influence on damage development.

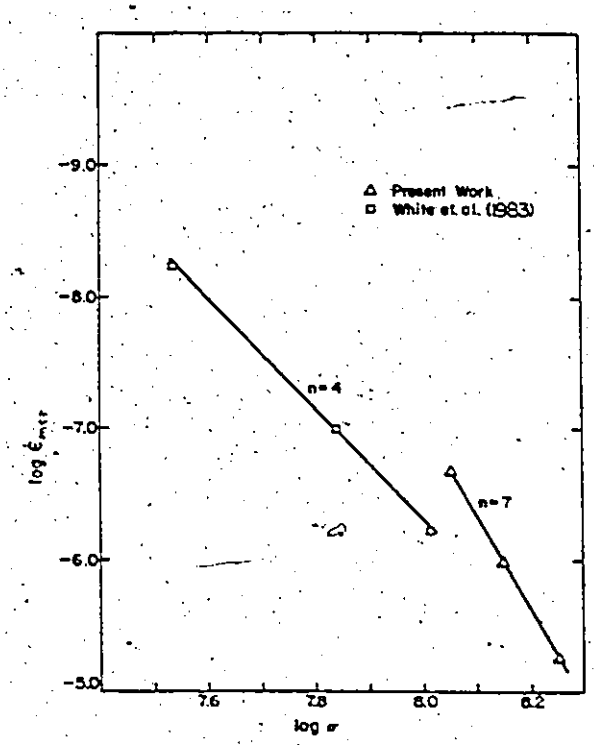

Fig. 6.5: Plot of log $\dot{\varepsilon}_{mcr}$ vs. log σ, revealing a power-law relationship between $\dot{\varepsilon}_{mcr}$ and the initial applied stress. Data from White et. al. (1983) are included for comparison.

6.3.2 Nature of Damage and its Distribution

The damage which developed during creep was entirely intergranular. In addition to the cavitation which accumulated in the interior of the sample, the concurrent initiation and growth of surface cracks was observed. These were initiated by the end of the primary creep stage (i.e., at strains below that at $\dot{\varepsilon}_{mcr}$), observed as offsets at the surface due to grain boundary sliding. The initial mode of surface crack propagation was through linkage with voids which developed along the grain boundary ahead of the crack, as seen in Figure 6.6a. At a later stage, when the crack length exceeded the grain facet size, wedge cracks were initiated at the grain boundary triple junction ahead of the crack. Linkage between the wedge and surface crack was via coalescence with cavities which developed along the boundary between them. An example of surface crack growth through the wedge-cracking mechanism is illustrated in Figure 6.6b.

In contrast to the surface crack observations, no internal cavitation was evident (at a magnification of 1250X) at strains less than that at the minimum creep rate. Very little cavitation was observed in a test stopped soon after the minimum creep rate was attained. The damage which subsequently developed consisted of both wedge cracking and r-type cavities. At the larger strains attained at higher stresses, the growth of large wedge cracks was more evident. These were seen to propagate along the grain boundary by linking with small voids laying ahead (Figure 6.7). Not all of the intergranular cavitation observed

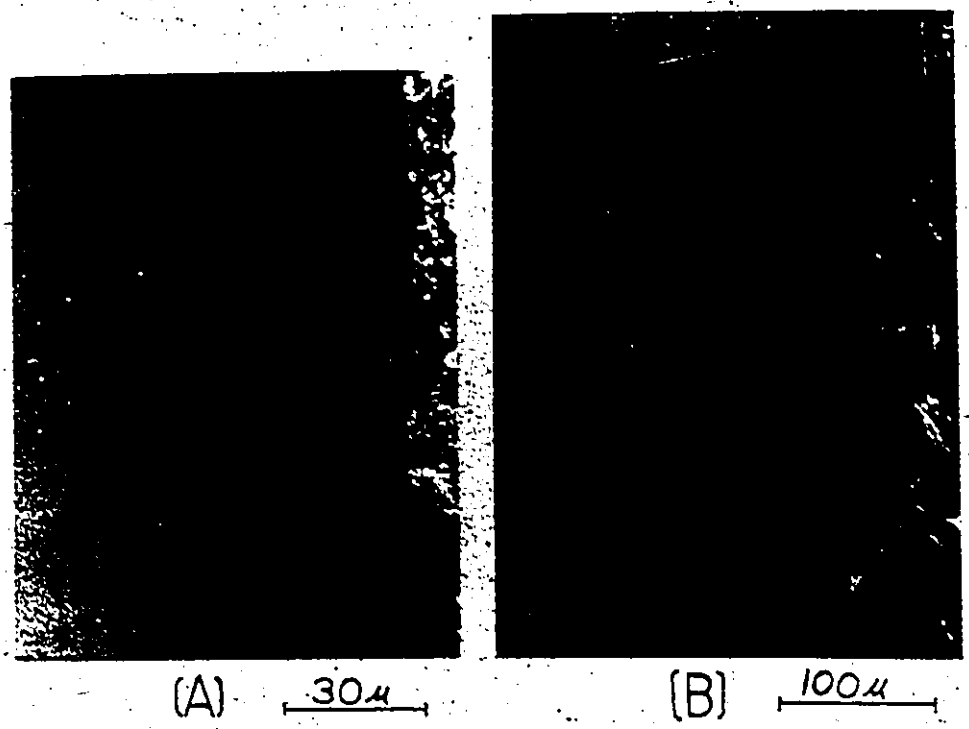

Fig. 6.6: Propagation of surface cracks: (a) Initial propagation involved only cavitation on the grain facet ahead of the crack. (b) Once having grown to the size of a grain facet, subsequent propagation involved a wedge-cracking mechanism.

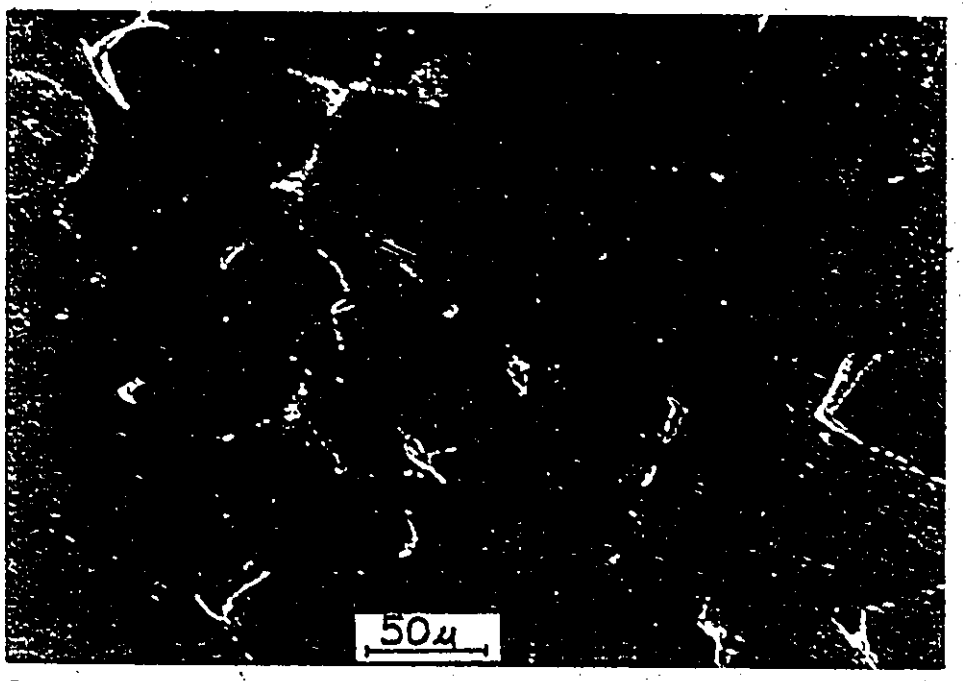

Fig. 6.7: Photograph illustrating wedge crack propagation via linkage with voids ahead on the grain boundary.

existed on grain boundaries with associated wedge cracks, however, this could be the result of the plane section not cutting through the wedge crack on a given grain boundary.

At low strains, damage in the sample interior was observed predominantly in the regions of small grain size. A microprobe scan (Figure 6.8) revealed the higher tin content of these regions. The level of cavitation and cracking accumulated in these zones was very high at the point at which significant damage became observable in the surroundings. At this point cracks traversing completely across the small-grained regions were observed. The level of damage accumulated in the large-grained regions separating the highly damaged zones was relatively low when final fracture occurred. This correlated with fracture surface observations. Although the fracture was predominantly intergranular, only small regions were cavitated. The remainder of the fracture surface was characterized by a rippled appearance with much less cavitation. A comparison of these two regions of the fracture surface is given in Figures 6.9a and b. Thus, the final fracture of the material between the heavily damaged zones is seen to occur with very little cavitation.

At lower stresses, the development of large surface cracks became more pronounced. These were seen to propagate at later stages through linkage with the damage which developed in the interior of the sample, as seen in Figure 6.10. An interaction between these two sources of damage in controlling fracture is thus suggested.

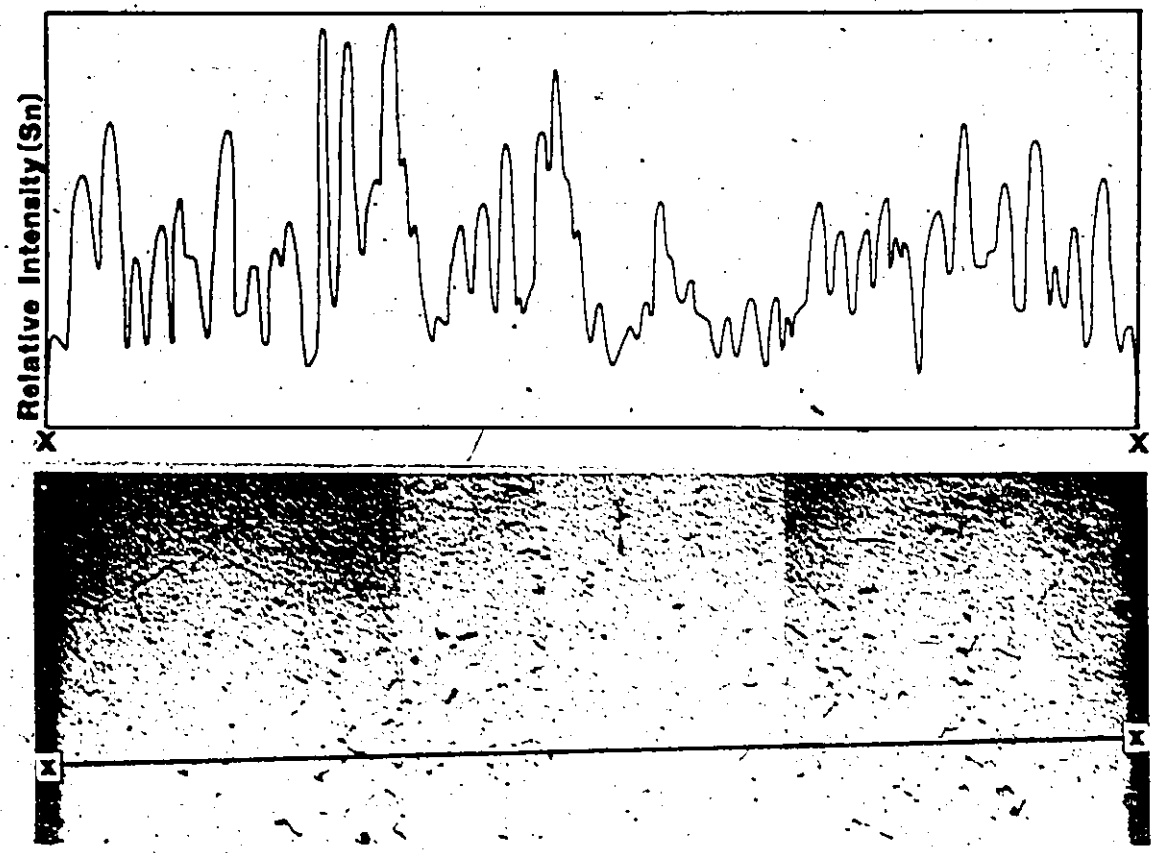

Fig. 6.8: Photograph (~ 32X) showing damage localized in regions aligned with the tensile axis (vertical). The microprobe scan for Sn along X-X (the intensity is relative to background) indicates that these regions with a locally high damage level are Sn-rich.

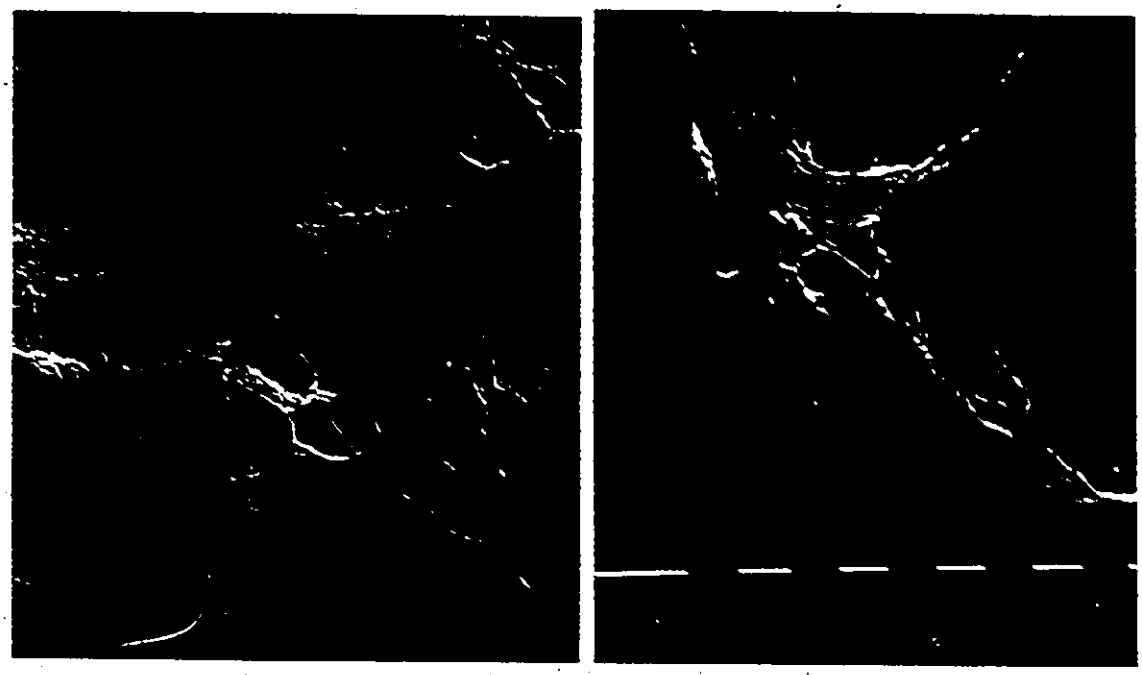

(a) (b)

Fig. 6.9: Fracture surface observations. Isolated regions of the fracture surface exhibited considerable cavitation, as in (a), while the remainder of the fracture surface was characterized by a rippled appearance with much less cavitation, as in (b). (Mag. 640X)

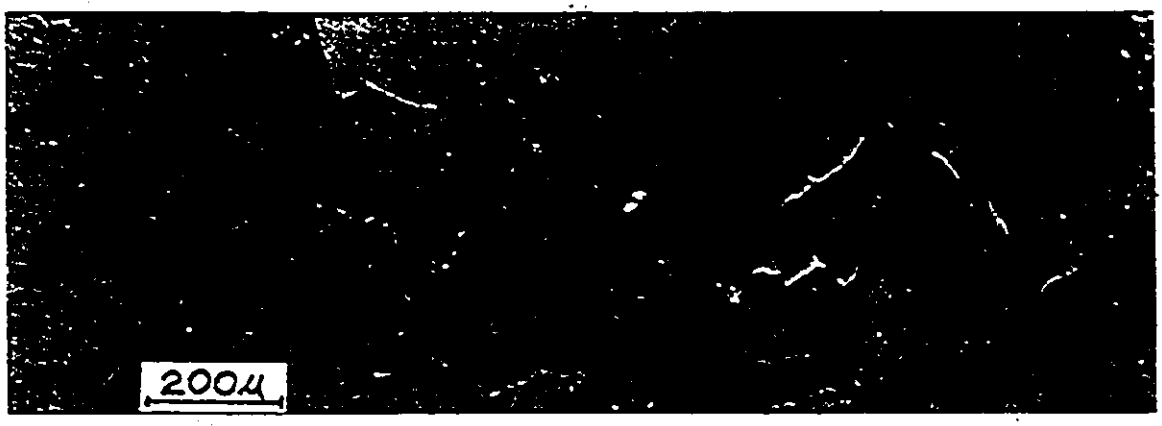

Fig. 6.10: Photograph illustrating interaction between a surface crack and interior damage. (Mag. 85X)

6.3.3 Analysis of Damage

The flaw (i.e., cavity and crack) size distributions obtained from tests interrupted at various stages in the damage accumulation process are given as frequency histograms in Appendix B. Only the important conclusions obtained from these results will be given here. Note however, that the data in Appendix B for surface and internal damage have been separated. The results for internal damage have been normalized to a sample section area of 15 mm^2, and those for surface cracking were normalized to the length of the edge at the surface of the sample which bounded this area, for the given sample. These frequency histograms may be used to provide an indication of the cavity or crack nucleation rates. They may also be used to distinguish whether the fracture criterion is given more adequately by an average damage level or a critical flaw size.

Figure 6.11 indicates the development of cavity number density in the sample interior as a function of strain, for each of the three stress levels. The strain used here was that given by the decrease in cross-sectional area, due to the presence of a slight neck in the sample. As the minimum cavity size recorded was 4 μ, these results do not strictly give the cavity nucleation behaviour. They include a considerable component of cavity growth in their determination. Thus, although at the given resolution the number density of cavities increases with strain, separation of the influence of continuous cavity nucleation from that of void growth or variations in void growth rate between grain boundaries could not be made. In addition, Dyson (1983)

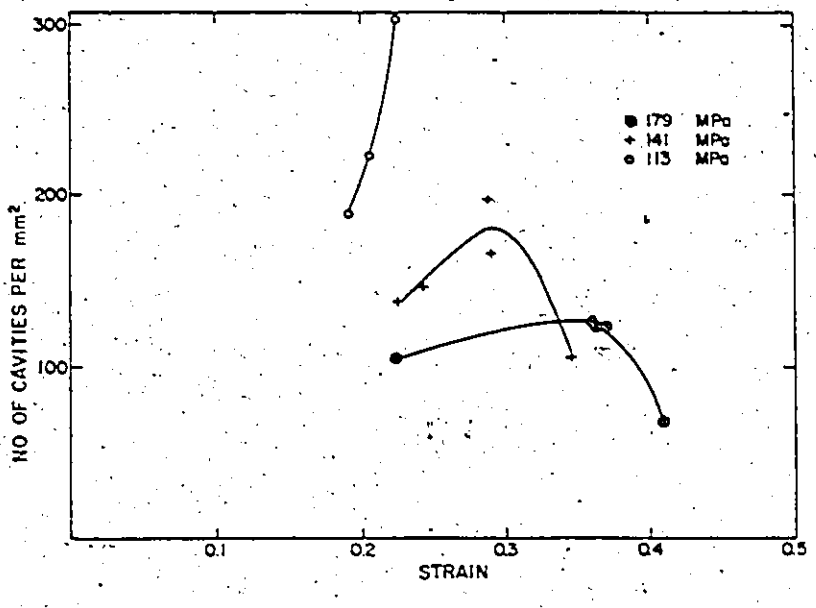

Fig. 6.11: Plot of cavity number density vs. strain, determined from cross-sections parallel to the tensile axis.

has noted that the cavity number density observed in cross-sections will be dependent upon the cavity size, so that results of the type given in Figure 6.11 should be interpreted with caution. However consideration of the cavity size distributions, most notably at the lower end, suggests that the number density of cavities is dependent upon the stress level, although an exact quantitative description based on the present data cannot be concluded. As the stress level decreases, the number of cavities observed at a given strain increases. Also, the increase in the observed number density with strain is greater at lower stresses.

At the larger strains attained in the tests performed at higher stresses, the number density begins to decrease. This effect is due to the coalescence of cavities.

The density of surface cracks was observed to remain roughly constant with strain. In all tests, most of the grain boundary/surface intersections resulted in crack initiation. These nucleated early in the creep life, as already stated.

The average internal damage level is given as a function of strain in Figure 6.12. Here, damage is defined as the average fraction of the sample diameter in the cross-section which was covered with cavities and microcracks, denoted in Figure 6.12 as the diameter fraction cracked. This value was obtained by summing the projected cavity/crack lengths normal to the tensile axis l_c, and dividing by the total projected grain boundary length normal to the axis in the area sampled, given by l_g. The length l_g was set equal to $n_g D$, where D is the average

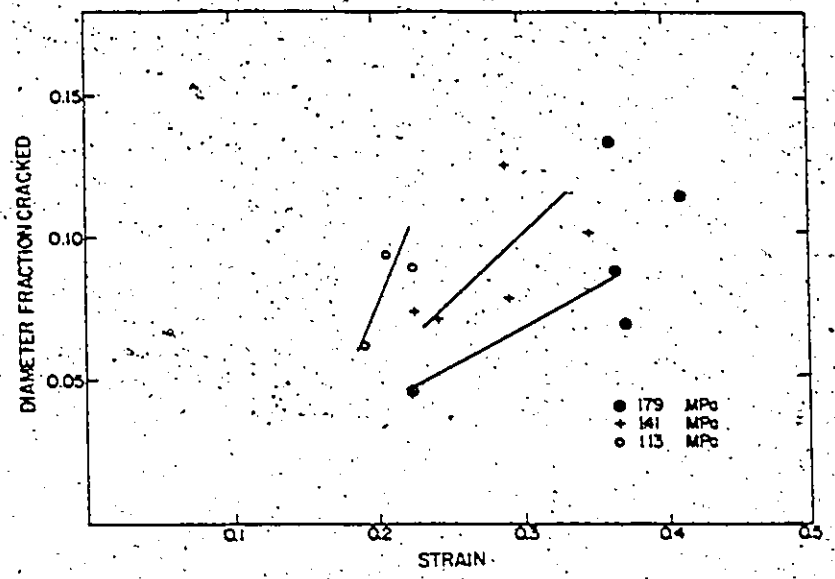

Fig. 6.12: Plot of average internal damage level vs. strain. Damage is expressed as the fraction of the sample diameter covered with cavities and interior cracks.

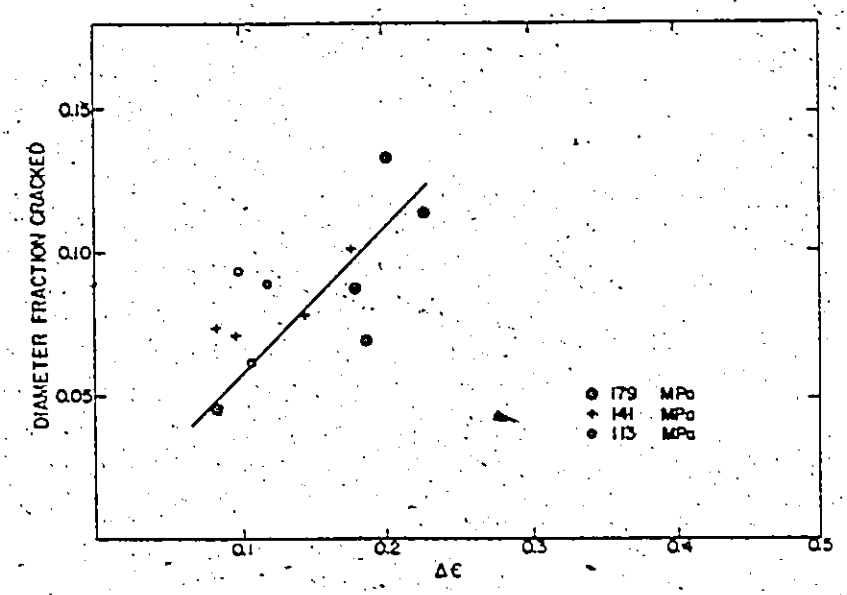

Fig. 6.13: Plot of average internal damage level vs. strain $\Delta\varepsilon$ beyond that at the minimum creep rate.

grain size and n_g is the number of average sized grains in the area sampled. As noted with the cavity number density, this damage parameter was observed to be both stress- and strain-dependent. At fracture, the level of internal damage supported was seen to increase with stress.

As the onset of observable damage in the sample interior correlated with the strain at the minimum creep rate, Figure 6.13 plots the average internal damage against the strain $\Delta\varepsilon$. We define $\Delta\varepsilon$ here as the strain beyond that at the minimum creep rate. A better correlation is obtained between the average damage level and $\Delta\varepsilon$ however, an influence of stress upon the damage accumulated at a given $\Delta\varepsilon$ is still evident in this plot.

The average fraction of the sample diameter lost to surface cracking is given in Figure 6.14. These values were obtained by normalizing the sum of crack lengths by the same total grain boundary length as the internal damage was. We can observe that the level of surface crack damage at a given strain, and the dependence of this damage upon strain is greater at lower stresses. This result was due to the development of several large surface cracks which grew rapidly in tests at the lowest stress level, a characteristic not observed at higher stresses. Indeed, metallographic observations suggest that, at the lowest stress level, the development of a critical-sized surface flaw controlled fracture. At higher stresses, the largest interior crack size observed was comparable to the largest surface crack, so that it was not apparent which component of damage controlled fracture.

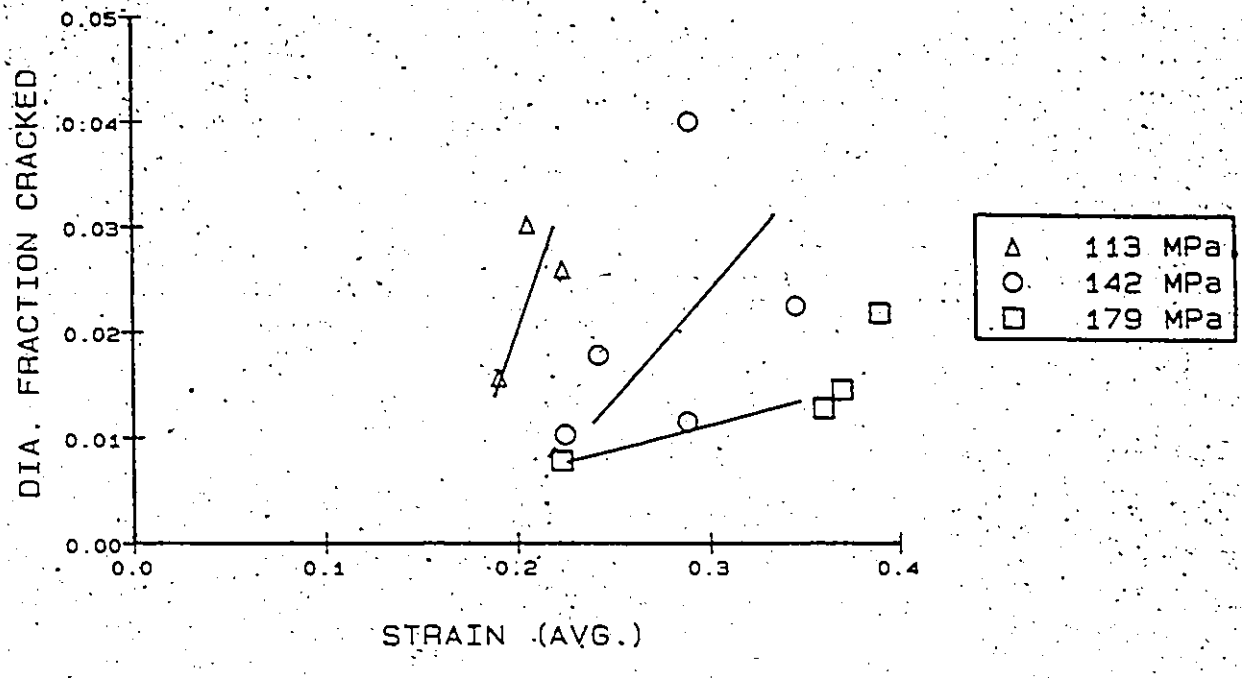

Fig. 6.14: Plot of average fraction of sample diameter covered with surface cracks vs. strain.

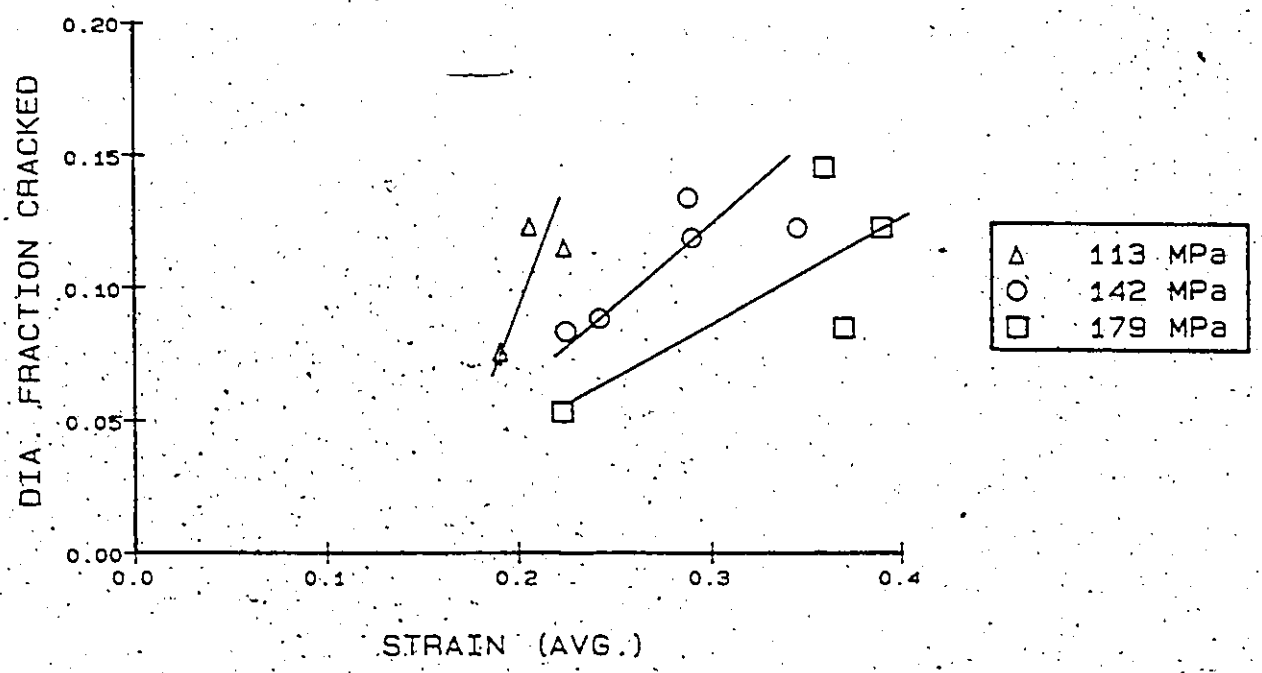

Fig. 6.15: Plot of the sum of the damage contributed by interior and surface damage vs. strain.

We note that the results in Figure 6.14 should not be interpreted as a loss in cross-sectional area. The large surface cracks which developed in the low stress tests often extended a significant distance around the sample circumference. This would result in a decrease in cross-section greater than that given by a loss in diameter fraction.

In Figure 6.15 the sum contribution of internal and surface damage components from Figures 6.12 and 6.14 is given. The level of total damage supported by the material at fracture appears to increase slightly with stress. However, consideration of the large surface cracks present in the low stress tests suggests that the average level of damage at failure is not significantly dependent upon the level of stress.

If the failure condition were given by an average net section stress, we would expect the total damage at fracture to increase with decreasing stress. Observations suggested that the development of large flaws were significant in determining failure. The average fraction of the specimen diameter covered with internal cracks larger than the average grain size is given in Figure 6.16. This parameter correlates well with strain, however, a weak dependence upon stress is observed. When these values are plotted against the tertiary strain $\Delta\varepsilon$, in Figure 6.17, the stress dependence is removed. Thus, while the nucleation and/or growth rate of small cavities may be stress-dependent, the propagation of wedge cracks is strain-controlled. The steep slope of this curve indicates that the growth rate of cracks larger than the average grain

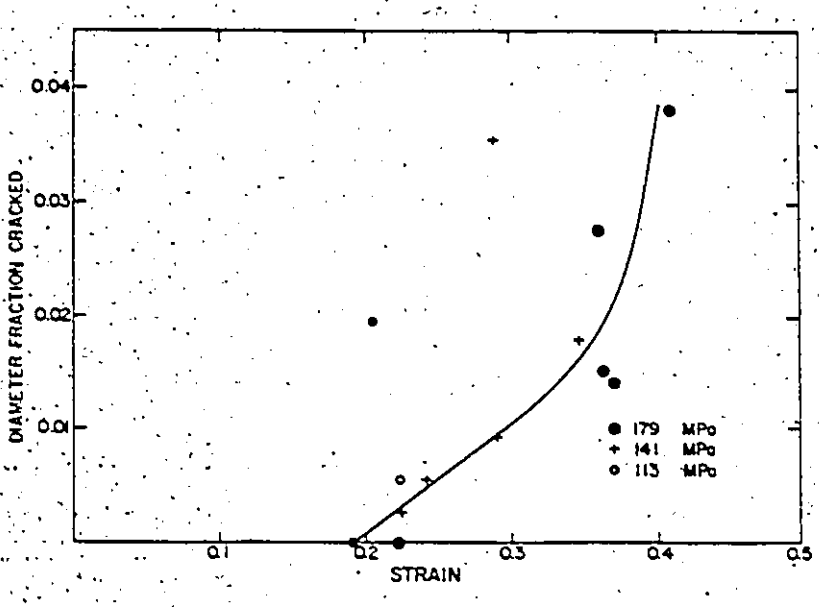

Fig. 6.16: Plot of average internal damage level vs. strain, where the damage is associated with cracks larger than the average grain size.

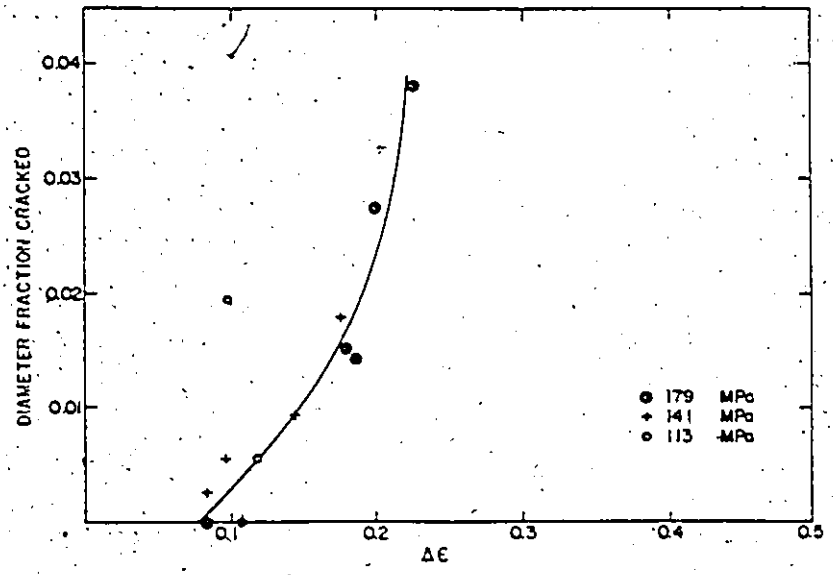

Fig. 6.17: Plot of the average internal damage level vs. the strain $\Delta\varepsilon$ beyond that at the minimum creep rate. The damage here refers to interior cracks larger than the average grain size.

size with strain is very rapid. This result, along with metallographic observations, suggest that the crack size influences the growth rate; large cracks grow rapidly. However, the largest internal cracks observed correlated with the dimensions of the solute-rich regions.

Figure 6.17 indicates a minimum strain below which no cracks larger than the average grain size were observed. This strain correlates well with the point at which the strain rate begins to rise rapidly (point B in Figure 6.3). Thus, the appearance of grain-size cracks in the interior influences the onset of the rapid increase in creep rate in the tertiary stage.

Note that the damage at fracture given in Figure 6.17 associated with large internal flaws increases with the applied stress level. However, at low stresses the material supports surface cracks which are considerably larger than the cracks which develop in the sample interior. That these large surface flaws are supported by the material with a lower average level of internal damage suggests that the critical flaw size is dependent upon the level of damage in the material.

6.4 Discussion

This study has served to illustrate the creep and damage accumulation behaviour in a single phase alloy, in which the solute level and grain size are inhomogeneously distributed. The regions which have a higher tin content are expected to be stronger in creep than the surrounding material with a lower solute level (Sherby and Burke, 1967),

that is, the high-solute regions will exhibit a slower creep rate for a given stress. In order to maintain strain rate compatibility within the material, upon loading long range stress redistributions must occur. The extent of this transient period and the level to which stresses are redistributed is dependent upon the relative constitutive behaviour of the two regions in the material, their geometry and distribution, and the stress level. We thus expect that the primary creep behaviour will be affected by the character of inhomogeneity in a material. The final stress distribution is such that the rate of total work of deformation by the applied load is minimized, resulting in a higher stress in the stronger regions of the material. It is important to point out that this modification of the stress field could alter the relative importance of a given deformation mechanism in a given region of the microstructure.

In the present material the strain at which the minimum creep rate was attained increased with stress, suggesting that transient stress redistributions are dependent upon the applied stress. Note that we do not imply here that the strain at which stresses are completely redistributed corresponds to that at the minimum creep rate. We only suggest that if the stress transients were dependent upon the applied stress, this could influence the strain at which the minimum creep rate occurred.

Because the initiation of the tertiary stage (i.e., the strain at which $\dot{\epsilon}_{mcr}$ was attained) was stress-dependent, and that the appearance of observable cavitation coincides with this strain, we have attempted

to correlate the development of internal damage with tertiary strain $\Delta\varepsilon$. A reasonable correlation between damage and tertiary strain was obtained for internal cracks larger than the average grain size. The onset of the rapid increase in strain rate in the late tertiary stage corresponded with the appearance of internal cracks of the order of the grain facet size. This result was also observed by Pavinich and Raj (1977).

The rapid growth of these facet-sized cracks occurred through the nucleation of wedge cracks at the triple junction ahead of the main crack, followed by coalescence with voids which developed along the boundary separating the two cracks. At the crack tip the constraint to grain boundary sliding is relieved, so that the stress concentration at the triple point ahead of the crack is expected to be enhanced. This would promote the nucleation of the wedge crack. The importance of grain boundary sliding in the coalescence between the main crack and the wedge crack was noted as a significant mechanism contributing in the crack growth process.

In addition to the influence of the accelerating damage level itself on the development of tertiary creep, an additional factor should be noted which could contribute to the effect of grain-sized cracks on the increase in creep rate. These cracks developed in the regions of high solute content, that is, the stronger component of the material. The dimensions of these regions normal to the tensile axis were, in most cases, only a factor of 2 to 4 times the average grain size. The development of a crack across a substantial portion of one of the inter-

dendritic regions would significantly reduce the strength of this region. The stress distribution and resulting deformation pattern in the material around the high-solute region would thus change, producing a higher creep rate.

The internal damage associated with small voids, and the development of surface cracking, however, did not correlate uniquely with strain. The levels of these components of damage, at a given strain, were observed to increase with decreasing stress.

Dyson (1983) has concluded from observations in several Nimonic alloys and Cr-Mo steels that the cavity number density is dependent only upon strain, and is independent of the stress level. That is to say, $\frac{dN}{d\varepsilon}$ is independent of stress, where N is the cavity number density and ε the total strain. The cavity resolution attained in this study limited the conclusions one could make with regards to the increased rate at which the cavity number density accumulated with strain at lower stresses. Thus we could not distinguish between the possibility that the cavity nucleation rate $\frac{dN}{d\varepsilon}$ increased at low stresses, and the effect of an increase in time required to reach a given strain. With a nucleation rate independent of stress level, the operation of a diffusional mechanism in the cavity growth process could result in larger voids at a given strain with decreasing stress. This is because the time to attain this strain via intergranular creep is a stronger function of stress than the void growth rate predicted by any current diffusional-growth

model. At low stress levels a greater fraction of the cavities which nucleate could grow to a size at which they could be resolved.

The processes of damage nucleation and growth should be viewed as a result of the deformation mechanisms which operate in a material. In the present material, observations suggested that grain boundary sliding contributed significantly to the total deformation rate. This was most evident at the sample surface. If we interpret the increased damage rate at low stresses as the result of an increased nucleation rate, some insight into the effect of stress on the cavity nucleation rate $\frac{dN}{d\varepsilon}$ in a single phase alloy can be gained by considering the stress dependence of grain boundary sliding versus that of matrix creep. It has been suggested (Hart, 1967b; Ashby, 1972) that grain boundary sliding rates have a weaker stress dependence than deformation through matrix (i.e., power-law) creep. The component of the total strain contributed by grain boundary sliding would thus increase with decreasing stress. Experimental observations (Garofalo, 1965) support this prediction. It is also important to note that this displacement is to a degree impeded at grain boundary triple junctions, where stress concentrations develop (Crossman and Ashby, 1975; Lau and Argon, 1977).

These effects could explain an increase in the cavity nucleation rate $\frac{dN}{d\varepsilon}$ at lower stresses. The density of cavities on a grain boundary has been observed to be dependent upon the amount of grain boundary sliding displacement (see Perry, 1974). Thus, at lower stresses where grain boundary sliding provides a greater proportion of the total

strain, at a given strain the cavity density might be expected to be greater, that is, $\frac{dN}{d\varepsilon}$ would increase. Also, the increased stress concentrations which develop at triple points could result in an increase in the rate of nucleation of wedge cracks.

The development of higher damage levels in the interdendritic regions could be the result of several factors. From the literature, grain boundary offset measurements indicate that boundary sliding contributes a greater proportion of the total strain as the grain size decreases (Garofalo, 1965). The grain size in the high-tin regions is smaller than in the surrounding material, thus, the grain boundary sliding promoted would increase the damage accumulation rate. The influence of composition on grain boundary sliding reported in the literature, however, is inconclusive (Garofalo, 1965). In aluminum, for example, some soluble elements increase grain boundary sliding effects, while others have little influence. In the present alloy, however, if grain boundary sliding rates are not as significantly affected by variations in solute content as the matrix creep strength, the increase in tin content in the interdendritic regions could enhance the relative importance of grain boundary sliding. The local damage accumulation rate would thus rise. In the surrounding material with a low solute level, the lower matrix creep strength would result in a decrease in the contribution which grain boundary sliding provides to total strain, and thus a decrease in damage nucleation rate.

The possible influence of tin on the grain boundary cohesive strength should also be noted (Gifkins, 1959). This could significantly affect the cavity nucleation rate.

As stated previously, the initiation and propagation of surface cracks was observed to involve a grain boundary sliding mechanism. As the stress level is lowered, one can rationalize from the above discussion that the rate of crack advance as a function of total strain would be more rapid. This effect, due to the increase in the fraction of total strain contributed by boundary sliding, could explain the observations of an increase in surface crack growth rates (as a function of strain) at lower stresses.

Thus, in summary, we have interpreted the increase in the rate of damage accumulation at lower stresses as the result of an enhanced void nucleation and crack propagation rate. This in turn was the result of an increased contribution that grain boundary sliding makes to the total strain as the stress level decreases. Recently Reidel (1985) has concluded that, if the cavity nucleation rate were dependent solely upon the strain rate (i.e., $\frac{dN}{d\varepsilon}$ independent of stress), a Monkman-Grant relationship describing the creep rupture behaviour could follow. In the present material, an increase in the strain dependence of cavity nucleation and surface crack growth rates at lower stresses could explain the decrease in the value of $\dot{\varepsilon}_{mcr} t_f$ observed at lower stresses.

The material used in the present study was very similar in both tin concentration and impurity levels to that investigated by White

et. al. (1983). Both alloys were cast under vacuum. However, the present alloy was sand-cast while in their work the material was chill-cast, resulting in a more uniform solute distribution and grain size (White, 1983). The anneal prior to creep testing at 600°C in both cases was the same. The average grain size in their material was 51 μ, which was comparable to that used in the current investigation.

As seen in Table 6.2 and Figure 6.5, there were marked differences between the two materials in both the ductility and creep strength. Figure 6.5 indicates that the present material exhibited a higher creep stress exponent, and at stresses near 100 MPa it was also stronger. Their material displayed a creep exponent of 4 while in the present material, a value of 7 was obtained. The latter value is somewhat high for f.c.c. materials (Jensen and Tien, 1981). However, inhomogeneous materials consisting of components with different creep strengths often exhibit a high creep exponent (Kelly and Street, 1972; Martin, 1980). Thus, the higher value of creep exponent obtained in an alloy of similar composition can be explained by the inhomogeneous solute distribution. The difference in creep strength between the two alloys, however, cannot be presently rationalized. The influence of both a solute distribution and a grain size distribution could contribute to the increase in strength. An example of the effect of an elongated grain aspect ratio in increasing the creep strength of oxide-strengthened nickel alloys was noted by Wilcox and Clauer (1972). This was attributed to a decrease in grain boundary sliding when grains are

oriented in the tensile direction. In the present alloy, the grain structure was equiaxed, however, the influence of variations in microstructure and composition upon grain boundary sliding and resulting deformation behaviour should be considered an important factor in determining the creep strength in this material.

The uniform composition and grain size in the material of White et. al. was reflected in the observation of a more uniform distribution of cavities and cracks. The damage level in the material used in the present study was significant only in the regions of high solute content. Once a crack has extended across one of the interdendritic, creep-brittle regions, it must propagate through material lower in tin content, with a lower matrix creep strength. The decrease in the relative contribution of grain boundary sliding in this material and the resulting decrease in cavity nucleation results in a decrease in crack growth rate. This could explain the observation that the largest internal cracks observed correlated with the dimensions of the high solute regions.

However, in the homogeneous alloy, if the average solute level were high enough that the effects of grain boundary sliding become significant, a high damage nucleation rate would occur throughout the material, resulting in low ductility. We should note in addition that the experiments of White et. al. were conducted at lower stresses than in the present study. This would further promote grain boundary sliding and higher damage nucleation rates than under the conditions studied here. These effects could be significant in decreasing the ductility.

The failure strains observed by White et. al. were very low, less than the strain at which the accumulation of damage was initially observed in the alloy used in this study.

6.5 Conclusions

An investigation of the creep and creep fracture behaviour in a single phase Ni-Sn alloy at 600°C was presented, in which the solute distribution followed the interdendritic solidification pattern.

A creep stress exponent of 7 was obtained for this material. This value is slightly high for a single phase metal, but could be the result of the solute distribution, effectively producing a composite material with the regions of high tin content being stronger in creep.

The interdendritic regions developed very high damage levels prior to fracture, while at failure the amount of intergranular cavitation and cracking in the surrounding material was relatively low. This was explained by an increase in matrix creep strength and the decrease in grain size in the regions of high solute content, enhancing the contribution which grain boundary sliding makes to the initiation of cavitation.

With decreasing stress, the damage observed at a given strain increased. Also, the development of large surface cracks occurred at low stresses. The level of damage at failure at the lowest stress was not significantly different from that at the highest stress, suggesting that at low stresses the development of a dominant flaw controls fracture. Fracture appeared to be surface-crack controlled at the low stress level.

The increase in the rate of damage accumulation with decreasing stress was also attributed to an increase in the fraction of the total strain due to grain boundary sliding. This deformation mechanism could contribute to a higher void nucleation rate at lower stresses, as well as to crack propagation via a wedge-cracking mechanism. An explanation for the decrease in ductility with stress was thus offered.

A comparison was made between the behaviour of the present material and a similar alloy which had a more homogeneous solute distribution. The present material was more ductile. This was attributed to the low solute regions, which prevented crack growth which had initiated in the interdendritic regions of high tin content. The distribution of damage in the homogeneous alloy was more uniform, and this resulted in lower ductility.

CHAPTER 7

CONCLUSIONS

The present study has been concerned with identifying the importance of the following two characteristics of damage accumulation in controlling fracture:

(i) The character of the spatial distribution of damage is significant in accelerating the development of damage to a fracture condition. Fracture criteria in heterogeneous microstructures often do not correlate with the average damage level. A critical-sized flaw or a region with a locally high damage level provides a more realistic predictor of the onset of fracture in these materials.

(ii) A complete physical description of the damage events occurring throughout the microstructure is necessary. Several different damage processes can be operating in a multiphase microstructure, associated with different conditions and mechanisms operating locally. These should be identified in the description of damage so that critical conditions for damage initiation and growth can be predicted, and appropriate fracture criteria proposed.

Parameters used to date to quantify damage have been global or average damage values, relating to the decrease in load-bearing section. Damage mechanics formulations have not given consideration to the effects of a non-periodic distribution of voids or microcracks. A model was presented which includes the effects of coalescence in a random, rather than periodic, array of voids for a ductile hole growth mechanism. Experimental observations (Teirlinck, 1983; LeRoy et. al., 1981) indicate that the rate of damage accumulation accelerates with the level of damage, which could be due in part to the coalescence of voids. The model illustrated the influence of coalescence on the increase in damage, in a dilute void distribution with an initially random degree of clustering. No physical or mechanical criterion for coalescence was proposed; a simple geometric condition was assumed in defining the onset of coalescence between two voids. An important prediction obtained from this analysis was the dependence of fracture strain upon the initial volume fraction of voids and the effect of the stress state history. For a simple uniaxial stress path the variation of fracture strain with volume fraction exhibited a stronger dependence than that predicted by fracture models assuming an average void spacing.

This model, however, yields only a global damage level, given by the net section loss. The development of a critical flaw or a region with a locally high damage level could not be predicted. It is important to note here that when the flaw size, or the level of damage becomes large enough that a significant volume of material (relative to the sample volume) is unloaded, the damage rate is accelerated further.

This effect, occurring at higher damage levels, is not accounted for in continuum damage mechanics analyses. A fracture mechanics approach would then yield a more appropriate prediction of subsequent failure.

Notwithstanding these arguments, a simulation of the development of the flaw size distribution due to void coalescence was given, again assuming an initially dilute random distribution of voids. Results were obtained only to a limited strain level, so that the influence of the hydrostatic stress state which develops in the neck of a tensile sample upon damage acceleration was not fully evaluated. Over the range of strain and stress state considered, however, the tail end of the void size distribution developed very slowly. Deviation from randomness in the distribution of void nucleation sites could thus significantly alter the development of large flaws.

However, details of the non-random spatial distribution of damage cannot be incorporated into the simulation procedure, which is essentially a continuum damage approach. Thus, the effects of heterogeneity in damage distribution to produce a critical flaw or a highly damaged region in a material cannot be treated in the present formalism of continuum damage mechanics.

Many models exist in the literature which analyze the nucleation criteria and growth rates involved in various damage processes. Many commercial materials however, have heterogeneous microstructures, with a distribution of local volume fractions of constituents which act as damage initiation sites. The incorporation of the results of these models into a realistic prediction of damage accumulation and fracture

in these materials requires a quantitative description of the distribution of damage. In an attempt to characterize quantitatively the level of clustering or periodicity in a distribution of discrete features, we have considered the use of the Dirichlet tessellation. The tessellation provides a description of the surroundings of each particle in the distribution. Properties of the cells constructed in the tessellation were evaluated with respect to their sensitivity to the degree of deviation in the distribution from randomness. It was concluded that the tessellation could provide useful quantitative indicators of either the level of clustering or periodicity in a distribution. In addition, the effectiveness of the tessellation results in describing anisotropy in a dispersion was illustrated. It is suggested that further investigation into the use of the tessellation to characterize the distribution of clusters of particles in a dispersion could offer a potentially useful approach to the correlation of fracture behaviour with the distribution of damage associated with second-phase particles.

The goal of the above approach is to enable a distribution of discrete microstructural features to be characterized quantitatively, and to use these results in the prediction of the distribution of damage in a material. From the predicted distribution of damage, appropriate fracture criteria could thus be evaluated. This method of characterizing particle distributions could find application in other areas, such as recrystallization, where the distribution of second phase particles can influence the distribution of recrystallization sites.

Engineering materials often contain several microstructural components, with the result that different local fracture processes can be associated with the different phases present. The effect of variations in the spatial distribution of damage is then complicated by the variety of damage processes which operate concurrently. The HSLA steels examined in this study are an example of the development of several components of damage in a complicated microstructure. Void development in the bands of pearlite was observed at both ambient temperature and at -196°C. The intergranular carbides contributed to void initiation in deformation at ambient temperature, however, at lower temperatures they were associated with intergranular fracture. The brittle bainitic component along the plate centre line fractured in a pattern which suggested that load was transferred to it from the surrounding ferrite.

Although non-metallic inclusions were present in relatively low volume fractions in these steels, they were very important in controlling fracture. At low temperatures, cleavage fracture initiated at the large equiaxed calcium-bearing inclusions in the calcium-treated steels. Although ductile void growth was observed, the cleavage initiated at the inclusions controlled final fracture. In the steels which were not calcium-treated, it was the orientation and location of the elongated sulphides which strongly influenced fracture. Their association with bainite in controlling fracture is an example of the interaction between microstructural components to result in a dominant source of damage. At room temperature, the inclusion orientation relative to the stress axes influenced fracture strains, most notably in the through-thickness

orientation. The clusters of elongated sulphides then effectively provided a crack in the bainite normal to the tensile direction. At low temperatures it was concluded that the presence of inclusions associated with the bainite was required for delamination to occur, and that the extent of delamination in the tensile sample was dependent upon the inclusion orientation. Other evidence of the influence of local microstructure in altering the local fracture process was observed in the region between two closely-spaced bands of pearlite. It was suggested that the alteration of the local stress state resulted in the intergranular fracture observed in this region.

The simultaneous accumulation of damage associated with these different microstructural features can result in competition between the various damage processes in controlling the final fracture condition and the mode of fracture. The process which dominates, or rather, results in final fracture may be altered by changing the temperature, stress level, or the stress state. However, in the construction of fracture maps for these steels in $\bar{\sigma}$ - P space (Ashby et. al., 1985), $\bar{\sigma}_{max}$ - $\bar{\varepsilon}$ space (Otsuka et. al., 1979) or $\bar{\varepsilon}$ - $\frac{\sigma_{mean}}{\bar{\sigma}}$ - T space (Shimura and Saito, 1980), the influence of pressure or temperature will not be expressed by a sharp boundary separating two modes of fracture. Variations in local conditions result in mixed-mode type fractures in a transition from one dominant mode to another. The width and position of the transition region is expected to be dependent upon the microstructural constituents in a material. It will also be dependent upon the distribution of

microstructure, as aggregation can influence the local fracture processes which operate.

The relationship between the operative deformation mechanism(s) and damage process(es) is important, as the resulting damage can be influenced by temperature and stress. In the steels studied here the increase in the flow stress of the ferrite matrix with decreasing temperature resulted in additional intergranular and cleavage fracture processes. However, at elevated temperatures, the stress dependence of the damage accumulation behaviour in the Ni-Sn alloy was explained if the contribution which grain boundary sliding makes to the total deformation varies with stress. If the nucleation of intergranular voids and wedge cracks are dependent upon grain boundary sliding, as has been observed in other investigations, we may rationalize the increase in damage level at a given strain as the stress level decreases. This observation could be the result of the larger component which grain boundary sliding contributes to the total strain at low stresses. As surface crack propagation was observed to involve a significant degree of grain boundary sliding, an increase in sliding component could also explain the transition to surface crack-controlled fracture at lower stresses.

The distribution of tin in the nickel alloy investigated here was very inhomogeneous. The variation in tin level resulted in a non-uniform distribution of damage, associated with the regions of high tin content. In the surrounding material with a lower level of tin, comparatively little damage developed at fracture. The influence of this

ductile material in retarding crack growth initiated in the high solute regions resulted in an increase in macroscopic ductility, in comparison with an alloy of comparable composition, but with a more uniform tin distribution (White et. al., 1983). Thus, the influence of a non-uniform distribution of damage is not necessarily detrimental to the fracture properties of a material.

In conclusion, we must regard the process of fracture in engineering materials as the result of the accumulation of damage. The total level of damage can accumulate through several fracture processes, which operate locally in different components of the microstructure. The association of different microstructural features can alter the local conditions, thus affecting the local fracture process. In addition, the spatial distribution of damage must be viewed as an important factor which can influence the overall, or global level of damage at which fracture occurs. The development of practical methods to quantitatively characterize inhomogeneity in distributions, such as the Dirichlet tessellation, in conjunction with a more quantitative understanding of the effect of local microstructural aggregation upon damage processes will lead to more realistic predictions of the fracture behaviour and the variability in behaviour expected in heterogeneous materials.

APPENDIX A

SOURCE LISTING OF PROGRAM FRCTUR

```
      PROGRAM FRCTUR
C
C     THIS PROGRAM CALCULATES COALESCENCE PROBABILITIES USING THE
C     R2 CRITERION. NOTE ALSO THAT THE R2 RADIUS OF THE COALESCED
C     VOID IS GIVEN BY THAT WHICH PROVIDES THE SAME VOID CROSS-
C     SECTIONAL AREA AS THE SMALLEST ENVELOP ABOUT THE TWO VOIDS.
C     I.E., A LOWER BOUND FOR THE COALESCED R2 IS CHOSEN.
C
      DOUBLE PRECISION RNUV(180,240),S(240),RNVADD,DELRNV
      DOUBLE PRECISION COM,DLRNV1,DLRNV2,DLRNV
      DIMENSION N2MAX(240),NC2MAX(240),R1(180),R2(240),DELR1(180,240)
      DIMENSION ARFROC(180,240)
      CHARACTER*64 FILEIP,FILEOP,FILEOC,FILFRC,FILSTA
      READ(5,3) FILEIP
      READ(5,3) FILEOP
      READ(5,3) FILEOC
      READ(5,3) FILFRC
      READ(5,3) FILSTA
3     FORMAT(A)
      OPEN(UNIT=20,FILE=FILEIP,STATUS='OLD',FORM='FORMATTED')
      READ(20,*) VFRC,ASPVD,W1,W2,FRCOAL,FVLENG
      READ(20,*) STRNUC,STRUTS,RNECK,STRFRC,RNVCRT,KCRIT,KFRAC
      READ(20,*) STRCOF,ALPHAP,PRESS,STREXP
      READ(20,*) ALPHA,RNVNUC,IMAX,JMAX,STRMIN
      CLOSE(UNIT=20,DISPOSE='SAVE')
C
C*******INPUT PARAMETERS*************************************
C********VFRC=INITIAL VOID VOLUME FRACTION
C********ASPVD=ASPECT RATIO(R01/R02) OF NUCLEATED VOID
C********W1=INTERVAL SIZE,AS A FRACTION OF R01, FOR THE R1 DIMENSION
C********W2=INTERVAL SIZE, AS A FRACTION OF R02, FOR THE R2 DIMENSION
C********FVLENG=VOID ASPECT RATIO ABOVE WHICH THE PARTICLE NO LONGER
C********CONSTRAINS THE LATERAL CONTRACTION OF A VOID.
C********STRNUC=VOID NUCLEATION STRAIN
C********STRUTS=STRAIN AT WHICH NECK INITIATES
C********RNECK=PROPORTIONALITY CONSTANT FOR NECK PROFILE FUNCTION
C********OF STRAIN
C********STRFRC=FRACTURE STRAIN
C********RNVCRT=CRITICAL NO. OF VOIDS/UNIT VOL. FOR A GIVEN R2 DIM.,
C********FOR WHICH THE RNV IS WRITTEN TO FILE
C********KCRIT=R2/R2(CURRENT,FOR AN ISOLATED VOID) OF A VOID SIZE,
C********FOR WHICH IF RNV EXCEEDS RNVCRT, THE FRACTURE CONDITION
C********IS DEFINED.
C********STRCOF,ALPHAP,STREXP=TERMS IN STRESS-STRAIN RELATION
C********EFFECTIVE STRESS=Y=STRCOF*(1.-3.*ALPHAP*PRESS)*STR**STREXP
C********RNVNUC=NO./UNIT VOL. OF VOIDS OF NUCLEATED SIZE AT STRNUC
C********STRMIN=MINIMUM STRAIN INCREMENT ALLOWED.
C********IMAX=MAX. NO. OF ROWS IN RNUV MATRIX
C********JMAX=MAX. NO. OF COLUMNS IN RNUV MATRIX
C********ALPHA=DEFINES FRACTION OF CURRENT R2 DIMENSION, FOR WHICH, IF
C********IF THE VOID SPACING IS LESS THAN 2*ALPHA*R2, THE VOIDS ARE
C********CONSIDERED TO COALESCE.
C********VARIABLES USED**********************************************
C********RNUV(I,J)=NO./UNIT VOL. OF VOIDS WITH DIMENSIONS:
C********R1=I*R01/W1, AND R2=J*R02/W2
C********DELRNV,DLRNV1,DLRNV2,DLRNV=CALCULATED COALESCENCE INTERACTIONS
C********BETWEEN TWO GIVEN VOID SIZE INTERVALS, IN(R1,R2) SPACE
C********DELR1(I,J)= DELTA R1 FOR THE VOIDS IN SIZE INTERVAL (R1,R2),
C********FOR THE STRAIN INCREMENT STRINC JUST INCURRED.
C********N2MAX,NC2MAX,N1MAX ARE CURRENT MAXIMUM COLUMN AND ROW NUMBERS,
```

```
C*******ABOVE WHICH RNUV(,) ELEMENTS ARE ZERO
C*******ARFROC(I,J)=CONTRIBUTION OF VOIDS IN SIZE INTERVAL (I,J) TO
C*******THE DECREASE IN CROSS SECTIONAL AREA, MADE INCREMENTALLY, SO
C*******THAT THE OCCLUSION-FACTOR MAY BE MADE. NOTE THAT THE OCCLUSION
C*******FACTOR CONSIDERS ONLY THE THE AREA FRACTIONS OF THE TWO VOID
C*******SIZE INTERVALS UNDER CONSIDERATION.
C*******ARFRAC(I,J)=SIMILAR TO ARFROC(I,J), NOT CONSIDERING THE
C*******JOHNSON-MEHL OCCLUSION FACTOR
      II=0
      OPEN(UNIT=20,FILE=FILEOP,STATUS='NEW',SHARED,FORM='FORMATTED')
      OPEN(UNIT=21,FILE=FILEOC,STATUS='NEW',SHARED,FORM='FORMATTED')
      OPEN(UNIT=22,FILE=FILFRC,STATUS='NEW',SHARED,FORM='FORMATTED')
      OPEN(UNIT=23,FILE=FILSTA,STATUS='NEW',SHARED,FORM='FORMATTED')
      WRITE(20,*) II
      WRITE(21,*) II
      WRITE(22,*) II
      WRITE(23,*) II
      CLOSE(UNIT=20,DISPOSE='SAVE')
      CLOSE(UNIT=21,DISPOSE='SAVE')
      CLOSE(UNIT=22,DISPOSE='SAVE')
      CLOSE(UNIT=23,DISPOSE='SAVE')
C
C     IF KFRAC=0, THEN THE KCRIT CRITERION FOR FRACTURE IS EMPLOYED,
C     WHICH GIVES THE FRACTURE CRITERION AS A VOID SIZE WHICH IS A
C     MULTIPLE(=KCRIT) OF THE THE CURRENT ISOLATED VOID SIZE.
C
C     IF KFRAC>1, THEN THE FRACTURE CRITERION IS A VOID SIZE WHICH IS
C     A MULTIPLE, OR A FRACTION(=FRCOAL) OF THE AVERAGE INITIAL VOID
C     SPACING(=(1./RNVNUC)**(1./3.)),NOT CORRECTED FOR THE DECREASE
C     IN CROSS-SECTIONAL AREA.
C     ASPVD=R01/R02
C
      VVOID=VFRC/RNVNUC
      R02=(3.*VVOID/(4.*3.14159*ASPVD))**(1./3.)
      R01=ASPVD*R02
      ARFRAC=1.5*VFRC
      DNM1=W1*R01
      DNM2=W2*R02
      D=.292
      SPCCRT=FRCOAL*(1./RNVNUC)**(1./3.)
      JCRIT=INT(SPCCRT/DNM2)+1
      DO 5 J=1,JMAX
      JJ=J
5     R2(J)=(FLOAT(JJ)-.5)*DNM2
      DO 6 I=1,IMAX
      II=I
      NJMAX(I)=0
6     R1(I)=(FLOAT(II)-.5)*DNM1
      DO 7 J=1,JMAX
      DO 7 I=1,IMAX
      ARFROC(I,J)=0.
7     RNUV(I,J)=0.D0
      FAC=4.*3.14159*ALPHA**2
      FAC2=.5+ALPHA/3.14159
      FC1=2.*3.14159
      I=INT(1./W1)+1
      J=INT(1./W2)+1
C*******R02JNC AND R01JNC ARE NUCLEATED VOID SIZES, AT THE CENTRE OF
C*******THE SIZE INTERVALS IN WHICH R01 AND R02 RESPECTIVELY ARE.
      R02JNC=R2(J)
```

```
      R01INC=R1(I)
      RNUV(I,J)=RNUNUC
      ARFROC(I,J)=FC1*R01*RNUV(I,J)*R02**2
      N2MAX(I)=J
      N1MAX=I
      NC1MAX=N1MAX
      DO 25 I=1,IMAX
25    NC2MAX(I)=N2MAX(I)
      R10=R01INC
      R20=R02JNC
      STR=STRNUC
      KCURR=3
C******START STRAIN INCREMENT*********************************
30    IF(STR.GT.STRFRC) GO TO 5000
      IF(STR.EQ.0.) STR=STR+0.005
      Y=STRCOF*(1.+3.*ALPHAP*PRESS)*STR**STREXP
      IF(STR.GT.STRUTS) GO TO 40
      THYDRO=.5-1.5*PRESS/Y
      GO TO 50
C*******BRIDGMAN CORRECTION FOR HYDROSTATIC STRESSES DUE TO NECK
40    THYDRO=.5-1.5*PRESS/Y+1.5*LOG(1.+.5*RNECK*(STR-STRUTS))
50    D=.28*(EXP(THYDRO)-EXP(-1.*THYDRO))
      STRINC=1.01*R01*W1/(R10*(1.+R20/R10+D))
      IF(STRINC.LT.STRMIN) STRINC=STRMIN
C*******CALCULATE VOID GROWTH VIA RICE/TRACEY GROWTH LAW AND SHIFT
C*******RNUV COMPONENTS DUE TO GROWTH DURING STRAIN INCREMENT STRINC
      R10=R10*(1.+STRINC*(1.+R20/R10+D))
      R20=R20*(1.+STRINC*(D-.5*(1.+R20/R10)))
C*******CHECK FOR PARTICLE CONSTRAINT ON AXIAL VOID CONTRACTION
      IF(R10.LT.R01INC) R10=R01INC
C*******CHECK FOR PARTRICLE CONSTRAINT ON LATERAL VOID CONTRACTION
      IF(R20.LT.R02JNC.AND.R10.LE.(FVLENG*R01INC)) R20=R02JNC
      DO 100 I=N1MAX,1,-1
      IF(N2MAX(I).EQ.0) GO TO 100
      DO 80 J=N2MAX(I),1,-1
      IF(RNUV(I,J).EQ.0.) GO TO 80
      GAMMA=1.+R2(J)/R1(I)
      DLR1=R1(I)*STRINC*(D+GAMMA)
      DLR2=R2(J)*STRINC*(D-.5*GAMMA)
      IF(R2(J).GT.R02JNC) GO TO 90
C*******CHECKM FOR PARTICLE CONSTRAINT ON AXIAL VOID CONTRACTION
      IF(DLR1.LT.0..AND.R1(I).LE.R01INC) DLR1=0.
C*******CHECK FOR PARTICLE CONSTRAINT ON LATERAL VOID CONTRACTION
      IF(DLR2.LT.0..AND.R1(I).LE.(FVLENG*R01INC)) DLR2=0.
90    RN1=R1(I)+DLR1
      RN2=R2(J)+DLR2
      IN=INT(RN1/DNM1)+1
      JN=INT(RN2/DNM2)+1
      IF(IN.GT.IMAX) IN=IMAX
      IF(JN.GT.JMAX) JN=JMAX
      DELR1(IN,JN)=DLR1
      RNVADD=RNUV(I,J)
      RNUV(IN,JN)=RNUV(IN,JN)+RNVADD
      RNUV(I,J)=RNUV(I,J)-RNVADD
      ARF=ARFROC(I,J)
      ARFROC(IN,JN)=ARFROC(IN,JN)+ARFROC(I,J)*R1(IN)
     *  *R2(JN)**2/(R1(I)*R2(J)**2)
      ARFROC(I,J)=ARFROC(I,J)-ARF
      IF(IN.GT.NC1MAX) NC1MAX=IN
      IF(JN.GT.NC2MAX(IN)) NC2MAX(IN)=JN
```

```
80      CONTINUE
100     CONTINUE
        IF(NC1MAX.GT.N1MAX) N1MAX=NC1MAX
        DO 110 I=1,N1MAX
        IF(NC2MAX(I).GT.N2MAX(I)) N2MAX(I)=NC2MAX(I)
110     CONTINUE
C       RNUV IS NOW UPDATED DUE TO VOID GROWTH IN THE CURRENT STRAIN
C       INCREMENT. NOW TO CALCULATE COALESCENCE PROBABILITIES, AND
C       UPDATE RNUV DUE TO VOID COALESCENCE.
C
        DO 500 I=1,N1MAX
C*******INTERACTIONS BETWEEN GIVEN VOID AND VOIDS IN SAME ROW, I.E.
C*******WITH SAME R1 DIMENSION.
        DO 450 J=1,N2MAX(I)
        IF(RNUV(I,J).LT.1.E-100) GO TO 450
        DO 300 JJ=J,N2MAX(I)
        IF(RNUV(I,JJ).LT.1.E-100) GO TO 300
        RNEW=(FAC2*(R2(J)+R2(JJ))**2-R2(J)*R2(JJ))**.5
        JNEW=INT(RNEW/DNM2)+1
        IF(JNEW.GT.JMAX) GO TO 300
        COM=FAC*R1(I)*RNUV(I,J)*RNUV(I,JJ)*(R2(J)+R2(JJ))**2/(2.*R1(I))
        DLRNV1=COM*DELR1(I,JJ)
        DLRNV2=COM*DELR1(I,J)
        DELRNV=0.5*(DLRNV1+DLRNV2)
C*******CHECK THAT DELRNV IS NOT GREATER THAN EITHER OF THE CURRENT
C*******VOID NO. DENSITIES. IF SO, FORCE THE COALESCENCE NO. TO BE
C*******  NO GREATER THAN EITHER OF THE NO. DENSITIES.
        IF(DELRNV.LT.RNUV(I,J).AND.DELRNV.LT.RNUV(I,JJ)) GO TO 200
        IF(DLRNV1.GT.DLRNV2) DLRNV=DLRNV2
        IF(DLRNV1.LE.DLRNV2) DLRNV=DLRNV1
        IF(DLRNV.LE.RNUV(I,J).AND.DLRNV.LE.RNUV(I,JJ)) GO TO 140
        IF(RNUV(I,J).LE.RNUV(I,JJ)) DELRNV=RNUV(I,J)
        IF(RNUV(I,JJ).LT.RNUV(I,J)) DELRNV=RNUV(I,JJ)
        GO TO 200
140     DELRNV=DLRNV
200     AFAC=FC1*R1(I)*DELRNV
        ARFRJ=AFAC*R2(J)**2
        ARFRJJ=AFAC*R2(JJ)**2
        ARFRJN=AFAC*R2(JNEW)**2*(1.-ARFROC(I,J)-ARFROC(I,JJ))
        ARFROC(I,J)=ARFROC(I,J)-ARFRJ
        ARFROC(I,JJ)=ARFROC(I,JJ)-ARFRJJ
        ARFROC(I,JNEW)=ARFROC(I,JNEW)+ARFRJN
        RNUV(I,JNEW)=RNUV(I,JNEW)+DELRNV
        RNUV(I,J)=RNUV(I,J)-DELRNV
        RNUV(I,JJ)=RNUV(I,JJ)-DELRNV
        IF(JNEW.GT.NC2MAX(I)) NC2MAX(I)=JNEW
300     CONTINUE
        IF(I.EQ.N1MAX) GO TO 450
C*******INTERACTIONS OF GIVEN VOID WITH OTHER VOIDS
        DO 700 II=I+1,N1MAX
        DO 600 JJ=1,N2MAX(II)
        IF(RNUV(II,JJ).LT.1.E-100) GO TO 600
        RNEW=(FAC2*(R2(J)+R2(JJ))**2-R2(J)*R2(JJ))**.5
        JNEW=INT(RNEW/DNM2)+1
        IF(JNEW.GT.JMAX) GO TO 600
        COM=FAC*RNUV(I,J)*RNUV(II,JJ)*(R2(J)+R2(JJ))**2/(R1(I)+R1(II))
        DLRNV1=COM*R1(I)*DELR1(II,JJ)
        DLRNV2=COM*R1(II)*DELR1(I,J)
        DELRNV=0.5*(DLRNV1+DLRNV2)
C*******AGAIN, CHECK THAT DELRNV IS NOT GREATER THAN EITHER OF THE
```

```
C*******CURRENT VOID NUMBER DENSITIES. IF SO, FORCE A MAXIMUM VALUE
C*******WHICH IS NO GREATER THAN EITHER OF THE VOID NUMBER DENSITIES
C*******OF THE TWO INTERACTING VOIDS.
        IF(DELRNV.LT.RNUV(I,J).AND.DELRNV.LT.RNUV(II,JJ)) GO TO 320
        IF(DLRNV1.GT.DLRNV2) DLRNV=DLRNV2
        IF(DLRNV1.LE.DLRNV2) DLRNV=DLRNV1
        IF(DLRNV.LE.RNUV(I,J).AND.DLRNV.LE.RNUV(II,JJ)) GO TO 330
        IF(RNUV(I,J).LE.RNUV(II,JJ)) DELRNV=RNUV(I,J)
        IF(RNUV(II,JJ).LT.RNUV(I,J)) DELRNV=RNUV(II,JJ)
        GO TO 320
330     DELRNV=DLRNV
320     AFAC=FC1*DELRNV
        ARFRJ=AFAC*R1(I)*R2(J)**2
        ARFRJJ=AFAC*R1(II)*R2(JJ)**2
        ARFRJN=AFAC*R1(II)*R2(JNEW)**2*(1.-ARFROC(I,J)-ARFROC(II,JJ))
       .ARFROC(I,J)=ARFROC(I,J)-ARFRJ
        ARFROC(II,JJ)=ARFROC(II,JJ)-ARFRJJ
        ARFROC(II,JNEW)=ARFROC(II,JNEW)+ARFRJN
        RNUV(II,JNEW)=RNUV(II,JNEW)+DELRNV
        RNUV(I,J)=RNUV(I,J)-DELRNV
        RNUV(II,JJ)=RNUV(II,JJ)-DELRNV
        IF(JNEW.GT.NC2MAX(II)) NC2MAX(II)=JNEW
600     CONTINUE
700     CONTINUE
450     CONTINUE
500     CONTINUE
C
C       N.B. THAT N1MAX REMAINS CONSTANT IN THE COALESCENCE STEP
C
C*******UPDATE MAXIMUM NO. OF COLUMNS IN EACH ROW
C
        DO 750 I=1,N1MAX
        IF(NC2MAX(I).GT.N2MAX(I)) N2MAX(I)=NC2MAX(I)
750     CONTINUE
C
C
        DO 770 J=1,JMAX
770     S(J)=0.D0
C
C
C*******WRITE UPDATED AVERAGE VOID AREA FRACTIONS TO FILE
        ARFRAC=0.
        AFROCT=0.
        DO 1000 I=1,N1MAX
        FC=FC1*R1(I)
        DO 900 J=1,N2MAX(I)
        IF(RNUV(I,J).EQ.0.) GO TO 900
        ARFRAC=ARFRAC+FC*RNUV(I,J)*R2(J)**2
        AFROCT=AFROCT+ARFROC(I,J)
900     CONTINUE
1000    CONTINUE
        STR=STR+STRINC
        OPEN(UNIT=20,FILE=FILEOP,STATUS='OLD',SHARED,ACCESS='APPEND',
     $  FORM='FORMATTED')
        WRITE(20,*) STR,ARFRAC
        CLOSE(UNIT=20,DISPOSE='SAVE')
        OPEN(UNIT=21,FILE=FILEOC,STATUS='OLD',SHARED,ACCESS='APPEND',
     $  FORM='FORMATTED')
        WRITE(21,*) STR,AFROCT
        CLOSE(UNIT=21,DISPOSE='SAVE')
```

```
C
C       WRITE CURRENT R2 VOID DIMENSION DISTRIBUTION TO FILE
C       NOTE THAT EACH INTERVAL IN THIS FILE IS A SUM OVER ALL VOIDS
C       IN THE (R1,R2) DISTRIBUTION HAVING THE GIVEN R2 DIMENSION,
C       REGARDLESS OF ITS R1 DIMENSION. THUS, THESE VALUES SHOULD NOT
C       BE CONSIDERED AS ACTUAL VOID NO. DENSITIES FOR A GIVEN R2
C       DIMENSION.
C
        DO 1080 J=1,JMAX
        DO 1080 I=1,N1MAX
1080    S(J)=S(J)+RNUV(I,J)
        OPEN(UNIT=23,FILE=FILSTA,STATUS='OLD',SHARED,ACCESS='APPEND',
     *  FORM='FORMATTED')
        WRITE(23,*) STR
        DO 1090 J=1,JMAX
1090    WRITE(23,*) S(J)
        CLOSE(UNIT=23,DISPOSE='SAVE')
C
C       CHECK FOR A FRACTURE CRITERION
C
        N2MX=0
        DO 1020 I=1,N1MAX
        IF(N2MAX(I).GT.N2MX) N2MX=N2MAX(I)
1020    CONTINUE
        IF(KFRAC.EQ.1) GO TO 3000
C*******THIS FRACTURE CRITERION CHECKS IF ANY CURRENT VOID SIZE INTERVAL
C*******(WHICH IS GREATER THAN KCRIT TIMES THE CURRENT R2 DIMENSION OF AN
C*******ISOLATED VOID) IS GREATER THAN RNVCRT.
        R20CHK=R20
        IF(R20CHK.LT.R02JNC) R20CHK=R02JNC
        JCURR=INT(FLOAT(KCURR)*R20CHK/DNM2)+1
        IF(N2MX.LT.JCURR) GO TO 30
        DO 1050 J=N2MX,JCURR,-1
        DO 1040 I=1,N1MAX
        IF(RNUV(I,J).EQ.0.) GO TO 1040
        IF(RNUV(I,J).GE.RNVCRT) GO TO 1060
1040    CONTINUE
1050    CONTINUE
        GO TO 30
1060    RNMX=0.
        DO 1070 I=1,N1MAX
        IF(RNUV(I,J).GT.RNMX) RNMX=RNUV(I,J)
1070    CONTINUE
        KCHK=INT(FLOAT(J)*DNM2/R20CHK)
        OPEN(UNIT=22,FILE=FILFRC,STATUS='OLD',SHARED,ACCESS='APPEND',
     *  FORM='FORMATTED')
C*******KCHK=MULTIPLE OF CURRENT R2 DIMENSION OF AN ISOLATED VOID, FOR
C*******WHICH THE RNUV OF A GIVEN SIZE INTERVAL IS GREATER THAN RNVCRT.
C*******STR=CURRENT
C*******RNMX=RNUV OF THE GIVEN VOID SIZE INTERVAL.
        WRITE(22,*) KCHK,STR,RNMX
        CLOSE(UNIT=22,DISPOSE='SAVE')
        IF(KCHK.GE.KCRIT) GO TO 5000
        KCURR=KCHK+1
        GO TO 30
3000    CONTINUE
        IF(N2MX.LT.JCRIT) GO TO 30
        DO 3400 J=N2MX,JCRIT,-1
        DO 3300 I=1,N1MAX
        IF(RNUV(I,J).GE.RNVCRT) GO TO 3450
```

```
3300    CONTINUE
3400    CONTINUE
        GO TO 30
3450    RNMX=0.
        DO 3460 I=1,NIMAX
        IF(RNUV(I,J).GT.RNMX) RNMX=RNUV(I,J)
3460    CONTINUE
        OPEN(UNIT=22,FILE=FILFRC,STATUS='OLD',SHARED,ACCESS='APPEND',
     &  FORM='FORMATTED')
        WRITE(22,*) SPCCRT,FRCOAL,STR,RNMX
        CLOSE(UNIT=22,DISPOSE='SAVE')
5000    CONTINUE
        STOP
        END
```

APPENDIX B

HISTOGRAMS OF MEASURED INTERNAL CAVITY/MICROCRACK AND SURFACE CRACK SIZE DISTRIBUTION IN Ni-Sn ALLOY

In Figures B.1 to B.14, the internal cavity and microcrack size distributions measured in the Ni-Sn specimens at various stages in the creep life are given. In Figures B.15 to B.27 the measured surface crack size distributions are given. The initial applied stress level and the strain at which the damage was evaluated is given on each figure.

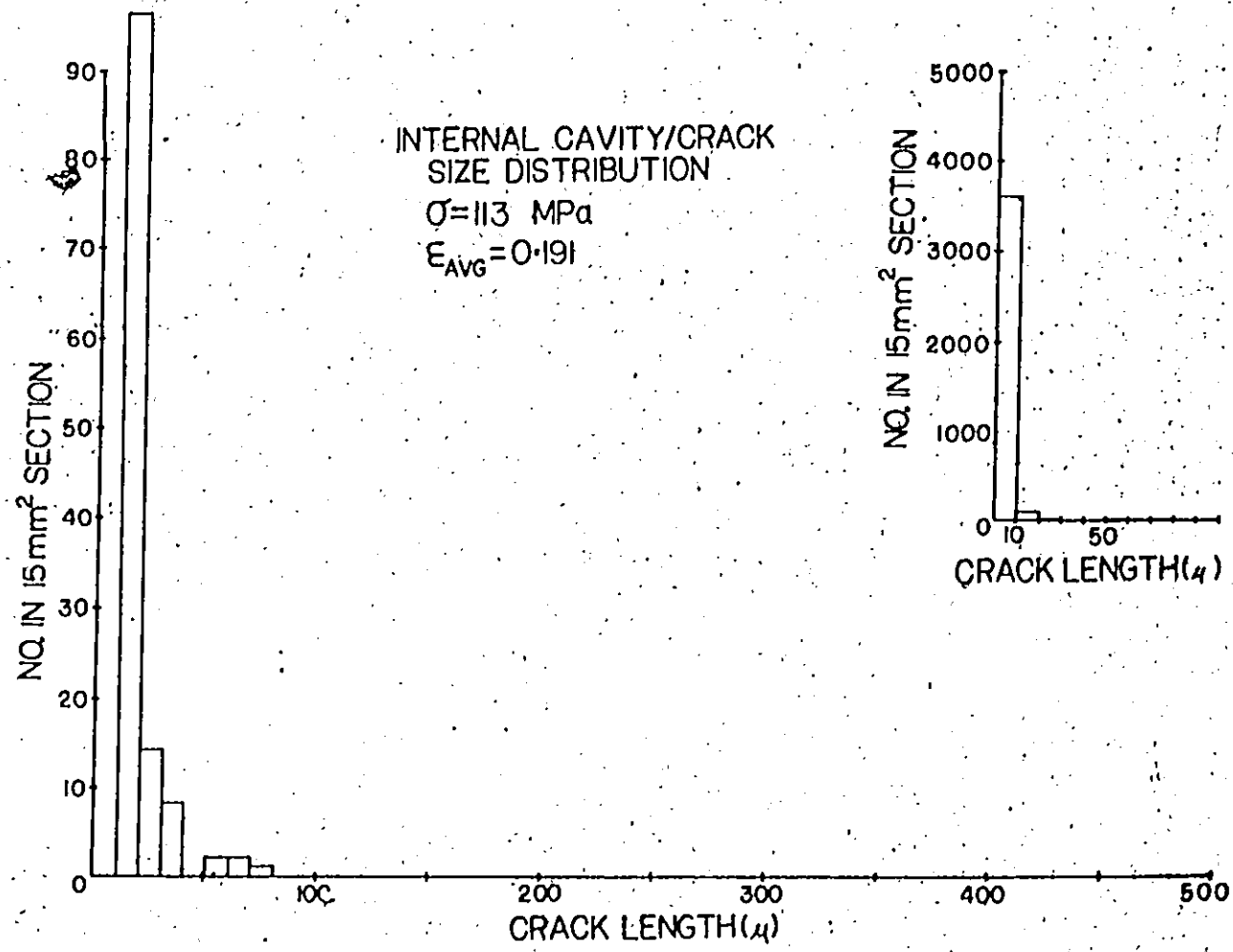

Fig. B.1: Histogram of the cavity/microcrack size distribution which developed in the sample interior, at a strain of 0.191. The initial applied stress was 113 MPa.

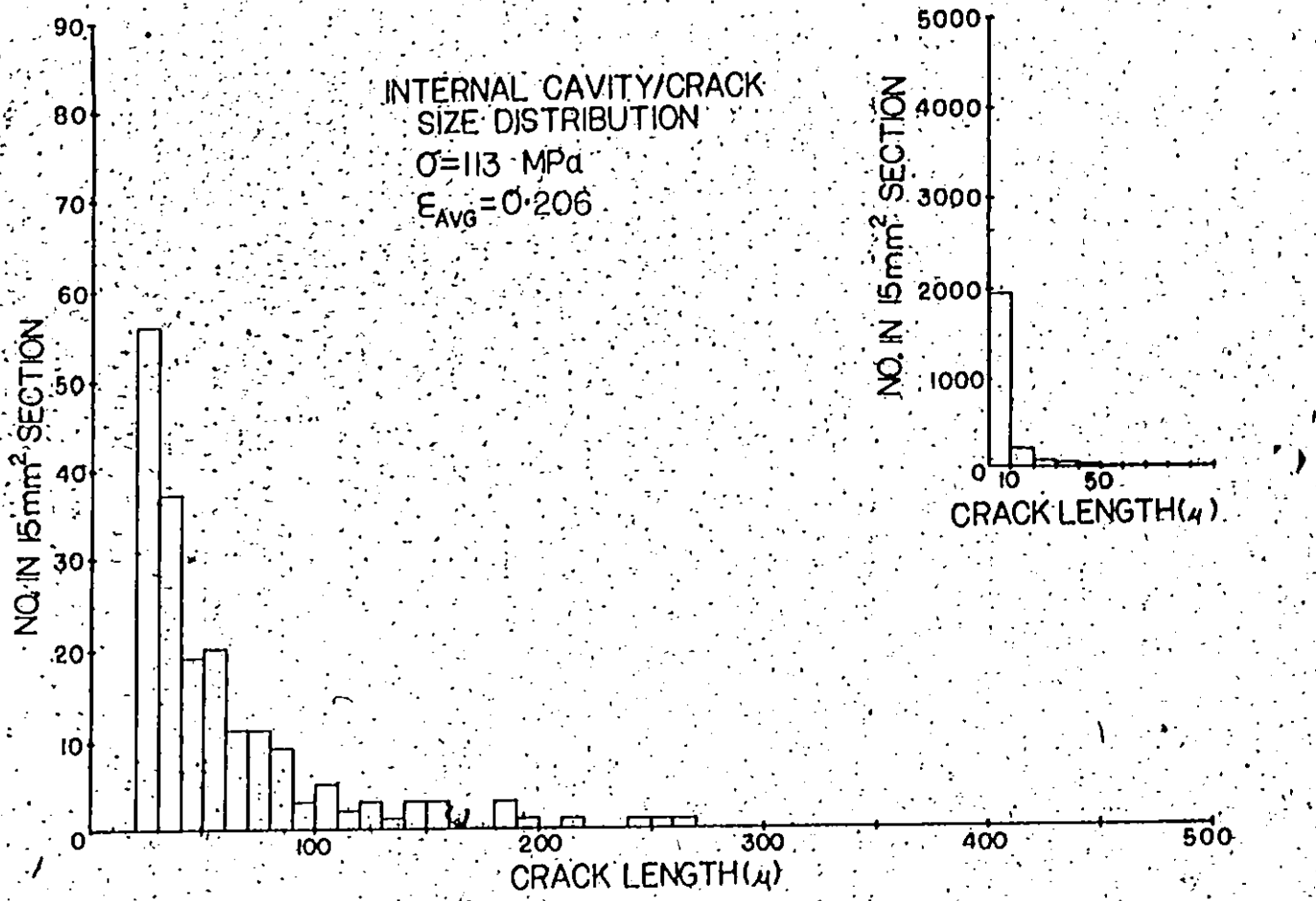

Fig. B.2: Histogram of the cavity/microcrack size distribution which developed in the sample interior, at a strain of 0.206. The initial applied stress was 113 MPa.

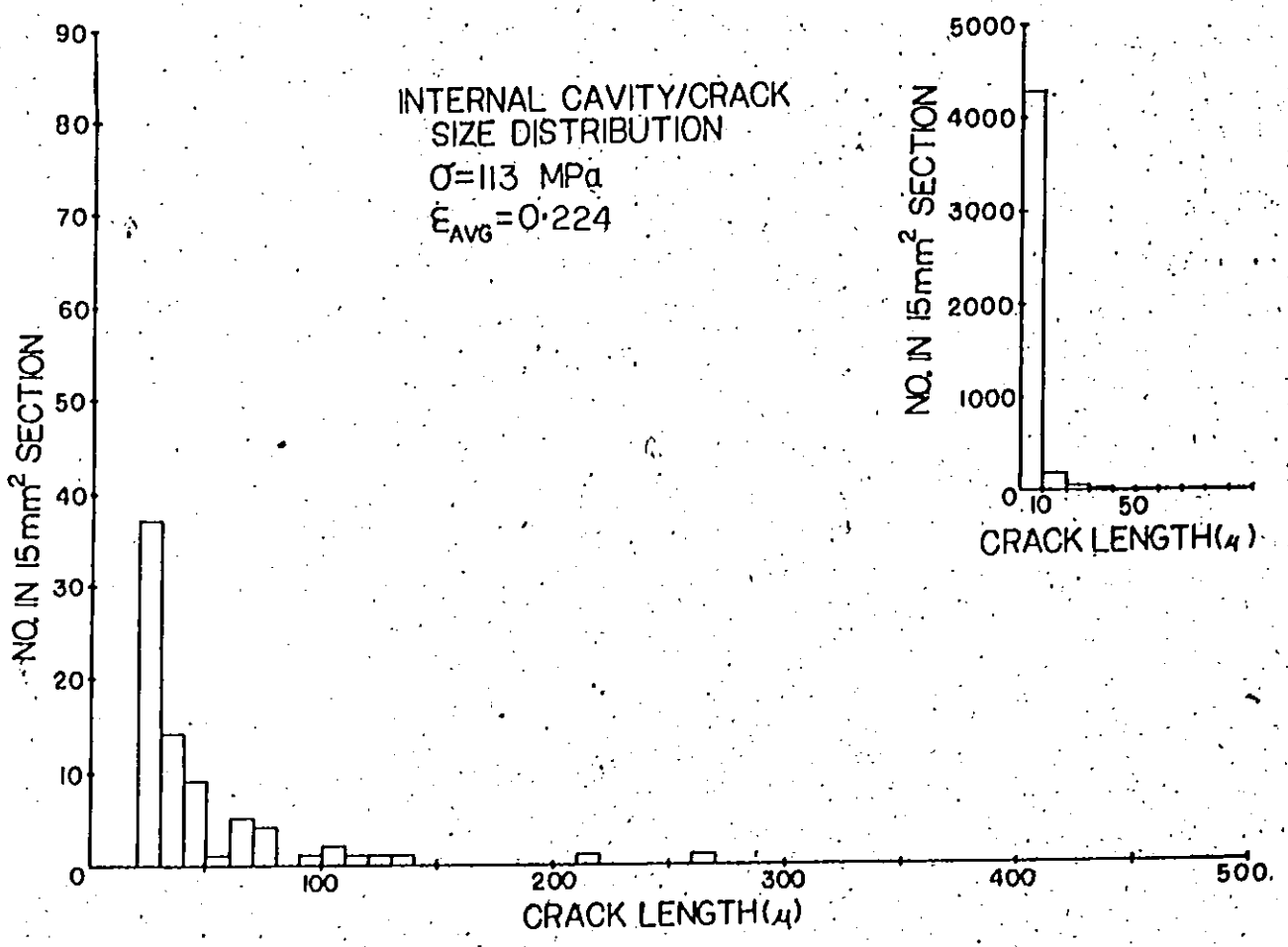

Fig. B.3: Histogram of the cavity/microcrack size distribution which developed in the sample interior, at a strain of 0.224. The initial applied stress was 113 MPa.

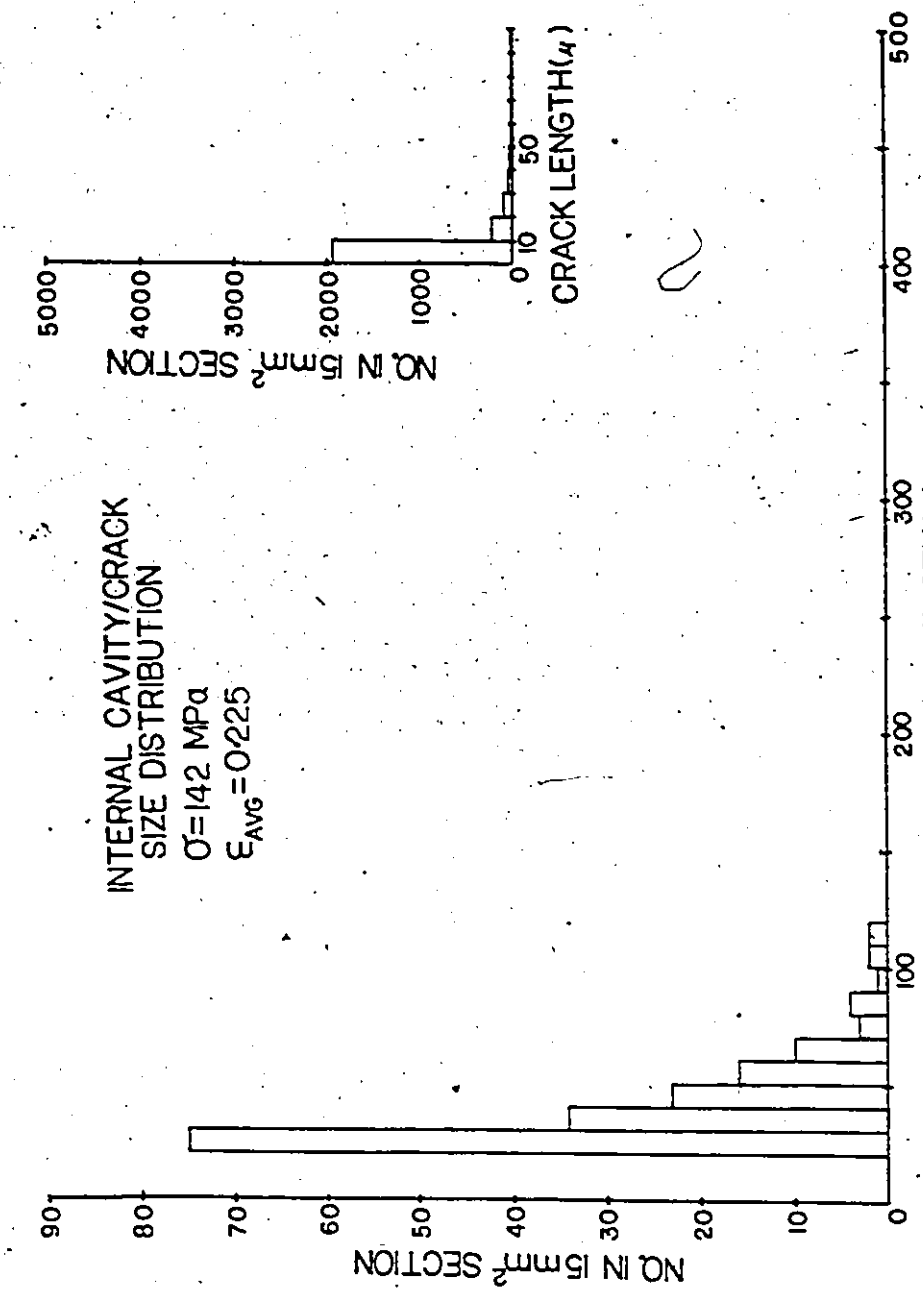

Fig. B.4: Histogram of the cavity/microcrack size distribution which developed in the sample interior, at a strain of 0.225. The initial applied stress was 142 MPa.

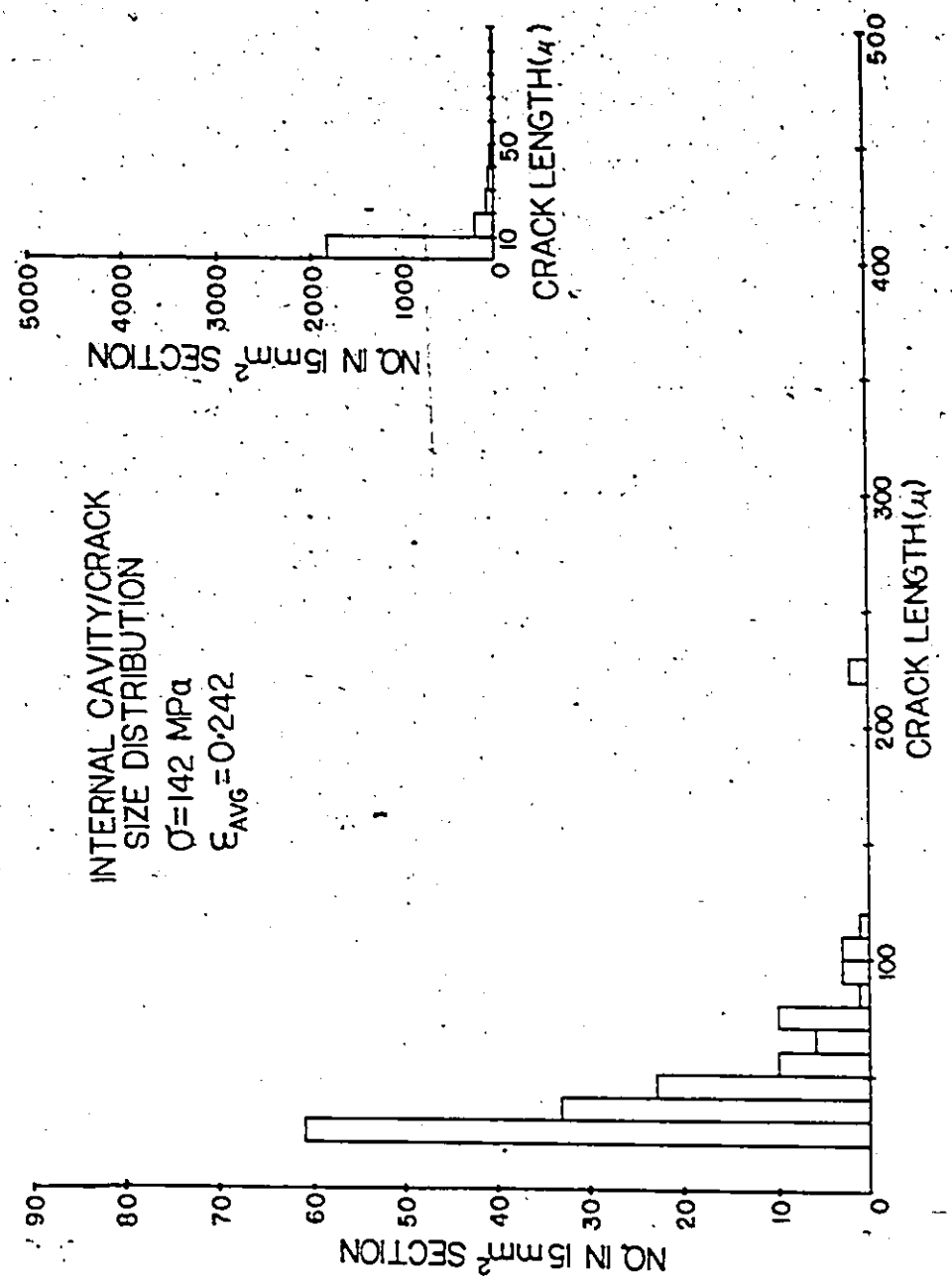

Fig. B.5: Histogram of the cavity/microcrack size distribution which developed in the sample interior, at a strain of 0.242. The initial applied stress was 142 MPa.

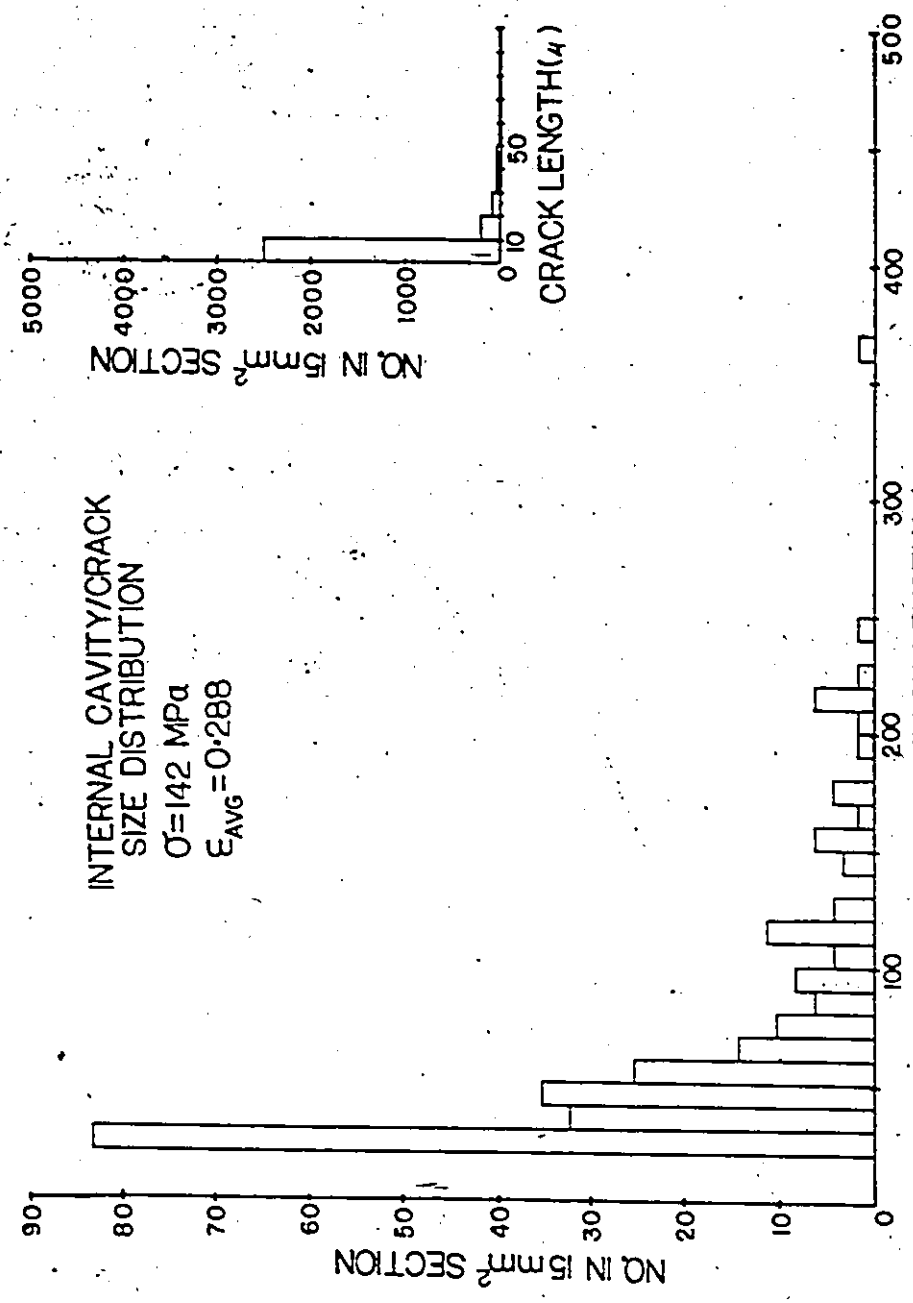

Fig. B.6: Histogram of the cavity/microcrack size distribution which developed in the sample interior, at a strain of 0.288. The initial applied stress was 142 MPa.

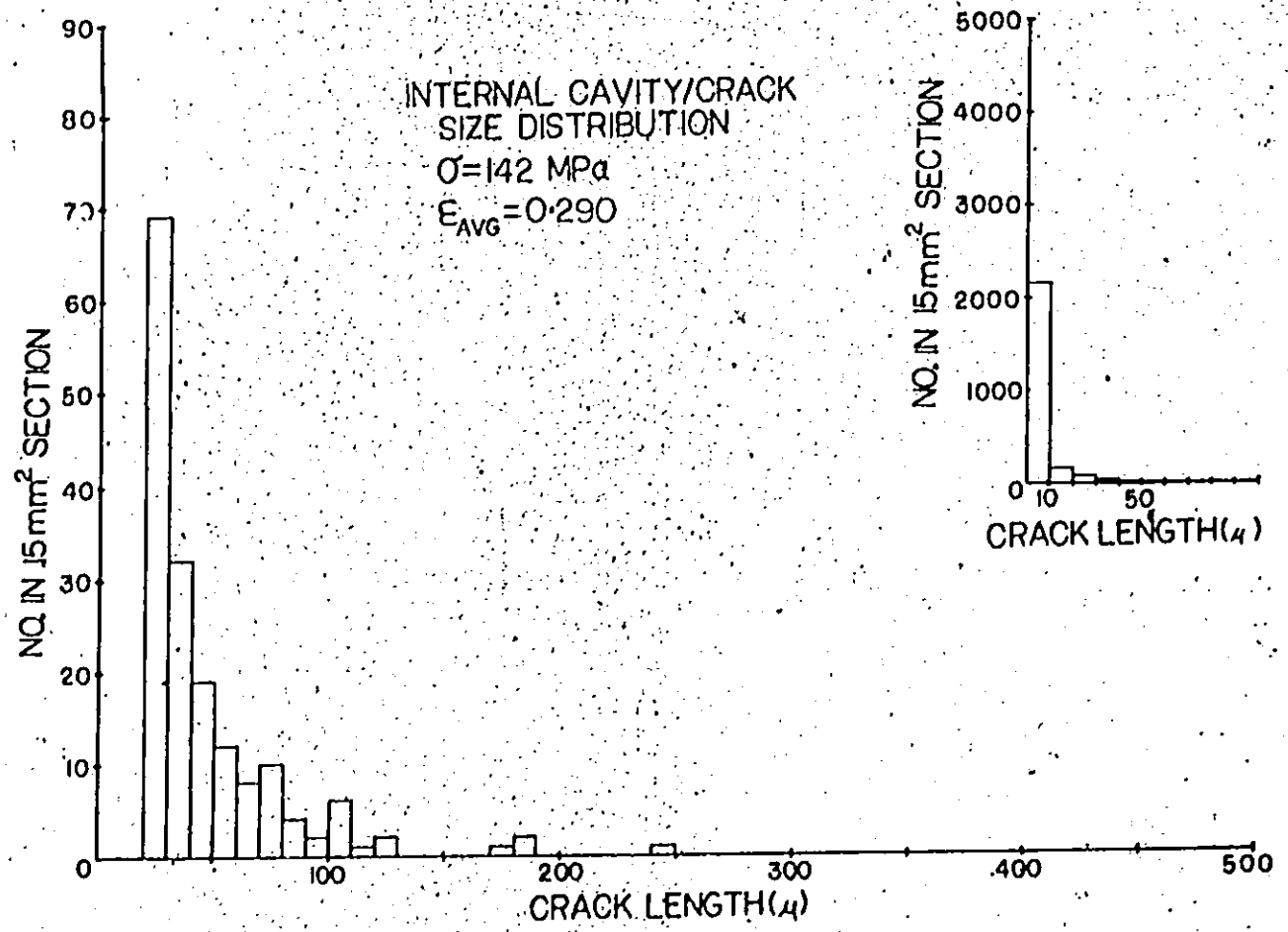

Fig. B.7: Histogram of the cavity/microcrack size distribution which developed in the sample interior, at a strain of 0.290. The initial applied stress was 142 MPa.

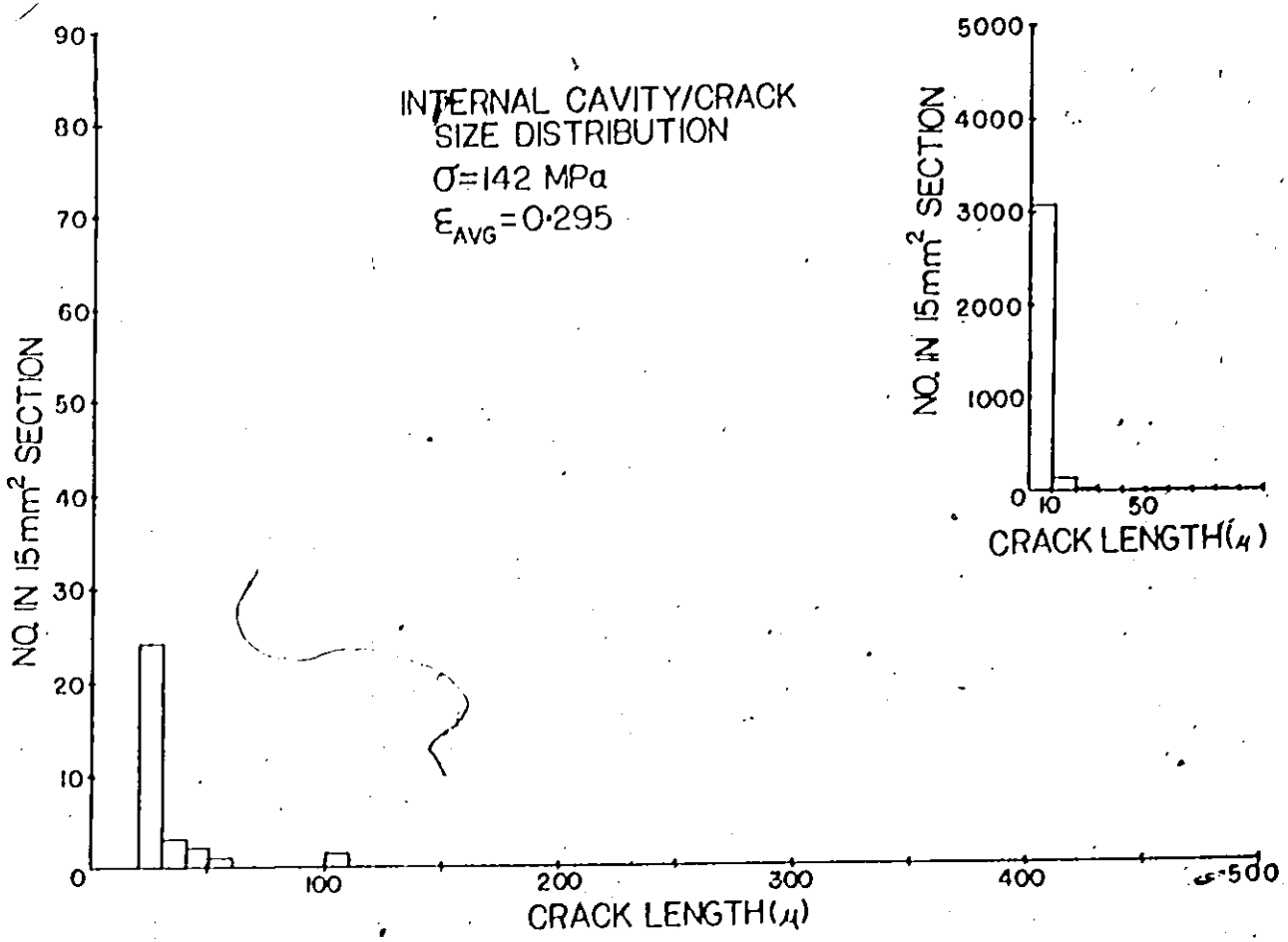

Fig. B.8: Histogram of the cavity/microcrack size distribution which developed in the sample interior, at a strain of 0.295. The initial applied stress was 142 MPa.

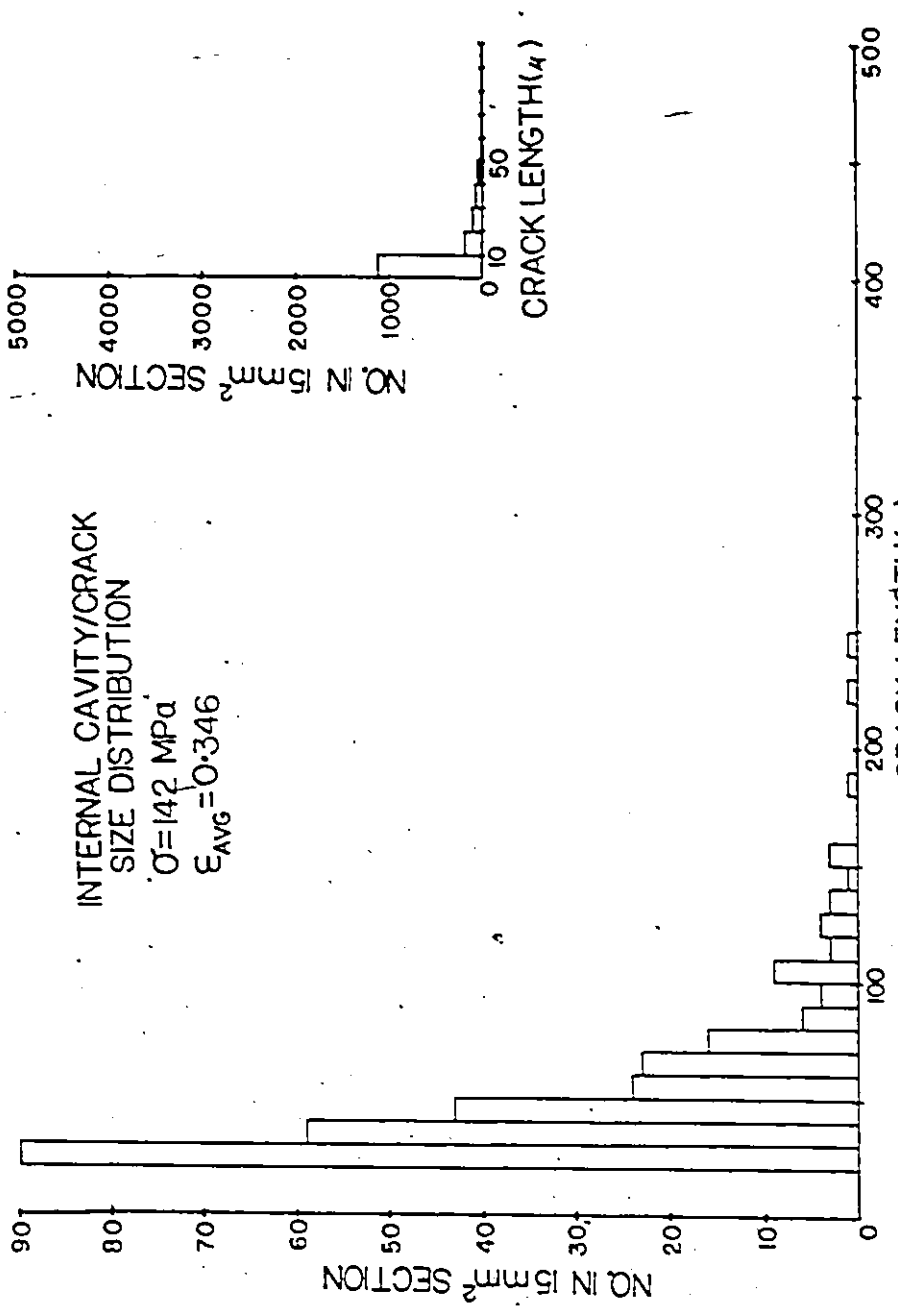

Fig. B.9: Histogram of the cavity/microcrack size distribution which developed in the sample interior, at a strain of 0.346. The initial applied stress was 142 MPa.

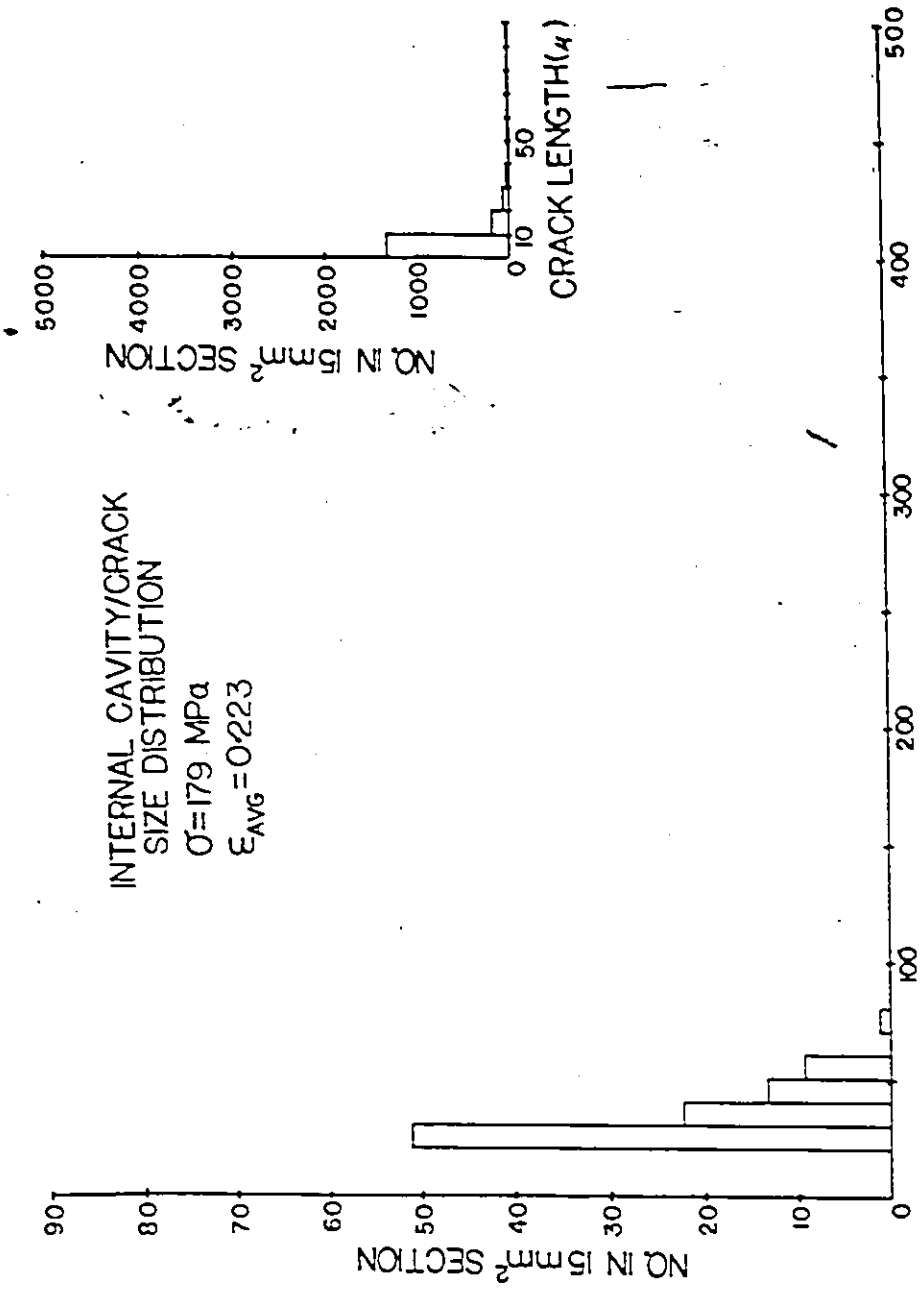

Fig. B.10: Histogram of the cavity/microcrack size distribution which developed in the sample interior, at a strain of 0.223. The initial applied stress was 179 MPa.

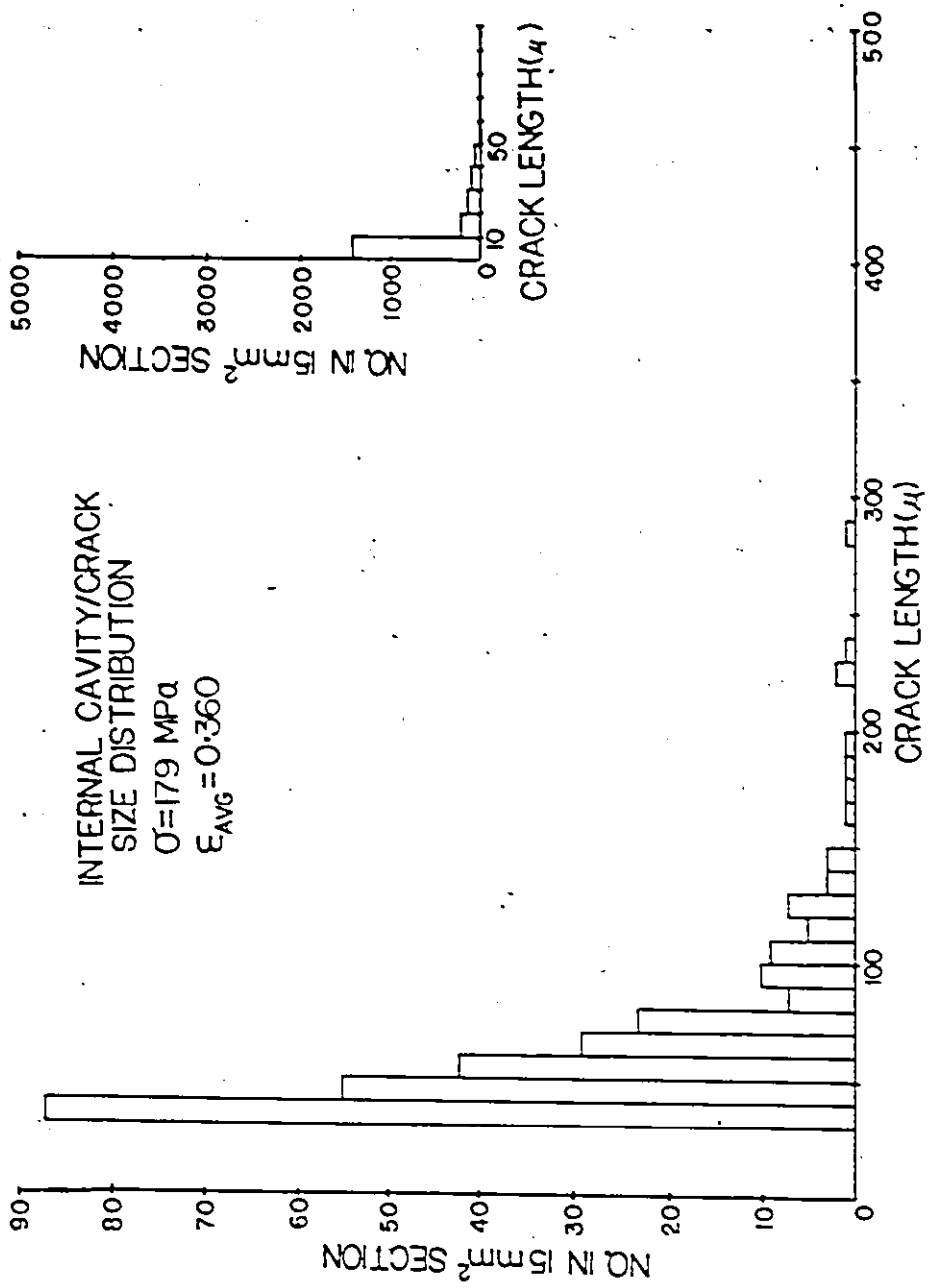

Fig. B.11: Histogram of the cavity/microcrack size distribution which developed in the sample interior, at a strain of 0.360. The initial applied stress was 179 MPa.

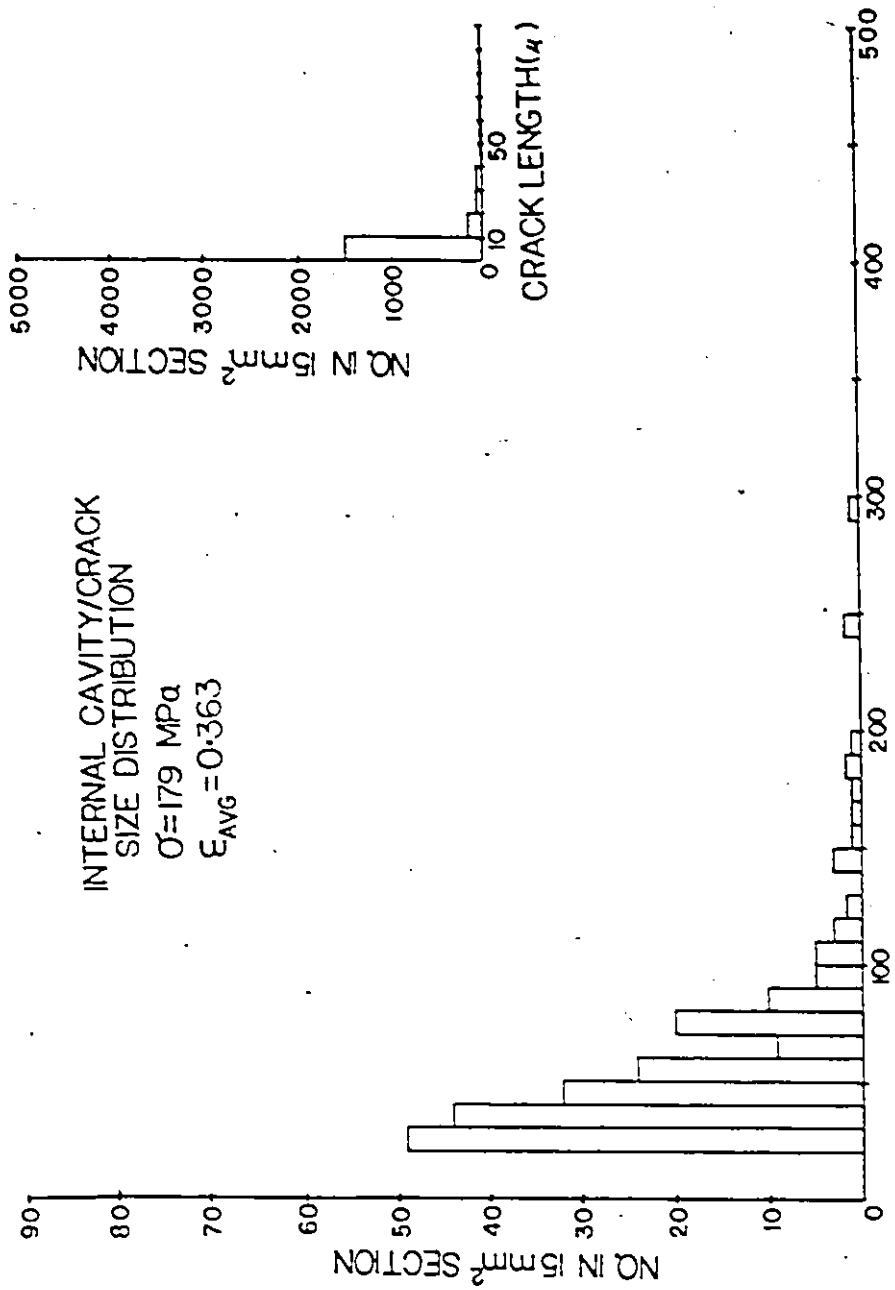

Fig. B.12: Histogram of the cavity/microcrack size distribution which developed in the sample interior, at a strain of 0.363. The initial applied stress was 179 MPa.

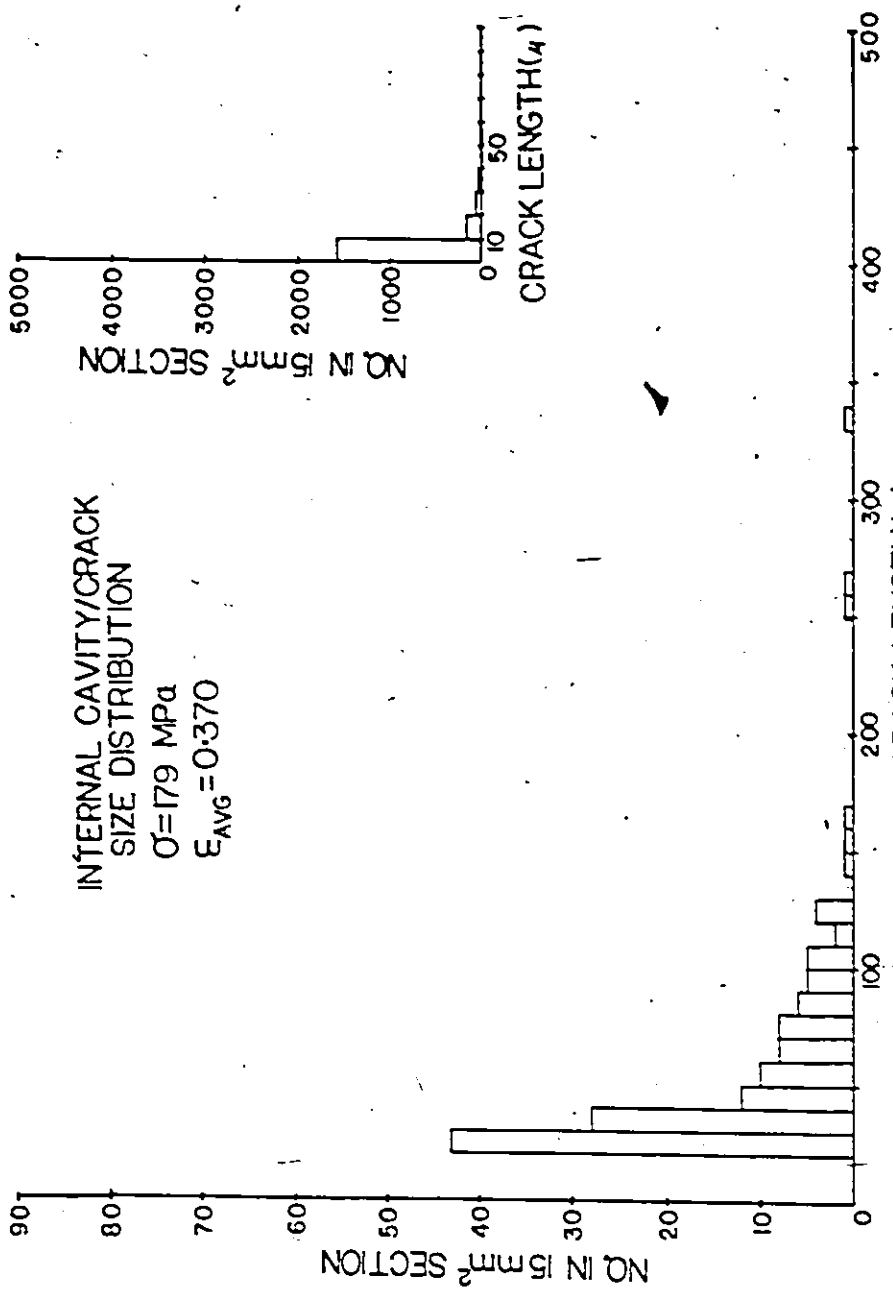

Fig. B.13: Histogram of the cavity/microcrack size distribution which developed in the sample interior, at a strain of 0.370. The initial applied stress was 179 MPa.

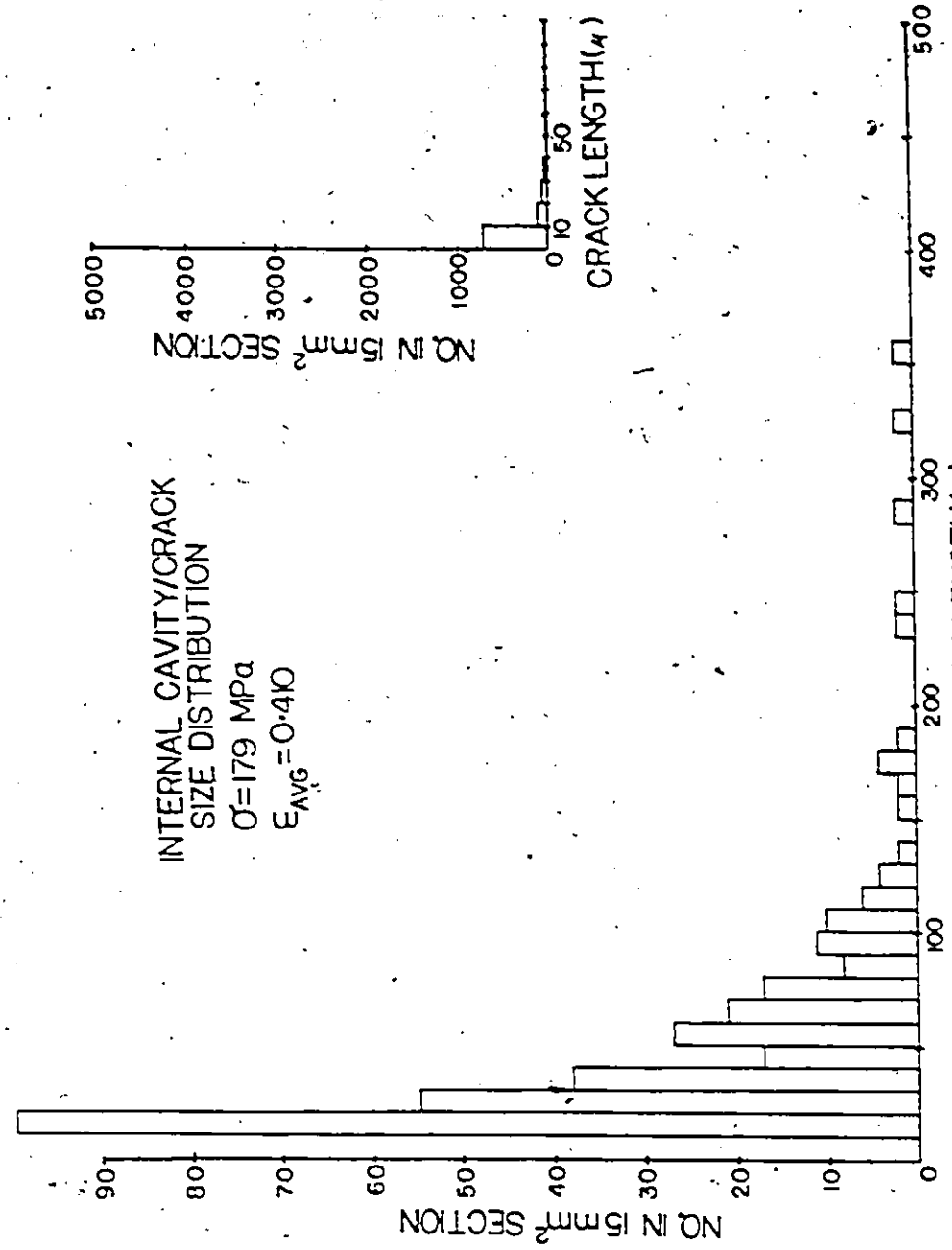

Fig. B.14: Histogram of the cavity/microcrack size distribution which developed in the sample interior, at a strain of 0.410. The initial applied stress was 179 MPa.

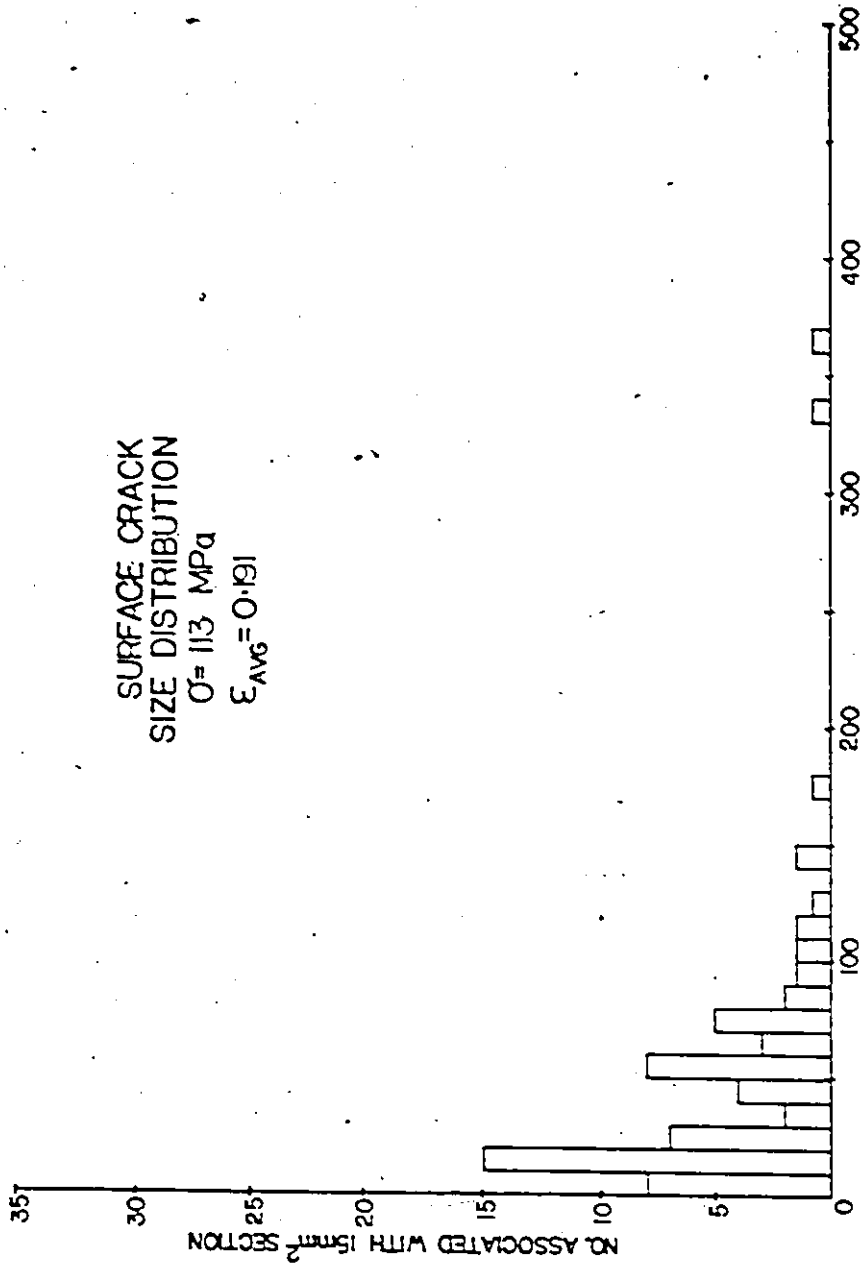

Fig. B.15: Histogram of the surface crack size distribution which developed at a strain of 0.191. Results have been normalized to a length of sample edge which bounds 15 mm^2 of sample in cross-section. The initial applied stress was 113 MPa.

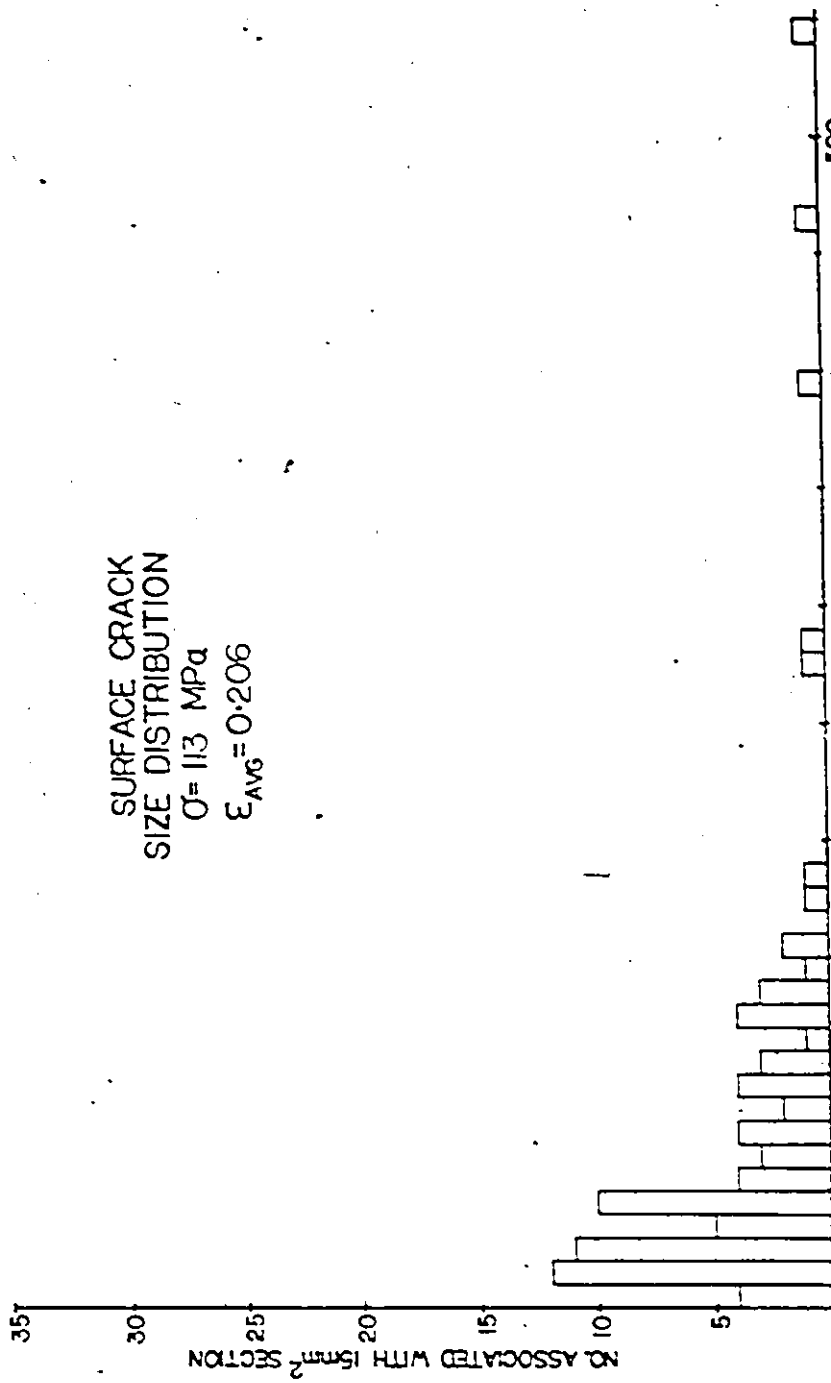

Fig. B.16: Histogram of the surface crack size distribution which developed at a strain of 0.206. Results have been normalized to a length of sample edge which bounds 15 cm^2 of sample in cross-section. The initial applied stress was 113 MPa.

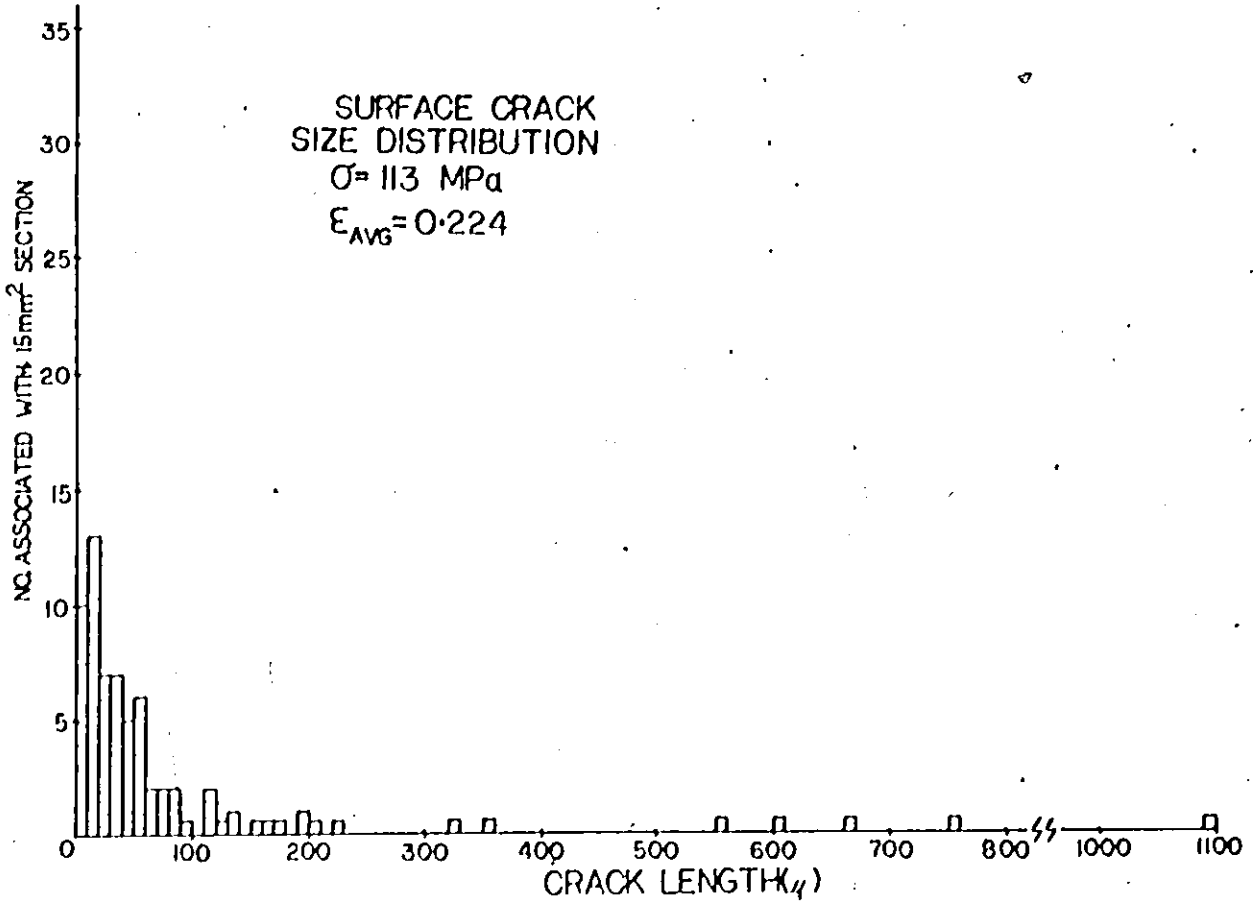

Fig. B.17: Histogram of the surface crack size distribution which developed at a strain of 0.224. Results have been normalized to a length of sample edge which bounds 15 mm^2 of sample in cross-section. The initial applied stress was 113 MPa.

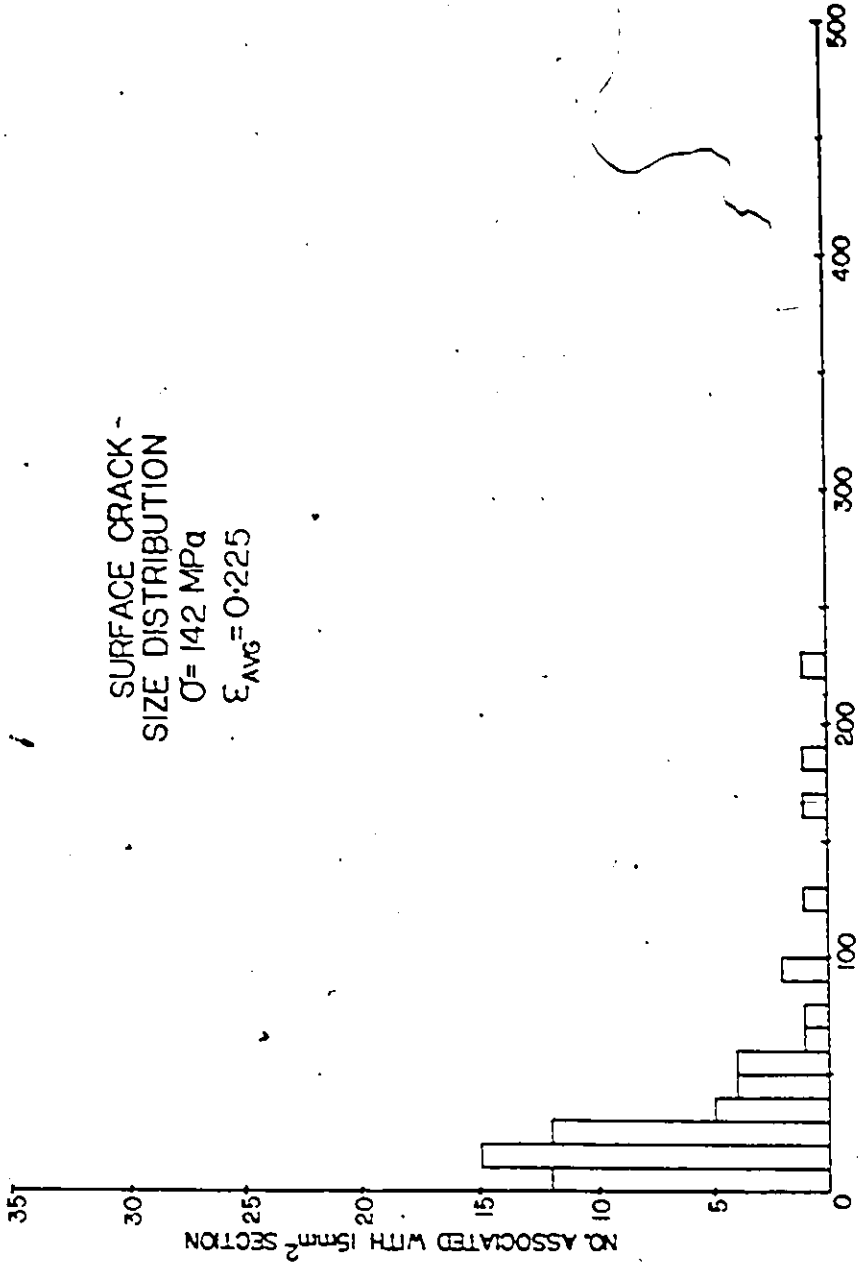

Fig. B.18: Histogram of the surface crack size distribution which developed at a strain of 0.225. Results have been normalized to a length of sample edge which bounds 15 mm^2 of sample in cross-section. The initial applied stress was 142 MPa.

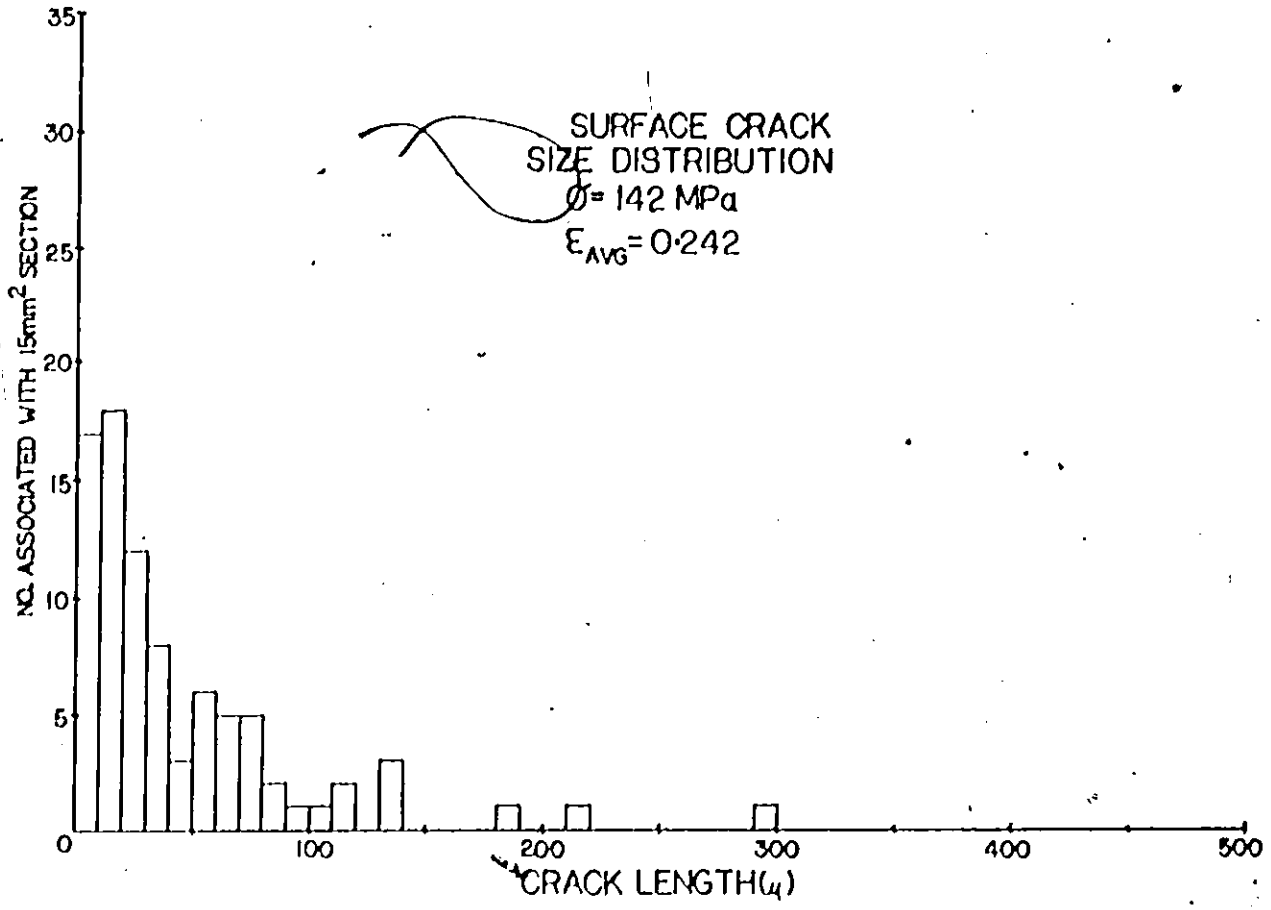

Fig. B.19: Histogram of the surface crack size distribution which developed at a strain of 0.242. Results have been normalized to a length of sample edge which bounds 15 mm^2 of sample in cross-section. The initial applied stress was 142 MPa.

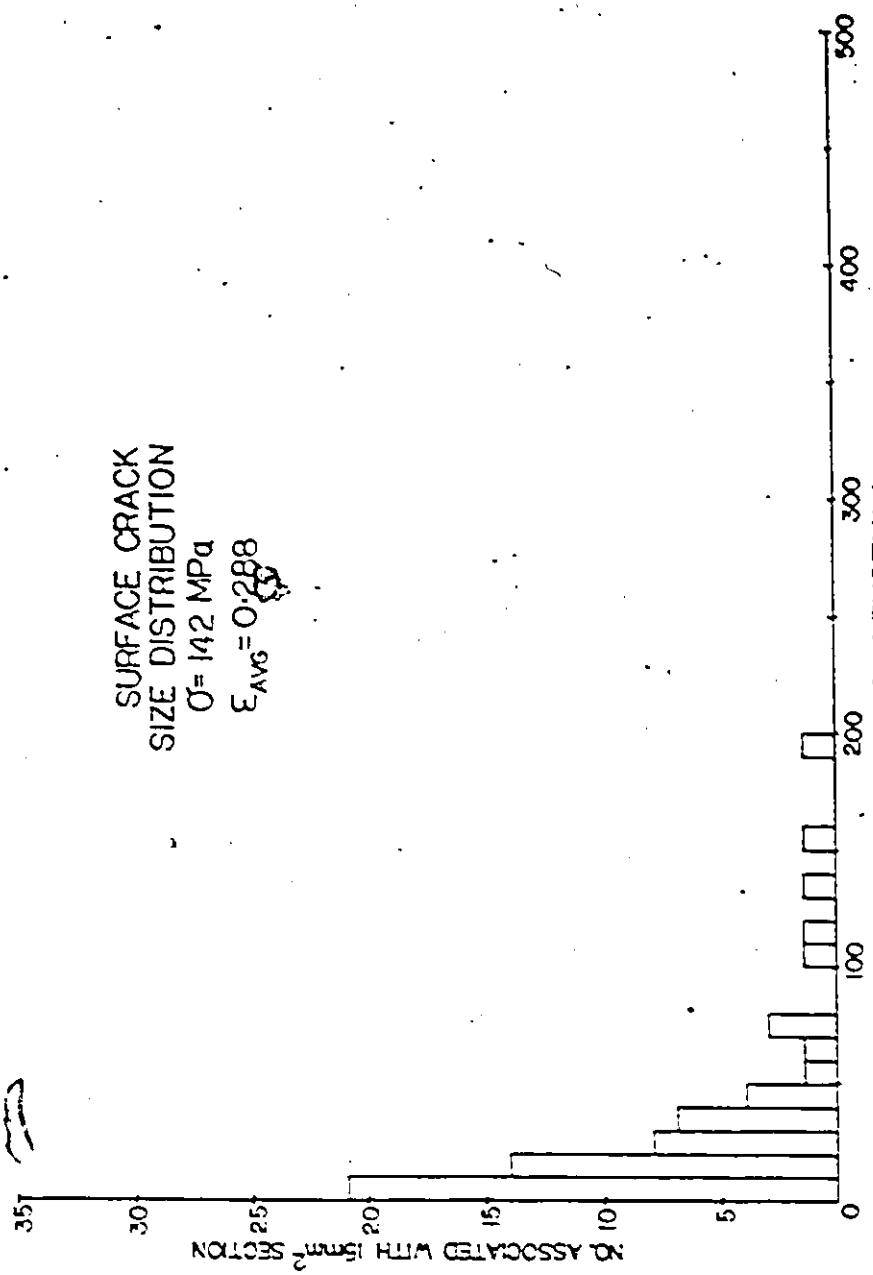

Fig. B.20: Histogram of the surface crack size distribution which developed at a strain of 0.288. Results have been normalized to a length of sample edge which bounds 15 mm^2 of sample in cross-section. The initial applied stress was 142 MPa.

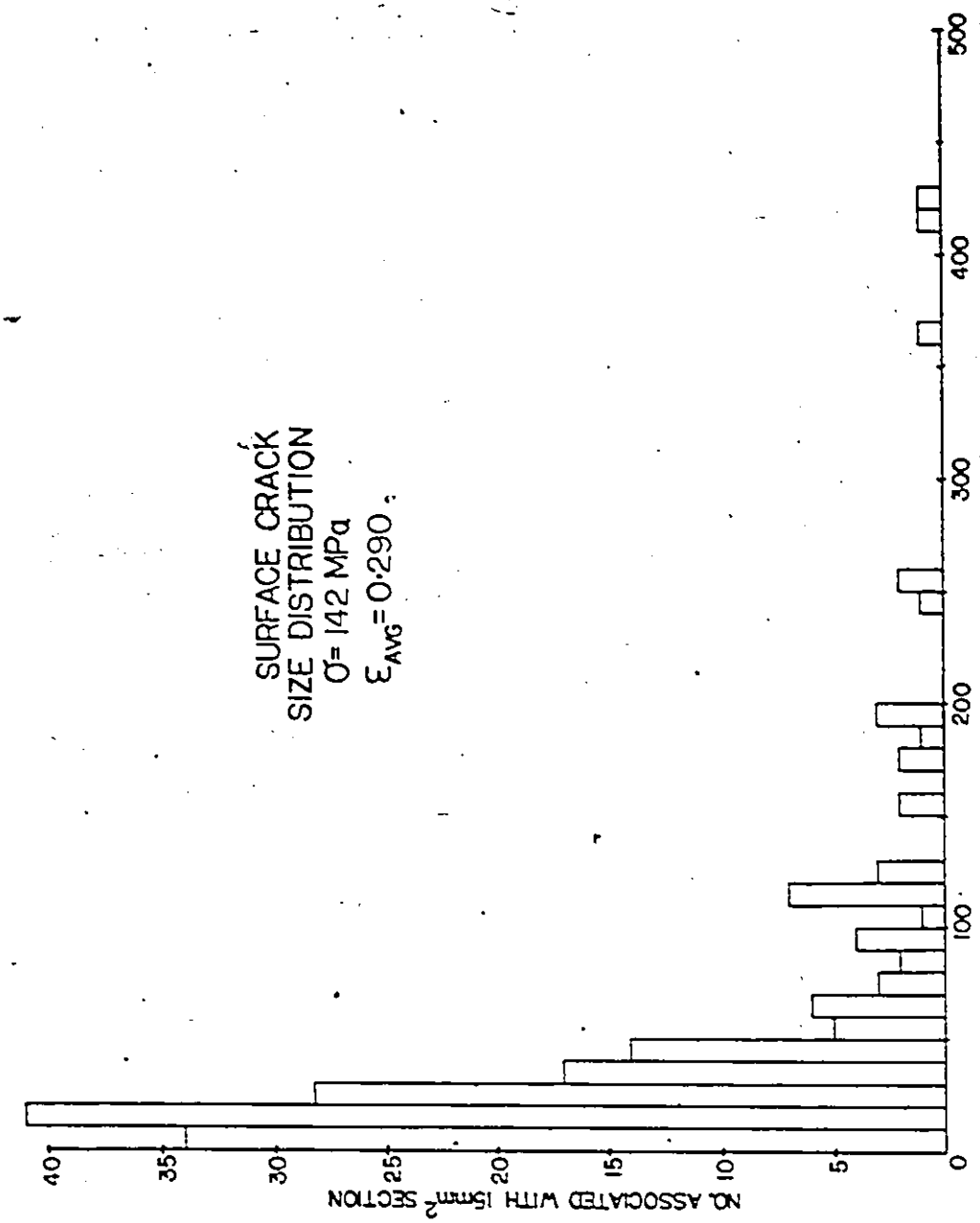

Fig. B.21: Histogram of the surface crack size distribution which developed at a strain of 0.290. Results have been normalized to a length of sample edge which bounds 15 mm^2 of sample in cross-section. The initial applied stress was 142 MPa.

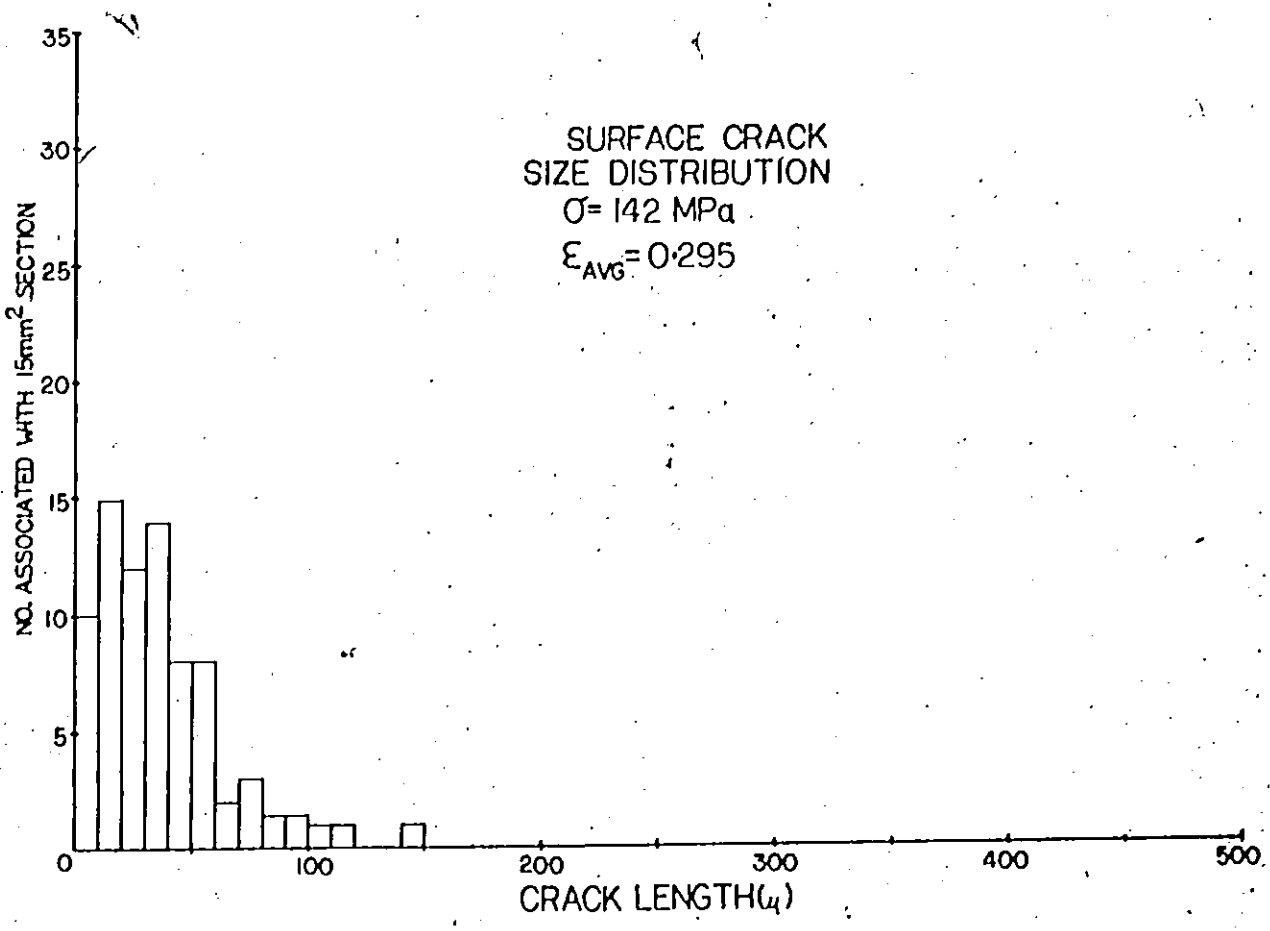

Fig. B.22: Histogram of the surface crack size distribution which developed at a strain of 0.295. Results have been normalized to a length of sample edge which bounds 15 mm^2 of sample in cross-section. The initial applied stress was 142 MPa.

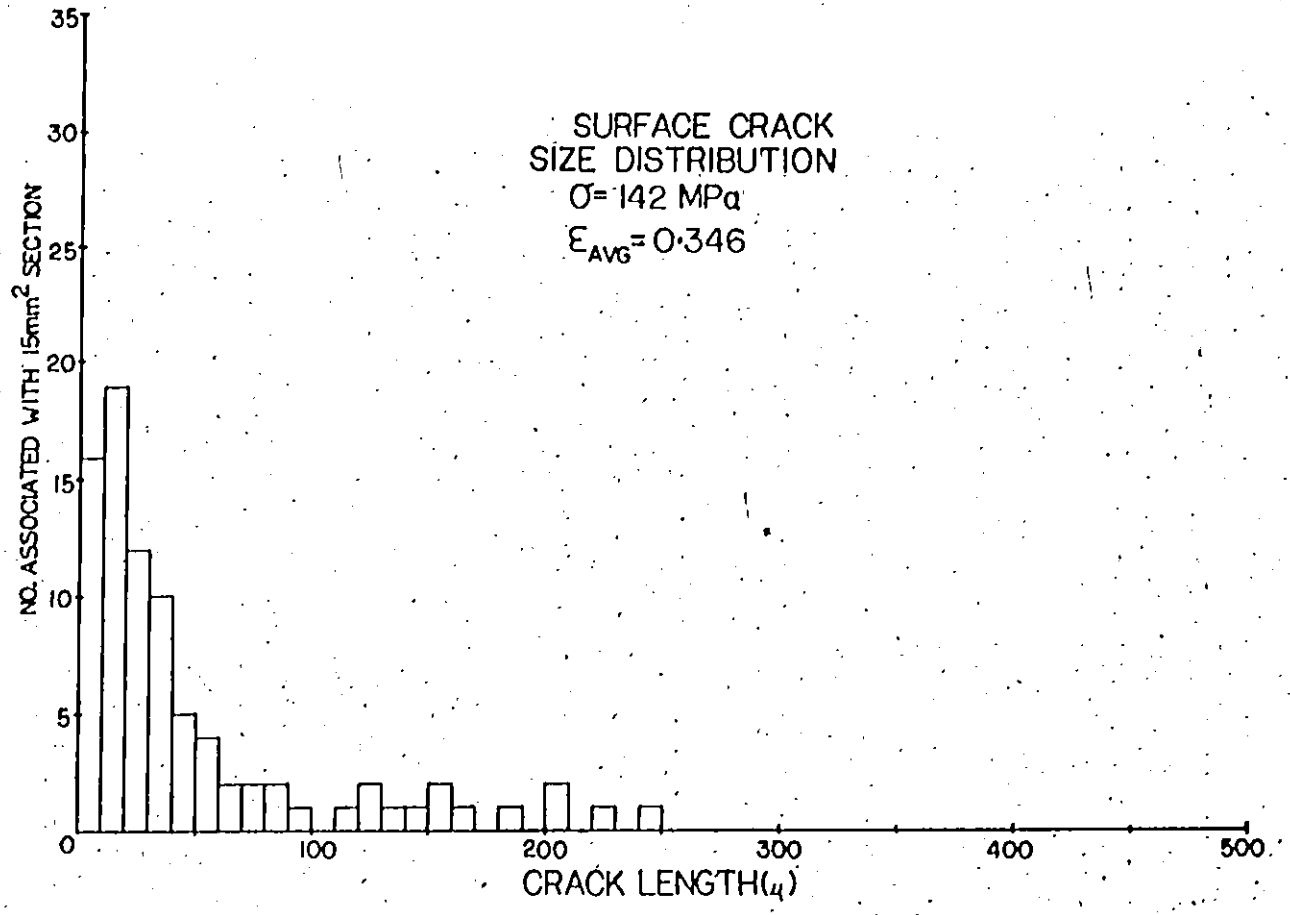

Fig. B.23: Histogram of the surface crack size distribution which developed at a strain of 0.346. Results have been normalized to a length of sample edge which bounds 15 mm^2 of sample in cross-section. The initial applied stress was 142 MPa.

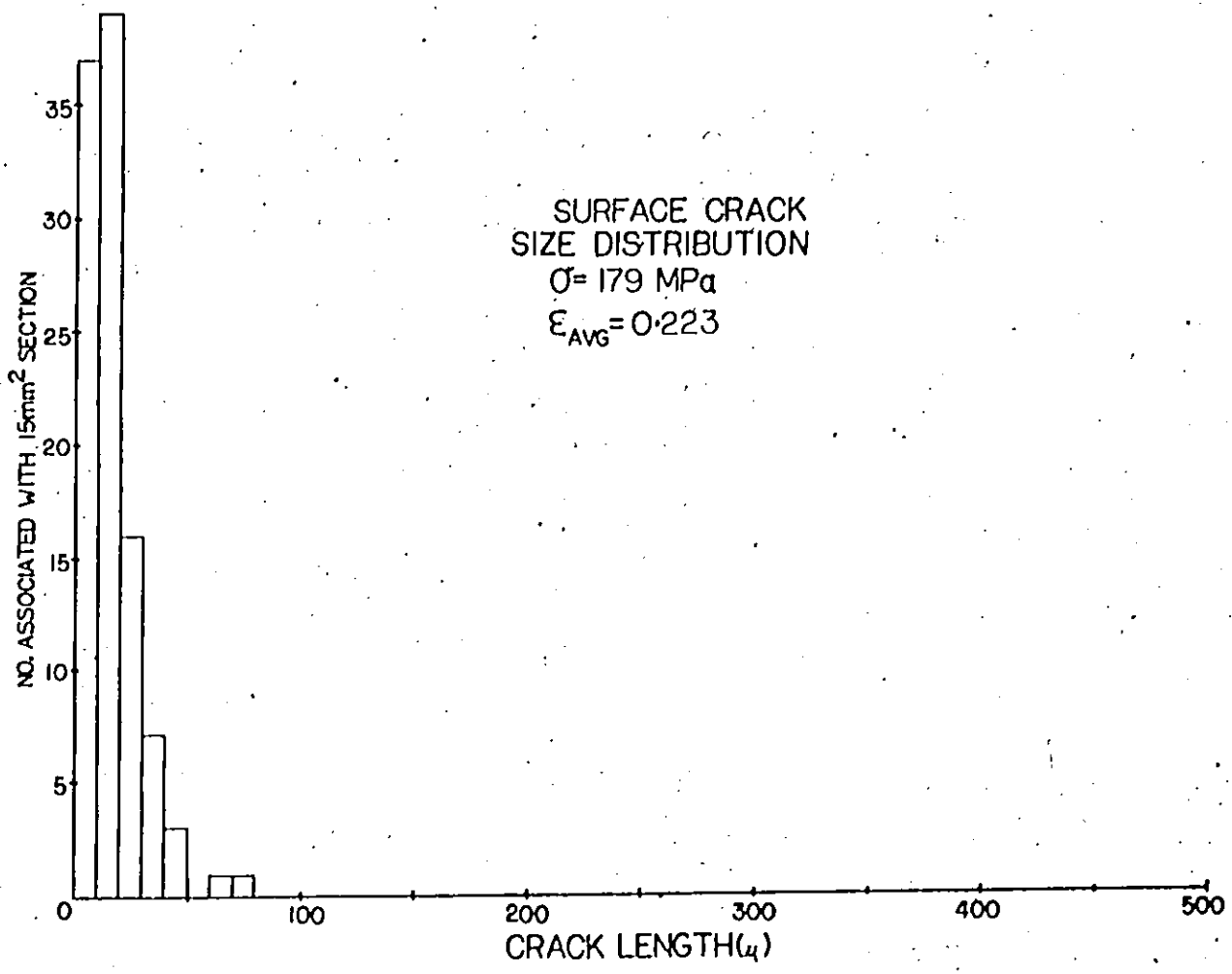

Fig. B.24: Histogram of the surface crack size distribution which developed at a strain of 0.223. Results have been normalized to a length of sample edge which bounds 15 mm^2 of sample in cross-section. The initial applied stress was 179 MPa.

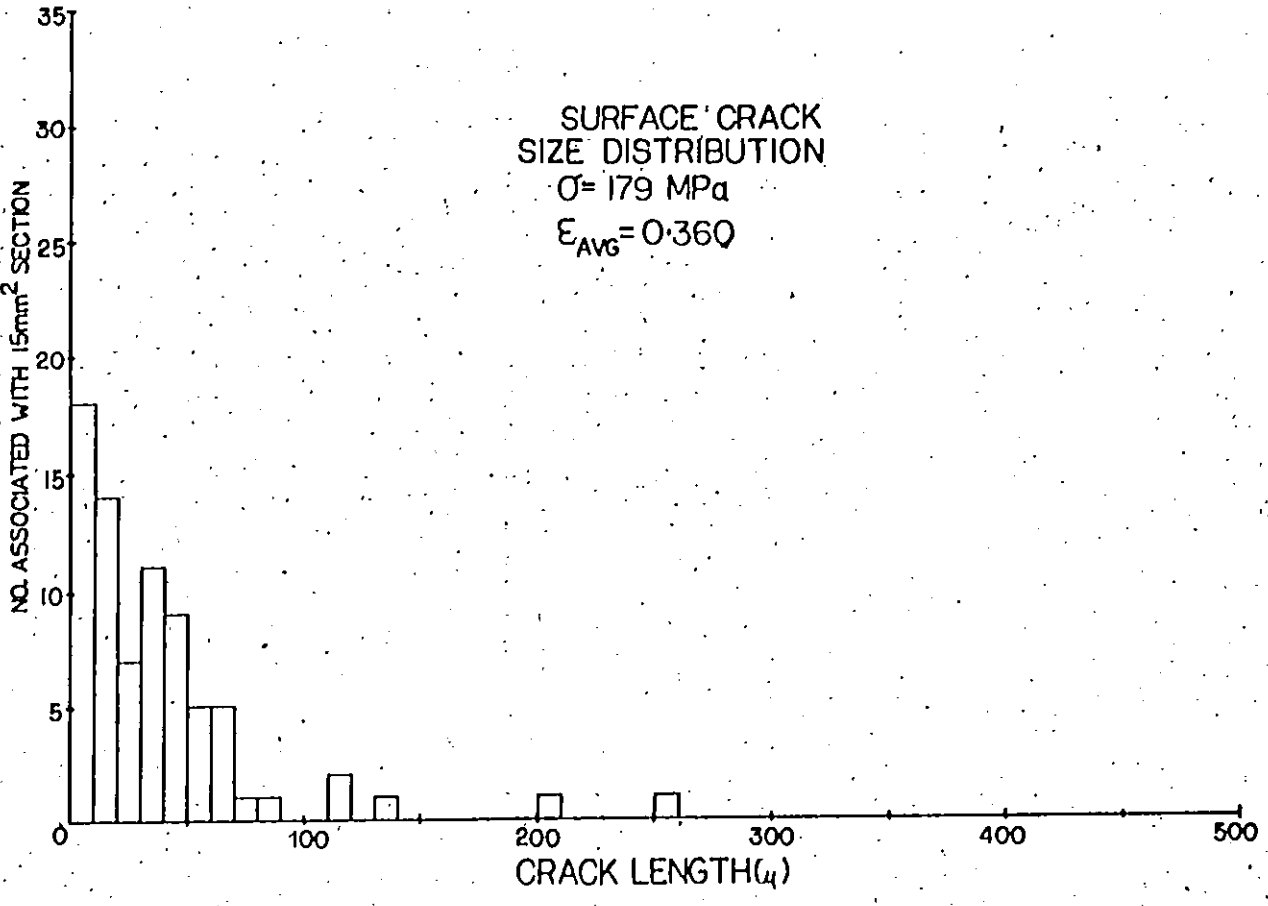

Fig. B.25: Histogram of the surface crack size distribution which developed at a strain of 0.360. Results have been normalized to a length of sample edge which bounds 15 mm^2 of sample in cross-section. The initial applied stress was 179 MPa.

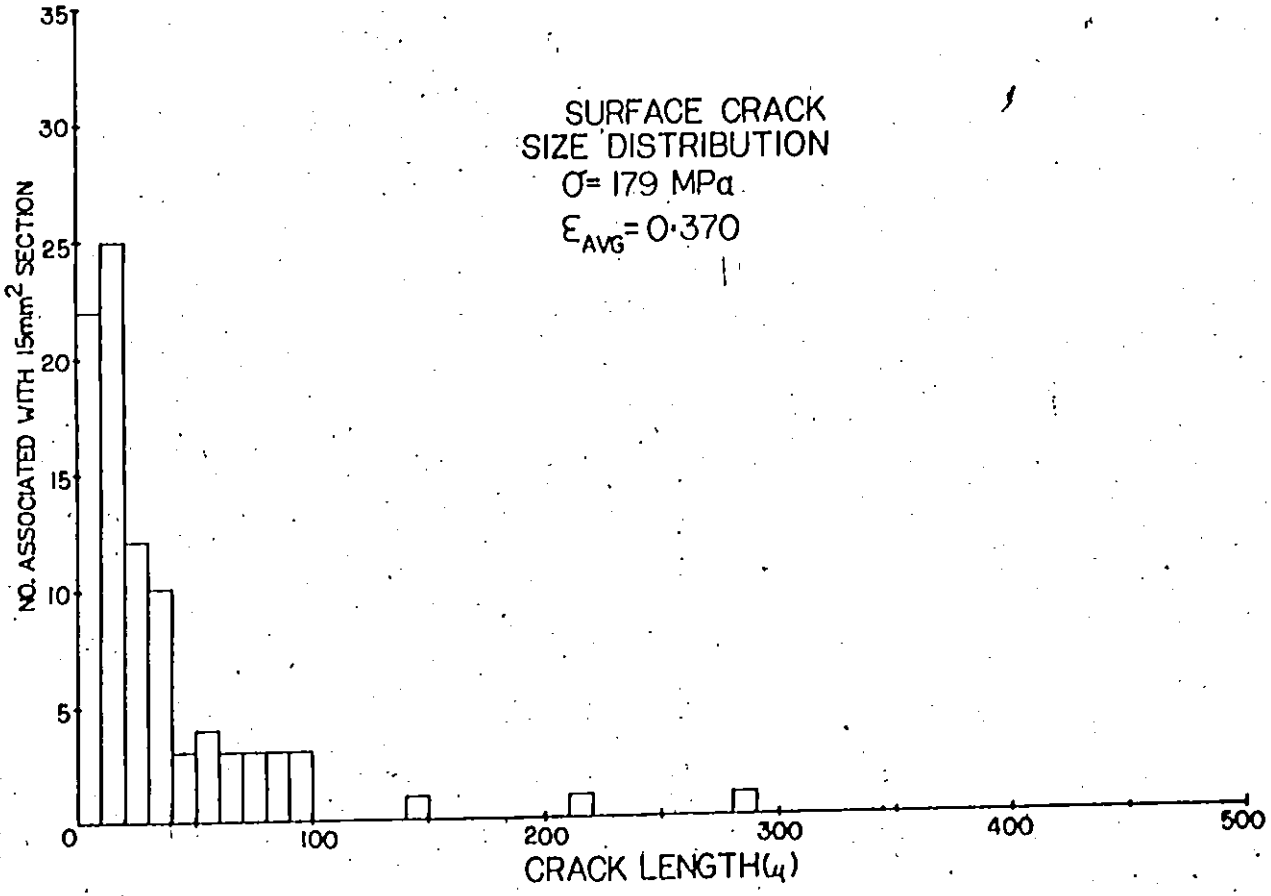

Fig. B.26: Histogram of the surface crack size distribution which developed at a strain of 0.370. Results have been normalized to a length of sample edge which bounds 15 mm^2 of sample in cross-section. The initial applied stress was 179 MPa.

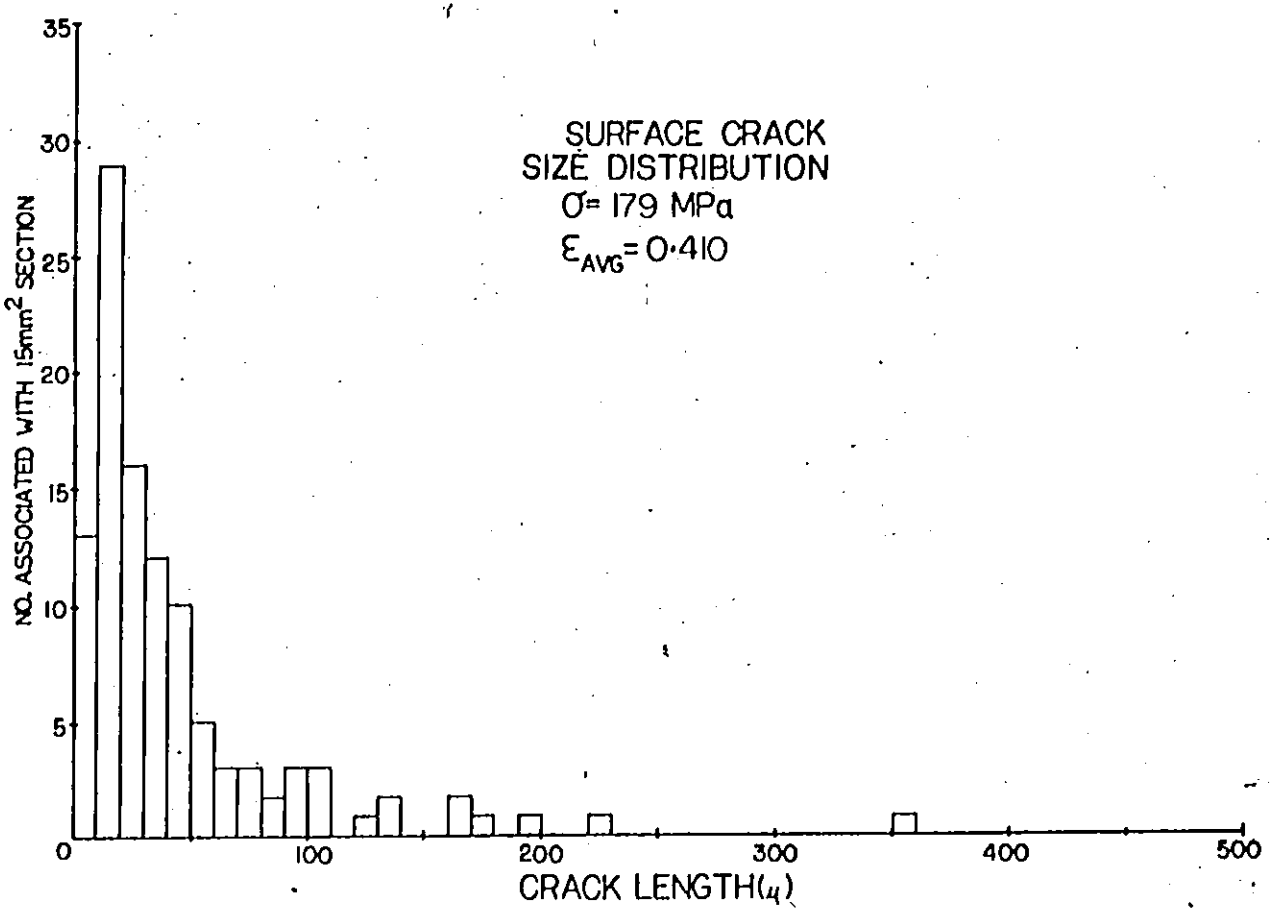

Fig. B.27: Histogram of the surface crack size distribution which developed at a strain of 0.410. Results have been normalized to a length of sample edge which bounds 15 mm^2 of sample in cross-section. The initial applied stress was 179 MPa.

REFERENCES

Anand, L., and Spitzig, W.A. (1980) J. Mech. Phys. Solids 28, 113.

Anand ,L., and Spitzig, W.A. (1982) Acta Met. 30, 553.

Anderson, P.M., and Rice, J.R. (1985) Acta Met. 33, 409.

Argon, A.S. (1982) in "Recent Progress in Creep and Fracture of Engineering Materials and Structures", B. Wilshire and D.R.J. Owen, eds., Pineridge Press, 1.

Argon, A.S. (1983) Scripta Met. 17, 5.

Argon, A.S., Chen, I.-W., and Lau, C.W. (1980) in "Creep-Fatigue-Environment Interactions", R.M. Pelloux and N.S. Stoloff, eds., Met. Soc. of AIME, 46.

Argon, A.S., Chen, I.-W., and Lau, C.W. (1981) in "Three-Dimensional Constitutive Equations and Ductile Fracture", S. Nemat-Nasser, ed., North-Holland Pub., 23.

Argon, A.S., and Im, J. (1975) Met. Trans. 6A, 839.

Argon, A.S., Im, J., and Needleman, A. (1975) Met. Trans. 6A, 815.

Argon, A.S., Im, J., and Safoglu, R. (1975) Met. Trans. 6A, 825.

Armitage, P. (1949) Biometrika 36, 257.

Ashby, M.F. (1966) Phil. Mag. 14, 1157.

Ashby, M.F. (1972) Surf. Sci. 31, 498.

Ashby, M.F., Ghandi, C., and Taplin, D.M.R. (1979) Acta Met. 27, 699.

Ashby, M.F., and Dyson, B.F. (1984) in "Proc. 6th Int. Conf. on Fracture", S.R. Valluri et. al., eds., Pergamon Press, Vol. 1, 3.

Ashby, M.F., and Embury, J.D. (1985) Scripta Met. 19, 557.

Ashby. M.F., Embury, J.D., Cooksley, S.H., and Teirlinck, D. (1985) Scripta Met. 19, 385.

Baker, T.J., and Charles, J.A. (1971) in "The Effects of Second-Phase Particles on the Mechanical Properties of Steel", Iron and Steel Institute, 79.

Baldi, G., and Buzzichelli, G. (1978) Met. Sci. 12, 459.

Balluffi, R.W., and Siegle, L.L. (1955) Acta Met. 3, 170.

Bansal, P.P., and Ardell, A.J. (1972) Metallography 5, 97.

Barnby, J.T., Shi, Y.W., and Nadkarni, A.S. (1984) Int. J. Frac. 25, 273.

Beremin, F.M. (1981) in "Three-Dimensional Constitutive Relations and Ductile Fracture", S. Nemat-Nasser, ed., North-Holland Pub., 185.

Beremin, F.M. (1982) in "Advances in Fracture Research", ICF5, Pergamon Press, Vol. 2, 809.

Bluhm, J.I., and Morrissey, R.J. (1966) in "Proc. 1st Int. Conf. Fracture", Sendai, Vol. 3, 1739.

Boettner, R.C., and Robertson, W.D. (1961) Trans. AIME 221, 613.

Boots, B.N. (1982) Metallography 15, 53.

Boyd, J.D. (1979) in "Toughness Characterization and Specifications for HSLA and Structural Steels", P.L. Mangonon, Jr., ed., Metallurgical Society of AIME, 216.

Bramfitt, B.L., and Marder, A.R. (1979) in "Toughness Characterization and Specifications for HSLA and Structural Steels", P.L. Mangonon, Jr., ed., Metallurgical Society of AIME, 236.

Briant, C.L., and Banerji, S.K. (1978) Int. Met. Rev. 23, 164.

Bridgman, P.W. (1952) "Studies in Large Plastic Flow and Fracture", McGraw-Hill, New York.

Brown, L.M. (1976) in "Proc. Conf. on Mech. Phys. of Fracture", Cambridge, England, paper 10.

Brown, L.M., and Embury, J.D. (1973) in "Proc. 3rd Int. Conf. on Strength of Metals and Alloys", Cambridge, England, 164.

Brown, L.M., and Stobbs, W.M. (1976) Phil. Mag. 34, 351.

Browstow, W., Dussault, J.-P., and Fox, B.L. (1978) J. Computational Phys. 29, 81.

Brozzo, P., Buzzichelli, G., Mascanzoni, A., and Mirabile, M. (1977) Met. Sci. 11, 123.

Burke, M.A., and Nix, W.D. (1975) Acta Met. 23, 793.

Butrymowicz, O.B., Manning, J.R., and Read, M. (1977) "Diffusion Rate Data and Mass Transport Phenomena for Copper Systems", Int'l Copper Research Ass'n Inc., 22.

Cane, B.G., and Greenwood, G.W. (1975) Met. Sci. 9, 55.

Chen, C.W., and Machlin, E.S. (1958) Trans. AIME 218, 177.

Cheng, J.-H., Embury, J.D., Shehata, M.T., Boyd, J.D., and McCutcheon, D.B. (1982) Can. Met. Quart. 21, 299.

Chin, G.Y., Hosford, W.F., and Backofen, W.A. (1964) Trans. AIME 230, 437.

Chuang, T.J., and Rice, J.R. (1973) Acta Met. 21, 1625.

Chuang, T.J., Kagawa, K.I., Rice, J.R., and Sills, L.B. (1979) Acta Met. 27, 265.

Clausing, D.P. (1970) Int. J. Frac. Mech. 6, 71.

Cocks, A.C.F., and Ashby, M.F. (1982a) Prog. Mat. Sci. 27, 189.

Cocks, A.C.F., and Ashby, M.F. (1982b) Met. Sci. 16, 465.

Cottrell, A.H. (1958) Trans. AIME 212, 192.

Cox, T.B., and Low, J.R. (1974) Met. Trans. 5, 1457.

Crain, I.K. (1978) Computers and Geosciences 4, 131.

Crossman, F.W., and Ashby, M.F. (1975) Acta Met. 23, 425.

Curry, D.A. (1980a) Met. Sci. 14, 319.

Curry, D.A. (1980b) Met. Sci. 14, 78.

Curry, D.A., and Knott, J.F. (1976) Met. Sci. 10, 1.

Curry, D.A., and Knott, J.F. (1978) Met. Sci. 12, 511.

Curry, D.A., and Knott, J.F. (1979) Met. Sci. 13, 341.

Diggle, D.J. (1979) Biometrics 35, 87.

Diggle, P.J. (1983) "Statistical Analysis of Spatial Point Patterns", Academic Press, London.

Dodd, B., and Atkins, A.G. (1983) Acta Met. 31, 9.

Dugdale, D.S. (1960) J. Mech. Phys. Solids 8, 100.

Dyson, B.F. (1976) Met. Sci. 10, 349.

Dyson, B.F. (1979) Can. Met. Quart. 18, 31.

Dyson, B.F. (1983) Scripta Met. 17, 31.

Dyson, B.F., Loveday, M.S., and Rodgers, M.J. (1976) Proc. Roy. Soc. Lond. A349, 245.

Dyson, B.F., and McLean, M. (1977) Met. Sci. 11, 37.

Dyson, B.F., and McLean, M. (1983) Acta Met. 31, 17.

Edelson, B.I., and Baldwin, W.M. (1962) Trans. ASM 55, 230.

Edward, G.H., and Ashby, M.F. (1979) Acta Met. 27, 1505.

Embury, J.D., and Burger, G. (1985) in "Effects of Inclusions and Residuals in Steels", Ottawa, Canada, to be published.

Embury, J.D., and Cooper, K. (1975) Can. Met. Quart. 14, 69.

Embury, J.D., Evensen, J.D., and Filipovic, A. (1977) in "Fundamental Aspects of Structural Alloy Design", R.I. Jaffee and B.A. Wilcox, eds., Plenum Pub., 67.

Evensen, J.D., Lereim, J., and Embury, J.D. (1979) in "Toughness Characterization and Specifications for HSLA and Structural Steels", P.L. Mangonon, Jr., ed., Metallurgical Society of AIME, 187.

Fisher, J.R., and Gurland, J. (1981a) Met. Sci. 15, 185.

Fisher, J.R., and Gurland, J. (1981b) Met. Sci. 15, 193.

French, I.E., and Weinrich, P.F. (1979a) Met. Trans. 10A, 297.

French, I.E., and Weinrich, P.F. (1979b) Mat. Sci. Eng. 39, 43.

Garafalo, F. (1965) "Fundamentals of Creep and Creep Rupture in Metals", MacMillan Co., New York, pp. 136-146.

Ghandi, C., and Ashby, M.F. (1979) Acta Met. 27, 1565.

Gifkins, R.C. (1959) in "Fracture", B.L. Averbach, D.K. Felbeck, G.T. Hahn, and D.A. Thomas, eds., John Wiley and Sons, 579.

Gil-Sevillano, J., Van Houtte, P., and Aernoudt, E. (1980) Prog. Mat. Sci. 25, 69.

Gilbert, E.N. (1962) Annals of Math. Stat. 33, 958.

Gladman, T., Dulieu, D., and McIvor, I.D. (1977) in "Microalloying 75", Union Carbide Corp., 32.

Goods, S.H., and Brown, L.M. (1979) Acta Met. 27, 1.

Goods, S.H., and Nieh, T.G. (1983) Scripta Met. 17, 23.

Goods, S.H., and Nix, W.D. (1978a) Acta Met. 26, 739.

Goods, S.H., and Nix, W.D. (1978b) Acta Met. 26, 753.

Grant, N.J., and Chaudhuri, A.R. (1965) in "Deformation and Fracture at Elevated Temperatures", N.J. Grant and A.W. Mullendore, eds., MIT Press, 105.

Green, P.J., and Sibson, R. (1978) Computer J. 21, 168.

Grieg-Smith, P. (1952) Ann. Bot. 16, 293.

Groom, J.D.G., and Knott, J.F. (1975) Met. Sci. 9, 390.

Gurland, J. (1972) Acta Met. 20, 735.

Gurson, A.L. (1977) J. Eng. Mat. Tech. 99, 2.

Hahn, G.T. (1984) Met. Trans. 15A, 947.

Hahn, G.T., and Rosenfield, A.R. (1966) Acta Met. 14, 1815.

Hancock, J.W., and Brown, D.K., (1983) J. Mech. Phys. Solids 31,1.

Hancock, J.W., and Cowling, M.J. (1980) Met. Sci. 14, 293.

Hancock, J.W., and MacKenzie, A.C. (1976) J. Mech. Phys. Solids 24, 147.

Hanna, M.D., and Greenwood, G.W. (1982) Acta Met. 30, 719.

Hart, E.W. (1967a) Acta Met. 15, 351.

Hart, E.W. (1967b) Acta Met. 15, 1545.

Hayhurst, D.R. (1972) J. Mech. Phys. Solids 20, 381.

Hayhurst, D.R., Trampczynski, W.A., and Leckie, F.A. (1980) Acta Met. 28, 1171.

Hayhurst, D.R. (1983) in "Engineering Approaches to High Temperature Design", B. Wilshire and D.R.J. Owen, eds., Pineridge Press Ltd., 85.

Hero, H., Evensen, J.D., and Embury, J.D. (1975) Can. Met. Quart. 14, 117.

Herring, C. (1950) J. Appl. Phys. 21, 437.

Hinde, A.L., and Miles, R.E. (1980) J. Statistical Comput. Simul. 10, 205.

Hippsley, C.A., and Druce, S.G. (1983) Acta Met. 31, 1861.

Hull, D., and Rimmer, D.E. (1959) Phil. Mag. 4, 673.

Hult, J., (1974) in "Topics in Applied Continuum Mechanics", J.L. Zeman and F. Ziegler, eds., Springer-Verlag, 137.

Hult, J. (1979) in "Mechanisms of Deformation and Fracture", K.E. Easterling, ed., Pergamon Press, 231.

Humphreys, F.J., and Stewart, A.T. (1972) Surface Sci. 31, 389.

Intrater, J., and Machlin, E.S. (1959) J. Inst. Metals 88, 305.

Irwin, G.R. (1962) J. Appl. Mech. 29, 651.

Janson, J., and Hult, J. (1977) J. Mechanique Appliquee 1, 69.

Jensen, R.R., and Tien, J.K. (1981) in "Metallurgical Treatises", J.K. Tien and J.F. Elliott, eds., Metallurgical Society of AIME, 529.

Johannesson, T., and Tholen, A. (1969) J. Inst. Metals 97, 243.

Johnson, A.E., Henderson, J., and Khan, B. (1962) in "Complex-Stress Creep, Relaxation, and Fracture of Metallic Alloys", H.M.S.O., London, Ch. 4.

Jokl, M.L., Vitek, V., and McMahon, C.J. (1980) Acta Met. 28, 1479.

Kachanov, L.M. (1958) Izv. Akad. Nauk S.S.S.R., Otd. Tekh. Nauk., No. 8, 26 (in Russian).

Kelly, A. (1972) "Strong Solids", 2nd ed., Oxford University Press.

Kelly, A., and Street, R.N. (1972) Proc. Roy. Soc. Lond. A328, 267.

Knott, J.F. (1966) J. Iron Steel Inst. 204, 104.

Knott, J.F. (1977) in "Fracture 1977", ICF4, University of Waterloo Press, Vol. 1, 61.

Knott, J.F. (1984) in "Proc. 6th Int. Conf. Fracture", S.R. Vallurri et. al., eds., Pergamon Press, Vol. 1, 83.

Knott, J.F., and Cottrell, A.H. (1963) J. Iron Steel Inst. 201, 249.

Kocks, U.F. (1966) Acta Met. 14, 1629.

Kotilainen, H. (1980a) in "Fracture and Fatigue", J.C. Radon, ed., Pergamon Press, 217.

Kotilainen, H. (1980b) Ph.D. Dissertation, Helsinki University of Technology, Otaniemi.

Kotilainen, H., Torronen, K., and Nenonen, P. (1982) in "Advances in Fracture Research", ICF5, D. Francois, ed., Pergamon Press, Vol. 2, 723.

Lau, C.W., and Argon, A.S. (1977) in "Fracture 1977', ICF4, University of Waterloo Press, Vol. 2, p. 595.

Leckie, F.A. (1978) Phil. Trans. Roy. Soc. Lond. A288, 27.

Leckie, F.A., and Hayhurst, D.R. (1974) Proc. Roy. Soc. Lond. A340, 323.

Leckie, F.A., and Hayhurst, D.R. (1977) Acta Met. 25, 1059.

Leckie, F.A., and Ponter, A.R.S. (1974) Ingenieur Arch. 43, 158.

LeRoy, G., Embury, J.D., Edward, G., and Ashby, M.F. (1981) Acta Met. 29, 1509.

Lewandowski, J.J., and Thompson, A.W. (1985) submitted to Met. Trans.

Lindley, T.C., Oates, G., and Richards, C.E. (1970) Acta Met. 18, 1127.

Low, J.R. (1954) Trans ASM 46A, 163.

Luo, L.G., Quarrington, A.I., and Embury, J.D. (1985) Eng. Fract. Mech. 21, 465.

Martin, J.W. (1980) "Micromechanisms in Particle-Hardened Alloys", Cambridge University Press.

MacKenzie, A.C., Hancock, J.W., and Brown, D.K. (1977) Eng. Frac. Mech. 9, 167.

McClintock, F.A. (1968a) J. Appl. Mech. 35, 363.

McClintock, F.A. (1968b) in "Ductlity", ASM, Metals Park, Ohio, 255.

McClintock, F.A. (1968c) Int. J. Frac. Mech. 4, 101.

McClintock, F.A., Kaplan, S.M., and Berg, C.A. (1966) Int. J. Frac. Mech. 2, 614.

McClintock, F.A., Parks, D.M., and Bassani, J.L. (1981) in "Fracture Mechanics of Ductile and Tough Materials and its Applications to Energy Related Structures", H.W. Liu, T. Kunio, V. Weiss, and H. Okamura, eds., Martinius Nijhoff Publishers, 3.

McLean, A., and Kay, D.A.R. (1977) in "Microalloying 75", Union Carbide Corp., 215.

McMahon, C.J., and Cohen, M. (1965) Acta Met. 13, 591.

McRobie, D.E., and Knott, J.F. (1985) Mat. Sci. and Tech. 1, 357.

Mancuso, J.F., and Li, C.Y. (1979) Met. Trans. 10A, 1719.

Mead, R. (1974) Biometrics 30, 295.

Meijering, J.L. (1953) Phillips Res. Repts. 8, 270.

Melander, A. (1979) Mat. Sci. Eng. 39, 57.

Melander, A. (1980a) Acta Met. 28, 1799.

Melander, A. (1980b) Scand. J. Metallurgy 9, 51.

Melander, A., and Stahlberg, U. (1980) Int. J. Frac. 16, 431.

Miles, R.E. (1970) Math. Biosciences 6, 85.

Miles, R.E. (1972) Adv. Appl. Prob., Suppl., 243.

Miles, R.E. (1974) in "Stochastic Geometry", E.F. Harding and D.G. Kendall, eds., John Wiley and Sons.

Mullendore, A.W., and Grant, N.J. (1965) in "Deformation and Fracture at Elevated Temperatures", N.J. Grant and A.W. Mullendore, eds., MIT Press, 165.

Nagumo, N. (1973) Acta Met. 21, 1661.

Needham, N.G., and Greenwood, G.W. (1975) Met. Sci. 9, 258.

Needleman, A. (1972) J. Appl. Mech. 39, 964.

Needleman, A., and Rice, J.R. (1980) Acta Met. 28, 1315.

Nieh, T.G., and Nix, W.D. (1979) Acta Met. 27, 1097.

Nieh, T.G., and Nix, W.D. (1980) Acta Met. 28, 557.

Nix, W.D., Matlock, D.K., and DiMelfi, R.J. (1977) Acta Met. 25, 495.

Oates, G. (1969) J. Iron Steel Inst. 207, 353.

Odqvuist, F.K.G. (1974) "Mathematical Theory of Creep and Creep Rupture", 2nd ed., Oxford:Clarendon Press, Ch. 11.

Ohno, N., and Hutchinson, J.W. (1984) J. Mech. Phys. Solids 32, 63.

Otsuka, A., Miyata,T., Nishimura, S., and Ohashi, M. (1979) in "Fracture Mechanics in Engineering Application", G.C. Sih and S.R. Valluri, eds., Sijthoff and Noordhoff, 111.

Palmer, I.G., and Smith, G.C. (1968) in "Oxide Dispersion Strengthening", G. Ansell, ed., Gordon Breach, New York, 253.

Pavinich, W., and Raj, R. (1977) Met. Trans. 8A, 1917.

Perra, M., and Finnie, I. (1977) in "Fracture 1977", ICF4, University of Waterloo Press, Vol. 2, 415.

Perry, A.J. (1974) J. Mat. Sci. 9, 1016.

Pharr, G.M., and Nix, W.D. (1979) Acta Met. 27, 1615.

Pickering, F.B. (1977) in "Microalloying 75", Union Carbide Corp., 9.

Pickering, F.B. (1978) "Physical Metallurgy and the Design of Steels", Applied Science Publishers.

Pickering, F.B. (1979), ed.,"Inclusions", Institution of Metallurgists, monograph no. 3.

Pickering, F.B. (1984) in "HSLA Steels: Technology and Applications", American Society for Metals, 1.

Piggott, M.R. (1980) "Load-Bearing Fibre Composites", Pergamon Press.

Rabotnov, Yu N. (1969) "Creep Problems in Structural Members", North-Holland, Amsterdam.

Raj, R., and Ghosh, A.K. (1981) Met. Trans. 12A, 1291.

Ratcliffe, R.T., and Greenwood, G.W. (1965) Phil. Mag. 12, 59.

Rhynsburger, D. (1973) Geog. Analysis 5, 133.

Rice, J.R. (1976) in "Proc. 14th IUTAM Congress", W. Koiter, ed., North-Holland Pub., 207.

Rice, J.R. (1981) Acta Met. 29, 675.

Rice, J.R., and Thomson, R. (1974) Phil. Mag. 29, 73.

Rice, J.R., and Tracey, D.M. (1969) J. Mech. Phys. Solids 17, 201.

Riedel, H. (1985) Z. Metallkunde 76, 669.

Ripley, B.D. (1979) J. Roy. Stat. Soc. B41, 368.

Ritchie, R.O., Knott, J.F., and Rice, J.R. (1973) J. Mech. Phys. Solids 21, 395.

Roach, S.A. (1968) "The Theory of Random Clumping", Methuen, London.

Rudnicki, J.W., and Rice, J.R. (1975) J. Mech. Phys. Solids 23, 371.

Schwartz, H., and Exner, H.E.(1983) J. Microscopy 129, 155.

Sherby, O.D., and Burke, P.M. (1967) Prog. Mat. Sci. 13, 325.

Shimura, M., and Saito, S. (1980) Sci. Rpts. of Res. Inst., Tohoku University 29, 50.

Sih, G.C. (1973) "Handbook of Stress Intensity Factors", Lehigh University, Bethlehem, Pennsylvania.

Smith, E. (1966) in "Proc. Conf. on the Physical Basis of Yield and Fracture", Inst. of Physics and the Physical Society, 36.

Smith, E., and Barnby, J.T. (1967) Mat. Sci. 1, 56.

Speich, G.R., and Dabkowski, D.S. (1977) in "The Hot Deformation of Austenite", J.B. Ballance, ed., Metallurgical Society of AIME, 557.

Spitzig, W.A. (1979) Acta Met. 27, 523.

Spitzig, W.A. (1983a) Met. Trans. 14A, 271.

Spitzig, W.A. (1983b) Met. Trans. 14A, 471.

Spitzig, W.A. (1985) Acta Met. 33, 175.

Spitzig, W.A., and Richmond, O. (1984) Acta Met. 32, 457.

Spitzig, W.A., Kelly, J.F., and Richmond, O. (1985) Metallography 18, 235.

Stanzl, S.E., Argon, A.S., and Tschegg, E.K. (1983) Acta Met. 31, 833.

Steele, J.H., Jr. (1976) Met. Trans. 7A, 1325.

Stroh, A.N. (1954) Proc. Roy. Soc. Lond. A223, 404.

Svensson, L.-E., and Dunlop, G.L. (1979) Can. Met. Quart. 18, 39.

Svensson, L.-E., and Dunlop, G.L. (1981) Int. Met. Rev. 26, 109.

Tanaka, T. (1981) Int. Met. Rev. 26, 185.

Tanaka, T., Enami, T., Kimura, M., Saito, Y., and Hatomura, T. (1982) in "Thermomechanical Processing of Microalloyed Austenite", A.J. DeArdo, G.A. Ratz, and P.J. Wray, eds., Metallurgical Society of AIME, 195.

Tanaka, T., Tabata, T., Hatomura, T., and Shiga, C. (1977) in "Microalloying 5", Union Carbide Corp., 88.

Taplin, D.M.R. (1969) Phil. Mag. 20, 1079.

Teirlinck, D. (1983) Ph.D. thesis, "Influence of the Stress State on Various Fracture Modes", McMaster University.

Thomason, P.F. (1968) J. Inst. Met. 96, 360.

Thomason, P.F. (1974) in "Prospects of Fracture Mechanics", G.C.Sih, H.C. van Elst, and D. Broek, eds., Noordhoff Int. Pub., 3.

Thomason, P.F. (1985a) Acta Met. 33, 1079.

Thomason, P.F. (1985b) Acta Met. 33, 1087.

Thomson, R.D., and Hancock, J.W. (1984a) Int. J. Frac. 26, 99.

Thomson, R.D., and Hancock, J.W. (1984b) Int. J. Frac. 24, 209.

Thomson, R.D., and Hancock, J.W. (1985) in "Proc. 6th Int. Conf. Fracture", S.R. Valluri et. al., eds., Pergamon Press.

Tracey, D.M. (1971) Eng. Frac. Mech. 3, 301.

Trampczynski, W.A., Hayhurst, D.R., and Leckie, F.A. (1981) J. Mech. Phys. Solids 29, 353.

Tvergaard, V. (1982) J. Mech. Phys. Solids 30, 265.

Ushijima, K., Sugitani, Y., Yamaguchi, S., Shiode, S., and Hashi, M., and Tomono, H. (1984) in "HSLA Steels: Technology and Applications", American Society for Metals, 403.

Wallin, K., Saario, T., and Torronen, K. (1984) Met. Sci. 18, 15.

Weaire, D., and Rivier, N. (1984) Contemp. Phys. 25, 59.

White, C.L. (1983) personal communication through D.S. Wilkinson.

White, C.L., and Padgett, R.A. (1982) Scripta Met. 16, 461.

White, C.L., Scniebel, J.H., and Padgett, R.A. (1983) Met. Trans. 14A, 595.

Wilcox, B.A., and Clauer, A.H. (1972) Acta Met. 20, 743.

Wilkinson, D.S. (1986) unpublished work.

Wilkinson, D.S., Abiko, K., Thyagarajan, N., and Pope, D.P. (1980) Met. Trans. 11A, 1827.

Wilkinson, D.S., and Vitek, V. (1982) Acta Met. 30, 1723.

Wilson, A.D. (1984) in "HSLA Steels:Technology and Applications", American Society for Metals, 419.

Wilson, W.G., and McLean, A. (1980) "Desulphurization of Iron and Steel and Sulphide Shape Control", Iron and Steel Society of AIME.

Wray, P.J., Richmond, O., and Morrison, H.L. (1983) Metallography 16, 39.

Yamamoto, H. (1978) Int. J. Frac. 14, 347.

Zener, C. (1948) Trans. ASM 40A, 163.